Wide-field anterior ocular surface morphometrics

Jennifer Marion Turner

Submitted for the degree of Doctor of Philosophy

School of Optometry and Vision sciences

Cardiff University

December 2011

NOTICE OF SUBMISSION OF THESIS:
POSTGRADUATE RESEARCH

CARDIFF UNIVERSITY
PRIFYSGOL CAERDYDD

DECLARATION

This work has not previously been accepted in substance for any degree and is not concurrently submitted in candidature for any degree.

Signed .... (candidate) Date 30-12-2011............

STATEMENT 1

This thesis is being submitted in partial fulfillment of the requirements for the degree of doctor of philosophy

Signed .... (candidate) Date 30-12-2011............

STATEMENT 2

This thesis is the result of my own independent work/investigation, except where otherwise stated.
Other sources are acknowledged by explicit references.

Signed .... (candidate) Date 30-12-2011............

STATEMENT 3

I hereby give consent for my thesis, if accepted, to be available for photocopying and for inter-library loan, and for the title and summary to be made available to outside organisations.

Signed .... (candidate) Date 30-12-2011............

NOTICE OF SUBMISSION OF THESIS:
POSTGRADUATE RESEARCH

CARDIFF UNIVERSITY
PRIFYSGOL CAERDYDD

STATEMENT 4: PREVIOUSLY APPROVED BAR ON ACCESS

I hereby give consent for my thesis, if accepted, to be available for photocopying and for inter-library loans **after expiry of a bar on access previously approved by the Academic Standards & Quality Committee.**

Signed .... (candidate) Date 30-12-11..............

Summary

The current understanding of anterior eye shape in humans is limited due to available technology and its accessibility. Accurate curvature metrics of specific areas of the peripheral cornea, corneo-limbal junction and anterior sclera have remained obscured by the limits of the palpebral aperture, since the upper and lower eyelids cover most of the vertical aspect.

This thesis starts by comparing the ‘gold standard’ keratometry measurements to commonly used topographic systems. Keratometric analogues were found to be significantly different and in addition provided spurious vertical anterior ocular surface (AOS) profiles. These findings revealed a need to establish an accurate model.

Magnetic resonance imaging (MRI) potentially offers the best opportunity to image the entire AOS structure. However, preliminary studies in this thesis demonstrated that the use of a 3-Tesla MRI scanner was unable to obtain sufficiently resolute data to meet requirements.

As an alternative, ocular impression taking techniques were adopted during the remainder of this thesis to acquire the AOS data. Eye casts from impression moulds were scanned using active laser triangulation and virtual 3-dimensional surfaces rendered. Further investigations defined the most suitable material for impression taking and the amount of deformation of the AOS caused by the procedure. The ocular impression casting and scanning process was examined for accuracy and reliability.

This protocol was used to sample a population of normal white European eyes in order to establish a database and define wide-field AOS variability. Volumetric and 2-dimensional topographic profiles were extracted from the digital 3-dimensional representation obtained, allowing for the analysis of point-to-point curvature differences. For the first time, the entire AOS shape has been defined with known accuracy. In addition, effects of myopic refractive error and gender are presented. This data is of potential importance to ophthalmic surgeons, ocularists, contact lens

practitioners, vision scientists and researchers, in the form of a digital archive of normal white European wide-field AOS topography as a reference source.

Acknowledgements

I am grateful for the invaluable support, advice and encouragement from all of these people, without whom I could not have completed this work.

Academic supervisors: Dr Christine Purslow and Dr Paul J Murphy
Advisor: Professor Keith Meek
Head of School: Professor Tim Wess
Sponsors: Cardiff University and Menicon Co. Ltd

Collaborators:
Fundamental research group (Japan): Tatsutoshi Nakajima, Dr Patricia Choppinet, Atsushi Kobayashi
Manufacturing and Engineering Centre (MEC), Cardiff University: Professor D Pham, Dr Hieu Le Chi
Cardiff University Brain Research Imaging Centre (CUBRIC): Professor Krish Singh, Dr John Evans
Aston University: Professor James Wolffsohn, Dr Amy Shephard, Dr Leon Davies

Menicon Summer Research Bursary recipient: Matthew Dobson

Fellow postgraduates and postdoctorates: Ditipriya Mukhopadhyay, Dr Ashley Wood, Dr Mohamed al-Bagdady, Dr Jyoti Khadka, Dr Felicity Gill, Dr Rhodri Woodhouse, Dr Phil Jones, Sachiko Nishimura, Dr Katharine Evans, Dr Katie Mortlock, Dr Craig Boote.

Administrators: Sue Hobbs, Steve Morgan, John Speck, Leanne Morrish

Inspiration: Professor Donald Korb, Professor Anthony Bron, Ronald Rabbetts, Professor Charles McMonnies, Professor Wolfgang Drexler, Professor Rachel North Professor C Ross Ethier, Richard Earlam.

Colleagues in the NHS: Dr Paul Davies, Mr A Raghu Ram, Sylvia Thompson

Friends: Dr Frank Rakebrandt, Dr Michael Crossland, Dan Erlich, Lynne Speedwell, Ken Pullum, Mr Nick Hawksworth, Nicole Levy, Andrew Radcliffe, Guy Pitt, Colin Millar.

Family: Benjamin and Amélie Jones, Ken and Maureen Turner, Brian Turner

Volunteers: Staff and students of Cardiff University

In memory of my grandfather Arthur Frederick Henry McElhinney and my friend Nicola Hartry

Abbreviations

ACS	Anterior corneal surface
AOS	Anterior ocular surface
ASC	Anterior sclera
ASI	Anterior sclera inferior location
ASIN	Anterior sclera infero-nasal location
ASIT	Anterior sclera infero-temporal location
ASN	Anterior sclera nasal location
AS-OCT	Anterior segment ocular coherence tomography
ASS	Anterior sclera superior location
ASSN	Anterior sclera supra-nasal location
ASST	Anterior sclera supra-temporal location
AST	Anterior sclera temporal location
CC	Central cornea
CEP	Cardiff eyeshape protocol
CLT	Corneo-limbal transition
CLTI	Corneo-limbal transition inferior location
CLTIN	Corneo-limbal transition infero-nasal location
CLTIT	Corneo-limbal transition infero-temporal location
CLTN	Corneo-limbal transition nasal location
CLTS	Corneo-limbal transition superior location
CLTSN	Corneo-limbal transition supra-nasal location
CLTST	Corneo-limbal transition supra-temporal location
CLTT	Corneo-limbal transition temporal location
GP	Gas permeable
I	Inferior
IN	Infero-nasal
IT	Infero-temporal
J-S	Javal-Schiötz Keratometer
N	Nasal
Orb	Orbscan IIz
PAC	Paracentral cornea
PACI	Paracentral cornea inferior location

PACIN	Paracentral cornea infero-nasal location
PACIT	Paracentral cornea infero-temporal location
PACN	Paracentral cornea nasal location
PACS	Paracentral cornea superior location
PACSN	Paracentral cornea supra-nasal location
PACST	Paracentral cornea supra-temporal location
PACT	Paracentral cornea temporal location
PCI	Peripheral cornea inferior location
PCIN	Peripheral cornea inferonasal location
PCIT	Peripheral cornea infero-temporal location
PCN	Peripheral cornea nasal location
PCS	Peripheral cornea superior location
PCSN	Peripheral cornea supra-nasal location
PCST	Peripheral cornea supra-temporal location
PCT	Peripheral cornea temporal location
PEC	Peripheral cornea
Pent	Pentacam
S	Superior
SD	Standard deviation
SEM	Standard error of the mean
SN	Supra-nasal
ST	Supra-temporal
T	Temporal

Table of Contents

Table of Figures

Table of Tables

Introduction

This thesis aimed to determine a method of collecting and representing anterior ocular surface contour data, in 3-dimensions, over an area encompassing the cornea, limbus and anterior sclera. A database of normal white European anterior ocular topography was created, from which morphometric descriptors were determined.

Customised treatment and increasingly higher visual expectations after anterior ocular surgery have increased the demand on technology to provide reliable, repeatable and precise surface contour metrics (Wang, Hill and Swartz, 2006). The optical zone of the cornea is critical in the planning and evaluation of corneal refractive surgery. The zone may vary from 3-7mm in diameter and is defined as the central spherical zone that overlaps the entrance pupil (Liu, Yang and Zhang, 2006). However, the peripheral zone, 4-11mm in diameter, plays an important role in the centration and fitting of corneal contact lenses (Gill, 2010). In a landmark study (Marriott, 1966), *in-vivo* scleral contours were assessed in an attempt to provide topographic information with which to improve the design of scleral contact lenses. The author found considerable variation in curvature, for example, a range of radii of curvature from 12.09mm to 28.75mm in the temporal sector.

The purpose of this work was to advance the ideas of Marriott using modern techniques, and to provide a topographic survey of the entire anterior ocular surface to a reproducibility of ±0.25D, the current industry standard (Huang, 2008). It has been acknowledged that this standard may not be achievable due to differences in tissue structure, since while the cornea is smooth and firm, the overlying conjunctiva is loose and mobile, and additionally confounded by methods of wide-field data collection.

This thesis has reviewed the current literature pertaining to the:

- Formation, structure and function of the anterior ocular surface;
- Modern methods of measurement, with an emphasis on those that may be suitable for primary surface data collection;

- Current methods of representing the anterior ocular surface in a clinical setting.

Chapter 1

Current understanding of anterior ocular surface topography and topographic representation

A review of the literature concerning the measurement of the anterior ocular surface (AOS) contour reveals a plethora of information focused mainly on the cornea. The cornea is part of the sclero-corneal envelope; the outer tunic of the globe, which is lubricated by the tear film, covered intermittently by eyelids and the supporting conjunctiva, and moved and deformed by the interaction of the extrinsic ocular muscles. These structures all contribute to the shape of the surface under scrutiny (Fig 1.1) – the red dotted line marks the position of the ora serrata - circumscribing the area between the muscle insertions and delineating the area of the AOS to be studied.

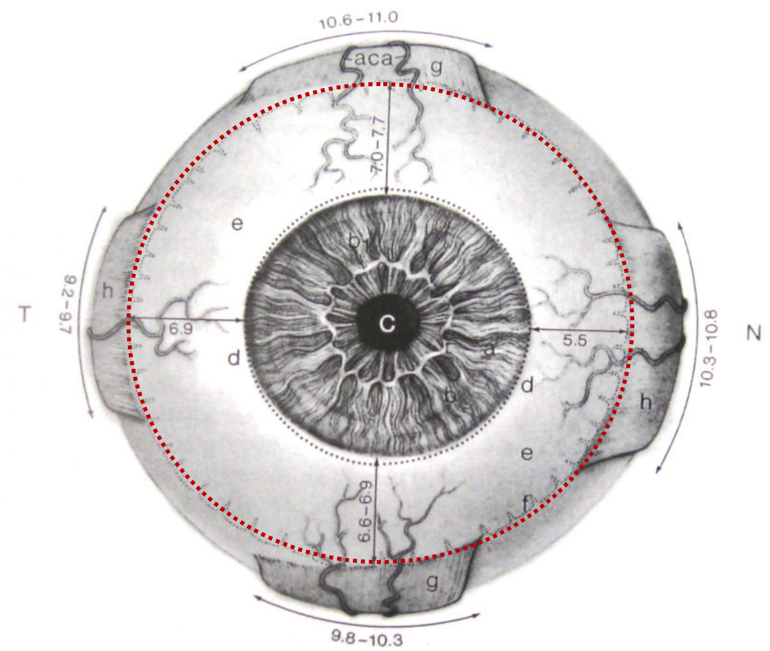

Figure 1.1: Anatomical features of the anterior ocular surface (Bron, Tripathi and Tripathi, 1997) a = cornea, b = iris, b1 = collarette of iris, c = pupil, d = external scleral sulcus, e = sclera, f = ora seratta, g = superior and inferior rectus tendons, h = medial and lateral rectus tendons. The measurements of distances from the cornea to the recti insertion and width of the recti insertions are in millimetres.

1.3 Globe Formation

1.3.1 Embryology

During the first 3 weeks of embryogenesis of the eye, development differentiates cell types into endoderm, mesoderm and ectoderm. These are organised into a neural tube structure. The tube closes at both the cephalic and caudal ends. At day 27 (Fig 1.2), the two optic grooves within the tube have formed into vesicles and envaginated towards the surface ectoderm initiating the lens placode.

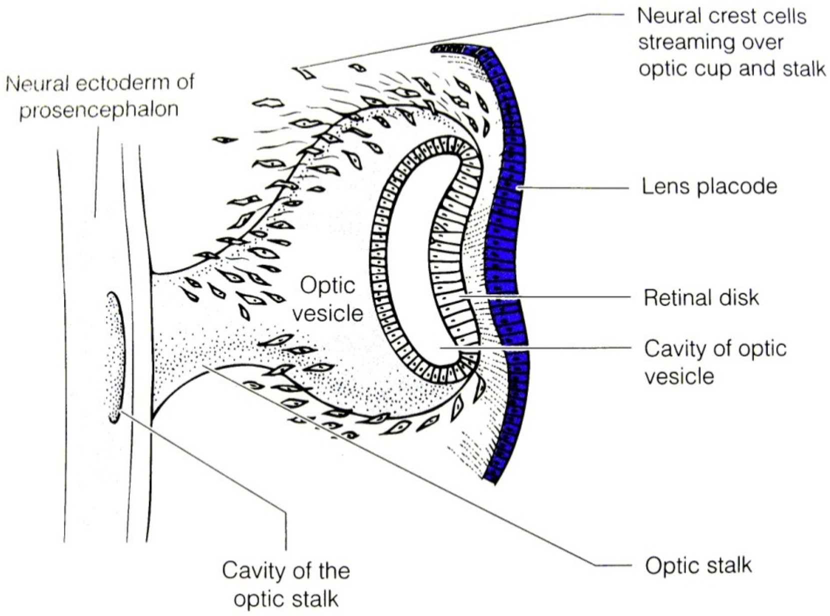

Figure 1.2: Day 27 of human ocular embryonic development (Forrester et al., 1999).

Cells from the neural crest migrate over the surface of the optic stalk and cup. By week 6, the first myofibrils of the extra-ocular muscles are formed from this mesenchyme, which condenses and by day 44 (Fig 1.3) has differentiated to form the developing sclera (Barishak, 1992). The primary cornea stroma is derived from cells of the surface ectoderm. Studies of chick corneas have shown migration of mesenchymal cells from the periphery to the primary stroma (Hay and Revel, 1969) with those present on the optic cup lip becoming the corneal endothelium. These cells are followed by a second wave of mesenchymal cells, which become corneal fibroblasts. The exact sequence of cell migration and highly-ordered deposition of collagen to form the transparent corneal structure is unknown (Quantock and Young, 2008).

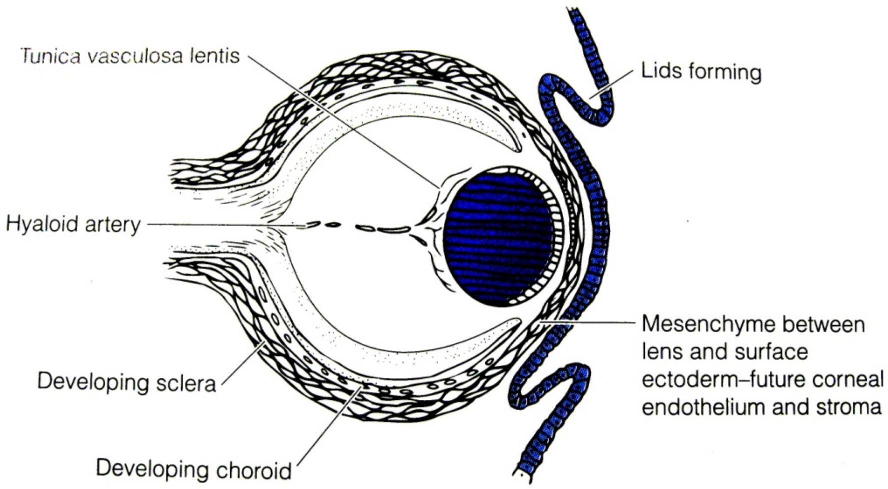

Figure 1.3: Day 44 of human ocular embryonic development (Forrester et al., 1999)

Errors of differentiation, cell migration and induction during the first 8 weeks cause congenital anomalies of the whole eye. Those anomalies occurring earlier in the process result in the most profound structural effect. Conditions such as teratoma, anophthalmos, microphthalmos with cyst, and colabomatous microphthalmos originate prior to 8 weeks (Alex, 2003). Between week 7 and 15, anomalies such as anterior segment disgenesis, persistent hyperplastic primary vitreous, congenital glaucoma, congenital cataract, microphthalmos and deformations of lid, muscle and orbit have been reported (Alex, 2003).

1.1.2 Growth and development

The distance between the anterior and posterior pole, otherwise called the axial length, of a full term infant is typically about 17mm (Fledelius and Christensen, 1996) and the eye is hypermetropic (Cook and Glasscock, 1951). Infants must therefore accommodate to focus distant and near objects onto the retina. With growth, the focal length of the combined corneal and lens system gradually reduces, and the focal plane approaches the retina as the globe elongates. This is the process of emmetropisation and by age 6 years the image and retinal plane ideally coincide. Figure 1.4 illustrates the process of emmetropisation.

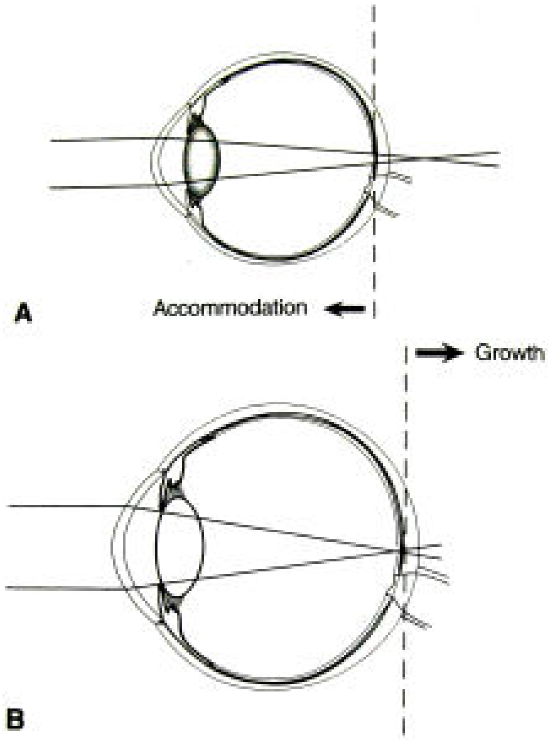

Figure 1.4: The process of emmetropisation (Marsh-Tootle and Frazier, 2006) A (top) shows the accommodation needed by infants to shift the image plane closer to the retina. B (bottom) emmetropia at 6 years, the axial length of most eyes is perfectly matched to the plane of focus of the eye.

The mean keratometry measurement for a newborn infant's cornea is 55D, which is 12D steeper than the average adult measurement (Gordon and Donzis, 1985). The corneal diameter increases from about 10mm in each direction in the neonate to typically 10.6mm vertically and 11.7mm horizontally in the adult (Gordon and Donzis, 1985).

After year 6, growth is slower, and a number of studies suggest that the globe reaches its adult size and stabilises around age 15 years (Adams and McBrien, 1992), (McBrien and Millodot, 1987) but further investigations have verified that adult onset-myopia first manifests after age 18, and it is unclear whether axial growth never ceased in these individuals or globe elongation occurred after a period of globe stability (Adams, 1987).

1.2 Anterior ocular surface location and structure

1.2.1 Location

Each globe is located in the anterior orbit (Fig 1.5), nearer to the roof and lateral wall than the other walls, occupying approximately one fifth of the orbital cavity (Bron et al., 1997)

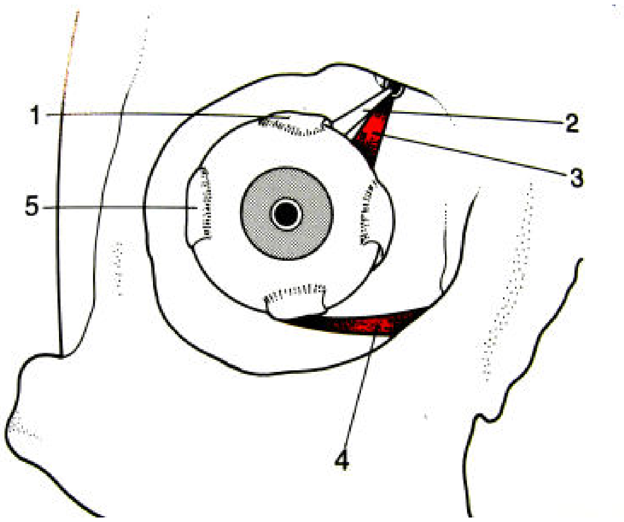

Figure 1.5: The location of the globe in relation to the orbit (Bron et al., 1997) 1 = superior rectus, 2 = reflected tendon of the superior oblique, 3 = muscle body of the superior oblique, 4 = inferior oblique muscle, 5 = lateral rectus muscle.

1.2.2 Macroscopic structure

The eyeball is not spherical, but consists of two modified spheres fused together at the limbus. The external scleral sulcus marks the transition between the two. The sclera (from the Greek word scleros meaning hard) is a white opaque, resilient and elastic tissue, comprising 90% of the globe circumference. It has an external radius of curvature of 12mm and internal radius of 11.5mm (Hogan, Alvarado and Weddell, 1971). Overlying the sclera are the episclera and bulbar conjunctiva (Fig 1.6). The episclera is a layer of loose connective tissue, which connects anteriorly to Tenon's capsule and posteriorly to the scleral stroma. Scleral thickness varies considerably: at the corneoscleral limbus it is 0.53±0.14mm, decreasing to 0.39±0.17mm near the equator, and is at its thickest at 1.00mm near the optic nerve insertion (Olsen et al., 1998)

The cornea is a transparent ellipsoid, with its shortest diameter in the vertical position. Typically the horizontal diameter is 11.75mm and vertical diameter is 10.6mm (Hogan et al., 1971). The cornea is a surface described as being both toric and aspheric (Mandell, 1961). Toricity is the curvature difference (measured in Dioptres) between two meridians perpendicular to each other. Asphericity is the numerical description of a curved surface that deviates from a perfect sphere. The cornea central anterior radius of curvature is typically 7.8mm and its posterior radius is 6.5mm (Hogan et al., 1971).

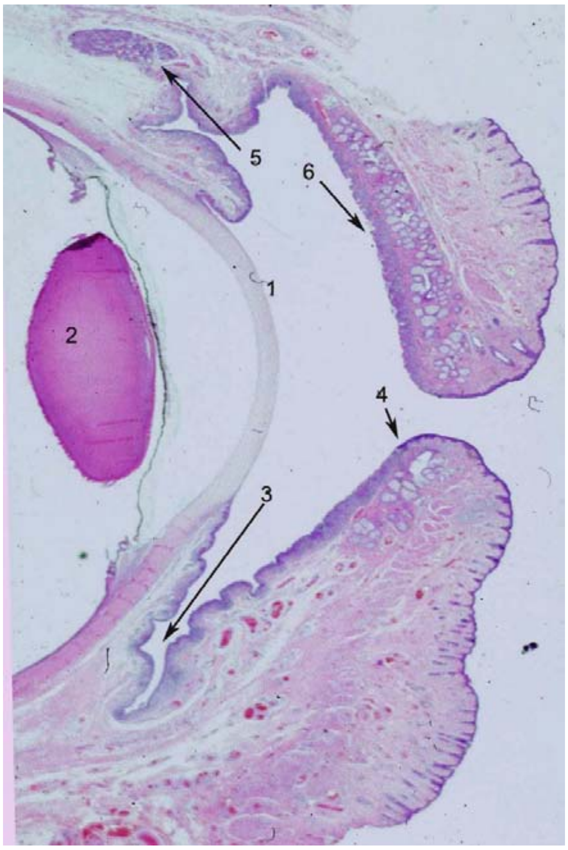

Figure 1.6: Location of the anterior ocular surface in relation to adnexa and internal structures, x5 Light microscope section (Glasgow, 2006) 1= cornea, 2 = crystalline lens, 3 = lower conjunctiva fornix, 4 = marginal conjunctiva, 5 = glands of Kraus, 6 = the conjunctival tarsus.

1.2.3 Microscopic and nanosopic structure of the anterior ocular surface

The cornea collagen fibril diameters are highly regulated. X-ray diffraction methods have determined that fibrils are all in the region of 31nm diameter in the central 8mm zone (Meek and Leonard, 1993) which then rises sharply, increasing to approximately 50nm diameter at the limbus (Boote et al., 2003). The collagen is found mainly in the stroma in lamellae, which form parallel to the tissue surface.

The cornea is made up of 5 layers. The epithelium, the most anterior structure, is covered by the pre-corneal tear film and is 6-9µm thick (Mishima, 1965) .The epithelium is composed of stratified squamous cells, 5 to 8 cells thick, and is continuous with the conjunctiva, where it losses it's smooth regular surface (Ruskell and Bergmanson, 2007). Beneath the corneal epithelium lies the anterior limiting layer or Bowman's layer which is not a basement membrane, but rather a cell-free layer of uniform thickness, of about 8-9µm (Bergmanson, 2006) which is composed of randomly arranged collagen fibrils. The arrangement of these collagen fibrils is believed to provide anchoring filaments and plaques for the stroma below (Bergmanson, 2006). The stroma is a dense layer of transparent connective tissue and makes up to 90% of the corneal thickness. Keratocytes are responsible for upkeep and repair of the collagen as there are no blood vessels present here. The cornea is 76% water and regulation of this is paramount to maintain transparency. The endothelium is a single-celled layer of squamous cells approximately 5 µm thick overlying the posterior limiting lamina or Decemet's membrane. It is the joint function of the epithelium and the endothelial pump that regulates corneal hydration to maintain transparency (Maurice, 1972). The water content also has an effect on the corneal thickness, which in the adult eye is about 535 µm centrally (range 445–600µm) and thickens by 23% peripherally (Doughty and Zaman, 2000).

The structure of the sclera is predominantly collagen with some 2% elastin fibrils found mainly in innermost layer (Watson and Young, 2004). Resident fibroblasts are surrounded by an extracellular matrix of collagen, elastin, glycoproteins and proteoglycans. Collagen types I, III, V and VI are found in the extracellular matrix, and electron microscope studies have demonstrated that collagen fibrils are present in a wide range of diameters, 25 – 230 nm, interwoven in an irregular and complex fashion (Yamamoto et al., 1997). Fibrils are grouped in bundles of 0.5–6.0µm, and arranged in a regular, parallel arrangement in the outer sclera. However, the inner layers contain an irregular collagen mesh of fibrils, and it is thought that this provides the rigid, but flexible nature of the tissue (Meller, Peters and Meller, 1997). In the posterior sclera, the region which has been associated with globe elongation has been studied and collagen fibre diameter gives rise to a trans-scleral gradient. A profile of different diameters, related to depth, has been shown in the tree shrew (animal model), and found to change with age (McBrien, Cornell and Gentle, 2001).

1.3 Anterior ocular surface topography

1.3.1 Corneal topography

The central zone of the cornea, often referred to as the apex, is approximately 4mm in diameter. There are a number of definitions used to determine the apical zone. The most recent is that of EN ISO 19980:2005, which relates to corneal topographers and states that 'the corneal apex is the location on the corneal surface, where the mean of the local principal curvature is the greatest' (BSI, 2005b). Similarly, Mandell defined the corneal cap as 'the central corneal area of maximum and constant meridional curvature' (Mandell, 1988). He considered the refractive power difference in this area to be less than 0.25D. Ludlam et al defined an area around the apex where 'the curvature varies less than 0.05mm' (Ludlam et al., 1967). Dingeldein and Klyce suggested that it was anatomically incorrect and arbitrary to divide the cornea into zones, but that it was useful for corneal refractive surgery and fitting contact lenses (Dingeldein and Klyce, 1989).

The peripheral zone of 4-11mm in diameter flattens gradually (increases in radius of curvature) towards the limbus, creating asphericity. After corneal refractive surgery for myopia this asphericity increases (Holladay, Dudeja and Chang, 1999) and following procedures of hypermetropia decreases (Llorente et al., 2004). It is this topographic information that is required to successfully fit and centre contact lenses. Using a keratometer the refractive power in the central 3mm (from 4 points) can be measured along 2 meridians. The curvature can be converted into dioptres using an assumed refractive index. The greater power or steepest meridian is usually in the vertical. The difference between the 2 meridians in the young normal population results in 'with-the-rule astigmatism' in most cases (Porter et al., 2001).

There are a variety of complex methods of deriving and evaluating anterior ocular surface contour beyond the 3mm zone. Topographers measure the surface characteristics of the cornea, each with slightly different formulae and techniques to derive the topographic map. The most commonly used systems are placido imaging or slit-scanning systems. From this data, a wide range of maps can be derived. These are frequently colour-coded for ease of interpretation. Axial curvature maps are obtained by measuring the curvature of the cornea at each point relative to a specific axis, predominantly the instrument axis (Fig 1.7). Each radius is measured as a distance from the point to the instrument axis along the normal. The assumption is made that the centre of curvature for that specific point is located along the instrument axis. The radius is the axial radius of curvature; this is mathematically acceptable for spherical surfaces only, hence it incurs significant error in the corneal periphery (Cohen et al., 2006)

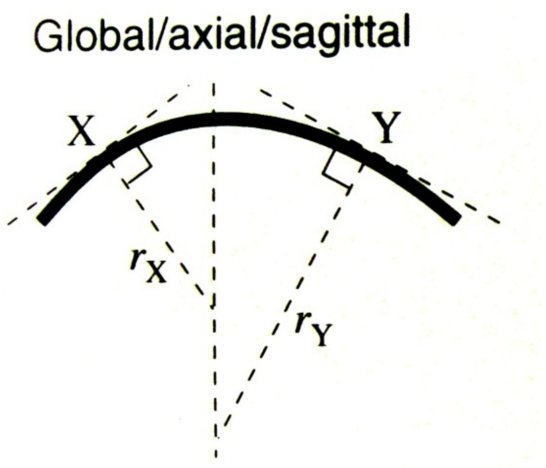

Figure 1.7: Axial radius of curvature: Showing 2 points X and Y on the same meridian of an asymmetric cornea. Radii are measured perpendicular to the surface locus (Corbett, Rosen and O'Brart, 1999a).

Axial maps do not reveal minor variations in local curvature. For a more anatomically accurate topography, tangential maps are better at determining peripheral corneal shape. These are sometimes called local curvature or instantaneous curvature maps. The axis of reference is different for each point (Fig 1.8) and there are a smaller number of mathematical assumptions (Roberts, 1994). Sharp power transitions are recognised more easily, as are focal irregularities. For this reason, this kind of map is used for contact lens fitting. When assessing corneal curvature, tangential maps offer an interpretation of steepness, which should not be confused with height. Similarly curvature metrics do not indicate a positive or negative direction of cahnge the direction of change. Elevation maps are the best way of depicting topography in relation to a plane.

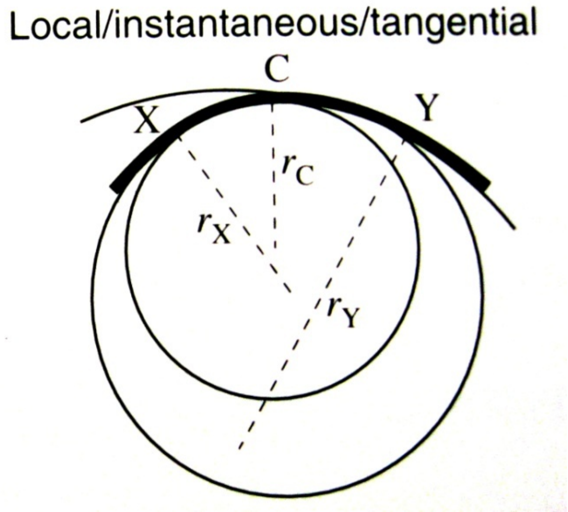

Figure 1.8: Tangential radius of curvature: Showing 2 points X and Y on the same meridian of an asymmetric cornea, C is the reference plane. Radii r_c, r_x and r_y are radii of curvature irrespective of optic or reference axis.

The topography of the cornea can be visualised by relating the primary data to a sphere that most closely resembles that specific surface (often called the ‘best fit sphere’). The points that coincide with the sphere are represented as the colour green, higher points as warmers colours and lower points as cooler colours. Changing the size, shape and alignment of the reference sphere has a profound effect on the appearance of the map. Some machines have fixed reference planes, while others can be selected by the operator (Cohen et al., 2006). Choices for the reference plane alignment include: floating, centred and pinned (Fig 1.9). This allows corneal refractive power to be represented as changes in curvature.

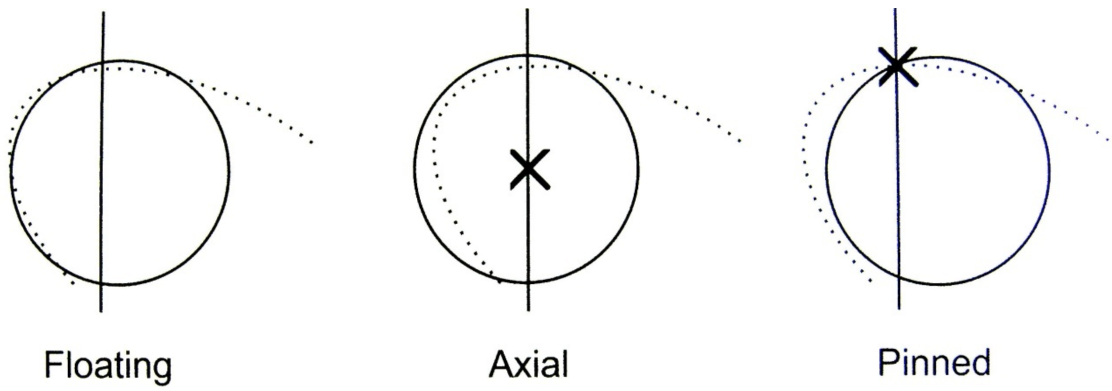

Figure 1.9: Reference surfaces used for elevation maps (Karpecki, 2006)

Normal corneal shape is aspheric, having a steeper radius of curvature (shorter) centrally, and flattening (increasing in radius of curvature) progressively towards the periphery (Dingeldein and Klyce, 1989). Descriptors that mathematically explain corneal shape are often simplified to a conic section using 2 parameters; apical radius and eccentricity. Conic sections can be derived from a circular, ellipsoid, paraboloid and hyperboloid functions (Fig 1.10) (Lindsay, Smith and Atchison, 1998). A typical cornea closely approximates a prolate conic section.

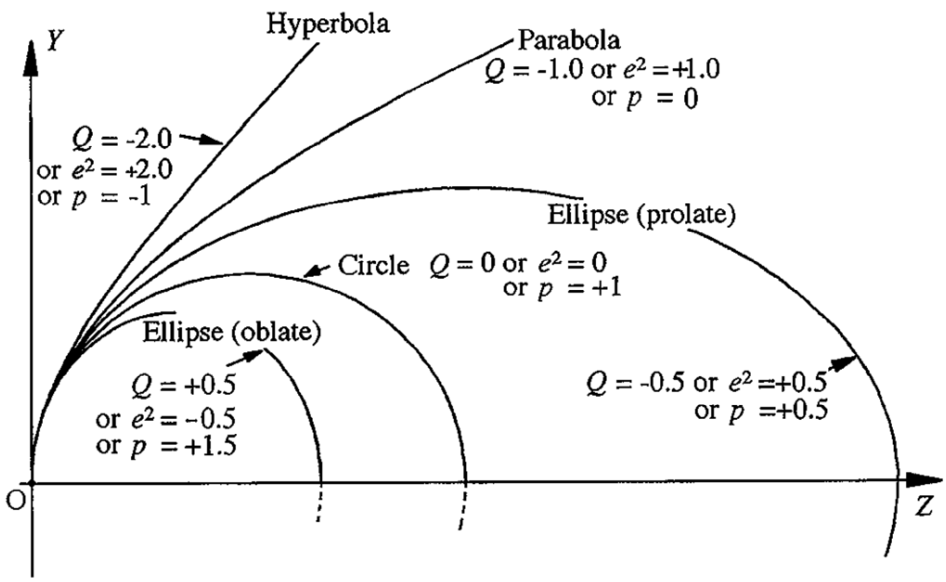

Figure 1.10: Diagram to illustrate different conic sections (Lindsay, Smith and Atchison, 1998).

The position of the apex is important for the design and fitting of contact lenses, and for the planning of corneal surgery. The apex is reported to be temporal to the vertical meridian in 63% of normal corneas, 21% were on the vertical meridian and 16.3% nasal to the vertical meridian (Tomlinson and Schwartz, 1979). Relative to the centre of the TMS-1 video-keratoscope, the site of the corneal apex was found supero-temporally to the visual axis (Rabinowitz et al., 1996).

1.3.2 Normal variations of corneal topography

Under normal conditions corneal topography varies with changes in the body's physiological functions. These are periodical and related to eyelid pressure, time of day, blinking, tear film stability and hormone levels. Age and gender affect hormone levels, which have an influence on topographic variation (Goto et al., 2001). A number of studies have shown that the cornea shape shifts from with-the-rule to against-the-rule astigmatism during the ageing process (Hayashi, Hayashi and Hayashi, 1995) (Goto et al., 2001) (Topuz et al., 2004). The changes may be caused by decreased inter-fibrilar spacing of collagen, accompanied by thickening of the collagen bundles (Malik et al., 1992). This is likely to alter the elasticity and rigidity of the structure. It is possible that decreased eyelid tension with age may be another reason for a trend towards a flattening vertical meridian (Zuguo, Yang and Zhang, 2006). The surface irregularity has been found to increase with age (Goto et al., 2001). However, evidence from a database of video-keratoscopic topography reported no significant differences in surface irregularity of subjects of different ages or gender. Over half of the subjects were white European.

Eyelid pressure has been shown to cause 'with-the-rule' astigmatism (Wilson, Bell and Chotai, 1982). The changes in corneal elevation caused by blinking have been investigated using difference maps of before and after blink. A recent study measured changes in topography during blinking in different gaze positions. It showed eyelid pressure is dependent on gaze, and topographic changes across the cornea define a characteristic wave-like pattern. The average changes in amplitude are 1.4-2.4μm (Shaw et al., 2008). Forceful eyelid rubbing is another significant influence on dynamic topographic changes that affect the cornea. Firm application of digital forces can increase intraocular pressure up to 4 times that of the average open eye intraocular pressure (McMonnies and Boneham, 2007). Eyelid squeeze blinking over the corneal surface can increase intraocular pressure up to 110mmHg. These measurements were made by direct methods using 23 gauge needle penetrating the right globe of a conscious human subject, which was in turn connected to a strain gauge. The pressure recordings were made on a calibrated visicorder indicating a cycle of intraocular pressure changes following the voluntary lid squeezing action by the subject (Coleman and Trokel, 1969).

Topography varies with changes in tear film quality and corneal thickness. The tear film forms a smooth and regular surface, but between blinking this stability is jeopardised if the tear film breaks-up. As a consequence, both the surface regularity index and the surface asphericity index were found to significantly alter if a significant pause in blinking was evaluated (Németh, Erdélyi and Csákány, 2001). Increased corneal hydration causes swelling and overall thickness increases. Results of a study using video-keratoscopy to measure four stages of hydration in eye-bank eyes have indicated central and peripheral corneal steepening (Ousley and Terry, 1996).

Hormone levels in females vary with the menstrual cycle. Estrogens have an effect on tissue hydration, with higher levels associated with increased water retention. Some evidence suggests that changes in topography occur during the cycle (Kiely, Carney and Smith, 1983).

1.3.3 Scleral topography

The limbus is a poorly-defined junction mostly seen as a continuous aspheric curve joining cornea to sclera (Pullum, 2007). The mathematical relationship between the cornea and sclera is not well understood. The normal scleral contour is not spherical and varies significantly according to quadrant and distance from the visual axis (Marriott, 1966). The diagrams below (Fig 1.11) show shadow photographs of ocular impressions in horizontal (180°) and vertical (90°) cross-sections of a normal eye. These show that the temporal sclera is steeper and offset temporally, whilst the nasal sector is the flattest. Many scleras have been observed to be torroidal in shape (Pullum, 2007).

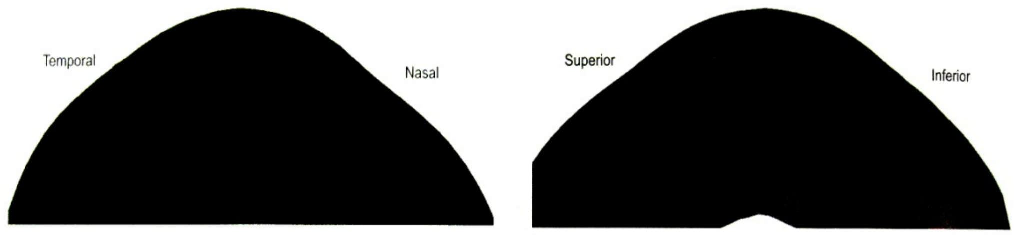

Figure 1.11: Shadow photographs showing anterior ocular surface contour of ocular impressions. These are profiles of 180° (nasal-temporal) (left) and 90° (superior-inferior) (right) (Pullum, 2007).

A method of measuring scleral curvature using a Marcher Scheimpflug camera (Case 2000 series, Marcher Diagnostics, Hereford, England) has been reported by the Nuffield Ophthalmology Laboratory at Oxford University. The objective was to calculate the exposed surface area of an open eye for tear film studies. The authors determined that the relationship between the corneal and scleral curvature was not constant and varied according to the profile orientation. The exposed interpalpebral temporal scleral area was flatter than the mean horizontal equatorial value of 12.5mm (Tiffany, Grande and Todd, 2004). The investigators altered the subject's fixation, to ensure the maximum area of surface exposure. Potentially this system could be adapted for surveying the anterior surface topography in its entirety, if an adequate referencing system and a protocol for curve fitting could be established.

Currently there is only one imaging technique capable of representing the limbus and anterior scleral contour for use in the clinical environment. This is anterior segment ocular coherence tomography (AS-OCT) imaging, described in detail in Chapter 2. AS-OCT imaging has facilitated improvements in scleral lens fitting selection and modifications, by *in-vivo* assessment of edge profiles, as well as apical and limbal clearance (Gemoules, 2008). In addition, valuable characterization of ocular surface architecture beyond the cornea has improved the prediction of soft contact lens fitting (Hall et al., 2011).

Literature reviews have revealed no system that offers a 3-dimensional representation of the entire AOS.

1.4 Anterior ocular surface function and biomechanics

The shape assumed by the cornea is most likely a combination of distension of the tissue by intraocular pressure (McMonnies and Schief, 2006) and the precise distribution of the structural components. Reverse geometry contact lenses have been used to subtly mould the cornea (termed accelerated orthokeratology) to enable low myopes the benefit of temporary refractive correction during the day without any optical device. Essentially this treatment changes the epithelial structure, flattening the cells so that the central corneal thickness reduces, peripheral thickness increases and the topographic profile becomes flatter in the central 6mm zone (Cheah et al., 2008). The cornea returns to its original shape and may be protecting the eye from micro volumetric changes (Johnson et al., 2007); this has implications for measurement of intraocular pressure.

Central corneal thickness has been found to be a biomarker for the overall structural thickness of the globe, and thin values of central corneal thickness have been linked to an increased prevalence of glaucomatous damage (Pakravan et al., 2007). The tensile strength is very low and is unevenly distributed through the corneal thickness, the lamellae can easily be teased apart (Meek, 2008) and is related to corneal hydration. As with the sclera, the corneal tissue is viscoelastic. Under prolonged stress the tissue will creep, that is slowly change shape or permanently deform; this may influence the tissue's behaviour under abnormal conditions like ectasia.

The sclera has a surface area of 16.3±1.8cm^2 calculated by computerised tracing methods, or 17.0±1.5cm^2 by volume displacement (Doughty and Zaman, 2000). Measurement of the surface area of the cornea is 1.3cm^2, or one-fourteenth of the total area of the globe (Maurice, 1969). The sclera has a multi-faceted role, providing a highly-resistant surface for the attachment of extra-ocular muscle insertions and protecting the intraocular structures. Its opaque quality prevents degradation of the retinal image by reducing internal light scattering. The resilience of the tissue enables the eye to move with only minor amounts of globe deformation or distortion.

It is this property that enables the regulation of intraocular pressure and helps to maintain the overall shape of the globe. The sclera is a viscoelastic structure which exhibits a two-phase response when deformed. Initially, a rapid but brief lengthening of the tissue followed by a slow stretching in the semi-fluid phase. The sclera is less extensible in the anterior and equatorial regions (Meek, 2008). When pressure is applied to the tissue it gradually deforms, and when this pressure is removed, the tissue recovers, but not to its initial conformation, which may be due to scleral creep (Siegwart and Norton, 1999).

Chapter 2

Current methods of measuring anterior ocular surface contour

The previous chapter reviewed the area of interest and the relevance of wide-field topography in the current clinical setting and reasons for pursuing this line of investigation. This chapter examines the currently available technologies for anterior ocular surface data collection and their suitability to wide-field topography.

To optimise the collection of the surface data a number of requirements must be met:

- The procedure should be non-invasive, to minimise the discomfort and effects on the ocular integrity of the subject.
- The data collection should be fast (up to 3-5 seconds), to ensure any motion artefact does not obscure the image, although this cannot be completely eliminated due to fine ocular movements used during fixation.
- The area of interest should encompass the entire anterior ocular surface as far as the extra-ocular muscle insertions.
- The number of data points collected for the surface should be in the order of 170,000 or more to provide sufficient data to render 3-D topographic virtual representations of the surface.
- No external force should be used to distort or deform the surface in question – this may not be possible if the eyelids occlude the peripheral superior and inferior regions of interest.
- Repeatability of 0.25D or 0.05mm, or less, in line with current technologies that measure corneal contour.
- True and accurate representation of curvature – this may not be possible given the mathematical constraints of multiple-curved surface descriptors. Best-fit curve-fitting with 4th order (or higher) polynomial functions may be required.

2.1 Comparison of reflections

In a pamphlet entitled "*Oculus; hoc est, fundamentum opticum* ", Christoph Scheiner described a system of measuring corneal curvature based on observing the image of a window reflected on the corneal surface and matching its size, by eye, with the window's reflection in a series of convex mirrors (glass spheres). This is thought to be the first documented evidence of the systematic measurement of the corneal shape (Scheiner, 1619).

Modern day ophthalmometers use the same principle to measure the radius of curvature of the central cornea. The image of an object of known size is reflected at a fixed viewing distance. The image size is a function of the radius of curvature of the reflecting surface, the pre-corneal tear film. Measuring the size of the image is achieved by doubling the image through a prism and lining the base of one image with the top of the other – this displacement equals exactly the height of the image (Esperjesi and Wolffsohn, 2007). With the height of the image now known, along with the viewing distance and the object size, the curvature of the reflecting surface can be calculated.

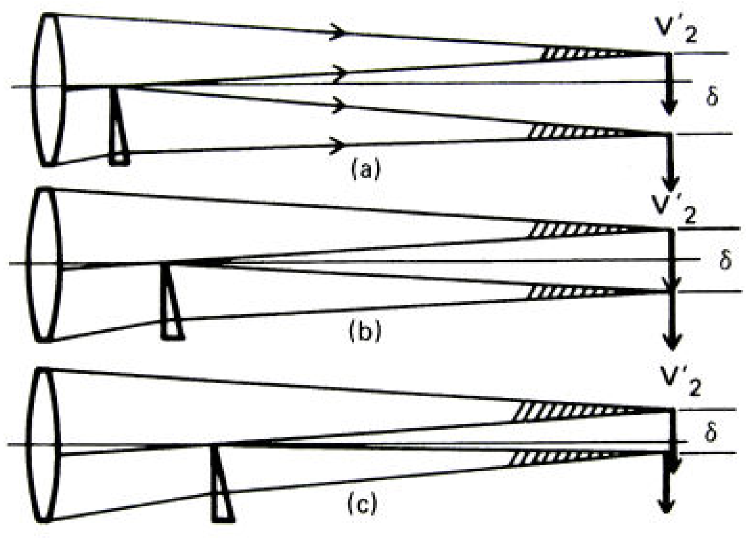

Figure 2.1: The doubling principle: using a prism travelling along the instrument axis (from left to right), V'_2 is the upper extremity of the doubled image. The diagrams (a), (b) and (c) show the how the prism is used to align the images to and so provide a measure of the displacement (Rabbetts, 1998a).

There are two doubling systems used in modern keratometric instruments:

Fixed doubling: where the amount of doubling is pre-determined and the mire is moved until the image produced is the pre-determined height. An example of this design; the Javal-Schiötz keratometer uses a Wollaston bi-prism to achieve this.

Variable doubling: where the object is set to a pre-determined size and the doubling system is varied until the image is displaced through its exact height. The two meridians can be measured simultaneously. This is used in the Bausch and Lomb (Fig 2.3), Zeiss CL110, Rodenstock and Zeiss Ophthalmometers (Rabbetts, 1998b)

In measuring the anterior corneal radius of curvature, the power of the front surface can also be calculated; assuming the refractive index of the cornea is 1.3375. The two-position instruments (e.g. Bausch and Lomb Keratometer) with circular mires (Fig 2.2) have the added advantage of the observer assessing changes of mire quality relating to corneal distortion, tear film instability and contact lens flexure (Hirji, Patel and Challender, 1989).

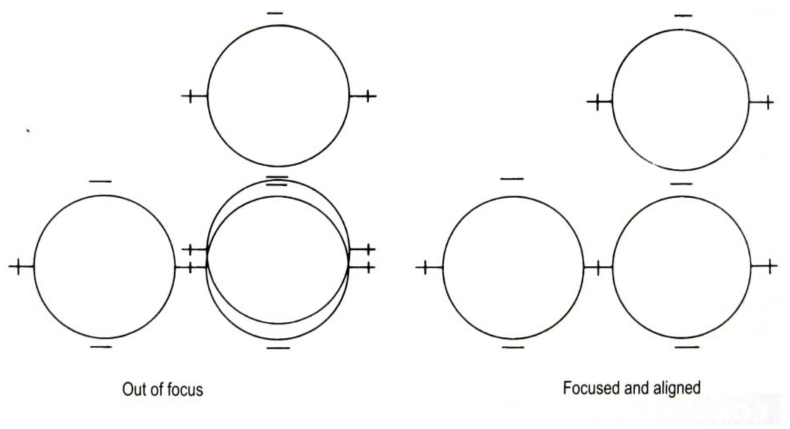

Figure 2.2: Bausch and Lomb Keratometer mires. The images must be aligned in both meridians (Esperjesi and Wolffsohn, 2007)

Figure 2.3: The Bausch and Lomb Keratometer.

The one-position instruments (e.g. Javal-Schiötz Keratometer) only assess corneal curvature in one meridian, so the instrument must be rotated to a second principal meridian, which may not be perpendicular if the astigmatism is not regular. The Javal-Schiötz mires are shown below (Fig 2.4).

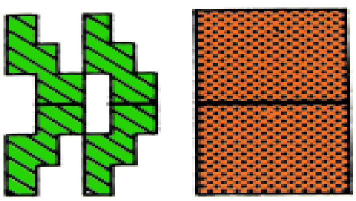

Figure 2.4: The Javal-Schiötz Keratometer mires: the steps on the green mire represent 1 dioptre intervals of astigmatism.

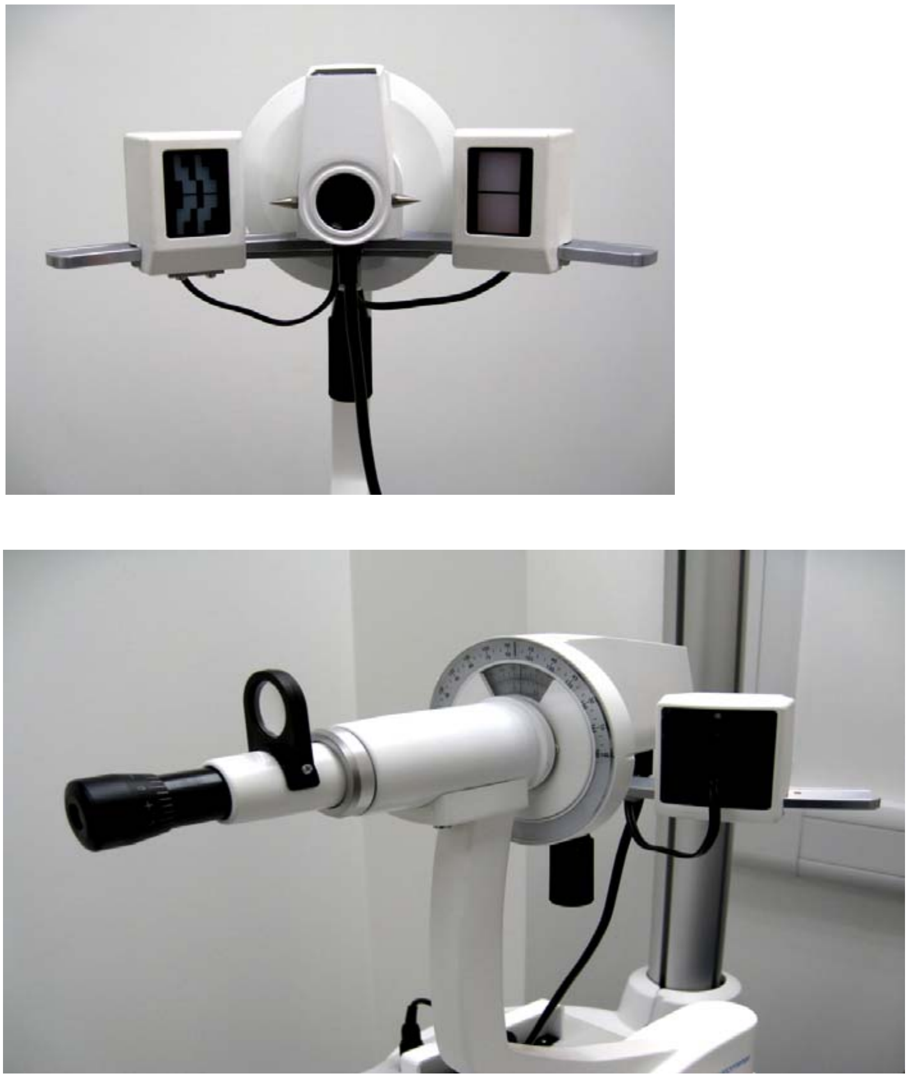

Figure 2.5: The Javal-Schiötz Keratometer.

Errors in keratometric measurement of the cornea include:

- Assumptions that the area approximately 1-1.7mm from the corneal apex (point of maximum curvature or shortest radius), which is used to reflect the mires, is of the same curvature as the apex.
- Inaccuracies of the paraxial ray theory; mainly spherical aberration
- Inadequate calibration and alignment
- Errors of focusing
- Proximal accommodation of the observer
- Poor reflected image quality caused by corneal distortion, disrupted tear film or poor patient fixation.

Keratometry is widely used as a method of providing a curvature to initiate the fitting of contact lenses and to assist in the power calculation for intraocular lens choice. However, this is a poor guide to any area beyond the central 3.0-3.5mm of the cornea. This is because the reflection observed when using a keratometer is the first Purkinje image, which is formed behind the cornea. The slope of the surface is measured at 2 separate perpendicular pairs of points along each meridian. The slope cannot be converted into height without further measurements (Corbett et al., 1999a).

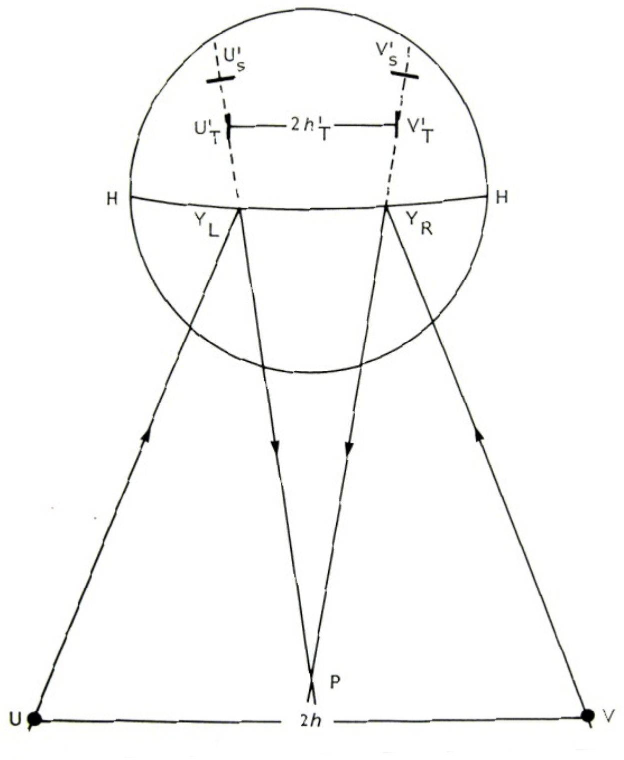

Figure 2.6: The keratometer's view of the cornea. U and V are the central points on the inner edge of the mires. The incident and reflected ray paths from U and V lie in a horizontal plane containing the points of incidence YL and YR (Bennett and Rabbetts, 1991).

Keratometry measurements are highly accurate and reproducible for regular sphero-cylindrical surfaces, such as the 2.6-3.7mm annulus centred on the corneal apex (Sunderraj, 1992). However, for irregular corneal shapes, 4 slope reference points provide insufficient information for the planning of surgical procedures or design of close fitting contact lenses.

Some keratometers have been re-designed to measure peripheral as well as central corneal curvature. Conventional instruments can be fitted with attachments for topographic use. For example, a modified Bausch and Lomb Keratometer mire has been used to increase the zone of measurement to 6mm and to calculate the corneal asphericity (Douthwaite and Sheridan, 1989).

2.2 Keratoscopy and Video-keratoscopy

In its simplest form, keratoscopy is a technique used to investigate the regularity of corneal contour by visual inspection of a reflected image over the central 4-6mm. The Placido disc, introduced in 1880 (Fig 2.7), consists of a series of concentric black and white rings on a flat paddle held in front of the subject. A light was placed above the subject's head, which shone onto the disc and corneal reflections of the black and white rings were observed through a central aperture, with or without a magnifying lens (Horner, Salmon and Soni, 2006).

Figure 2.7: Placido's Disc

This technique provides a gross assessment of the corneal shape when viewed directly. By photographing these reflected images, mathematical analysis can determine the curvature of the cornea at different points across its surface, thus providing a topographic map. This is a challenging mathematical problem which is rarely carried out manually, therefore until the mid-1970's, corneal shape analysis was principally carried out using the keratometer for precise central measurement, or by Placido disc subjective observation for gross assessment.

Photo-keratoscopy used polaroid photographs of the reflected corneal rings and the radius of curvature was identified from the resultant image using a comparator to magnify this image to equal a known standard set of rings. The amount of magnification required to match the standard ring set was directly related to the radius of curvature (Rowsey, Reynolds and Brown, 1981). With advances in electronics and computing, the possibility of reconstructing a virtual corneal surface became more plausible. The keratoscope rings were recorded electronically, and programmed mathematical algorithms extrapolated the measurements and processed the data to provide graphical representations. The images could be analysed automatically and quickly in a clinical environment. This technique was referred to as video-keratography, and the new devices known as video-keratoscopes. One of the first such instruments to be available commercially was the Wesley-Jessen Photo-Electronic Keratoscope (PEK) (Bibby, 1976).

The video-keratoscopy system works by capturing a video image of the reflected rings and measuring the angular size of a series of points on the rings. A polar co-ordinate system is imposed on the video image and each point is specified by both its distance from the instrument axis and its meridian. The image is reconstructed point-by-point and each point is assigned a curvature value (Clark, 1973).

The images in Figure 2.8 show the locations of the surface data collected using keratometric methods and the positioning of the target mires for the photo- and video-keratoscopes.

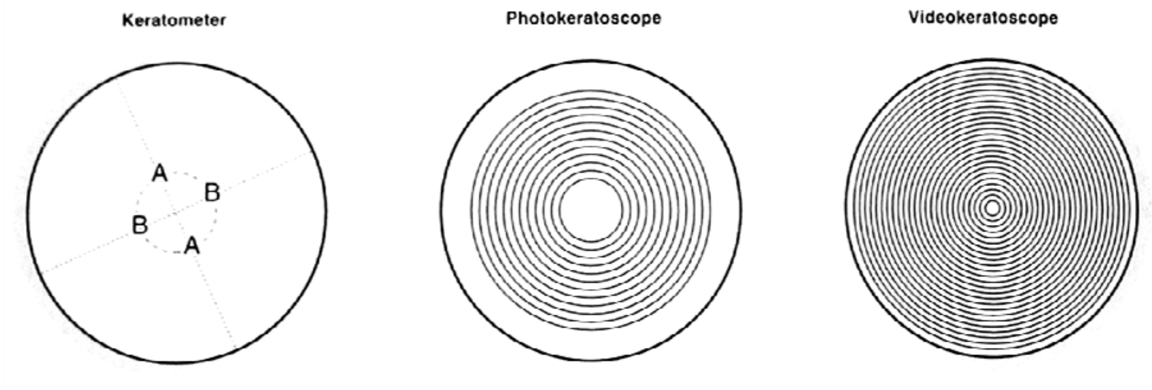

Figure 2.8: Diagram to show the location of corneal measurements using keratometer mires, photo-keratoscope (12 rings) and computer-assisted video-keratoscope (25 rings) (Corbett, Rosen and O'Brart, 1999d)

Marked astigmatism causes the rings to appear elliptical, while structural abnormalities of the cornea cause distorted or asymmetrical reflections.

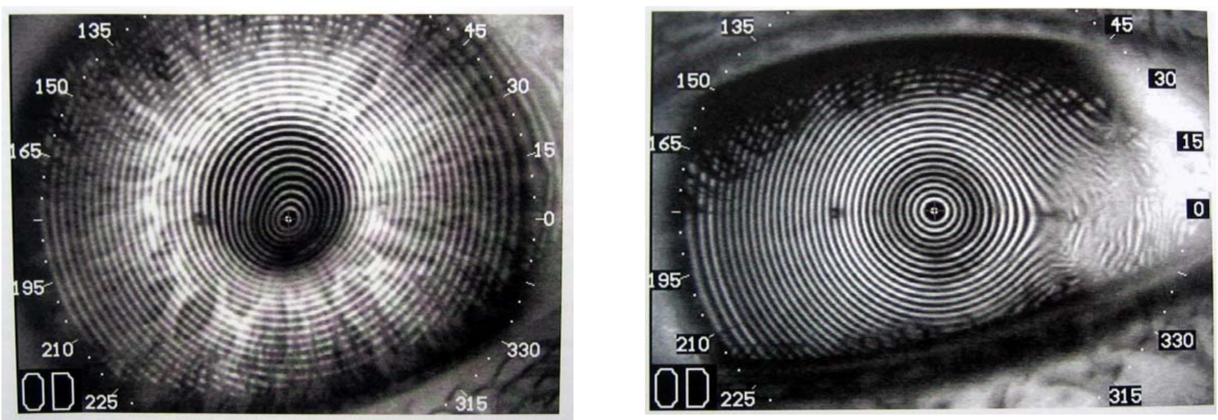

a) b)

Figure 2.9: Distortions to the reflected video-keratoscopy mires caused by (a) severe corneal ectasia, and (b) pterigium (Corbett, Rosen and O'Brart, 1999b)

There are currently a number of systems that are commercially available that have similar benefits and limitations. In 1995, the Orbscan (Orbtek, Bausch and Lomb Inc, NY) became available. This instrument used a novel technique of a scanning-slit; a parallelepiped beam to image the anterior and posterior corneal surfaces, and the anterior surface of the lens and the iris. The system first detects the anterior edge of each slit. Triangulation is then required to map complex surfaces like the anterior eye and this is achieved by direct methods, in which a ray intersects with the calibrated outer surface of the slit beam providing vector co-ordinates x, y and z. The short focal length camera (169.55mm), when aligned, is focused most sharply at a plane 1mm behind the corneal apex when collecting the images of the slit scans (Cairns and McGhee, 2005). This represents a large potential source of error in measuring surgical or pathologically altered corneas.

In 1999, the Orbscan II (Orbtek, Bausch and Lomb Inc, NY) was released, which incorporated a placido disc system in addition to the slit-scan technology (Fig 2.10). The placido disc is used to calculate the surface curvature of the cornea and the slit-scanning technique is used to measure anterior segment surface geometry, and so provide the absolute surface elevation of the optical surfaces.

During image acquisition the placido disc is illuminated and the reflected concentric mires stored as a black and white image. Then images of the 40 slits, 12.50mm high and 0.3mm wide, are collected from a light source projected onto the cornea at an angle of 45°, 20 slits from the right and 20 from the left. The back-scattered light is captured by a digital video camera, which records 2-dimensional images. The image of the placido disc is found behind the camera plane, in the posterior cornea (Applegate and Howland, 1995a).

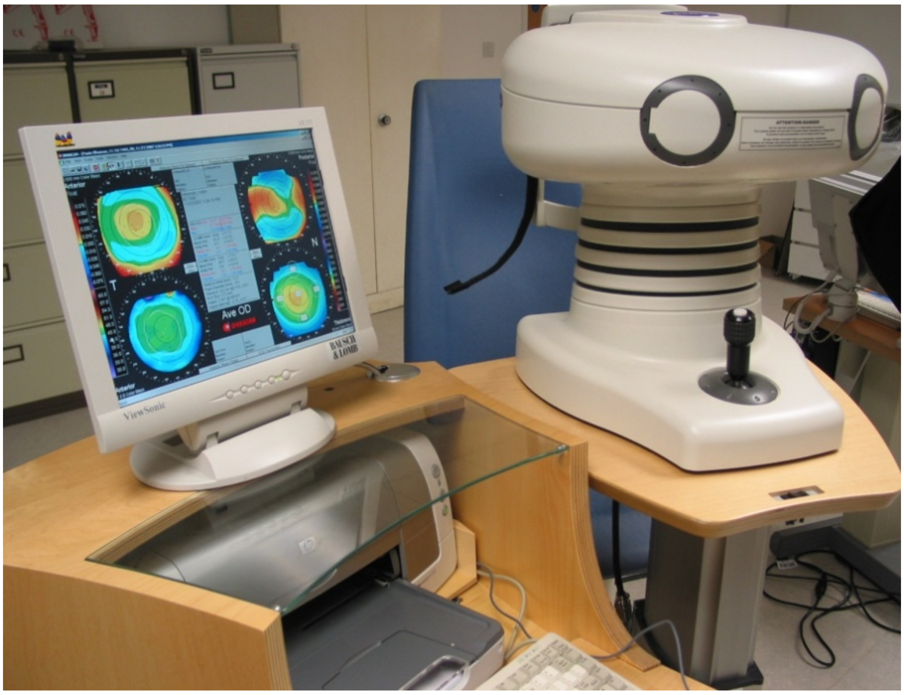

Figure 2.10: The Orbscan IIz (Orbtek Inc, Salt Lake City, UT)

Analysing the placido disc reflection provides a normal to the anterior surface using the visual axis as reference. Tangential topography can be extracted by adjacent data providing local curvature change. A refractive index of 1.376 is used for calculating the local dioptric power of the cornea. Displays of differences in height between the anterior surface and a floating best-fit sphere (BFS) are presented as colour coded maps (Fig 2.11), allowing small changes in surface shape to become more obvious to the observer. The anterior ocular surface is described using best-fit polynomial functions described in a 3-dimensional Cartesian co-ordinate system (Cairns, Collins and McGhee, 2003). The graphical representation on the top left of the captured display shows the tangential anterior topography related to the reference sphere. A database of normal human corneal 'patterns' (Rabinowitz et al., 1996) is used to provide normal surface elevation patterns and establish a baseline for comparative studies involving abnormal ocular conditions.

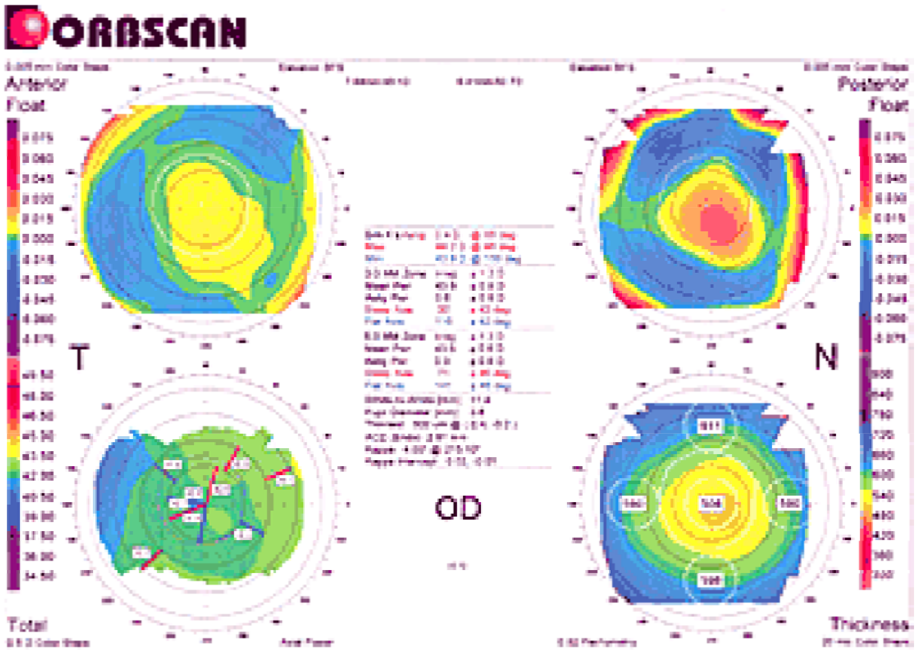

Figure 2.11: Diagram to illustrate the layout of the graphical representation (Quad map) of the anterior ocular surface, as depicted by Orbscan IIz technology.

Using specially-designed test surfaces, the Orbscan II had been found to be extremely accurate (Cairns et al., 2002). However, this accuracy does not easily translate to the human cornea. Indeed, no system that adequately models the optic section of the cornea has been discovered (Cairns et al., 2002). If the inherent inaccuracies of the placido-based systems are taken into consideration, then large (up to 200μm), but repeatable, errors (±10μm) in measurements are noted, which become more variable towards the periphery. Paraxial assumptions, that ray bundles (beyond the central 3mm zone) are always incident normally to the surface, increasingly fail, and the likelihood of the true surface being represented by relative elevation maps is doubtful.

A study comparing Javal-Schiötz keratometry measurements with Orbscan II simulated keratometry measurements on a group of 15 normal subjects found the mean keratometry measurements to be steeper by 0.16mm than the Orbscan results. This difference was statistically significant ($p<0.001$) (Leyland, 2004). Hence, in the absence of a 'gold standard' to define true anterior ocular surface topography, clinically direct comparison methods of quantitative curvature differences are the only robust usage of the Orbscan IIz system to study anterior corneal topography. However, investigation of AOS topography is limited by the need for a good reflection from the smooth and transparent cornea, and is so confined to the central 8-9mm, meaning that it cannot be extended to beyond the corneo-limbal transition.

The most recent advances in video-keratoscopy are seen in three-dimensional stereo-topography. The AstraMax (LaserSight Technologies Inc., Winter Park, FL) is a multi-dimensional corneal imaging system. The technology utilises a highly-detailed re-designed placido disc with three cameras, rather than the one used in conventional video-keratoscopy systems (Wang, Hill and Swartz, 2006). The advantages are:

- Overlay of reflective grid and 3 cameras creates a true 3-D image
- 35,000 data points are collected in a single shot
- Data acquisition time is as little as 0.2 seconds
- Data is captured simultaneously by all 3 cameras

This system, however, only provides data for the central 8mm of the cornea, and the technology has limited use for the assessment of wide-field topography due to its reliance on smooth, transparent media for reflective imaging.

2.3 Intra-operative raster photogrammetry

Aerial photography used for mapping the earth's surface uses a well-documented system called photogrammetry. Images are taken from two or more different positions and common points on each image are identified. Mathematical triangulation then provides 3-dimensional co-ordinates for each point. This technique has been adapted to measure the corneal surface and was used in the mid-1990s, when planned refractive surgery required an accurate guide to the true contours of the anterior corneal surface to help predict the outcome of the procedures.

The PAR corneal topography system (CTS) (Par Microsystems Corporation, New Hartford, NY) was a computer-driven imaging system that used close-range photo-grammetry (raster-photo-grammetry) by projecting a grid onto the cornea to produce a topographic map of the surface. The system could be adapted to measure across a 12mm diameter area of the anterior ocular surface, which allowed measurement beyond the corneo-limbal junction. It was initially developed in 1988 (Warnicki et al., 1988) using a 2-dimensional grid with a point density spacing of 0.22mm, providing approximately 1700 data points on the cornea. The system did not require a smooth reflective surface or precise spatial alignment, and to enhance the quality of the grid image, the tear film was stained using topical fluorescein. The grid was then projected through a cobalt blue excitation filter and viewed through a yellow barrier filter to improve visibility.

The topographic maps were presented in the same way as standard video-keratoscopy using colour contours (Fig 2.12) and including the relative elevation derived from best-fit spheres.

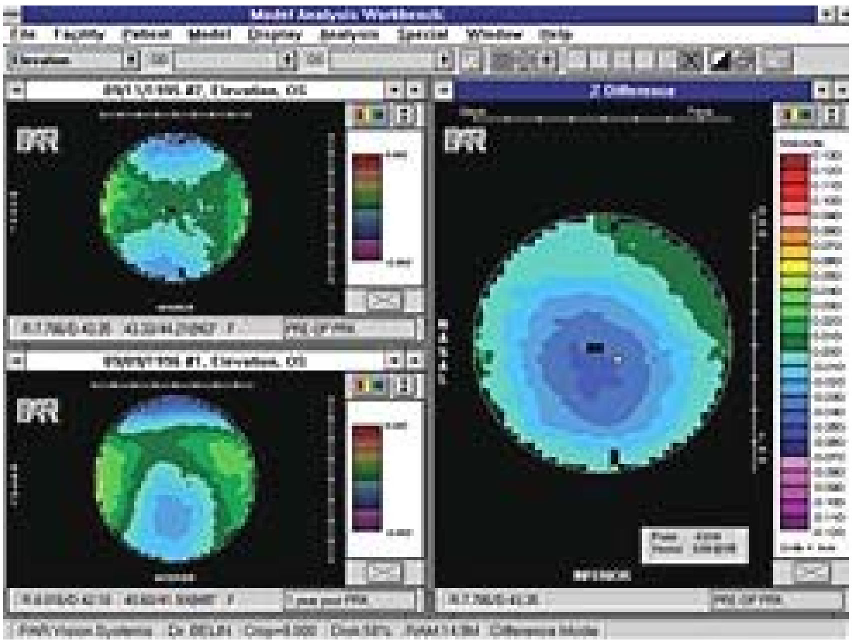

Figure 2.12: An elevation map from the now obsolete PAR CT system (Swartz et al., 2006)

The measurement of the central 8mm zone of the cornea was repeatable to within ±0.07D (Belin et al., 1992) but the standard error of the measurements was significantly more than the competing placido disc based systems and so the PAR CTS was discontinued. The Orbscan II was able to provide a multitude of descriptors, including corneal thickness and posterior corneal curvature, which was viewed by industry as having better potential. So while this system has the potential for providing non-invasive, fast, wide-field anterior ocular surface topography to meet the requirements of this work, the technology is unfortunately not available.

2.4 Other projection-based systems

These systems measure the anterior ocular surface in terms of elevation or height above a reference plane using images projected onto the cornea. A number of systems have been reported in the literature including holographic interferometry and Moiré interferometry, but which are no longer commercially available.

In contrast to systems using ring reflections, these 2 technologies use reflected interference patterns generated on the corneal surface by 2 parallel sine-wave gratings (Moire interference), or 2 coherent beams or wave-fronts (laser interference). A large number of data points can be collected from analysis of the interference pattern. This can only be carried out on transparent corneas. The contours on the corneal maps are lines of equal height, rather than equal slope. Due to the complexity of the normal corneal shape, measurements of height will map its true shape. This technology can even map the entire cornea and limbus to resolutions in the order of 2-5μm (Corbett et al., 1999a). The reconstruction of the surface is not biased by alignment with the visual axis or corneal apex, therefore the accuracy of shape is uniform across the whole surface.

It could be speculated that, as this technology was tested and developed in the early to mid-1990s, the limiting factor for making it commercially viable then was the available computer processing power. A large amount of data is generated from each image and instantaneous topography is a requirement for the clinical setting. This may be revisited in light of the more recent developments in wave-front aberration analysis and the desire to understand pathology of the eye *in-vivo*.

2.5 Scheimpflug Photography

Theodor Scheimpflug was an aerial photographer who found that photographs taken from a hot air balloon or kite suffered from areas of defocus due to the camera plane not coinciding with the image plane. Subsequently, he filed a patent with the British Patent Office in 1904 describing an instrument for the correction of perspective distortion in aerial photographs. Aerial images from a balloon or a satellite have a great commonality with images of the cornea. The objects for both are curved and 3-dimensional, and they need to be depicted without distortion.

The image captured by a camera is focussed by adjusting the lens or lens system to focus on the object of interest. Flat or planar objects are easily imaged as the camera and image plane can be adjusted to coincide. The photograph provides a 2-dimensional representation (Fig 2.13). A 3-dimensional object is a more complex challenge: to image the object sharply depends on the depth of focus of the system. This is controlled by the aperture size and the focal length of the lens or lens system used. The aperture that is used for Scheimpflug imaging is a slit-beam, and the lens system is aligned according to the perspective correction technique described by Scheimpflug (Fig 2.14).

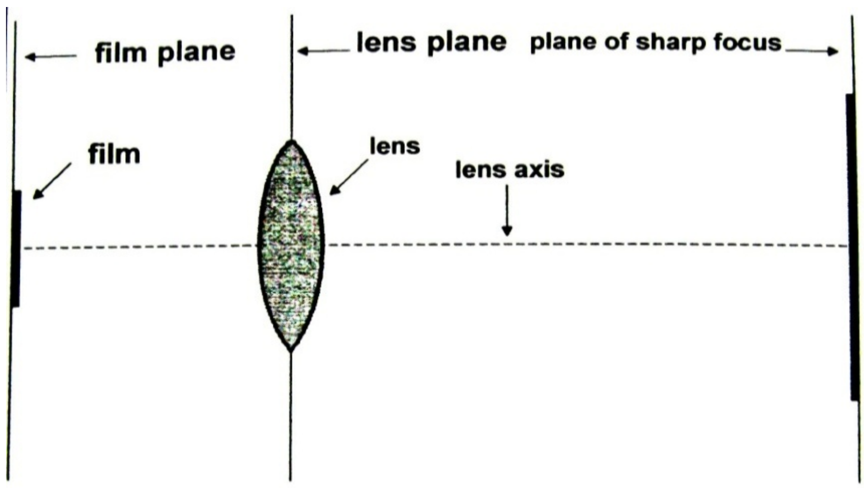

Figure 2.13: Image and object planes align when collecting images with conventional photographic methods.

The lens focusing the image must be placed on the line of intersection (Scheimpflug Line) to artificially extend the depth of focus and ensure the image of the curved surface is focused simultaneously.

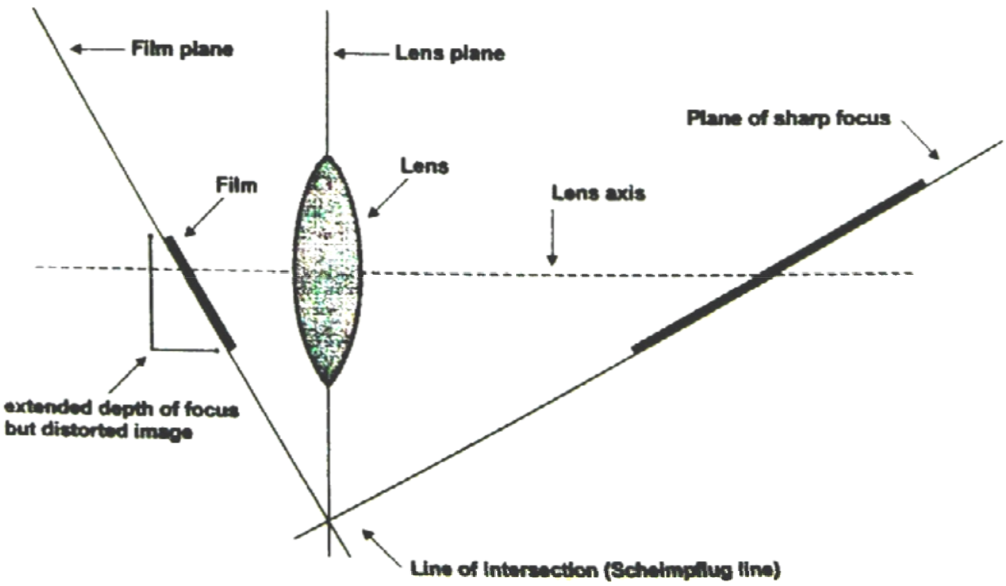

Figure 2.14: The Scheimpflug principle. The lens must be placed at the line of intersection to increase the depth of focus.

The principle has been used in ophthalmic imaging for many years in the Nidek EAS-1000 and Topcon SL-45. However, a more recent commercially available model is the Pentacam (Oculus Optiikgeräte GmbH, Wetzlar, Germany), which has been specifically designed to image the anterior segment of the eye (Fig 2.15). The instrument rotates about the visual axis providing up to 50 images in 2-3 seconds, while illuminating the eye using a monochromatic slit-light source (blue LED at 475nm) to produce an optic section. Each image has 500 elevation data points, so generating up to 25,000 point for each surface. The system is able to make appropriate adjustments to correct unwanted eye movements using a second camera, however the exact mechanism for this remains unclear (Swartz, Marten and Wang, 2007).

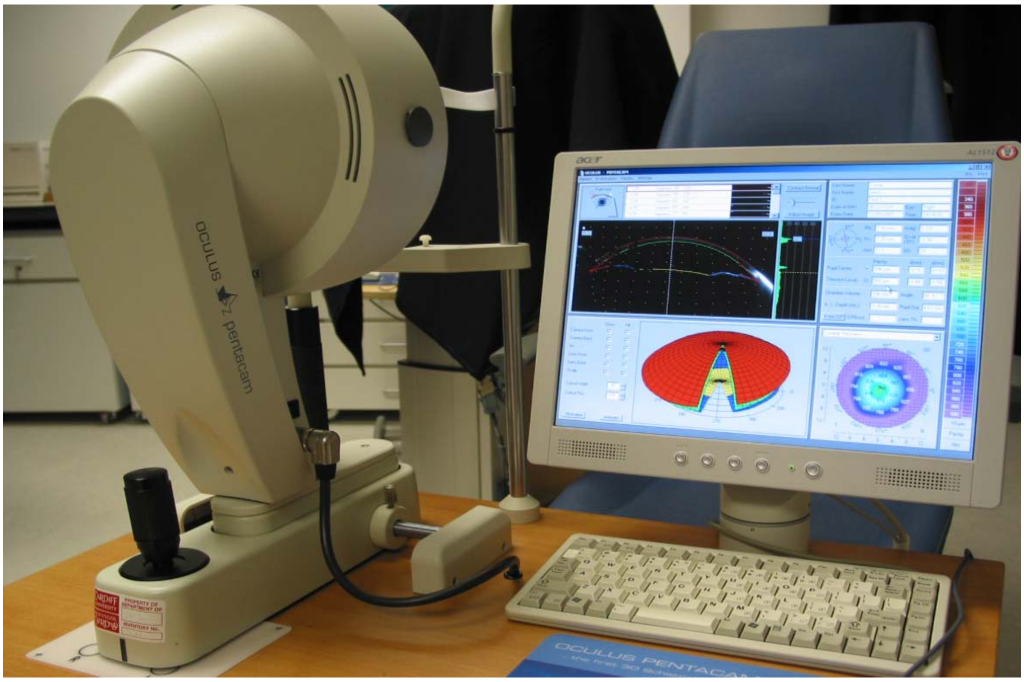

Figure 2.15: Pentacam (Oculus Optiikgerate GmbH, Wetzar Germany)

Elevation-based topography has been modernised for the Pentacam using the principles applied to the topographic output of the PAR CTS described above (Belin et al., 1995). The anterior surface data is used to construct a 3-dimensional representation, which can be compared to a series of reference surfaces:

- Best-fit sphere
- Best-fit ellipsoid
- Best-fit toric ellipsoid

It is an assumption that the reference surface, the regular shape that is chosen by the operator, is a sensible approximation of the normal cornea. The reference surface provides a method of representing subtle changes in elevation. In the past, investigators have attempted to compare individual corneas to an average normal shape (Belin et al., 1992). However, there is a large variation in corneal shape and this average was not thought to present a clinically useful reference surface. In practice, the positioning and alignment of the best-fit sphere (BFS) is influenced by any surface distortion of the cornea.

The software for the Pentacam (Belin/Ambrosio Enhanced Ectasia option) is designed to increase the sensitivity to ectatic changes by finding the 4mm optic zone centred on the thinnest portion of the cornea and exclude this from the reference shape calculation. In this way, the radius of curvature of the BFS is not affected by any protrusion (i.e. not reduced). This enhanced BFS uses all the data in the 8mm central area of the cornea, excluding the 4mm zone. Using this enhanced BFS, the normal corneal elevation differences are minimally affected, however any protrusions or cones are more pronounced.

The default Pentacam display shows standard BFS anterior surface elevation maps, giving the radius of curvature for both anterior and posterior corneal surfaces, and the position relative to the float. The maps on the middle of the display are exclusion maps, showing elevation differences using enhanced BFS, and finally the lower maps are the difference between the standard and enhanced BSF elevation (Belin and Khachikian, 2008).

The Pentacam system can also be used to image the anterior chamber and the density and dimensions of the crystalline lens. The system incorporates an optical correction factor to provide accurate topographic information. The precise mechanism for this has not been published. A recent study reports the anterior surface repeatability of ±0.28D in a group of 35 normal volunteers (Shankar et al., 2008)

2.6 Very-high definition ultrasonography

Ultrasound technology is more familiarly used in the medical field for antenatal care, but it is also important for ocular imaging of the globe. The ultrasonic systems used rely on high frequency sonic pulses generated by piezoelectric crystals that assess the time taken between the emission of an acoustic signal from the crystal and its return to the crystal, when reflected from ocular tissues of differing sonic refractive indices, to build up a picture of the ocular structures (Wolffsohn, 2008). Accurate anatomical dimensions and locations are required when planning surgery, as well as investigating ocular pathology.

In 2002, a very-high-frequency (VHF) digital B-scan system became available from Ultralink (LLC Florida, USA). This arc scanner uses sterile normal saline at 33˚C as the acoustic coupling medium between the eye and the transducer. The patient's head is placed on a chin-rest with their torso bent at a 45° angle, and the test eye fitted with an eyecup that seals the saline-filled scanning compartment. A broad-band 50MHz VHF US lithium niobate transducer (bandwidth 10-60MHz) sweeps in a reverse arc, high-precision mechanism to collect the images. The scan sweep is designed to follow the contours of the cornea and proprietary software transforms the data with a digital signal-to-noise ratio optimiser. The images collected can be displayed on screen as a profile as shown in Figure 2.16.

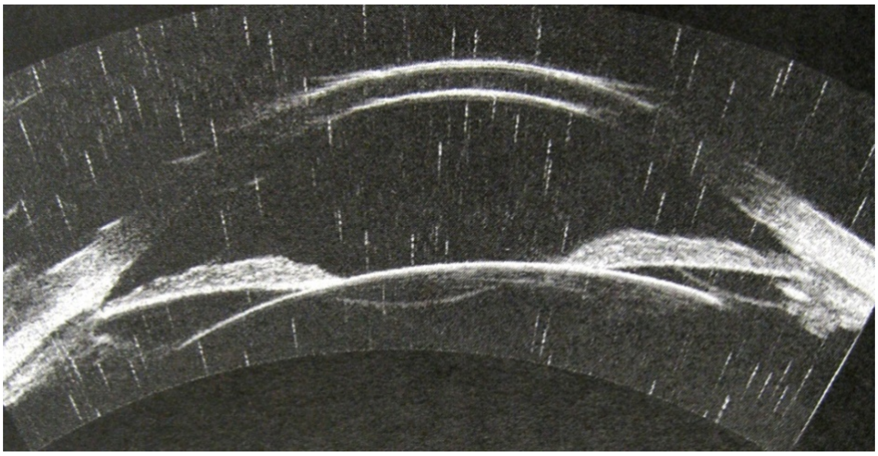

Figure 2.16: B-Scan anterior segment profile from Artemis 2 VHF ultrasound system (Pinero, Belen Plaza and Alio, 2008).

Studies are still underway to determine the accuracy of the surface reproducibility and the accuracy of anterior ocular surface contour (Reinstein et al., 2006). It is possible that the trajectory of the ultrasonic beam, if not perpendicular to the surface, could produce distortion and warpage in the refraction of the beam, and thus in the image collected. The angle of incidence is reported to be kept at a maximum of ±10° of the surface by virtue of the arc scan motion (Reinstein et al., 2006). The system is designed to ensure that the refractive index of the acoustic coupling medium is as close to that of the cornea as possible (n=1.307), however it is likely that this small difference may also cause inaccuracies of curvature, which would exclude it from feasible use in this study.

2.7 Anterior segment ocular coherence tomography

Ocular coherence tomography (OCT) is used as standard clinical practice for the investigation and monitoring of retinal pathology and abnormality. Ultra-high resolution imaging offers *in-vivo* real-time imaging of 3-dimensional transverse sections of the retina. The resolution is good enough to observe individual cell structure and function (Drexler and Fujimoto, 2008).

OCT is an extension of low-coherence reflectometry, and the heart of the system is a fibre-optic Michaelson interferometer, which is illuminated by low-coherence light from a super-luminescent diode. Sample reflections are combined with reflections from a reference mirror. The amplitude and delays of the signal caused by changes in the tissue density and boundary reflectivity are measured by scanning the reference mirror position and recording the amplitude of the interferometric signal at the same time. The longitudinal delay of sample reflections can be determined to high resolution (Huang et al., 1991).

OCT technology was used to scan the anterior segment by investigators as early as 2000 using the available retinal scanners (Bechmann et al., 2001). However, these instruments had several design flaws; retinal scanners were too slow to map the cornea (400 axial scans per second), motion artefacts distorted the surface contour, and the laser wavelength (roughly 830nm) scattered heavily in the opaque scleral tissue. By using longer wavelengths of 1310nm in the AS-OCT Visante™, the intensity could be increased without exceeding the safety eye exposure limits, and hence the scanning could be 20 times faster (ANSI, 2000). A speed of 4000 axial scans per second was demonstrated (Radhakrishnan et al., 2001). The final hurdle was to decide on scan geometry (Fig 2.17), which was found to offer the best quality image if it was carried out in a rectangular fashion (Huang and Izatt, 2008).

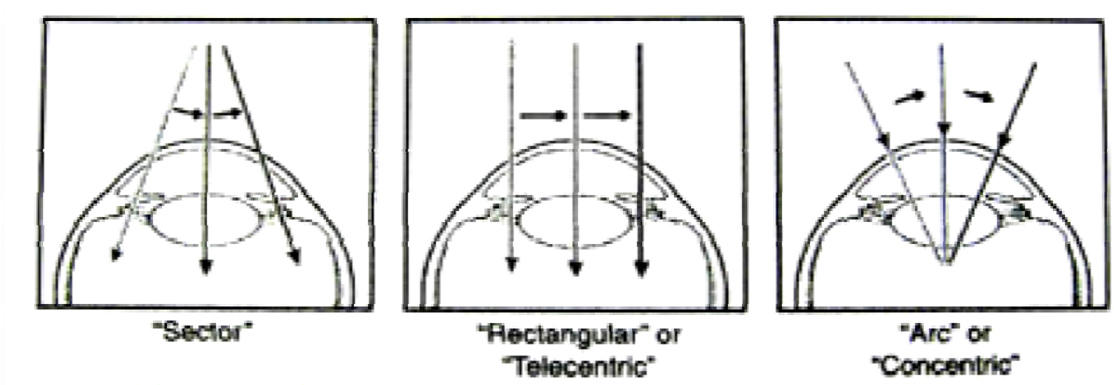

Figure 2.17: Diagram to show different scan geometries (Huang, Li and Tang, 2008).

Using this method of scanning, a bright specular reflection offers a central landmark for registration (the highest point of corneal elevation when aligning the visual axis with the target). With the standard software, the resolution is approximately 18μm axially and 60μm transversely (Baïkoff, 2006). There is a certain amount of curvature distortion that occurs due to the refraction of the A-scan at the air-tear interface and subsequent increase in refractive index of the cornea. The image below (Fig 2.18) shows the screen representation of the cornea.

Figure 2.18: Transverse section through the cornea using AS-OCT Visante scanning.

Huang et al have developed a ‘de-warping’ algorithm using Fermat’s principle, to correct the beam deflection and transform the optical path length to the physical path length using accepted corneal refractive indices. Curvature representation by the AS-OCT Visante™ has been further investigated by the Ophthalmic Research Unit at Aston University using spheres of known diameters. A curvature correction factor has been calculated and applied to the central 10mm zone of the cornea (Dunne, Davies and Wolffsohn, 2007).

The developers of the AS-OCT Visante™ system have combined OCT and placido disk technologies (in the Visante® *Omni*) in order to provide corneal topographic presentation and corneal power calculations. Future work continues to increase the speed of the scanning to up to 115,000 axial scans per second (Oh et al., 2005) so that this can be done. Scan depth would also need to be increased from the 3mm currently used for retinal imaging to 4mm for corneal mapping.

The AS-OCT Visante ™ (Fig 2.19) has a 16mm by 6mm scan that can be single, dual or quad-line scans. The scan orientation for quad scans can be altered in 5° intervals. Each scan is centred around the specular reflection from the highest point of elevation, whilst aligning the visual axis with the fixation target. The reproducibility of the anterior surface curvature is reported to be 0.75D or 0.15mm (Huang et al., 2008)

This technology provides a significant improvement to the currently available non-invasive systems of anterior surface data collection. It may be possible to use this system to collect anterior ocular surface data for this study, but some doubt has been cast over the reproducibility and accurate depiction of the corneal contour, related to current design limitations of the AS-OCT system.

Figure 2.19: AS-OCT Visante™ (Carl Zeiss, Meditec Inc., Dublin, CA)

2.8 Nuclear Magnetic Resonance Imaging

Magnetic resonance imaging (MRI) offers the opportunity to obtain 3-dimensional anatomical and volumetric information of the eye. MRI also offers the possibility of capturing anterior ocular surface topography in a non-invasive manner with minimal risk to the subject (John, 2000). For ocular and orbital imaging, refinements have been made to improve the definition of the images collected (Obata et al., 2006), (Georgouli et al., 2008). The improvements, the use of specialised surface coils and systems to reduce motion artefacts, have enabled ophthalmologists and scientists to visualise fine structures within the eye, including the crystalline lens and its zonules (Georgouli et al., 2008) and to identify the containment structures of the globe, the corneo-scleral envelope (Detorakis et al., 2003) and the internal vitreous cavity (Singh, Logan and Gilmartin, 2006).

The imaging process involves a strong magnetic field that aligns the nuclei of the hydrogen atoms found in the water of the body's tissues. Radio frequency (RF) fields are used to alter the alignment of these magnetised fields and cause the hydrogen nuclei to produce a rotating magnetic field detectable by the scanner.

Specially designed surface coils for emitting RF near to the eye enable high-resolution images to be obtained (Schueler et al., 2003).

Figure 2.20: Discovery MR750 3.0T (GE Healthcare, Buckinghamshire, UK)

Separate slices of the eye and orbit are taken and these images can be re-constructed into cross-sections or regions of anatomical interest. Obata et al were able to obtain images using a synchronised blinking sequence of 1mm slices of the globe in axial section. Profile sampling by collecting data from the edge of each slice and in between is limited by the resolution, how distinct the edges appear and the number of slices obtained.

Images of normal tissues depend on the proton density of the structure, with high proton density producing intense signals, and by the power of the nuclear shield of the protons. T1 and T2 are different types of image resulting from inherent tissue characteristics in response to different magnetic and RF fields applied. Fat has loosely-bound water molecules that act as a weak shield, so in T1-weighted images fatty tissue has high signal intensity and characteristically is displayed as white (Fig 2.21). In T2-weighted images (Fig 2.22), high signal intensity is associated with free water, and this enables excellent discrimination of corneal oedema and the vitreous in ocular images (Wirtschafter, Berman and McDonald, 1992), (Singh et al., 2006) T1-weighted images can be acquired with high-speed scanning and are best suited to delineating the anterior ocular surface contour (Georgouli et al., 2008).

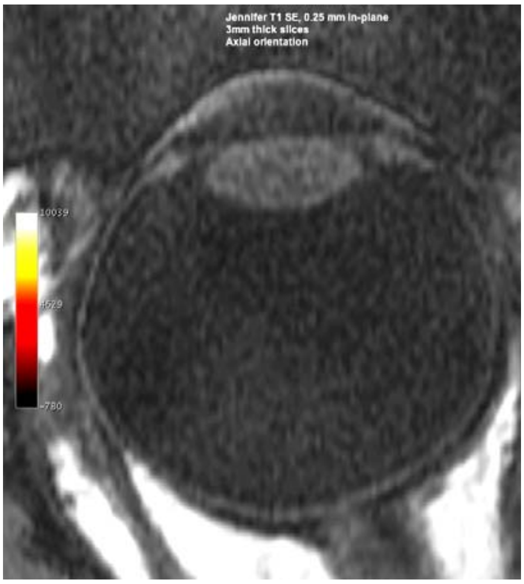

Figure 2.21: T1-weighed MRI image: using a protocol designed by Professor Krish Singh (CUBRIC, Cardiff University) showing the anatomical detail on a 3mm slice of the authors eye.

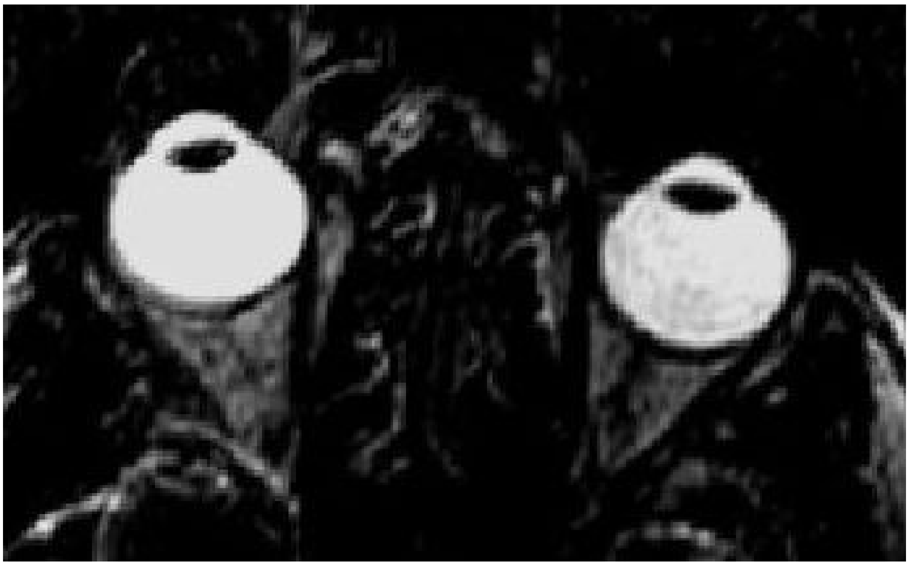

Figure 2.22: T2-weighed Image of the two globes: Showing internal free water in the vitreous cavity (white is water), (courtesy of Professor Krish Singh (CUBRIC, Cardiff University)).

There are no studies yet that examine reproducibility of measurement of the anterior surface, although measurements of crystalline lens thickness using T1-weighted images showed excellent intersession repeatability for 2 subjects, mean lens thickness of 3.75 ±0.02mm [SEM] and 4.45 ±0.04mm [SEM] for 3 different scanning sessions with no significant difference between measurements ($p< 0.001$ for both subjects) (Koretz et al., 2004).

The MRI representation of the eye is free of optical distortion and thus has the potential to permit visualisation of the entire anterior ocular surface *in-situ*, a unique advantage over other methods of data collection. Surface accuracy can be enhanced using standard model phantom systems (Phillips, Medical Systems, Best, The Netherlands) (Obata et al., 2006). These provide a 3-dimensional intensity distribution to correct contrast distortion caused by variations in the surface coil sensitivity, because the effect of the radio frequency emitted from the coil is not uniform across the surface. The speed of data collection may also be a confounding factor. T1-weighed images may take up to 10 minutes to collect a series of slices depending on the scan protocol. Subjects are expected to maintain steady fixation and remain still throughout the collection process. Imaging of the anterior ocular surface is explored further in Chapter 4.

2.9 Ocular impression taking

Matching the shape of the ocular surface has been paramount to the successful manufacture and wearing of corneal and scleral contact lenses since they were first introduced in the late 1890s. However, the origin of the concept for ocular impression extends further back than that to JFW Herschel in 1845, who suggested that '...*an actual mould of the cornea might be taken and impressed on some transparent medium'*. In 1888, Adolf Eugen Fick was experimenting with rabbit eyes by making moulds of the cornea and constructing glass shells to fit these (Fick, 1888). In the early 1900s, Carl Zeiss of Jena was also making glass contact lenses to correct vision using a grinding process, although the success of the system was limited by the short period of time patients could tolerate wearing these devices (Lamb and Sabell, 2007).

Josef Dallos, a physician at the Eye Clinic of the Royal Hungarian Peter Pazmany University investigated a number of materials for impression-taking in the early 1930s. He used a material called Negocoll (derived from seaweed) on a cadaver face and noted that the corneal surface was reproduced in a smooth and uniform fashion. He used a wax-like material to prepare a positive cast and was convinced that this method was suitable for ophthalmic impressions (Lamb and Sabell, 2007). Later, Theodore Obrig also used Negocoll to produce corneal impressions using funnel-shaped blown glass shells. These had a hollow handle, which he filled with cotton wool to stop the Negocoll liquid escaping. The shells were marked on the surface with spots to distinguish right from left (red for right and blue for left). These marks also indicated the location of the nasal canthus on an otherwise spherical shell. The shells were further modified to include multiple perforations in the tray and the shape formed into an oval based on his observations of a large number of casts (Obrig, 1938). Modern impression trays are still designed in a similar fashion and are moulded from acrylic with perforations, hollow handles, and red and blue demarcations, although these now mark the 12 o'clock position (Fig 2.23). The trays are oval and available in set of 6, 3 pairs of small, medium and large (Cantor and Nissel, Northamptonshire, UK).

Figure 2.23: Modern acrylic impression trays in a set of six.

Moulding of the anterior ocular surface contour is still used by a small number of practitioners to design and fit fluid-filled, sealed and fenestrated scleral lenses.

These lenses are indicated for virtually any complexity of corneo-scleral contour (Pullum, Whiting and Buckley, 2005). However, they are often considered the last resort when all other contact lens rehabilitation options fail (Segal et al., 2003). The process involves a skill rarely taught, but occasionally demonstrated, on undergraduate BSc Optometry courses. The practice is therefore confined to hospital optometry and ophthalmology departments and a handful of specialist community practitioners.

Figure 2.24: Modern ocular impression taking technique: The impression tray with material is shown in contact with the anterior ocular surface.

The modern methods of impression-taking involve the use of addition-polymerising polyvinylsiloxane (Pullum, 2007) to form the shape of the complete surface including that covered by the eyelids by direct contact (Fig 2.24). The effect of the bulk of the material and the tray on the surface contour is unknown. The method is limited by its invasive nature, psychological barrier to the subject and the small range of impression trays available for use. Chapter 6 describes the development of an improved system of impression topography data collection and a novel method of scanning the resultant cast to render a virtual 3-dimensional surface.

<u>Summary Table</u>: Potential methods for measuring wide-field anterior ocular surface contour

Instrument or Technique	Year	Method of data collection	Area	Accuracy	Repeatability	Advantages	Limitations	Data sampling
Javal-Schiötz Keratometer	1880	Reflection and image displacement	Central cornea Up to 3.5mm zone	0.051mm	0.074mm or 0.37DS vertically and horizontally	Considered 'gold standard' Non-invasive	No peripheral measurements without excessive time usage No elevation	4 per surface
Orbscan IIz	1999	Placido disc reflections and slit-scanning beam	Up to 5mm with slit-scan Up to 9mm with placido disc	0.20mm centrally (3.5mm zone) and 0.70mm peripherally compared to test surfaces	0.05mm or 0.25D	Well established Fast (2 seconds) Non-invasive	No peripheral measurements More accurate in central 3.5-5.0mm zone	9600 per surface
AstraMax	Prototype 2007	Modified placido disc grid and photographic triangulation	10.00mm central zone Not yet published	Not published	Not published	Very fast (0.2 seconds) Large number of data points Non-invasive	No peripheral measurements No commercially available instrument	35,000 per surface

Instrument or Technique	Year	Method of data collection	Area	Accuracy	Repeatability	Advantages	Limitations	Data sampling
PAR Corneal topography system (PAR CTS)	1988	2-dimensional grid reflection and fluorescein dye enhancement Raster-stereography	Up to 12mm - just beyond the limbus	0.004mm	±0.07D or 0.014mm (central 8mm zone)	Does not require smooth reflective surface or precise spatial alignment	No commercially available instrument Measurements limited to exposed eye surface Invasive – needs fluorescein to enhance image	1700 per surface
Maastricht Topographer	1979	Moiré contour fringes observed when 2 gratings superimposed on to fluorescein-coated tear film	Up to 20mm in horizontal meridian	0.0006mm centrally (10mm zone) 0.023 mm peripherally (14-19 mm zone)	0.00003 mm centre and 0.003 mm peripherally	Fourier transform-based reconstruction algorithm, not reliant on ocular alignment	Measurements limited to exposed eye surface Invasive – needs fluorescein to enhance image	170,000 per surface

Instrument or Technique	Year	Method of data collection	Area	Accuracy	Repeatability	Advantages	Limitations	Data sampling
Pentacam	2003	Scheimpflug photography, rotating slit-beam	Up to the limbus (approx 10-11mm)	Not published	±0.14D or 0.028mm	Fast Can hold up eyelids	Image distortion compensation (undisclosed) Sclera causes hyper-reflectivity	25,000 per surface for 50 slit-scan images
Artemis 2	2002	Very high frequency digital ultrasound arc scanner	Potentially beyond the limbus approx 12mm	Not published (0.005mm for thickness measurements)	Not published	Unknown	Invasive, may deform the AOS No correction factor for acoustic distortion	Not available
AS-OCT Visante™	2005	Interference of coherent light (laser)	Maximum 16mm	Approx 0.018mm axially	0.79D or 0.158mm	Fast (1-2 seconds) Medium wide field	Motion artefact (design limitation) Curvature correction factor No anatomical validation	Not available but AutoCAD sampling from 40 profiles 100,000

Instrument or Technique	Year	Method of data collection	Area	Accuracy	Repeatability	Advantages	Limitations	Data sampling
Discovery MR750 3.0T MRI scanner	2003	Magnetic field and radio frequency field alignment	Complete globe, entire AOS	Not published	Approx 0.018mm transversally on crystalline lens	Non-invasive Provides complete AOS data	Motion artefacts due to blinking Limited number of slices ? Resolution Expensive	Not available but AutoCAD sampling from 20 profiles 50,000
Ocular impressions and cast scanning using Hyscan 45c (CEP)	2008	AOS impression, cast and scanning by active laser triangulation	Entire AOS	±0.001mm	+0.008mm ±0.02 centrally	Complete AOS Excellent data sampling source	Compound error from multiple procedures ±Compression Very labour intensive Invasive	200,000+ per surface

This chapter has reviewed potential methods of acquiring morphometric data of the AOS aiming to establish a system of accurate and reliable data acquisition for the entire topographic profile *in-vivo*, represented as a virtual 3-dimensional model (see Summary Table). The following investigation will compare two common ocular topographic technologies with traditional keratometry.

Chapter 3

Comparison of the Javal-Schiötz keratometer, Orbscan IIz and Pentacam to evaluate corneal topography

Following on from the review of methods available for evaluation of the anterior ocular surface contour in Chapter 2, the next investigation explores the assumptions and compromises made by three instrument manufacturers in the absence of a definitive or anatomically accurate 3-dimensional reference surface.

Ocular surface topography by specular reflection techniques and Scheimpflug imaging is commonly used in clinical practice to provide accurate and reliable measurements of the anterior corneal shape (ACS). The challenge for modern instrument manufacturers is to design system algorithms that are able to convert the captured digital images into a keratometric analogue that compares favourably to the 'gold standard', non-automated keratometry measurements. Each company has derived its own algorithms based on several assumptions. The resulting topographic representations of the ACS are affected by the extent to which each manufacturer relies on each assumption and so the derived result may not provide an accurate description of the 'true' shape. It also follows that the different instruments may also produce slightly different results in comparison to each other.

Comparison of these methods has been undertaken previously by other authors investigating corneal thickness variation in which ACS is a vital component of the measurements (Buehl et al., 2006a). Results have shown that while central corneal thickness measurements are similar enough to be interchangeable (Bourges et al., 2009), (Amano et al., 2006), (Kim et al., 2007), peripheral thickness measurements recorded at only a few positions (4 points, 1.5mm from the instrument axis) revealed differences of -2.7 to 7.5μm, along with poorer repeatability of the scan in the paracentral cornea (Buehl et al., 2006b). It has been suggested that these differences could be attributed to acquisition or image processing analysis (Bourges et al., 2009).

A longitudinal study carried out using the Orbscan IIz and Pentacam to evaluate posterior corneal surface changes following refractive surgery found that the correlation between the machines was poor and variable (Kim et al., 2009), suggesting that representation of the ACS and image processing methodology could be improved.

To date no studies have evaluated the relationship between 'traditional' keratometry and the ACS variability according to location of these two methods. This is of value to pre-operative planning procedures prior to cataract and refractive surgery, fitting of contact lenses and monitoring topographic changes caused by ocular disease and trauma, which all require accurate and reliable morphometrics beyond the paracentral cornea.

The main aim of this thesis is to investigate anterior ocular surface shape, and while these techniques are limited to the cornea surface due to their method of imaging (Chapter 2), the more advanced methods that will be used in the later chapters (Chapters 5-8) are not available to the common practitioner. The first step must therefore be to investigate how two readily-available instruments compare, in order to establish a possible precedent for the later studies.

3.2 Aims and Objectives

This study aimed to compare the measurement of anterior corneal topography using three different instruments: Javal-Schiötz keratometer (OM-4, Topcon Instruments Ltd, Tokyo, Japan), Orbscan IIz (Bausch & Lomb, Orbtek Inc., Salt Lake City, UT) and Pentacam (Oculus Optiikgeneräte GmbH Wetzler, Germany) on a large normal population.

The hypotheses proposed were:

- Keratometry and keratometric analogues show excellent agreement between all 3 instruments within the central 3mm zone of the cornea.

- Axial curvature measurements compared between Orbscan IIz and Pentacam are significantly different and clinicians will need to be aware of such differences and alter their practice accordingly.

3.3 Method

3.3.1 Subjects

Measurements from the right eyes only of 124 subjects were included in the study, (78 ♀ and 46 ♂), mean age of the cohort was 24.71±6.61 years [SD] (range 17.61 to 42.55). Ethical approval was obtained from the Cardiff University School of Optometry and Vision Sciences Ethics Committee. All subjects were treated in accordance with the Tenets of the Declaration of Helsinki and each provided informed, written consent. Volunteers were recruited from the staff and students of Cardiff University and subjects were excluded if they were pregnant or breastfeeding, had any ocular or systemic condition known to affect the structure or characteristics of the anterior ocular surface, were taking any medication known to affect the ocular surface, had worn rigid contact lenses in the preceding 6 weeks or soft lenses in the preceding 2 weeks and were not white European. This ethnic bias was chosen because it has been shown that ethnicity affects ocular surface morphometrics (Matsuda et al., 1992).

3.3.2 Experimental procedure

All measurements were carried out during a single session by the same investigator. Measurements were carried out in the following order:

1. Central keratometry using the Javal-Schiötz Topcon OM-4 keratometer **(J-S)**; three readings were taken of each right eye and a mean value recorded.
2. Corneal topography using the Pentacam **(Pent)**; The 3-D scan mode was used to record 25 images per second, with the system set to automatic release enabling automatic image acquisition. Unreliable measurements were repeated until three satisfactory readings were recorded (see Chapter 2).

3. <u>Corneal topography using the Orbscan IIz **(Orb);**</u> This instrument uses slit-scanning technology to project 40, 12.5 x 0.30 mm slit beams, 20 from the right and 20 from the left onto the corneal surface at a 45° to the instrument axis. The operator triggered the acquisition sequence after appropriate alignment of the instrument mires clearly on the ACS (see Chapter 2). Three images of the right eye were taken and a mean value assigned.

3.3.2.1 Measurements recorded for keratometry and keratometric analogues

The Orb produces Sim-K values for the maximum and minimum curvature values along the principal meridians of the cornea at a diameter of 3.0 to 3.2 mm from the instrument axis (Srivannaboon et al., 2007). Orb Sim-K values were recorded from the 'quad-map' output screen (Fig 3.1), with values designated in the same fashion as previously described.

<u>Figure 3.1</u>: Sim-K (radius of curvature) values provided by the Orbscan II quad map display output screen

Similarly, the Pentacam displays a Rh value for the horizontal radius of curvature and Rv for the vertical radius of curvature, with meridians determined on the 3mm 'ring' of the cornea and with the two major meridians lying, by definition, at 90° to each other (Fig 3.2).

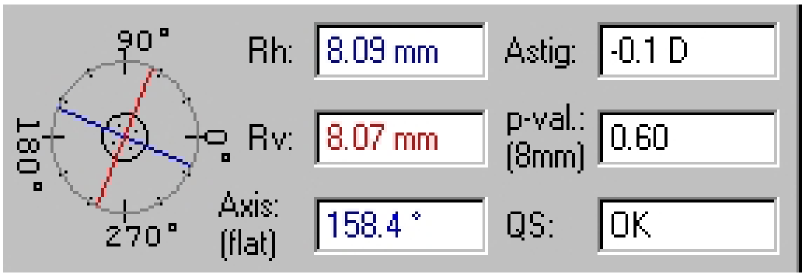

Figure 3.2: K-Values (radius of curvature) provided by the Pentacam overview display output screen.

Readings of the J-S non-automated keratometer were taken for the principal meridians and designated either horizontal or vertical according to the rule that axes up to 45° either side of 180° were assigned to the horizontal analysis, and axes up to 45° either side of 90° were assigned to the vertical analysis.

Axial (sagittal) topographic profiles of Orb and Pent were sampled from the output screen at 0.5mm intervals using an overlay reference grid. The radii of curvature were analyzed in the horizontal and vertical meridians. The profiles were aligned according to the instrument axis (designated 'Apex') and divided into annuli or zones, units of 1mm from the apex (Fig 3.3). The cumulative mean radii of each zone were compared to the J-S keratometry value (used to describe the standard 3mm central corneal curvature) in an attempt to compare differences in region curvature variation.

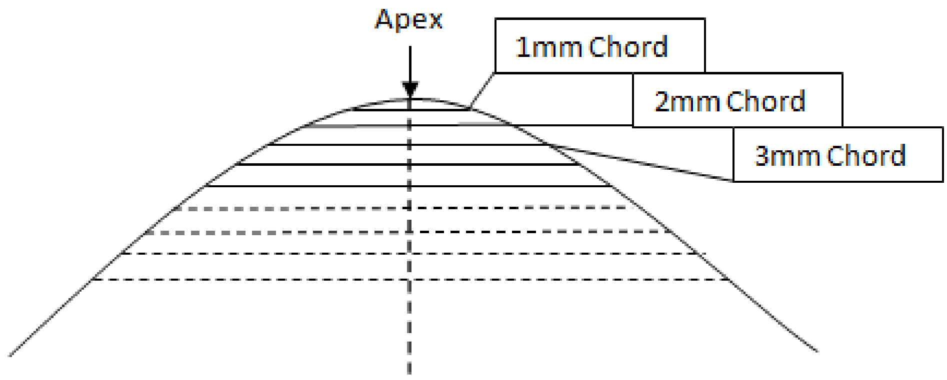

Figure 3.3: Diagram to show the area of profile included in each zone of cumulative mean radius of curvature.

3.3.2.2 Axial radius of curvature – profiles and zones

The 'traditional' Javal-Schiötz keratometer measures the axial radius of curvature (Bennett and Rabbetts, 1991), which has been verified on aspheric surfaces with conic sections approximating the ACS (Douthwaite and Burek, 1995). Therefore axial curvature was used for visual representation comparisons.

Profiles of the axial topographic output across the corneal surface, in the horizontal and vertical meridians, were sampled from the Orbscan (Fig 3.4) and Pentacam display screens (Fig 3.5).

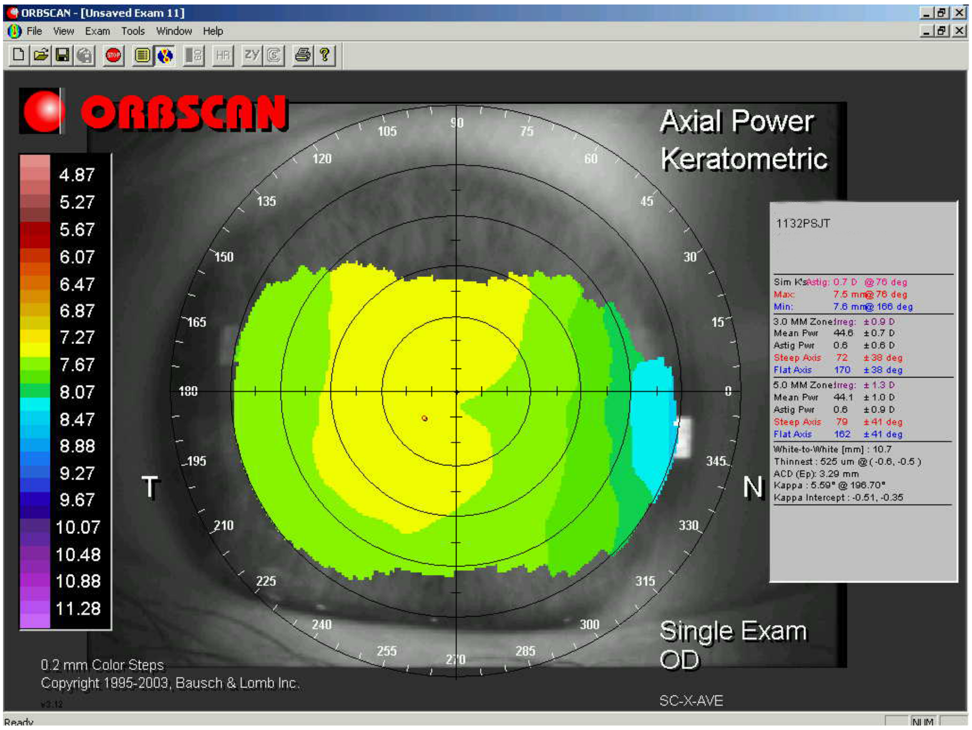

Figure 3.4: Orbscan IIz; Axial power keratometric output display (Scale bar set to radius of curvature).

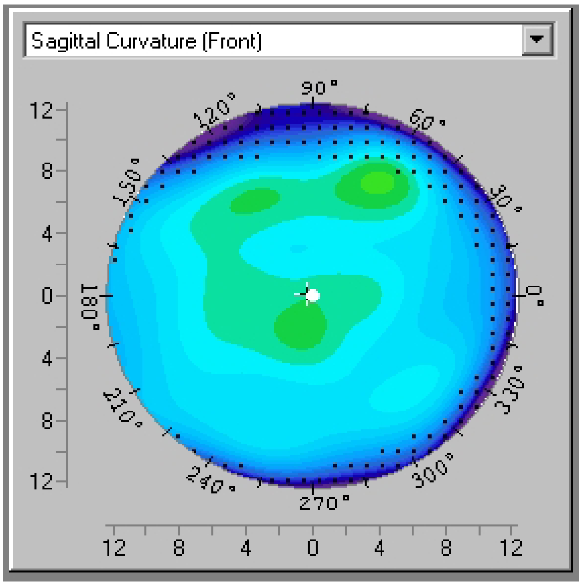

Figure 3.5: Pentacam; Sagittal curvature (Front) display output.

Hovering the cursor over a specific point on the screen, prompted a display of the corneal radius of curvature of that location. Starting at the central point and moving either horizontally or vertically in 0.5mm steps, the axial radius of curvature profile was obtained. To optimize the accuracy of cursor positioning, a transparent overlay was used, centred on the horizontal and vertical axis origin (0°H/0°V, designated 'Apex'). This ensured precise and comparable (x,y) co-ordinates on each output-display. Data was collected for the complete display output, that is, up to 12mm in the horizontal and vertical meridians. The limit of the profile was determined by the available data for each subject, which was limited by the reflective properties of the pre-ocular tear film and by the extremities of the vertical palpebral aperture.

The data from the profiles was then aligned according to the instrument axis and divided into a series of annuli of 1mm steps from the apex (Fig 3.3). A cumulative mean radius of curvature was calculated for each zone.

3.3.3 Statistical analysis

All data was collated with Excel 2007 (Microsoft®, Redmond, DC), and analyzed within SPSS v13 (SPSS Inc, Armonk, NY). Tests for normality were carried out and mean K-readings from the non-automated J-S keratometer were compared to Orb Sim-Ks and Pent K-values in the principal meridians, using analysis of variance (ANOVA) to examine the differences between methods.

The Bland and Altman method (Bland and Altman, 1986) was used to assess the between-instrument agreement: J-S versus Orb, J-S versus Pent and Orb versus Pent. This provided a more sophisticated method of comparison than correlation analysis as the plot provides a means with which to assess the magnitude of disagreement (error and bias), and reveals outliers and trends.

For the cumulative mean radii of curvature calculated for each section of the 2-dimensional ASC profile, the data was compared using a two-way between groups ANOVA with Bonferroni post-hoc testing. The area of analysis was limited to 8mm horizontally and 4mm vertically, due to interference from the eyelids and eyelashes.

3.4 Results

Horizontal profile

Table 3.1 compares the mean radii of curvature values for conventional keratometry measurements in the horizontal meridian: J-S, Orb ('Sim-K') and Pent ('K-Values') and cumulative mean radii values for sections of corneal profile according to location.

Area of interest	Mean radius of curvature (mm±SD) for N=124					
	J-S	ORB	PENT	J-S vs ORB	J-S vs PENT	ORB vs PENT
Mean Keratometry	**7.82±0.23**	**7.80±0.31** ('Sim-K')	**7.86±0.29** ('K values')	**p=0.072**	**p<0.001**	**p<0.001**
Apex		7.72±0.32	7.78±0.29	p=0.010	p=0.409	p<0.001
1mm zone		7.73±0.32	7.80±0.30	p=0.025	p=1.000	p<0.001
2mm zone		7.74±0.31	7.81±0.30	p=0.046	p=1.000	p<0.001
3mm zone		7.75±0.31	7.81±0.30	p=0.080	p=1.000	p<0.001
4mm zone		7.75±0.32	7.81±0.30	p=0.143	p=1.000	p<0.001
5mm zone		7.77±0.32	7.82±0.30	p=0.303	p=1.000	p<0.001
6mm zone		7.78±0.32	7.84±0.30	p=0.694	p=1.000	p<0.001
7mm zone		7.80±0.32	7.86±0.30	p=1.000	p=0.857	p<0.001
8mm zone		7.82±0.32	7.89±0.30	p=1.000	p=0.195	p<0.001

Table 3.1: Comparison of radius of curvature (mm) measures in the horizontal meridian: for keratometric analogues (second row), instrument axis (designated apex) and mean regional curvature allocated as zones up to 8mm using J-S, Orb and Pent.

When comparing the keratometry measures between instruments, the Orb 'Sim-K' presents slightly steeper radii of curvature, 7.80 ±0.31mm [SD] than the J-S, 7.82 ±0.29mm [SD], although this was not statistically significant (p=0.072). The Pent 'K-values' were significantly flatter than the J-S and Orb, 7.86 ±0.29mm compared to

7.82 ±0.29mm (J-S) and 7.80±0.31mm (Orb); both these comparisons were highly significant ($p<0.001$).

The cumulative radii of curvature means for the series of zones that originated from the instrument axis (designated apex) along the horizontal profile are shown in Table 3.1. Each zone represented a section of the profile equidistant from the apex, i.e. the 2mm zone extended 1mm either side of the apex (Fig 3.5). The Orb measurements flatten on average 0.05 ±0.04mm [SD] when comparing the apex zone radius to each of the other 8 zones (cumulative mean values increasing from 7.72 to 7.82 ±0.32mm). These measurements were significantly different to the spherical profile of the J-S instrument at the apex through to the 2mm zone (apex $p=0.010$, 1mm zone $p=0.025$, 2mm zone $p= 0.046$) but lacked statistical significance from zones 3 to 8mm ($0.080<p<1.000$) The Orb radii across each zone were significantly steeper than the Pent measurements across the entire profile (Zones 1 to 8, all $p<0.001$). The significance values decrease for J-S vs Orb from apex to 8mm zone from $p=0.010$ to 1.000. This trend is not mirrored in the J-S versus Pent results, with the majority highly insignificant ($p=0.857$ to 1.000) in zones 1 to 7, but closer to significance at the apex ($p=0.409$) and zone 8 ($p=0.195$).

Vertical Profile

Area of Interest	Mean radius of curvature (mm± [SD]) for N=124					
	J-S	ORB	PENT	J-S vs ORB	J-S vs PENT	ORB vs PENT
Mean Keratometry	**7.67±0.29**	**7.64±0.31** (‘Sim-K’)	**7.70±0.29** (‘K-values’)	**p<0.005**	**p<0.001**	**p<0.001**
Apex		7.72±0.32	7.77±0.29	p=0.543	p=0.010	p<0.001
1mm zone		7.70±0.31	7.74±0.29	p=1.000	p=0.116	p<0.005
2mm zone		6.27±0.51	7.73±0.29	p<0.001	p=0.201	p<0.001
3mm zone		6.67±0.42	7.73±0.29	p<0.001	p=0.231	p<0.001
4mm zone		7.68±0.31	7.73±0.29	p=1.000	p=0.195	p<0.001

Table 3.2: Table to show comparison of radius of curvature (mm) measures in the vertical meridian: keratometric analogues (second row), instrument axis (designated apex) and mean regional curvature allocated as zones up to 8mm for J-S, Orb and Pent.

Table 3.2 shows the mean radius of curvature values for conventional keratometry measurements in the vertical meridian: J-S, Orb (‘Sim-K’) and Pent (‘K-Values’). The mean Orb value of 7.64± 0.31mm [SD] was significantly steeper than both J-S 7.67± 0.29mm [SD] ($p<0.005$) and Pent 7.70± 0.29mm [SD] ($p<0.001$). The Orb versus Pent comparison showed a trend of steeper radii values for the Orb, highly significant across the entire profile (Zones 1 to 4, $p<0.001$).

Comparisons of the cumulative mean radii showed a surprising steepening in radius of curvature along the 2 and 3mm zones of the Orb profile (2mm Zone; 6.27±0.51 and 3mm Zone; 6.67±0.42) these findings were statistically significant (both zones $p<0.001$). The Pent values steepen from apex to 4mm zone (Zones 1 to 4; 7.74±0.29 to 7.73±0.29), contrary to expectations, however these differences in radii were not statistically significant ($0.116<p<0.231$). The Pent measurements were found to be consistently flatter than Orb across the entire profile, differences between radii measurements were highly significant ($0.001<p<0.005$).

The between instrument agreement is illustrated in Figures 3.6 to 3.8.

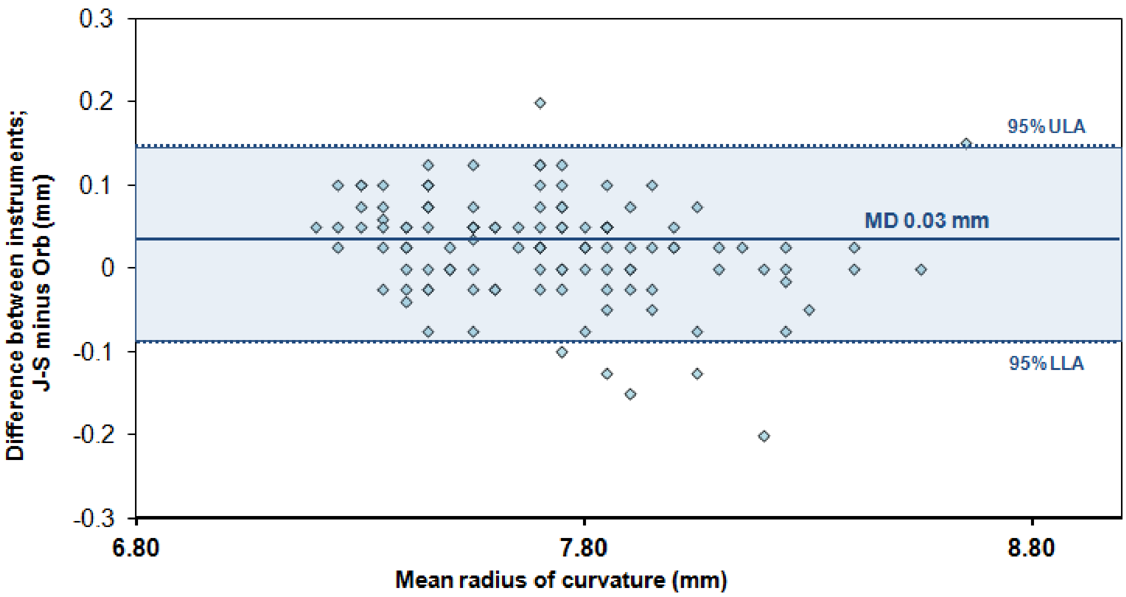

Figure 3.6: Bland-Altman plot showing the limits of agreement (95% Upper limit of agreement (ULA) ,95% Lower limit of agreement (LLA) and Mean difference (MD)) of mean keratometry measurements between J-S and Orb (J-S – Orb).

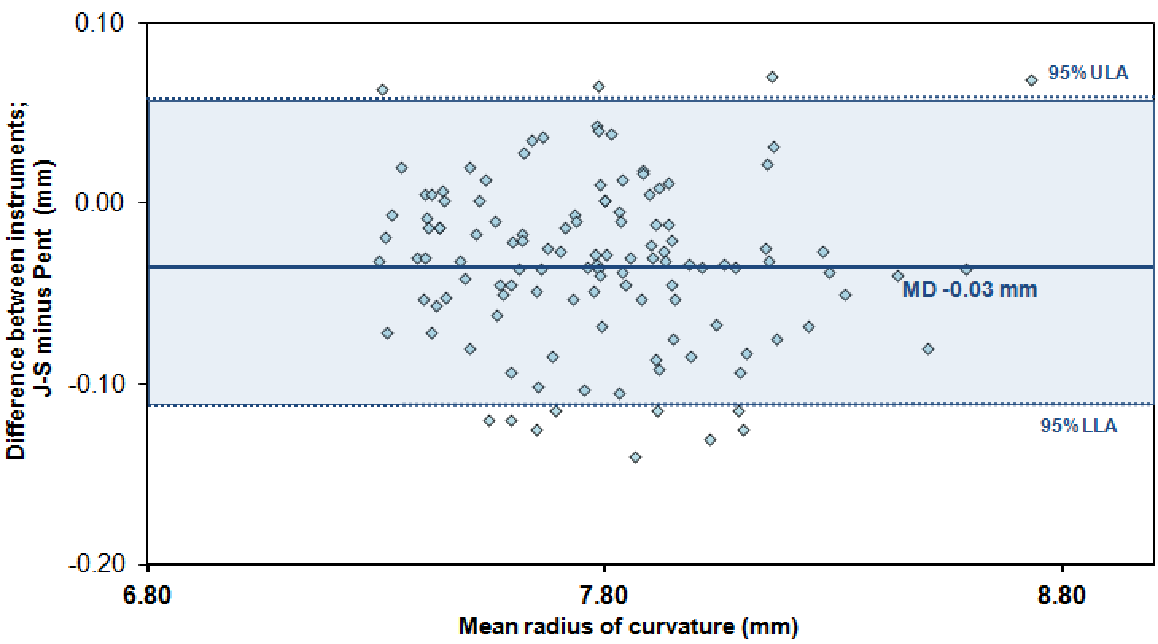

Figure 3.7: Bland-Altman plot showing the limits of agreement (95% Upper limit of agreement (ULA) ,95% Lower limit of agreement (LLA) and Mean difference (MD)) of mean keratometry measurements between J-S and Pent (J-S – Pent).

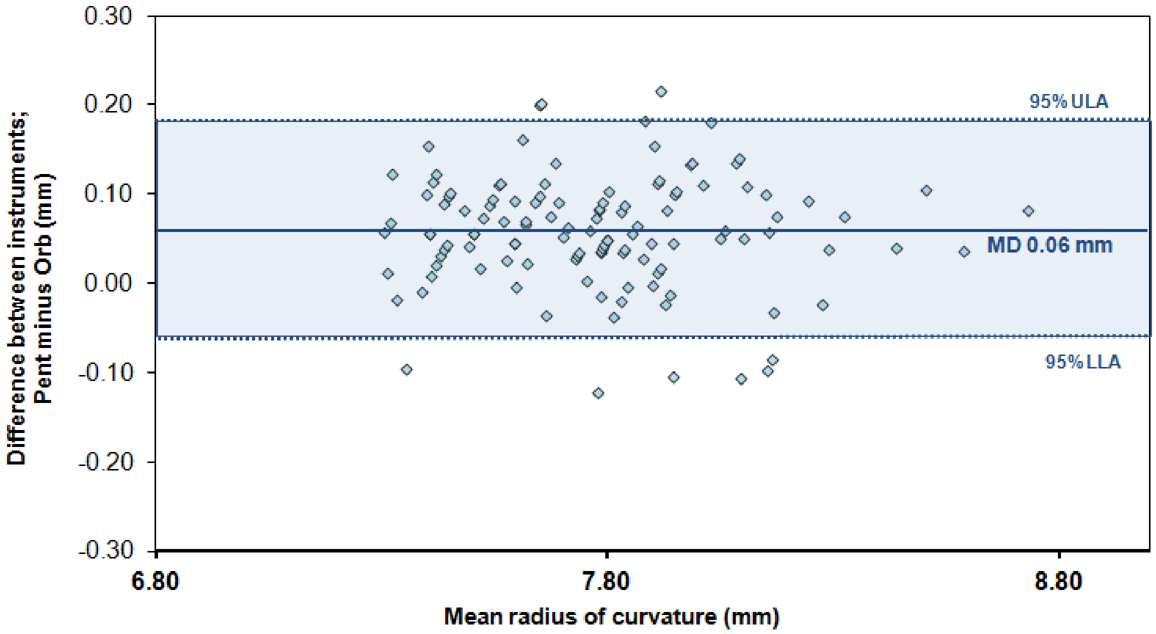

Figure 3.8: Bland-Altman plot showing the limits of agreement (95% Upper limit of agreement (ULA) ,95% Lower limit of agreement (LLA) and Mean difference (MD)) of mean keratometry measurements between Pent and Orb (Pent – Orb).

The majority of data collected fell within the 95% limits of agreement (LoA) designated by the Bland-Altman method. The LoA for Orb compared to J-S and Pent were found to be ±0.12mm and ±0.09mm for J-S compared to Pent, showing close inter-instrument agreement for keratometric analogue measures. There was a negative bias (tendancy to measure flatter) of -0.03 mm in radii data measured using Pent compared to J-S, a positive bias (tendancy to measure steeper) of 0.06 mm in radii data measured with Orb compared to Pent and 0.03 mm in radii data measured with Orb compared to J-S.

The graphs in Figures 3.9 and 3.10 show a visual comparison of curvature profiles for J-S, Orb and Pent in the horizontal and vertical meridians. The J-S keratometry represented as an arc of the mean keratometric radius of curvature of the particular profile, the x and y axes were scaled at a ratio of 1:1.

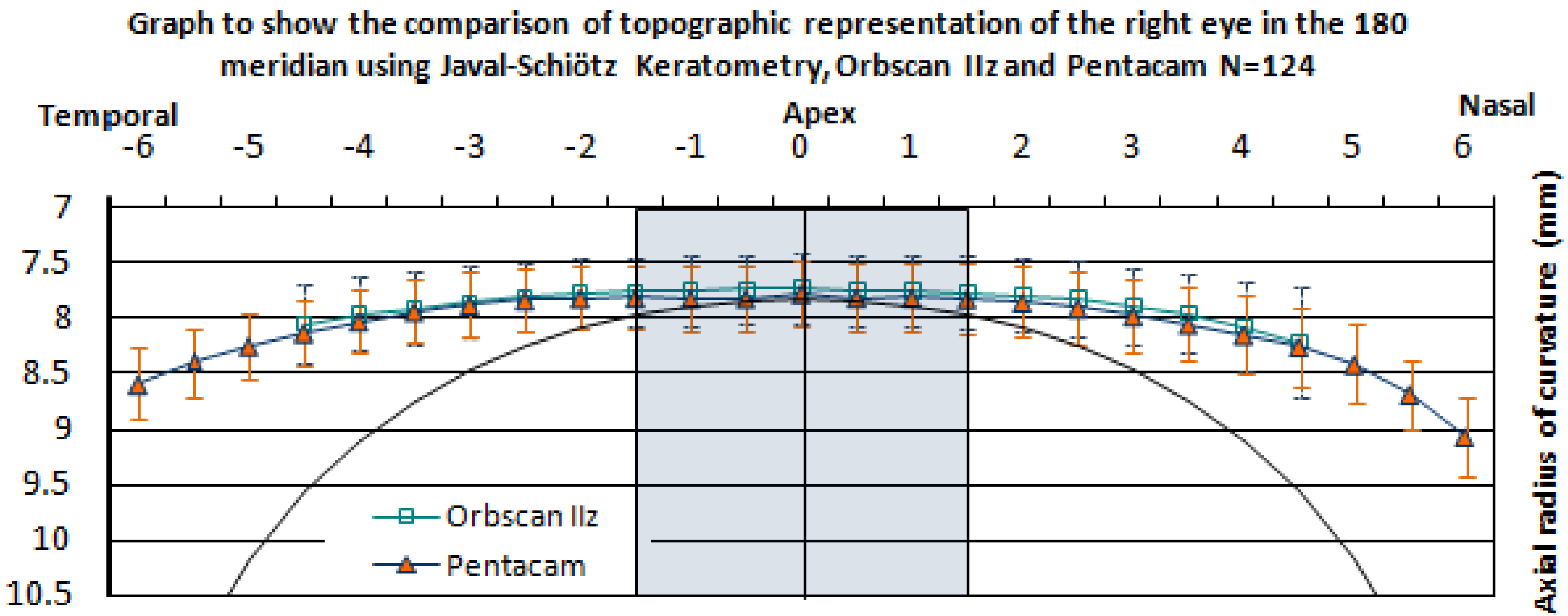

Figure 3.9: A comparison of axial curvature profiles of J-S, Orb and Pent in the horizontal meridian. The solid black line indicates a spherical profile that represents a theoretical 2-D J-S profile interpolated from the mean keratometry value of the group. The grey shaded area shows the location of central cornea within which keratometry measurements are estimated to have been taken using J-S instrumentation (Error bars signify 1 SD either side of the mean value)

The horizontal profile provided by the axial radius of curvature output from Orb and Pent was similar to the J-S arc in the region 0.5mm either side of the instrument axis (apex). The temporal profile of Pent was a similar shape to Orb, with the Orb profile consistently slightly steeper. The nasal profile showed increased flattening of the Pent profile widening the curvature difference in the corneal periphery compared to Orb.

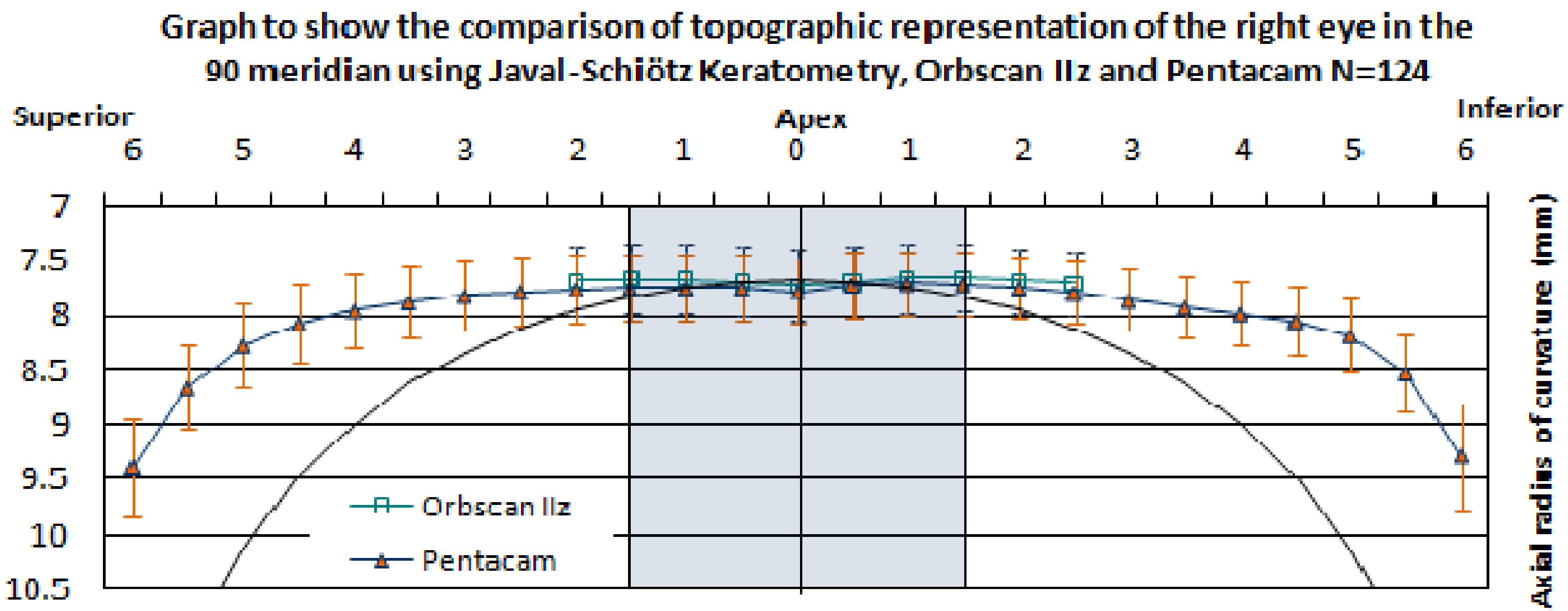

Figure 3.10: A comparison of axial curvature profiles of J-S, Orb and Pent in the vertical meridian. The solid black line indicates a spherical profile that represents a theoretical 2-D J-S profile interpolated from the mean keratometry value of the group. The grey shaded area shows the location of central cornea within which keratometry measurements are estimated to have been taken using J-S instrumentation. Error bars signify 1 SD either side of the mean value.

In the vertical meridian there was a negative curvature inflection (dip) observed in the central profiles of Orb and Pent, incongruous with the J-S arc representation. Both Orb and Pent profiles met the J-S arc at 1mm from the instrument axis and then flattened in an identical pattern in both superior and inferior directions. The Orb data curve was seen to maintain a consistent slightly steeper profile than the Pent curve.

3.4 Summary

3.4.1 Keratometric analogues

- Horizontal meridian; Pent was flatter than J-S and Orb (Pent>J-S>Orb)
- Vertical meridian; Orb was steeper than J-S along the paracentral cornea section (zones 2-3mm), Pent was consistently flatter than Orb.
- 95% LoA; ± 0.12mm between Orb and J-S, Orb and Pent. Closest agreement ± 0.09mm between J-S and Pent
- Bias; Orb tended to read steeper than J-S (0.03mm) and Pent (0.06mm) Pent tended to read flatter than J-S (-0.03mm)

3.4.2 Mean regional curvature variability

- Horizontal meridian; Orb was steeper than J-S near to the apex (up to 2mm zone), Pent was consistently flatter than Orb.
- Vertical meridian; Orb was steeper than J-S along the paracentral cornea section (zones 2-3mm), Pent was consistently flatter than Orb.

3.4.3 Visual profile comparison

- Horizontal profile; Orb and Pent were similar to J-S in central 1mm zone, Orb consistently steeper in periphery, Pent increasingly flatter in nasal periphery.
- Vertical profile; Orb and Pent central ‘dip’. Orb consistently steeper than Pent in periphery.

3.5 Discussion

In the absence of a standardized anatomical model for central corneal curvature the interpretation of results collected throughout this study are limited to the relationships between these three devices. The comparisons made during the course of this investigation suggest that axial radii measurements vary and this has implications both clinically and for the remainder of this thesis.

3.5.1 Clinical implications

A curvature correction factor would be required for keratometric analogue 'translation' between Orb and Pent. Pent measures exhibit a positive bias +0.06mm when compared to Orb. This is unlikely to affect soft contact lens fitting choice, but it may be important when selecting a rigid gas permeable trial lens, where the clinically significant difference is 0.05mm (specified by back optic zone radius). A similar magnitude of bias (-0.05mm) has been reported in comparisons between the Grand Seiko Auto Ref/Keratometer WAM-5500 (Japan) and J-S (Sheppard and Davies, 2010), although the method of calculating radius of curvature was not stated. The bias reported between the IOLMaster (Zeiss Instruments, Germany) and J-S for mean corneal curvature values was -0.03mm (Santodomingo - Rubido et al., 2002).
For intraocular lens calculations, the 0.3D difference in corneal power calculated from the positive bias between Orb and Pent keratometric analogues would not be considered clinically significant in refractive terms since the limits of agreement for subjective refraction are reported to be ±0.42D (Smith, 2006). This compares with the accuracy of calculating intraocular lens power using keratometric analogues from either the Galilei™ dual Scheimpflug analyser (Ziemer Ophthalmic Systems AG, Switzerland) or Keratron placido-disk topographer (Opticon 2000, Italy), mean errors were found to be 0.21± 0.18D [SD] and 0.23± 0.22D [SD] respectively (Savini et al., 2011).

By implication the keratometric analogues provided by Orb, Pent and traditional J-S keratometry measurements are interchangeable when considering intraocular lens power selection prior to cataract surgery, but require interpretation with caution for contact lens fitting. The peripheral interpretation of corneal curvature (values appear flatter than expected) may influence practitioners to chose a steeper than optimal initial fitting lens in particular, when fitting larger diameter (10-16mm) designs of gas permeable contact lenses.

3.5.2 Thesis implications

However undesirable, keratometric analogues recorded using Orb and Pent were found to be significantly different to those provided by the 'traditional' J-S keratometer. Factors influencing these differences can be attributed to;

Instrument repeatability; J-S repeatability has been reported to be ±0.051mm, with a correction factor required of 0.044-0.053mm (depending on curvature magnitude), caused by mire image raypaths suffering from oblique astigmatism (Bennett and Rabbetts, 1991). Excellent instrument repeatability has been reported for anterior curvature for Orb 0.0002±0.0007mm (SD) centrally on test surfaces (Cairns and McGhee, 2005) and for Pent 0.0000±0.0300mm (SD) from a average of 3 readings (Chen and Lam, 2009). This suggested that the lack of uniform precision of the J-S measurements contributed to the variability observed between keratometry values compared to Orb and Pent.

Vertical profile 'dip'; It appears improbable that the central corneal curvature profile exhibits 'dip' observed only in vertical meridian centred at the apex (Fig 3.11).

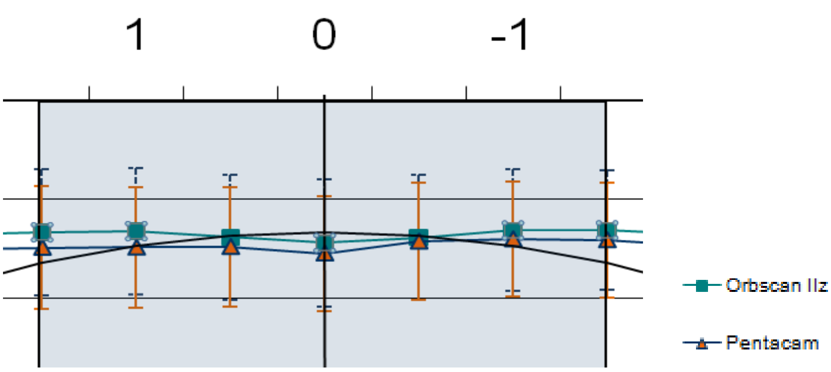

Figure 3.11: Diagram to show the representation of the corneal apex vertical profile according to measurements made using J-S, Orb and Pent (n=124)

A mean difference of -0.05±0.15mm was recorded at the lowest point of inflection with the mean J-S apical measure 7.67± 0.29mm [SD] (range 7.15 to 8.75) compared to Orb 7.72± 0.32mm [SD] (range 7.10 to 8.60). This zone is reported to have the tear film thickness of 3-10.4μm (King-Smith et al., 2000) The influence of blinking on this region is negligible, with differences in instantaneous power found to be insignificant ($p>0.05$) (Buehren et al., 2001). Changes in topography between 1.4 -2.4μm are attributed to eyelid pressure (Shaw et al., 2008). Therefore, this 50μm concave 'indentation' may, in part be attributed to an artefact caused by algorithmic interpolation of an area not sampled by reflection due the positioning of the Orb camera, compounded by the vertical slit-image missing the apex location and the use of low order polynomial functions or smoothing splines (Cairns, Collins and McGhee, 2003) to interpolate intermediate data points. In a precision study investigating Orb assessment of ACS, the central 2.5mm internal diameter data was rejected due to lack of precision based on placido-disk methodology (Applegate and Howland, 1995b). The small size of the reflected rings imaged at the apex exhibit very small changes in size where the ACS has been found to be most regular and therefore ilicit less detectable differences when compared to the test reference grid. Larger rings provide improved precision (Douthwaite and Parkinson, 2009). The exact influence of each of these contributing factors remains unknown.

Similarly Pent relies on a camera positioned on the instrument axis for image capture and must interpolate missing data. Additionally in both cases this may be an unwanted effect caused by mathematical manipulation of curvature data to provide keratometry analogues which match traditional keratometry values. Given the proprietary nature of the topographic algorithms used it is not possible to determine the weight that each set of assumptions has on the output. However the data from both sources provides a visually similar ACS representation over the central 4mm in the vertical meridian.

When comparing corneal power values measured with standard keratometry methods and small-mire keratometry, a statistically significant difference in the representation of changes in values was observed in early corneal morphometric experiments (Mandell, 1963). In improving the accuracy of keratometry measurements of the periphery, it was noticed that the ACS profile topography was markedly different (Fig 3.12). In other words, if assumptions used with J-S keratometry about the central ACS 3.3-3.5mm (Lehmann, 1967) are applied to the entire profile, this will inevitably result in inaccuracies in the periphery.

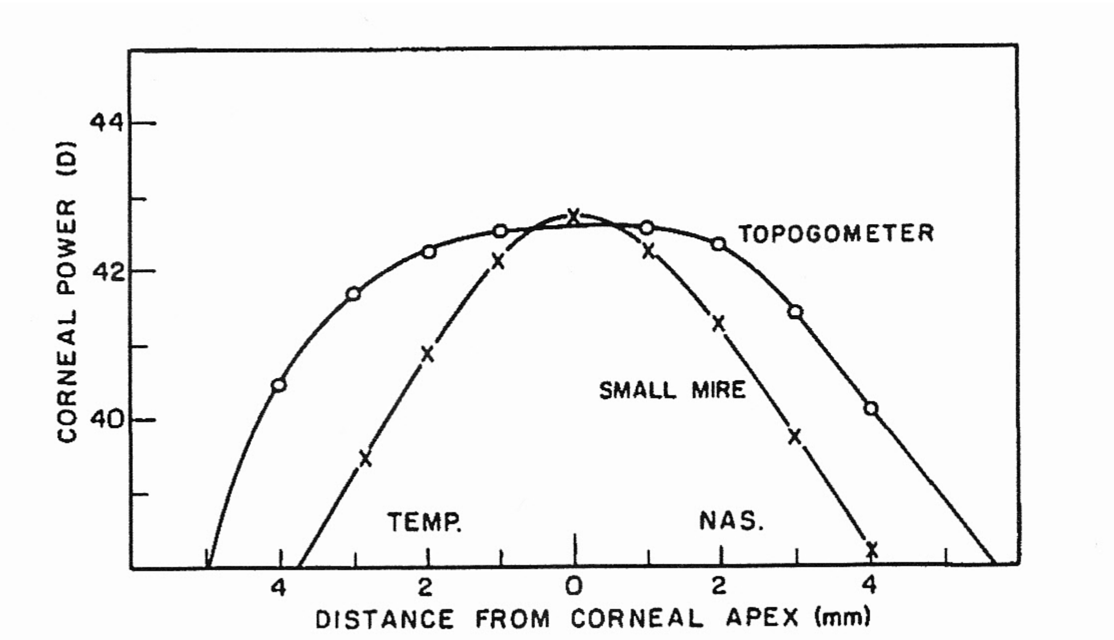

Figure 3.12: Difference in power values using small-mire and standard keratometry (Topogometer) to measure the periphery of a typical cornea (Mandell, 1963)

This supports the argument that manipulating the ACS to provide equivalent keratometric analogues distorts the profile representation. As Orb and Pent measurements were significantly different, this suggests that the methods of mathematical modelling of the two instruments were incompatible. In essence, both approaches have reached a compromise in order to accommodate a multi-use platform

Randomising measurements: Test randomisation was not carried out during the course of this study. In order to minimise carry over effects from either operator or instrument, keratometry measurements required a randomised sequence during data collection. These effects may have contributed to significant differences found and require further evaluation.

.

3.6 Conclusions

- When carrying out biometry prior to cataract surgery, central keratometry measurements from J-S, Orb ('Sim-K') and Pent ('K-Values') are interchangeable.
- Clinically significant differences were found between Orb 'Sim-K' and Pent 'K-Values'. Pent axial curvature measurements were found to be consistently flatter than Orb across both horizontal and vertical profiles. Therefore, topographic data from Pent cannot be used in conjunction with Orb Fitscan RGP fitting software.
- A negative curvature inflection or 'dip' was observed in the vertical profiles of Orb and Pent. This does not concur with direct observations of the central cornea made with slit-lamp bio-microscope or contact lenses. Ostensibly this represents an artefact caused by proprietary algorithmic interpolation, resulting from the manipulation of the curvature data to provide 'traditional' keratometry analogues. This was compounded by limitations of image collection methodology as discussed earlier. The precise influence of each of these factors remains unknown

Current understanding of the corneal shape relies on central sphericity and this has been exploited in the design of the J-S Keratometer. The more sophisticated technology available in Orb and Pent instrumentation, has extended the reaches of AOS profile measurement without accurate anatomical reference. The next step for this thesis was to investigate the best method of defining a 'true' representation of the anterior ocular surface shape, which will satisfy the needs of Ophthalmic surgeons, the contact lens industry, and researchers.

Chapter 4

Investigating anterior ocular surface morphometrics using 3- Tesla Magnetic Resonance Imaging

The previous chapter highlighted the issues associated with determining the morphometric descriptors of the ACS in the absence of a definitive representation of the surface in question, combined with the influence of the historic development of measurement techniques which had formed the accepted fundamental interpretation of corneal topography. The aim of this thesis is to establish a 'gold standard' wide-field morphometric 3-D profile of the entire AOS. Having considered all available technologies with which to carry out this task (Chapter 2), magnetic resonance imaging (MRI) offered the most promising opportunity to optimise surface data collection using non-invasive, non-contact, 3-dimensional reconstruction techniques. This chapter outlines preliminary investigations carried out to confirm the suitability of this technique for wide-field anterior ocular surface data acquisition.

4.1 Introduction

MRI is a method of generating cross-sectional images of internal body structures *in-vivo* based on the physical phenomena of nuclear magnetic resonance. Body tissues, such as the globe and associated structures, contain abundant hydrogen nuclei, which can be aligned using a strong external magnetic field. If a highly specific radio frequency pulse is applied during the alignment, the energy state of the hydrogen protons increases for the pulse duration and then drops to its prior state, emitting electromagnetic waves. These signals are picked up by the scanner and a brightness intensity profile attributed to individual pixels, which are composed into picture elements and formed into images reconstructed using mathematical algorithms (Wichmann, 2002). Using localiser images, regions of interest can be isolated and a series of 2-D contiguous images acquired in the same plane through the tissue, building a picture of the anatomical presentation and topographic structure (Koretz et al., 2004). The strength of the magnetic field used varies with the make and model of MRI scanner, the investigation of ocular tissues as been carried out using 1.5, 3 and 7 Tesla magnets (Richdale et al., 2009)

MRI has been used to identify orbital disease and retro-bulbar masses (Moseley, Brant-Zawadski and Mills, 1983), to study functional anatomy of the extra-ocular muscles and their relation to the orbital connective tissues (Detorakis et al., 2003), to characterise the 2- and 3-dimensional shape of internal globe structure in myopia (Cheng et al., 1992, Atchison, Jones and Schmid, 2004, Singh et al., 2006), to study changes in anterior segment anatomy caused by presbyopia (Koretz et al., 2004),(Strenk, Strenk and Guo, 2006), and to quantify the axial misalignment between the crystalline lens and cornea (Chang, Wu and Lin, 2007). MRI has been used to reveal parts of the globe *in-vivo* normally obscured by overlying structure, for example peripheral parts of the crystalline lens usually screened by the iris (Strenk et al., 1999) and the ciliary body hidden by the sclera (McCaffery et al., 2002). Since a significant proportion of the AOS under scrutiny is covered by the upper and lower eyelid tissue, MRI offers a potentially viable method of imaging the entire AOS in an undisturbed state. Given that the average vertical palpebral aperture in the white European population is reported to be 9.67mm (Read et al., 2006b), this may expose a further 17mm in the vertical meridian for topographic evaluation without relying on speculi or lid manipulation. In addition, images can be taken in the subject's primary position of gaze to limit any changes in topography caused by extreme ocular excursions.

There are 2 types of image acquired during MR scanning, which are differentiated by the radio frequency pulse signal decay. The first is the signal decay of the sum vector parallel to the strong external magnetic field – named T1 relaxation. This type of MRI protocol encourages protons bound to macromolecules to fast relaxation, transferring excess energy to the environment (Wirtschafter et al., 1992). These images (Fig 4.1), showing structures containing healthy fat as bright white or hyper-intense, can be obtained with high-speed scanning protocols, which are effective at reducing motion artefacts encountered during eye scanning (Detorakis et al., 2003), (Berkowitz et al., 2001), (Schueler et al., 2003), (McCaffery et al., 2002), (Lemke et al., 2001), (Patz et al., 2007).

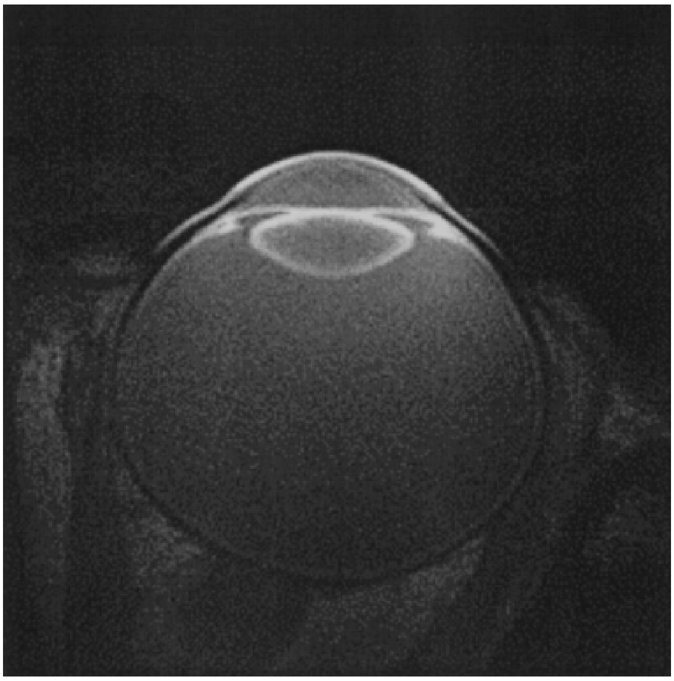

Figure 4.1: T1-weighted MR image of the right open eye of a 42 year old subject using a customised eye imaging radio frequency coil and 1.5 Tesla external magnetic field (Koretz et al., 2004).

The second type, T2 or transverse relaxation, is the signal decay of the sum vector perpendicular to the external magnetic field. This causes a slow loss of coherence out-of-phase, resulting in energy exchange with adjacent small molecules (Wirtschafter et al., 1992). The imaging protocols are slow, prone to motion artefacts and depict free-water found in high concentration in the anterior chamber and vitreous as white or hyper intense (Fig 4.2). This imaging protocol has been used to measure axial length (Akduman et al., 2008) and aqueous-vitreous volume as a surrogate for 3-D globe surface representation in myopia (Singh et al., 2006). Attempts have been made to improve image resolution using a rhythmic blink sequence synchronised to the optimised T2 imaging protocol (Obata et al., 2006), and, in addition, polyurethane head moulds have been constructed to minimise body movement (Berkowitz et al., 2001). Also, addition and re-alignment techniques have been used during image processing (Obata et al., 2006).

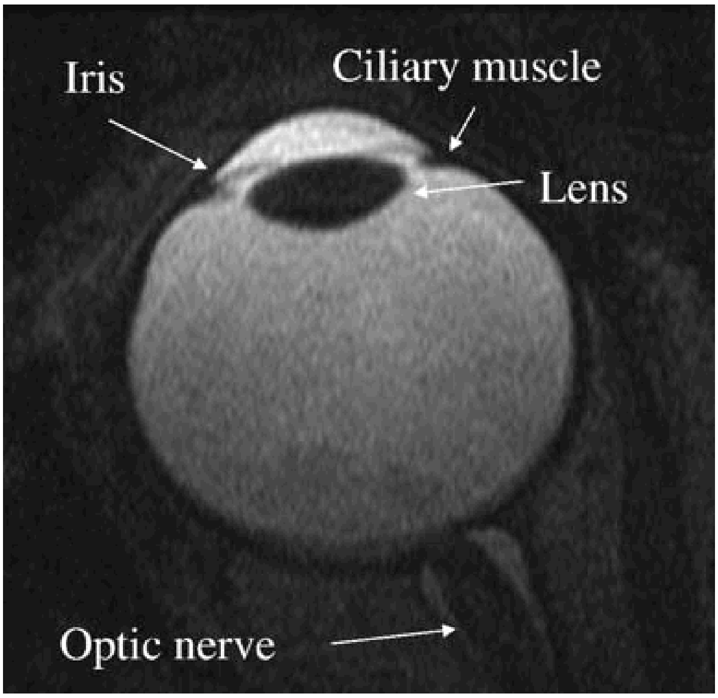

Figure 4.2: T2-weighted MR image using a microscopic imaging radio frequency coil, blink synchronisation, re-slicing and re-alignment image processing with 1.5 Tesla external magnetic field (Obata et al., 2006)

Measurement of the fine structures of the human eye *in-vivo* using a 1.5 Tesla external magnetic field did not produce successful differentiation of the central or peripheral cornea with either T1 or T2 imaging sequences (Patz et al., 2007). The MR scanning system available for use at Cardiff University Brain Imaging Research centre (CUBRIC) provides a 3-Tesla external magnetic field, this offers hope of further improvement in resolution. However, this occurs at the expense of increased sensitivity to the motion artefact.

In-plane resolution of MR images using a 1.5 Tesla scanner has been reported to have improved from 0.40mm to 0.10mm using small custom surface radio frequency coils (Richdale et al., 2009). One millimeter slice scanning, at thickest, is required for adequate 3-D reconstruction (Obata et al., 2006). This study demands topographic accuracy to at least within tolerances for contact lens manufacture ±0.05mm (BSI, 2006), to ensure adequate alignment to ocular surface contours and minimise mechanical insult to the sensitive tissues. It is the requirement of this investigation to seek to optimise scanning protocols to further improve 2-dimensional image resolution.

The characteristics of the ‘ideal’ topographic data set include:

- Minimal deleterious effects on the AOS or any body tissues; no permanent or damaging effects caused by exposure to the external magnetic field or radio frequency waves.
- No lasting discomfort, during or preceding the procedure; for MRI examination the entire subject must be brought into a narrow shaft of the equipment to ensure that their position is central to the magnetic field and offers optimal homogeneity. This can cause anxiety to claustrophobic subjects. Internal trauma may be caused by metallic-ferromagnetic foreign bodies or implants, e.g. pacemakers or aneurism clips moving when exposed to the high external magnetic field. For these reasons, extreme care was taken to carefully select subjects and strict adherence to safety protocols was observed.
- High accuracy; this investigation seeks to establish a ‘gold standard’ topographic representation of the AOS, in the absence of previous data, and therefore scanning needs to be to the highest standard.
- Excellent differentiation of the external cornea and scleral architecture to ensure a detailed and anatomically authentic contour of the AOS can be extracted in 2-D and reconstructed into a 3-D digital model.
- Imaging protocols that enable <1mm slices to be taken during contiguous image acquisition allowing sufficient data between images to reconstruct a 3-D surface representation.
- Short image acquisition times to optimise motion artefacts incurred by movements of the globe, eyelids and head.
- Compatible image scaling in all planes and dimensions to provide accurate AOS reconstruction.

4.2 Aims and Objectives

This study used a 3-Tesla MR imaging system; Discovery MR750 3.0T (General Electric Medical Systems, Waukesha, WI) to collect a 3-dimensional data set with which to reconstruct an accurate representation of the AOS *in-vivo*.

The hypotheses proposed are:

- 3 Tesla MR imaging can provide accurate morphometric data of the AOS without deformation or invasive intervention.
- A series of 3 Tesla 2-D MR images of axial sections through the globe can procure sufficiently resolute data with which to differentiate the AOS and reconstruct digital 3-D representations.

4.3 Materials and Methods

4.3.1 Experimental procedure

Four subjects were included in this preliminary study, (2 ♀ and 2 ♂), mean age of the group was 37.85 ±4.28 years [SD] (range 31.51 to 40.14). Volunteers were recruited from the staff and students of Cardiff University, and subjects were excluded if they were pregnant or breastfeeding; had any ocular or systemic condition known to affect the structure or characteristics of the anterior ocular surface; were taking any medication known to affect the ocular surface; had worn rigid lenses in the preceding 6 weeks or soft lenses in the preceding 2 weeks; did not contain any metallic-ferromagnetic implants or foreign objects; and were not known to be claustrophobic. All subjects were treated in accordance with the tenets of the Declaration of Helsinki (2004) and institutional guidelines.

The subjects attended for 2 sessions of 1.5 hours duration. Each participant was scanned in a whole-body MRI scanner 3 Tesla, Discovery MR750 3.0T(General Electric Medical Systems, Waukesha, WI). MR images were collected with an eight-channel phased array head coil, which is able to rapidly scan both eyes simultaneously with high signal-to-noise ratio. A T1-weighed spin-echo pulse sequence was selected first to differentiate muscle and soft tissue from the AOS.

Initially, a series of localiser images were acquired so that subsequent axial slices were aligned perpendicular to the corneal apex. Seven contiguous slices were simultaneously acquired with a 3mm slice thickness with a 4cm field of view resulting in 0.25mm in-plane resolution. Following this, T2-weighed fast spin echo sequences were carried out resulting in 30, 1mm thickness slices with a 10cm field of view. The subjects were asked to fixate during both types of sequence on a distant object with both eyes open, viewed through a mirror mounted on the head coil.

4.3.2 Optimising T1-weighted MR imaging sequences

Further measures were taken to optimise in-plane image resolution:

- Application of Lacri-lube® (Allergan Ltd, Bucks, UK) containing wool and mineral oils in a thick ocular ointment, to the right eye prior to MR imaging. T1-weighted sequences have been shown to image proton bound macromolecules eg fat and lipids as hyperintense or white structures. It was hoped that a layer of Lacri-lube® would enhance the contrast of the AOS and improve the surface delineation.
- A custom-designed blink artefact reduction system was used during imaging. The subject was provided with an electronic switch inside the MR scanner, which enabled the user to temporarily pause the pulse sequence when blinking was necessary.
- Previous studies had not combined blink artefact reduction and enhanced surface delineation

4.3.3 Optimising T2-weighted MR imaging sequences

These longer sequences required periods of up to 10 minutes acquisition time. Further measures used to minimise motion artefacts were:

- Applying a large diameter thick bandage contact lens; it was hoped that a thin layer of hydrogel-bound water would improve contrast at the air-surface interface and enhance AOS delineation.
- Imaging both eyes simultaneously.

- Using the custom-designed blink artefact reduction system described in the previous section.

4.4 Results

4.4.1 T1-weighted images

Figure 4.3: T1-weighted MR image for subject JT showing the best resolved differentiation of the AOS, slice thickness at minimum 3mm.

This method of MR imaging provided the quickest scan time 6.5 minutes, with optimal in-plane resolution of 0.25mm. The application of Lacri-lube® did not offer further improvement in AOS differentiation.

4.4.2 T2-weighted images

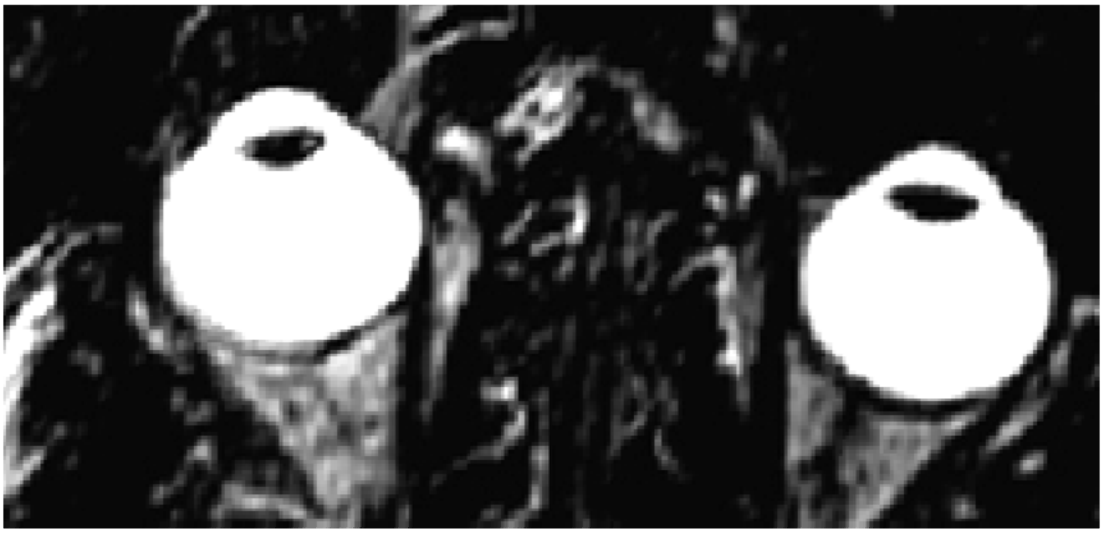

Figure 4.4: T2-weighed MR image of both eyes of subject JT using optimised pulse sequence protocol and blink artefact reduction technique.

This imaging technique was not able to differentiate the AOS using available optimisation of motion artefacts and pulse sequence protocol. The application of large thick contact lenses to the AOS did not improve the differentiation further.

4.5 Discussion

This study found that T1-weighed images using 3 Tesla MR protocols could not provide sufficient in-plane resolution to meet the requirements of the application; to provide the accuracy necessary to design and manufacture contact lenses. Two factors limited the standard of data collected:

- Open eyelids during MR imaging sequences create an air-cornea magnetic field in-homogeneity from magnetic susceptibility differences. These imperfections distort the surface geometry and cause signal loss (Bert et al., 2006). The addition of radio frequency coils positioned directly around the eye has been found to improve the signal to noise ratio up to 16 times over the standard orbital scan (Koretz et al., 2004) and offer a chance of further improved surface differentiation. However these were not available for the study.

- Compromises made during the pulse sequence protocol optimisation necessitated the use of multi-slice 2-dimensional sequences with slice thickness at a minimum of 3mm and scan times of greater than 5 minutes. These compromises cause gaps in the 2-D slice acquisition and partial volume errors from large slice thicknesses (Richdale et al., 2009). The resolution was also hindered by involuntary micro-saccades during fixation that occur a number of times per second (Rolfs, 2009).

T2-weighed images showed more promise in the likelihood of collecting 1mm or thinner slices, however surface differentiation was compromised. This again may be improved with the use of additional surface radio frequency coils positioned near the eye. T2 protocols using 3 Tesla MR fields have been optimised for measurements of globe volume (Singh et al., 2006), but these do not detect smaller ocular structures including the cornea. Since this study was carried out, further work has been carried out using a 7 Tesla external magnetic field to determine whether higher field strength can allow improved resolution (Fig 4.5) and reduced scan time. The results showed that using an optimised T1 pulse sequence, imaging scan durations could be reduced to 30-40 seconds and slice thickness reduced to 0.10 to 0.50mm (Richdale et al., 2009).

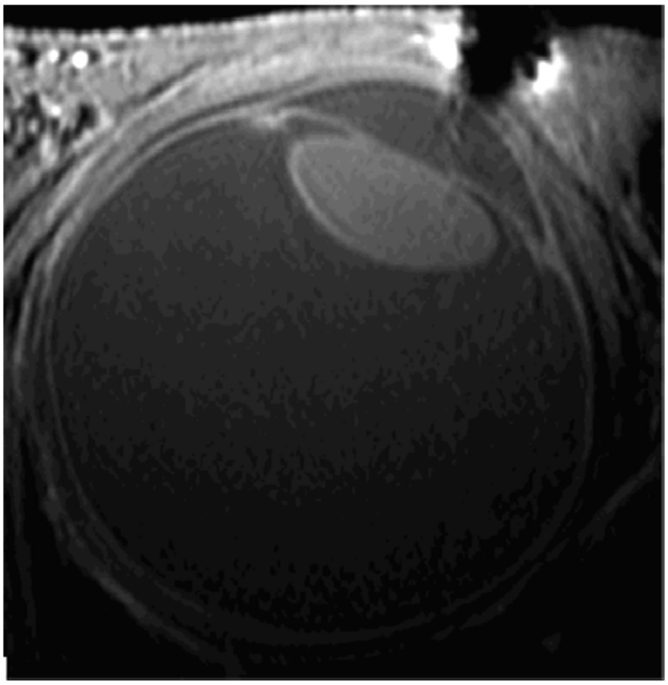

Figure 4.5: T1-weighed 7 Tesla MR image using an optimised scanning and image processing protocol (Richdale et al., 2009).

4.5 Conclusion

Optimised protocols for T1- and T2-weighed MR imaging using a 3-Tesla external magnetic field were unable to provide sufficient data to adequately reconstruct an accurate representation of the AOS. Further work using additional eye surface radio frequency coils and a 7-Tesla external magnetic field offers the best opportunity to achieving this goal.

Chapter 5

Ocular impression-taking – which material is best?

Chapter 2 described the technologies currently available to provide morphometric descriptors of the AOS. It has been shown that there are inherent challenges associated with each method of measurement. Given that this work aims to provide a 'gold standard', wide-field morphometric analysis of the AOS, it is a pre-requisite that the chosen method of data collection be optimised.

5.1 Introduction

The purpose of taking an impression of any surface is to mould the negative dimensions of the structure and make a model of the 'positive' physical properties which provides an accurate representation of the shape, parameters and spatial relationships. The acceptable magnitude of error implicit in the impression taking process is determined by its application, for example manufacturing gas permeable contact lenses requires high accuracy: in the region of ±0.05mm, commensurate with the manufacturing tolerances of British Standards 18369-2 (BSI, 2006). In this study, the accuracy of the model or cast in comparison to the ocular surface *in-vivo* will be scrutinised in Chapter 7. This chapter reports on an investigation to evaluate the clinical validity of modern impression materials.

The characteristics of the 'ideal' impression material include:

- Minimal deleterious effects on the AOS; no permanent or damaging effects caused by the material covering and setting on any tissues of the exposed ocular adnexa.
- No lasting discomfort during or after the procedure; topical anaesthetic is used to block the highly sensitive corneal innervation.
- High accuracy; this investigation seeks to establish a 'gold standard' topographic representation of the AOS, of the highest quality.

- Excellent dimensional stability; to ensure that the material is not deformed by plaster pouring, or degraded by environmental conditions or physical manipulation.
- Good flow characteristics, and reasonable in-eye working time; allowing sufficient time for material to be applied to the impression tray and inserted without setting.
- Rapid curing or setting time; to reduce the amount of time required by the subject to remain fixated with the contralateral eye, reducing artefacts incurred by random eye movements.
- Excellent compatibility with gypsum dental stone; some impression materials are known to cause chemical degradation of the gypsum cast surface.
- Unaffected by temperature and environmental conditions.

Cold irreversible hydrocolloids or alginates (eg Orthoprint), which have been used for ocular impressions since the introduction of Ophthalmic Moldite (Obrig, 1943), exhibit poor dimensional stability and poor tear strengths, leading to inaccurate casts and the need for multiple impression-taking procedures (Storey, 1987), (Imbery et al., 2010). The impressions formed are affected by the level of air flow around the impression, which causes evaporation of water from the gel resulting in shrinkage; (1) by water, which causes the gel to expand by imbibition and absorption; (2) by high relative humidity, which induces syneresis and shrinkage; and (3) by in-organic salts, which affect the gel and cause physical changes that are dependent on their osmotic potential (O'Brien, 2002).

As dental impression materials evolved, the possibility of improved accuracy and biocompatibility encouraged experimentation with polysulphide rubber for eye impressions (Storey and Vale, 1970). However, this material was abandoned after human test subjects experienced prolonged discomfort following the impression and required anaesthetic ointment (5% Lignocaine HCl) to counteract the eyelid pain during the procedure, which caused distortion of the gypsum cast (Storey, 1972). Much later, encouraged by clinical safety and success in the ocular prosthetics field, further investigations were carried out on another group of materials (polyvinylsiloxanes), which contained silicone-addition reaction elastomers (Storey, 1987). Panasil C (Kettenbach GmbH, Germany) was adopted by a number of ophthalmic practitioners in the United Kingdom and it provided the means for significant progress in the manufacture of impression-moulded gas permeable, scleral lenses (Pullum, 1987). Following the withdrawal of this product in 1993, several alternatives have been used, including Panasil light body (Kettenbach GmbH, Germany) (Brammar et al., 1995) and Tresident (Shütz Dental Group GmbH, Germany) (Pullum, 2002).

It is well known that polyvinylsiloxane reproduces the greatest detail of all dental impression materials (Chee and Donovan, 1992). Indeed, the material provides sufficient detail to identify individuals by fingerprint analysis (Parthasaradhi et al., 2005). This level of accuracy is defined by the British Standards Institute BS 4823 which requires that all Type 3, light-bodied elastomeric materials to be able to reproduce a line 0.020mm in width (BSI, 2001). In addition, these materials have been found to have very low shrinkage, 0.05-0.1%, during the polymerising process (Williams and Craig, 1988) and they are well-matched to the setting expansion of Type IV gypsum plaster, which is used to cast the impression (Ragain et al., 2000). Polyvinylsiloxane materials, which have been found to have excellent long-term dimensional stability, are not susceptible to changes in humidity and do not undergo further chemical reactions or release by-products (Chee and Donovan, 1992). Tests carried out on intact rabbit skin concluded that the primary skin irritation of polyvinylsiloxane can be considered negligible (Mazzanti et al., 2005). For these reasons it is considered a superior alternative to the irreversible hydrocolloids. However the effects of the material on the tear film and adnexa, although considered clinically acceptable, have not been the subject of scientific rigour.

5.2 Aims and Objectives

This study used a single–blind, randomised control trial to assess the efficacy and clinical validity of a polyvinylsiloxane (Tresident) compared to an irreversible hydrocolloid (Orthoprint) for ocular impression taking.

The hypotheses proposed are that:

- Tresident (Shütz Dental Group GmbH, Germany) offers a quicker, more effective and clinically viable method of obtaining ocular impression topography compared to the traditional Orthoprint (Zhermack SpA, Italy).
- Orthoprint causes significantly more superficial punctuate staining of the corneal epithelium than Tresident.

5.3 Method

5.3.1 Materials

5.3.1.1 Orthoprint (Zhermack SpA, Italy)

Orthoprint is a yellow, dust-free, alginate, irreversible hydrocolloid impression material, which conforms to specifications BS 4269-2 (BSI, 1991). It is mixed at a ratio of 9g of powder to 18ml of sterile water at 23°C to form a solution, which has a working time of 1 min 5 secs and a setting time of 1 min 50 secs. This permits 45 secs for stable contact with the ocular surface. Colder water retards setting and warmer water speeds up setting. If the plaster mould is not poured straight away, the impression can be placed in a hermetically-sealed bag at room temperature (23°C) and gypsum pouring deferred for 48 hours. Plaster Types 3 and 4, according to BS 6873 (BSI, 2000), are recommended for use by the manufacturers (Zhermack SpA, Italy).

Figure 5.1: Orthoprint packaging (Zhermack SpA, Italy)

The aqueous reaction occurs between calcium sulphate dehydrate and an alginate salt composed of alternating and homopolymeric sequences of D-mannuronate and L-guluronate units, derived from seaweed (Cook, 1986). Commercial alginate impression materials are known to contain: (1) a filler, usually diatomaceous earth, to increase rigidity and aid mixing, (2) a reaction retarder, such as tetra-sodium pyrophosphate, (3) a pH modifier, such as magnesium oxide; and a setting aid, in this case potassium fluorotitanate.

The material provides good surface detail (Hansson and Eklund, 1984), is easy to use and mix, is cheap and has a long shelf-life, numbered in years (O'Brien, 2002). The setting time can be controlled with water temperature and, as a gel, it is non-toxic and non-irritant (Powers and Sakaguchi, 2006). However, it has relatively poor dimensional stability, compared with elastomers, and a low tear energy (Nallamuthu, Branden and Patel, 2006). It is incompatible with Type 1 and 2 gypsum plaster (Morrow et al., 1971), reacts to humidity, and has a very short on-eye setting time (45 secs). The mixing process is messy and dependent on operator handling. Automated mechanical mixing has been shown to increase speed and quality of alginate sol, eliminating casting imperfections (Craig, 1988). For these reasons, the use of alginate for ocular impression-taking has been superseded by silicone rubber based materials.

5.2.1.2 Tresident (Shütz Dental Group GmbH, Germany)

Tresident is a low viscocity, addition-polymerising, polyvinylsiloxane precision impression material with hydrophilic properties, which conforms to BS 4823 (BSI, 2001). It is supplied in an auto-mix dual cartridge, which requires a dispensing gun to advance equal quantities of each siloxane-based component through a purpose-designed mixing canula (Fig 5.2).

Figure 5.2: Injector DS 50 (Dreve Otoplastik GmbH, Germany), with a Tresident dual cartridge and mixing canula.

Tresident is automatically mixed to a predetermined amount and provides a working time of 1 min 15 secs, with a setting time of 2 mins 45 secs, giving a total setting time of 4 mins. During this time, the impression tray and material must be held against the ocular surface under gentle pressure.

Moulds can be poured from 1 hr to 14 days after the procedure. Impressions may be re-poured to produce casts, which are as accurate as the original, for up to 7 days (Lewinstein and Craig, 1990) but to do so the impression material must be kept in a dry place at 18-25°C. Re-heating the impression to 37°C before pouring the plaster has been demonstrated to improve accuracy of casting. However it is doubtful if this is clinically significant (Chew, Chee and Donovan, 1993).

The two components of the material are a polymethyl hydrogen siloxane copolymer of moderately low molecular mass, which contains silane terminal groups, and an accelerator material of a similar molecular weight, which contains vinyl-terminated polydimethyl siloxane. When mixed, the silane and vinyl groups react, catalysed by chloroplatinic acid (a homogenous metal complex catalyst). The cross-linking that occurs during the polymerisation process (Fig 5.3) causes minimal dimensional change and there are no by-products (Mandikos, 1998).

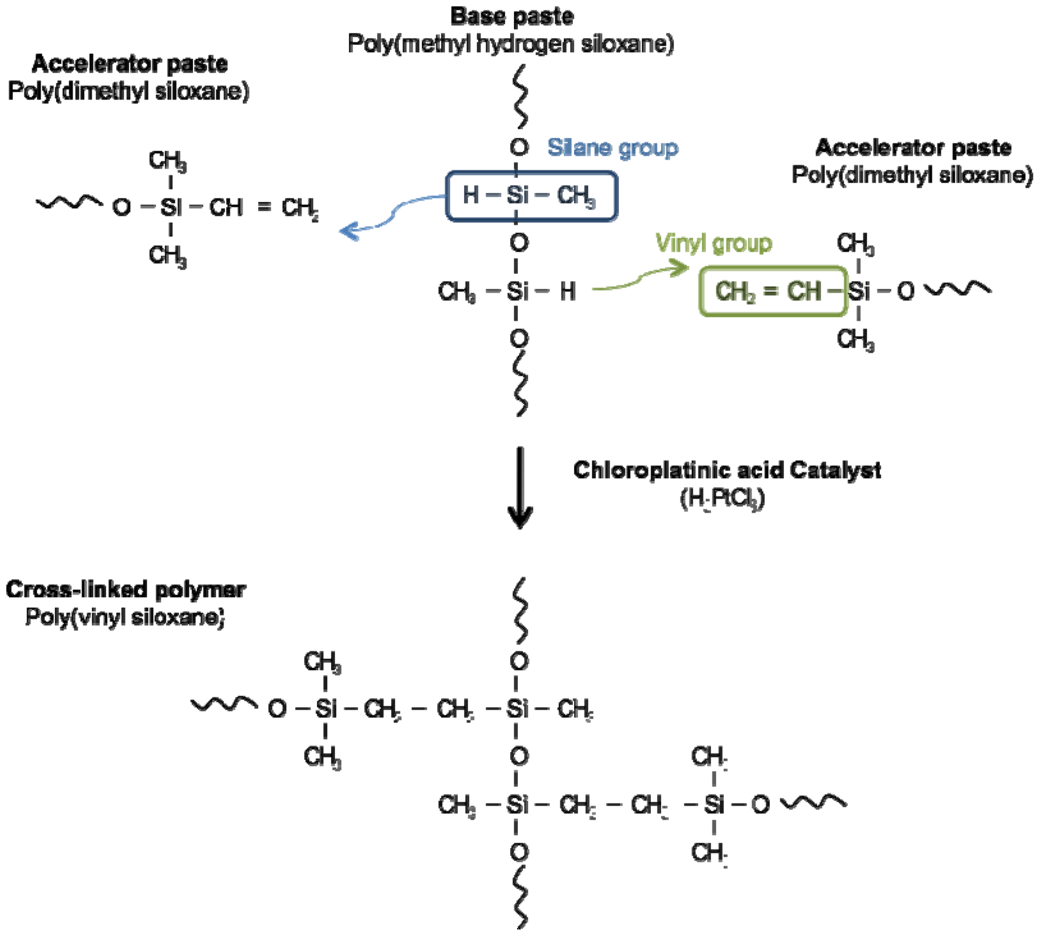

Figure 5.3: The accelerator polymer is terminated with vinyl groups which cross-link to the silane terminal groups on the base polymer when activated by a platinum salt catalyst. This is an addition reaction and there are no by-products (Mandikos, 1998).

Both pastes contain fillers, amorphous silica and a low molecular weight retarder to delay the onset of polymerisation. Additionally, the base paste has an emulsifying surfactant that improves the wettability of the impression. Colouring agents are added to distinguish between the two pastes and aid the evaluation of mixing.

Figure 5.4: Tresident packaging (Shütz Dental Group GmbH, Germany)

The following table 5.1 compares the properties and characteristics of Orthoprint and Tresident, current ocular impression materials

	Tresident	Orthoprint
Material type	Silicone elastomer	Alginate
Reaction type	Addition polymerisation	Irreversible hydrocolloid
Components	Base paste: silicone polymer dispersion and reactive species, filler and surfactant to increase hydrophilic properties. Catalyst paste: silicone polymer dispersion and reactive species, catalyst, hydrogen scavenging agent, filler and pigments (Mandikos, 1998).	Soluble alginate reacts with calcium sulphate to produce insoluble calcium alginate gel, potassium fluotitanate to counteract interaction with gypsum setting, filler, retarder, pH modifier and glycol to reduce dust (McCaffery et al., 2002).
Smell	None	Vanilla odour and flavour
Detail reproduction	Reproduce lines <0.020mm. Unknown effect of pH	Reproduce lines <0.75mm Improved in alkaline pH (Anastassiadou, Dolopoulou and Kaloyannides, 1995)
Linear dimensional change	<1.5%	Variable with temperature and humidity
Elastic recovery	>99%	97.3%
Deformation	1.3-5.6%	11%
Tear strength	High 1640-5260 g/cm	Low 380-700 g/cm
Clinical history	First used in Britain 1977: Ann Arnold-Silk (Storey, 1987)	First used by in America 1943: Theodore Obrig (Lamb and Sabell, 2007)
Mixing technique	Dual chamber cartridge using proprietary mixing canula and dispensing gun	By hand using rubber bowl and metal spatula. De-ionised water added to powder.
Quantities	Quantities of each paste predetermined by means of cartridge and dispensing system	9g powder to 18ml water
Working time	1 min 15 secs	1 min 5 secs
On-eye time	2 mins 45 secs	45 secs
Setting time	4 mins	1 min 50 secs
Gypsum die pouring	After 1 hr up to 14 days with no special conditions	Immediately or up to 48 hrs later if stored in hermetically sealed bag at 23°C
Number of casts	Up to 7	1
Environmental effects	0.2 – 1% shrinkage after 24 hrs. Higher temperature reduces setting time, unaffected by humidity.	Cold water retards setting time, shrinks up to 1.28% after 24 hrs if not stored at high humidity (Miller, 1975).
Cost	£32.47 for 100ml	£9.95 for 500g of powder

Table 5.1: Comparison of ocular impression material properties; Tresident and Orthoprint.

5.2.2 Experimental procedure

Twenty subjects were included in the study, (13 ♀ and 7 ♂), mean age of the cohort was 31.10 ±4.62 years [SD] (range 25.77 to 39.73). The volunteers were recruited from the staff and students of Cardiff University, and subjects were excluded if they were pregnant or breastfeeding; had any ocular or systemic condition known to affect the structure or characteristics of the anterior ocular surface; were taking any medication known to affect the ocular surface; had worn rigid contact lenses in the preceding 6 weeks or soft contact lenses in the preceding 2 weeks; and were not white European. This ethnic bias was chosen because it has been shown that ethnicity affects ocular surface morphometrics (Matsuda et al., 1992), (Leite et al., 2010). Ethical approval was sought in accordance with the Tenets of the Declaration of Helsinki (2004) from the Cardiff School of Optometry and Vision Sciences Ethics Committee.

The subjects attended for 2 sessions, each of 1 hour duration. Each session was scheduled at the same time on each day. Two experienced practitioners carried out the study, one to carry out the ocular impression procedures (Investigator 1, JT) and the other to observe and assess the clinical signs (Investigator 2, DM). The practitioners carried out their investigations in separate rooms without any knowledge of the others results. A randomly generated list of subjects was provided by an external administrator who had no knowledge of the study protocol.

5.2.2.1 Session 1

The subject arrived and was assessed by Investigator 2 for baseline measurements, these included LogMar visual acuity, tear break-up assessment using Tearscope Plus™ (Keeler Ltd, Windsor, UK), phenol red threads (Menicon Co Ltd, Japan), and grading of clinical signs using the CCLRU grading scales. Fluorescein sodium dye (Fluoret strips, Chauvin, France) was used to provide an assessment of ocular surface integrity using a slit-lamp bio-microscope. Measurements were carried out in the following order:

1. **Best-corrected LogMAR acuity** using Bailey-Lovie LogMAR distance acuity chart (Sussex Vision International Ltd, West Sussex, UK) at 3m direct viewing. Recommended luminance 160 cd/m2.

2. **Tear volume with Phenol red threads**, Zone-Quick™ (Menicon Ltd, Japan).
3. **Instillation of fluorescein**, using Fluoret strips (each strip impregnated with approximately 1 mg of fluorescein sodium BP) moistened with 0.9% physiological saline.
4. **Tear break-up time using Tearscope Plus™** (Keeler Ltd, Windsor, UK), with fine grid insert.
5. **Assessment of ocular integrity** using CCLRU grading scales, interpolated to 0.1 unit increments: bulbar redness; limbal redness; lid redness; lid roughness; type, extend and depth of corneal staining.
6. **Ocular impression;** in a separate room, the ocular surface of both eyes was anaesthetised by Investigator 1 using two drops of 0.5% Proxymetacaine HCL Minims (Chauvin Pharmaceuticals Ltd., Kingston-Upon-Thames, UK), who then carried out an impression procedure (see Section 5.2.3.1) to one ocular surface (randomly assigned) using one of the 2 materials. After impression taking, the ocular fornices were irrigated with 0.9% saline and the subject returned to the room of Investigator 2 who repeated the battery of tests detailed above.

5.2.2.2 Session 2

When the subject arrived, Investigator 2 repeated the battery of clinical tests carried out the day before, followed by Investigator 1 taking an ocular impression with the alternative material. Investigator 2 repeated the battery of clinical tests following a saline wash-out post-impression procedure.

5.2.3 Clinical techniques

5.2.3.1 Ocular impression procedure

Each subject was positioned sitting upright and facing forward. A distant target was provided to align the visual axes, using the contralateral eye for fixation. Both eyes were anaesthetised with 0.5% Proxymetacaine HCL eye drops and the procedure carefully explained to the subject. An impression tray was chosen from the set of 3 sizes, of maximum internal shell diameters of 23, 24 and 25mm (Cantor and Nissel Ltd, Brackley, UK). These trays were moulded from acrylic with hollow stems, 32mm in length, marked with red circular indentations providing an anatomical registration in the 12 o'clock position (in relation to the cornea). The tray was selected by offering the 3 sizes up to the closed eye and choosing the largest in relation to the aperture and the global contour. Impression material was dispensed onto the internal surface of the shell covering the entire surface with 1.5 – 2.5mm (Eames et al., 1979) of Tresident or Orthoprint.

Figure 5.5: Photograph of 25mm diameter impression tray holding Tresident material prior to insertion.

The subject was instructed to 'look down' whilst remaining in the head upright position. The tray was inserted quickly under the top eyelid, the subject was asked to 'look up' in order for the lower lid to be freed and the shell held between both eyelids. The tray was carefully positioned to locate the cornea at the centre of the shell; the investigator supported the stem and ensured that the subject maintained composure and optimal fixation.

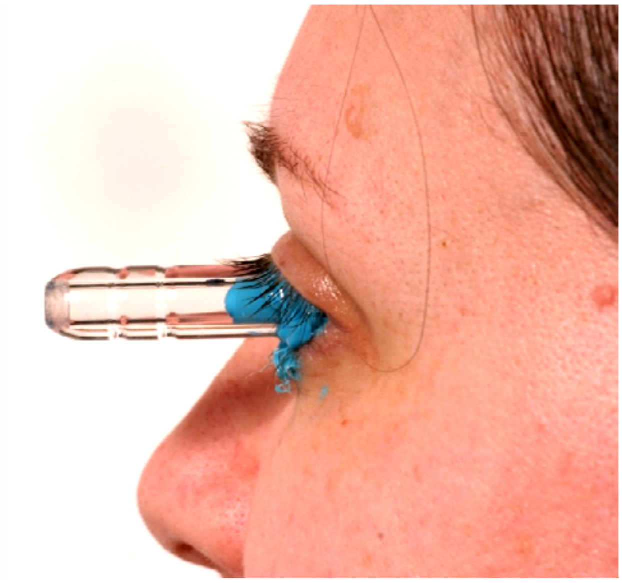

Figure 5.6: Photograph to show the position of tray and Tresident during impression procedure.

After setting of the material, the tray and impression was removed by freeing the lashes of the upper lid and removing the material from the eye surface in one piece. Any material remnants were collected and the fornices irrigated with 0.9% physiological saline. The impression trays were disinfected immediately after use; rinsed in saline for 30 seconds, cleaned with liquid detergent, rinsed again for 30 seconds and disinfected in sodium hypochorite 10,000ppm for 10 mins. Further saline rinses were carried out before the trays were stored dry for the next subject (Buckley, 2010).

5.2.3.2 LogMAR visual acuity measurement

Best-corrected visual acuity was measured using a Bailey-Lovie visual acuity chart at 3m direct viewing. Subjects were asked to read the letters on the chart starting with the largest and were permitted to stop when 3 or more of the 5 letters was missed or incorrect. Visual acuity score was obtained by assigning 0.02 LogMAR units to each letter.

5.2.3.3 Measurement of tear quantity using Phenol red threads

A two-ply cotton thread (0.2mm) impregnated with phenol red dye was used to assess tear quantity. The bent end was placed in the inferior fornix on the temporal side and remained in position for 15 seconds. On removal, the length of thread that had undergone a colour change from red to yellow was measured, and recorded in mm.

Figure 5.7: Photograph to show the position of phenol red thread in the lateral portion of the lower fornix Zone-Quick™ (Menicon, 2010).

5.2.3.4 Invasive tear break-up assessment using Tearscope PlusTM

Invasive tear break-up time was assessed with the use of fluorescein dye. The subject was asked to blink and then hold their eye open as long as possible. The measurement was taken in seconds between the blink and the first appearance of a discontinuity in tear film coverage. Three values were recorded for each eye and the median used for comparison.

5.2.3.5 Quantifying clinical signs using CCLRU grading scale

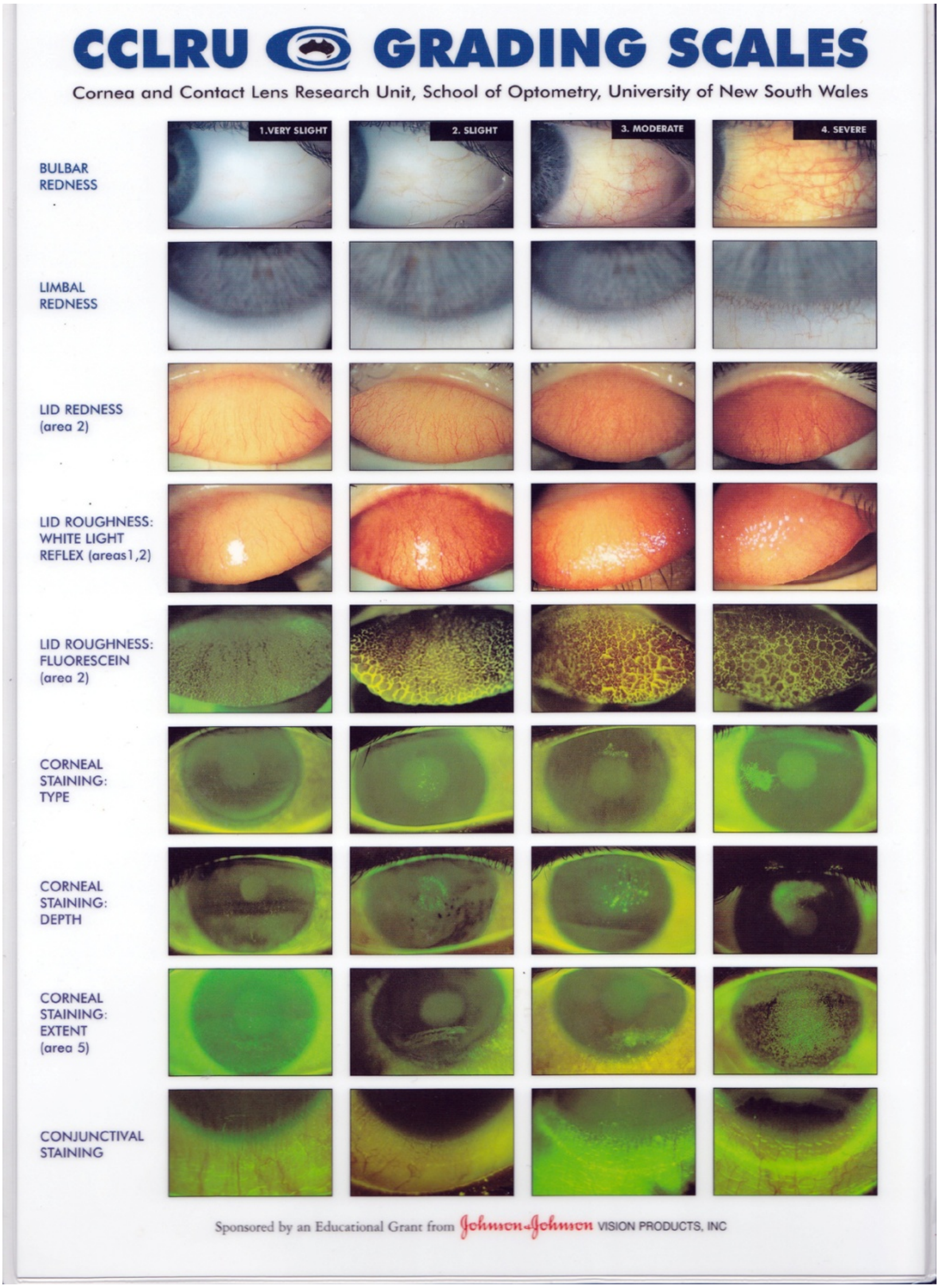

Figure 5.8: CCLRU grading scales – front (Cornea and Contact Lens Research Unit, School of Optometry, University of New South Wales).

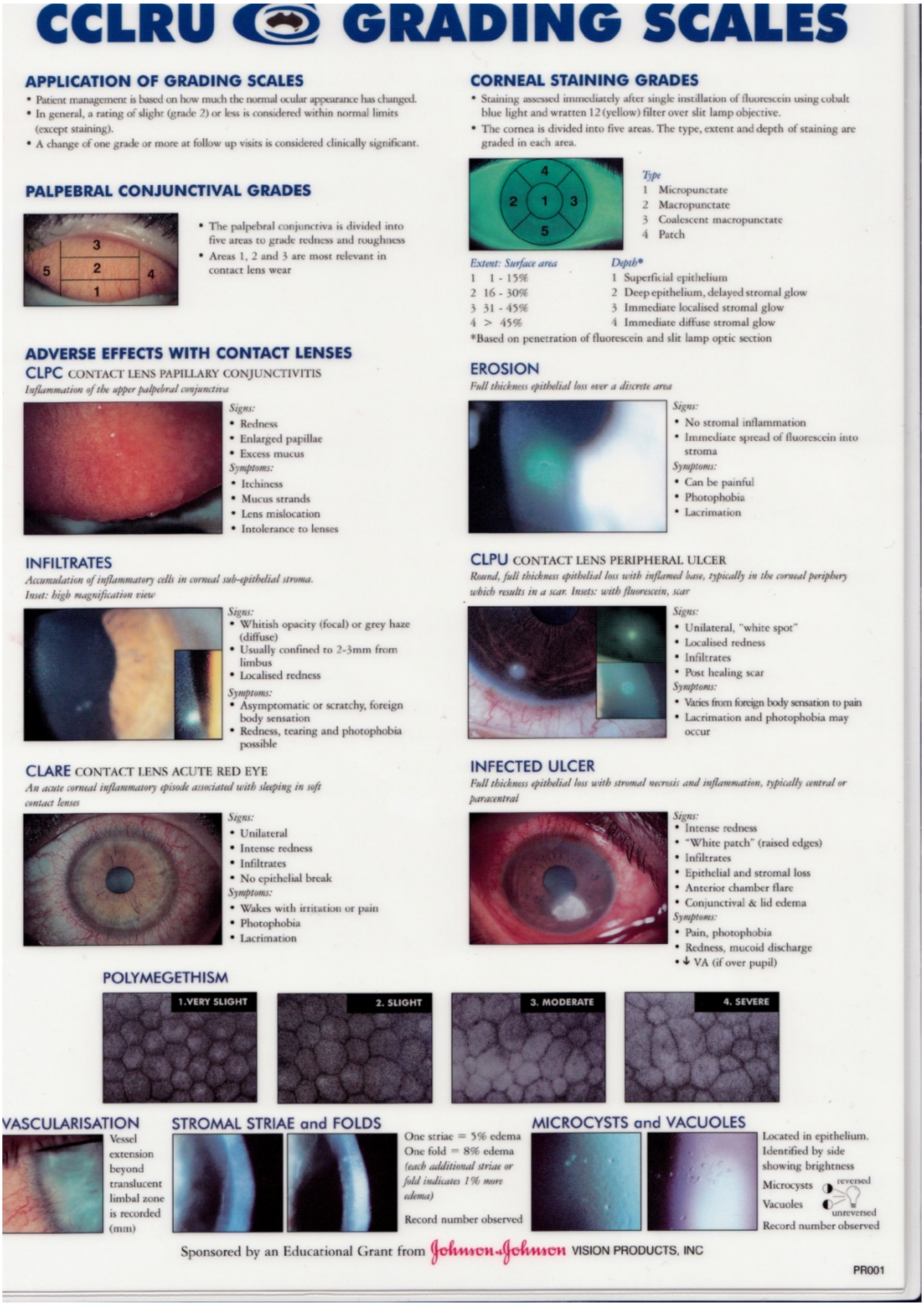

Figure 5.9: CCLRU grading scales - back (Cornea and Contact Lens Research Unit, School of Optometry, University of New South Wales).

The CCLRU grading scale provides a set of photographs and illustrations to enable the quantification of changes to ocular surface and palpebral conjunctiva. The ocular surface was assessed using a slit-lamp bio-microscope (10x magnification) under diffuse, white illumination and numerical values assigned to bulbar redness, limbal redness, lid redness, lid roughness, and corneal staining, in increments of 0.1 (Bailey et al., 1991).

5.2.4 Statistical analysis

All data was collated with Excel 2007 (Microsoft, Redmond, Washington, USA), and analysed within SPSS v13 (SPSS Inc, Armonk, NY, USA). The data distribution was evaluated for normality using the Kolmogorov-Smirnov statistic. Comparisons were made of clinical signs assessed before and after each impression procedure, and paired t-tests used to determine statistical significance at the 95% level.

5.3 Results

5.3.1 LogMAR Acuity:

This was found to be slightly reduced by 0.5 letters, on average, following impression using either material, but this was not statistically significant.

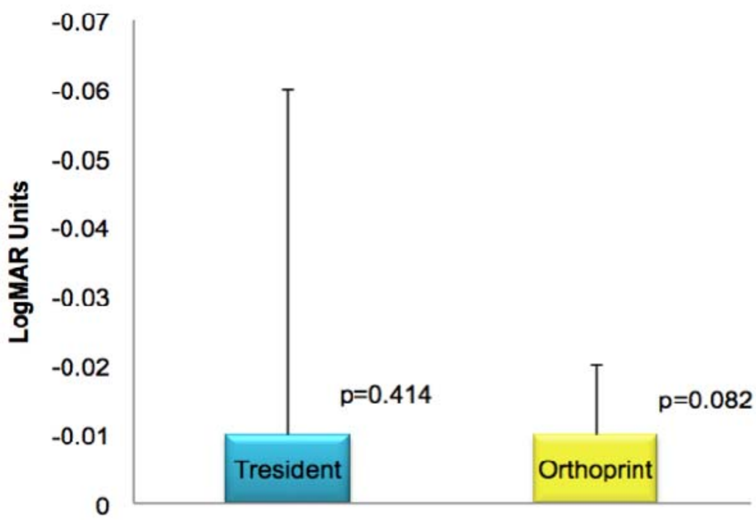

Figure 5.10: Change in best-corrected visual acuity following impression taking using Tresident and Orthoprint.

Clinical Outcome	Mean differences in measurements pre- and post-impression procedure (unit±SD)		Statistical significance		
	Tresident	Orthoprint	Tresident T-test	Orthoprint T-test	Tresident vs Orthoprint
LogMAR acuity (Log Units)	-0.01±0.13	-0.01±0.21	p=0.414	p=0.082	p=0.593

Table 5.2: Best-corrected visual acuity scores pre- and post-impression taking with Tresident and Orthoprint, mean difference in measurements for the cohort and statistical significance.

5.3.2 Tear volume (Phenol red test)

Following the impression procedure with both materials, the length of thread found to change colour increased, and this was clinically significant after Orthoprint was used.

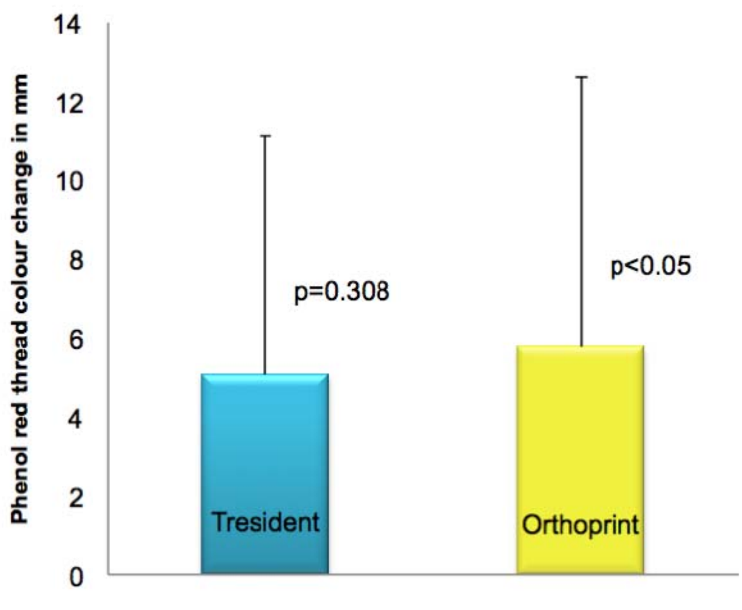

Figure 5.11: Difference in length of colour change recorded for Phenol red threads (mean ±SD) pre- and post-impression taking using Tresident and Orthoprint.

Clinical Outcome	Mean differences in measurements pre- and post-impression procedure (unit±SD)		Statistical significance		
	Tresident	Orthoprint	Tresident T-test	Orthoprint T-test	Tresident vs Orthoprint
Phenol red test (mm)	5.06±6.22	5.76±5.81	p=0.308	p<0.05	p=0.829

Table 5.3: Differences in length of colour change recorded using Phenol red threads pre- and post- impression taking with Tresident and Orthoprint, mean difference (±SD) in measurements for the cohort and statistical significance.

An additional +5.76±5.81 mm [SD] length of yellow cotton was measured following the use of Orthoprint, which was statistically significant ($p<0.05$). Tear volume after Tresident use increased an additional +5.06±6.22 mm [SD], but this was not statistically significant ($p=0.308$).

5.3.3 TBUT

This was found to be reduced following impression-taking with both materials, but was not clinically significant:

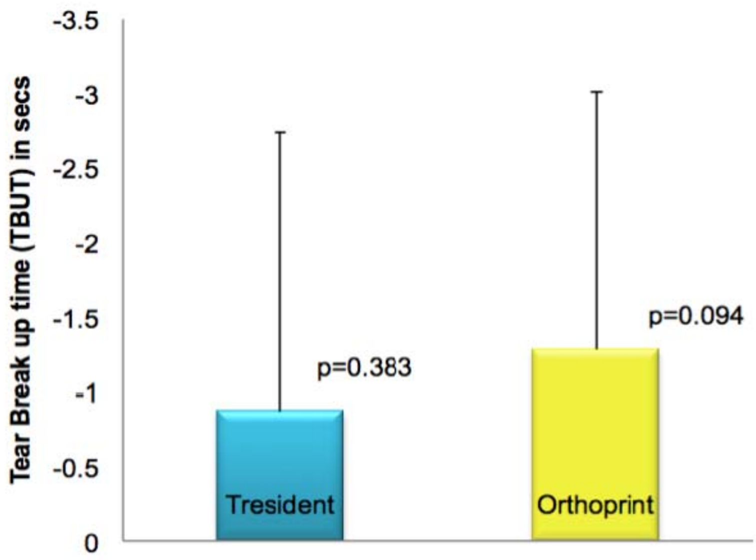

Figure 5.12: Differences (mean ± SD) in TBUT pre- and post-impression taking using Tresident and Orthoprint.

Clinical Outcome	Mean differences in measurements pre- and post-impression procedure (unit±SD)		Statistical significance		
	Tresident	Orthoprint	Tresident T-test	Orthoprint T-test	Tresident vs Orthoprint
TBUT (secs)	-0.87±2.61	-1.28±2.03	p=0.383	p=0.094	p=0.265

Table 5.4: TBUT pre- and post-impression taking with Tresident and Orthoprint, mean difference in measurements (±SD) for the cohort and statistical significance.

Mean TBUT was 7.16±1.40 secs pre- and 6.68±1.27 secs post-Tresident impression, with a difference of -0.87±2.61 secs, which was not statistically significant (p=0.383). Mean TBUT was 7.42±1.55 secs pre- and 6.61±1.33 secs post-Orthoprint impression, giving a larger difference of -1.28±2.03 secs, but which did not reach statistical significance (p=0.094).

5.3.4 Ocular redness

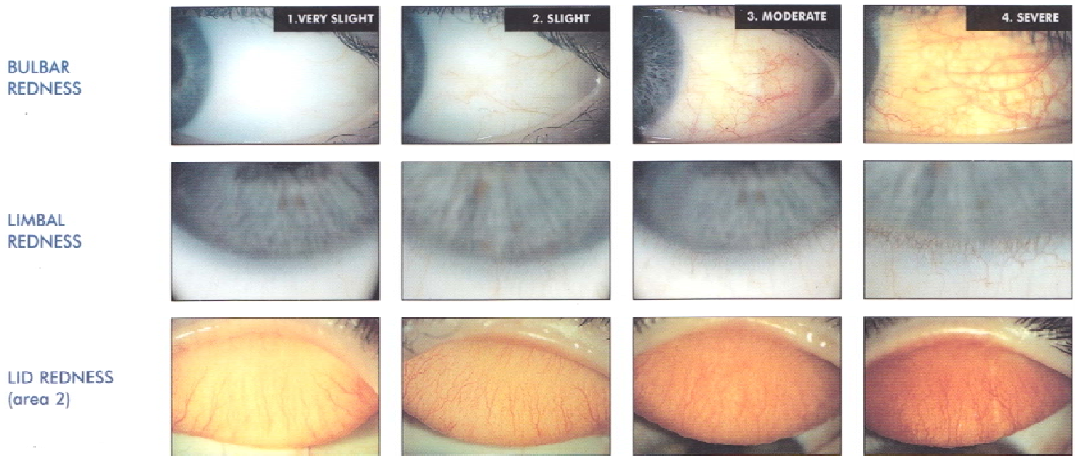

Figure 5.13: CCLRU grading scales for bulbar, limbal and lid redness (Cornea and Contact Lens Research Unit, School of Optometry, University of New South Wales).

Ocular redness was found to increase following impression taking with both impression materials. A statistical difference was found between the numerical values assigned to bulbar redness after Orthoprint compared to Tresident (p=0.0231).

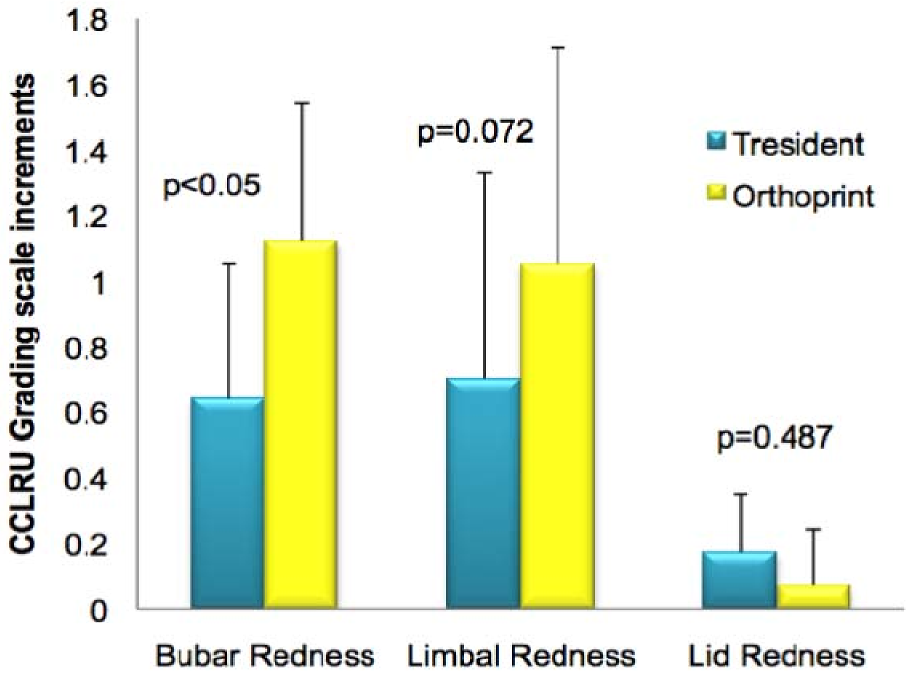

Figure 5.14: Differences (mean ±SD) in the clinical grading of bulbar, limbal and lid redness, pre- and post - impression taking using Tresident and Orthoprint.

Clinical Outcome	Mean differences in measurements pre- and post-impression procedure (unit±SD)		Statistical significance		
	Tresident	Orthoprint	Tresident T-test	Orthoprint T-test	Tresident vs Orthoprint
Bulbar Redness (CCLRU units)	0.64±0.58	1.12±0.42	p<0.001	p<0.001	p<0.05
Limbal Redness (CCLRU units)	0.70±0.31	1.05±0.28	p<0.005	p<0.005	p=0.072
Lid Redness (CCLRU units)	0.17±0.32	0.07±0.35	p<0.05	p=0.157	p=0.487

Table 5.5: Clinical grading of ocular redness pre- and post-impression taking with Tresident and Orthoprint, mean difference in measurements (±SD) for the cohort and statistical significance.

Bulbar redness increased following impression taking with Tresident +0.64 ±0.58 units ($p<0.001$), with a substantially greater change in redness following the use of Orthoprint +1.12 ±0.42 units ($p<0.001$). The mean difference in bulbar redness between the two materials was statistically significant ($p<0.05$). Similarly, limbal redness increased following impression taking, +0.70 ±0.31 units ($p<0.005$) after Tresident use and +1.05 ±0.28 units ($p<0.005$) after Orthoprint, however the mean difference between changes in bulbar redness when comparing the two materials was not statistically significant ($p=0.072$).

There was a small change in lid redness recorded after impression-taking. For Tresident this was 0.17 ±0.32units, which was statistically significant ($p<0.05$). However, the change was smaller after Orthoprint use (0.07 ±0.35 units) and was not statistically significant ($p=0.487$).

5.3.5 Lid roughness

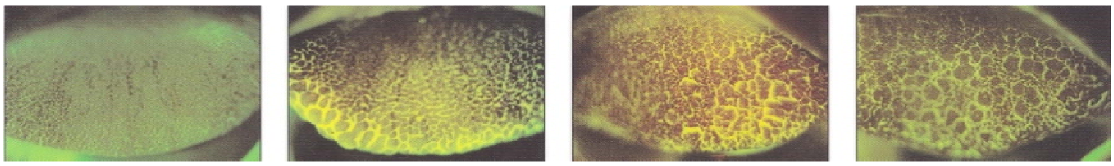

Figure 5.15: CCLRU grading scale for lid roughness (Cornea and Contact Lens Research Unit, School of Optometry, University of New South Wales).

The clinical grading of lid roughness was found to increase following impression taking with Tresident (0.03 ±0.25 CCLRU units), but this was not statistically significant ($p=0.459$). Orthoprint had no detectable effect on lid roughness.

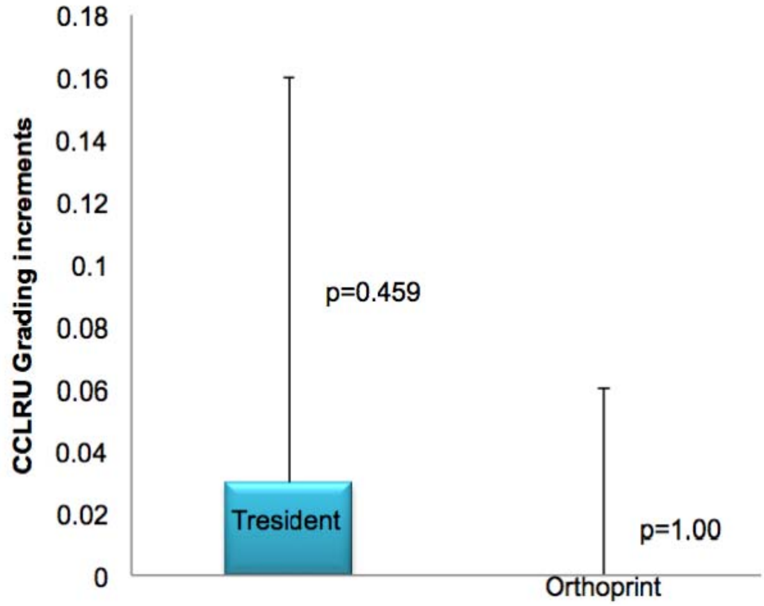

Figure 5.16: Differences (mean ±SD) in the clinical grading of lid roughness following impression taking using Tresident and Orthoprint.

Clinical Outcome	Mean differences in measurements pre- and post-impression procedure (unit±SD)		Statistical significance		
	Tresident	Orthoprint	Tresident T-test	Orthoprint T-test	Tresident vs Orthoprint
Lid Roughness (CCLRU units)	0.03±0.25	0.00±0.40	p=0.459	p=1.00	p=0.506

Table 5.6: Clinical grading of lid roughness pre- and post-impression taking with Tresident and Orthoprint, mean difference (±SD) between measurements for the cohort and statistical significance.

5.3.6 Corneal staining

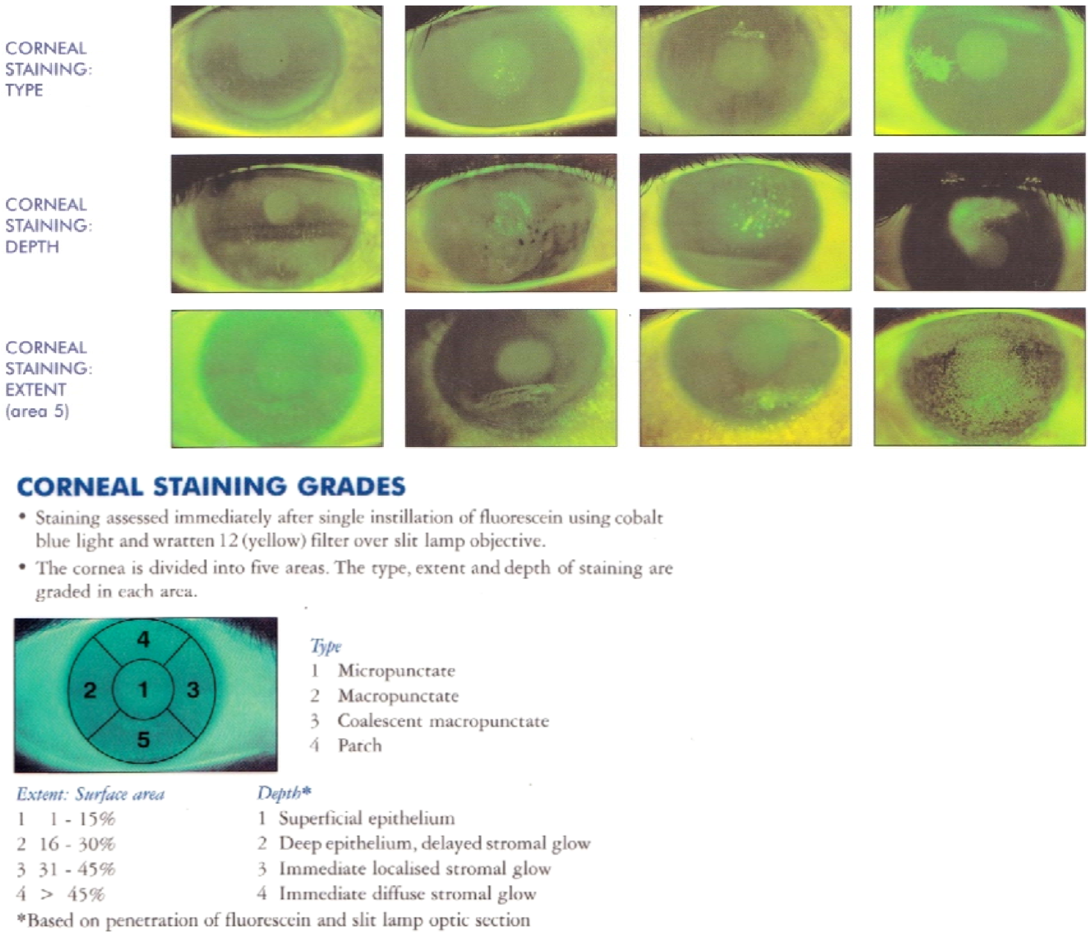

Figure 5.17: CCLRU grading scales for corneal staining (Cornea and Contact Lens Research Unit, School of Optometry, University of New South Wales).

The clinical grading of corneal staining following impression-taking increased for both materials, although a statistically significant comparison was confined to Orthoprint.

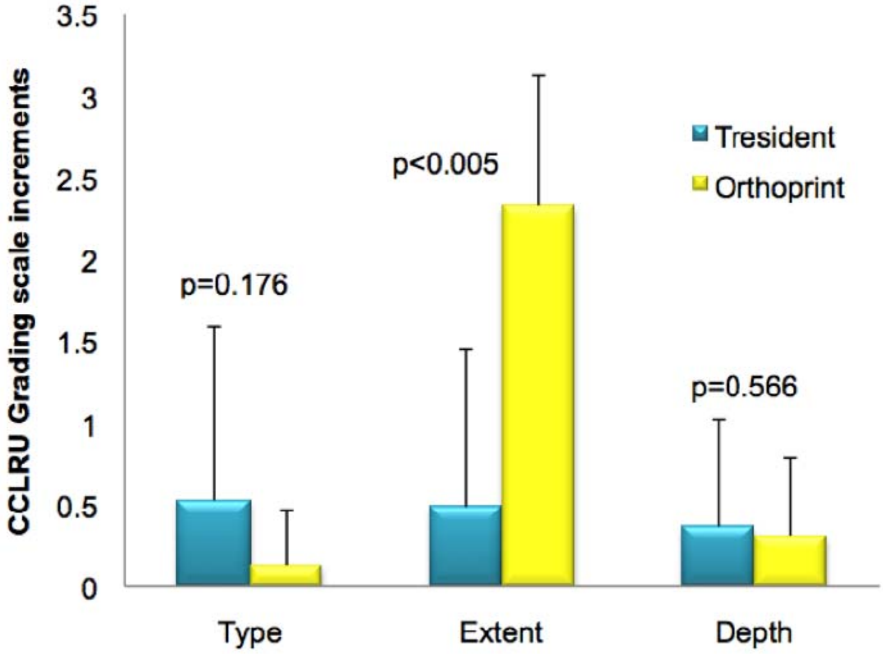

Figure 5.18: Differences (mean ± SD) in clinical grading of corneal integrity following impression taking using Tresident and Orthoprint.

Clinical Outcome	Mean differences in measurements pre- and post-impression procedure (unit±SD)		Statistical significance		
	Tresident	Orthoprint	Tresident T-test	Orthoprint T-test	Tresident vs Orthoprint
Type of corneal staining (CCLRU units)	0.53±0.41	0.13±0.34	p=0.167	p=0.341	p=0.176
Extent of corneal staining (CCLRU units)	0.49±0.65	2.33±0.46	p=0.209	p<0.001	p<0.005
Depth of corneal staining (CCLRU units)	0.37±0.47	0.31±0.40	p=0.219	p<0.05	p=0.566

Table 5.7: Clinical grading of corneal staining pre- and post-impression taking with Tresident and Orthoprint, mean difference (±SD) between measurements for the cohort and statistical significance.

Corneal staining with fluorescein was recorded following impression-taking with both materials. Staining type was micro-puncate and superficial after Orthoprint; 0.13 ±0.34 units (p=0.341), but was macro-punctate after Tresident; 0.53 ±0.41 units (p=0.167). However, these changes were not statistically significant. The extent of staining was found to increase substantially after Orthoprint impression to 2.33 ±0.46 units (p<0.001). These measurements indicate that, on average, 22% of the corneal surface (range 15-45%) was covered by staining. The recorded increase in extent of staining after Tresident was small (0.49 ±0.65 units), which was not statistically significant (p=0.209) and the surface area stained was, on average, 10% (range 1-22%). Changes in the depth of staining were found to be small (0.31±0.40 units after Orthoprint, 0.37±0.47 after Tresident) changes which were statistically significant after Orthoprint, p<0.05, but not after Tresident (p=0.219).

5.4 Clinical summary

- Visual acuity was unaffected by either material (clinically significant criterion Test-retest ± >2.4 letters (Raasch, Bailey and Bullimore, 1998)).
- Tear volume increased with Orthoprint, but this was not clinically significant (clinically significant criterion >7 mm (Golding and Brennan, 1993)).
- TBUT was marginally disrupted by both materials, but was not clinically significant (clinically significant criterion ± >3 secs (Johnson and Murphy, 2005)).
- Ocular redness increased with both materials;
- Bulbar redness , - Orthoprint induced an abnormal hyperaemic response in over half of the cohort (clinically significant criterion CCLRU grading > 2.6 units (Murphy et al., 2007) (Pult, 2008)). Trésident increased bulbar redness within clinically acceptable limits (>0.4 units difference, <2.6 units post-impression).
- Limbal redness – Both materials increased limbal redness, Orthoprint greater than Trésident, but within normal limits (<2.4) (clinically significant criterion > 2.4 units (Pult, 2008)).
- Lid redness – Increased slightly following use of both Orthoprint and Trésident, Orthoprint had less effect (unknown clinically significant criterion).
- Corneal staining was significantly greater after Orthoprint impression (clinically significant criterion > 0.5 units (Dundas, Walker and Woods, 2001));

  Orthoprint – 15-45% of the cornea, micropunctate, fluorescein penetrated superficial epithelium

  Trésident – 1-22% of the cornea, macropunctate, fluorescein penetrated superficial epithelium.

5.5 Discussion

This study has provided evidence to support the use of Trésident (Shütz Dental Group GmbH, Germany) as the impression material of choice, with less preparation time, combined with a more effective and clinically viable method of carrying out ocular impression-taking, compared to the traditional Orthoprint (Zhermack SpA, Italy). It has been shown that Orthoprint causes a clinically significant superficial micro-punctate staining of the corneal epithelium, leading to a prolonged red eye response. Following the use of Tresident, ocular signs were within normal limits, with minimal corneal staining. This leads to several clinical implications:

5.5.1 Increased hyperaemia

This cohort appeared to represent a typical example of the young normal population, concurrent with findings of other studies measuring normal bulbar and limbal hyperaemia (Murphy et al., 2007), (Pult, 2008), (Gill, 2010).

Study	No of Subjects	CCLRU Bulbar hyperaemia	CCLRU Limbal hyperaemia
(Murphy et al., 2007)	N=121	1.93±0.39	Not measured
(Pult, 2008)	N=120	1.82±0.39	1.62±0.46
(Gill, 2010)	N=47	1.70±0.21	1.51±0.30
This study	N=20	1.72±0.41	1.42±0.28

Table 5.8: Comparison of normal clinical signs of bulbar and limbal hyperaemia graded using CCLRU scales.

Bulbar and limbal hyperaemia are collectively associated with what is commonly referred to as a 'red eye'. Increased ocular hyperaemia is a warning of hypoxia, inflammation, infection, hypersensitivity and trauma (Leibowitz, 2000). In this case, the most likely cause of hyperaemia was contact with the AOS. Therefore it is not surprising to find that the conjunctiva responds to this invasive procedure by increasing its blood supply. This is most likely due to a combination of mechanical and physiological factors. After the use of Orthoprint, 7 subjects reported a foreign body sensation accompanied by a slightly red eye, which persisted for up to 24 hrs after the procedure. These subjects were monitored carefully, provided with ocular lubricants and all symptoms resolved spontaneously. Inflammatory signs were not observed on the tarsal conjunctiva or the dermis of the lids, both areas where in contact with Orthoprint. A red eye caused by superficial trauma and resulting in no loss of tissue integrity will resolve after a few minutes. This suggests that there may be a chemical reaction occurring at the ocular surface interface, which could be attributed to:

- Mixing: Poor mixing of the alginate, resulting in one or a combination of the chemical constituents causing damage to epithelial cell integrity. Potassium fluorotitanate (chemical modifier) is listed as a hazardous component on the Orthoprint data safety sheet according to Dir.2001/58/EEC. 1-3% of the composition is made up of this chemical, and if in contact with eyes, it advises to wash immediately with water for at least 10 mins.
- Unknown contaminant: A faulty or contaminated batch of alginate.
- Residual chemical complex: A chemical residue left on the ocular surface after the gel is formed, which was not removed by copious irrigation with 0.9% physiological saline.
- Increased permeability of the cornea: Removal of multiple epithelial cells caused by physical contact with a setting alginate medium, allowing chemical contamination of the deeper layers of the epithelium. In addition anaesthetic instillation can cause reduced corneal sensitivity, reduced blink frequency and can precipitate abnormal drying of the AOS (Lyle and Page, 1975), encouraging adherence of the impression material to the epithelium. Toxic interactions between anaesthetic and corneal epithelial cells have been found to cause loss or damage to surface microvilli and deposition onto the cell membranes (Boljika, Kolar and Vidensek, 1994).
- Combination: All or some of the factors above.

Average bulbar redness using CCLRU scales in the normal population is reported to be 1.93 units, with scores of 2.6 units considered abnormal (Murphy et al., 2007). Eleven subjects had scores greater than this following the use of Orthoprint for ocular impression, which had an average score of 3.14±0.37 units (range 2.7 to 3.8 units). This constitutes an abnormal bulbar hyperaemic response in over half the cohort after an ocular impression using Orthoprint. In contrast, 6 subjects had scores above normal, with an average of 3.31±0.41 units (range 2.8 – 3.8 units) after the procedure using Tresident.

The irritation of ocular tissues by irreversible hydrocolloids has been studied on white adult New Zealand rabbit eyes (Moergeli et al., 1985) and clinical observations in human eyes found a range of responses to the material, ranging from slight dehydration and irritation of the tissues to transient corneal abrasions (Storey, 1987). Ocularists described capillary dilation, tissue oedema and prolific tearing. The study concluded that the impression material, similar in formulation to Orthoprint, elicited a significant acute inflammatory response in the rabbit conjunctiva on histological examination. The authors attributed the tissue insult to the granular alginate material rubbing against the corneal and conjunctival tissue interface, concurrent with blinking and eye movement. Additionally they speculated, as in this study, that the chemical setting aids, bimetallic fluorides may have had a toxic effect on the ocular tissues. The effects of the inflammatory response lasted 24 to 72 hours, leaving no permanent tissue damage (Moergeli et al., 1985).

5.5.2 Increased corneal staining

The measurements of baseline or pre-impression corneal staining were reported to be almost twice the average score found in a study carried out to establish background staining in normal eyes (Dundas et al., 2001). This study also suggests that a score of >0.5 should be considered unusual, the findings in this study may be influenced by a relatively small sample size and an older median age found to have more staining (Norn, 1970).

Study	No of Subjects	Median age (yrs)	CCLRU Corneal Staining
(Dundas et al., 2001)	N=102	22	0.33±0.23
(Pult, 2008)	N=33	-	0.13±0.36
(Gill, 2010)	N=47	26	0.23±0.39
This study	N=20	33	0.66±0.55

Table 5.9: Comparison of normal clinical signs of corneal staining graded using CCLRU scales.

It is commonly accepted that fluorescein staining of the cornea represents compromised epithelial integrity (Morgan and Maldonado-Codina, 2009). A red eye, accompanied by corneal staining, is intuitively taken as an unhealthy ocular situation and good practice advocates monitoring for signs of deterioration and treatment if necessary.

A number of factors may have contributed to the extensive superficial staining observed on the cornea following the use of Orthoprint for impression taking:

- Anaesthetic use: 0.5% Proxymetacaine HCl has been associated with increased corneal permeability to fluorescein (Green and Tonjum, 1971). The use of anaesthetic prior to ocular impression-taking may contribute to the corneal staining, however this effect may be considered minor given that the eyes following Tresident use were significantly less stained.
- Removal of epithelial cells: Impression cytology uses the adherent properties of the epithelial cells of the cornea and conjunctiva to study the changes to cell morphology that occur in ocular surface disease (Murube and Rivas, 2003). Cellulose acetate filter material is cut into strips and pressed against the cornea and conjunctiva to harvest cells for investigation (Nelson, 1982). The corneal macro-punctate staining pattern following the use of Tresident suggests that a number of cells may have been removed in a similar fashion, adhering to the polyvinylsiloxane material. This may offer cytologists a novel collection technique.
- Toxicity: The mechanism for observing corneal staining is typically to use surface fluorescein pooling or ingress around epithelial cells (Morgan and Maldonado-Codina, 2009). However, surface toxicity cannot be adequately explained in this manner. If Orthoprint does indeed cause a chemical interaction with tear mucins or membranes of the corneal and conjunctival epithelial cells, then fluorescein may be staining the affected cell complexes. Thus the increased sensitivity reported by subjects after Orthoprint may be a result of the ‘toxic’ interaction that remains until the surface cells are sloughed off. The initial increased cell permeability by proxymetacaine anaesthesia may encourage the acute inflammatory response and increase subsequent corneal staining observed.

- Damage to corneal integrity caused by one or a multitude of factors during ocular impression-taking requires careful monitoring and consideration given that any denudation of epithelium increases the risk of infection (Keay et al., 2006).

5.6 Conclusion

The use of Orthoprint during ocular impression-taking caused an abnormal hyperaemic response to the bulbar conjunctiva, accompanied by significant superficial corneal staining. This may be attributed to a toxic reaction between the material and the eye surface, exacerbated by mechanical abrasion caused by eyelid movement and granular material apposition. However, further investigation would be necessary to establish the exact nature of this interaction.

Tresident was found to be the impression material of choice. This study found less redness and clinically insignificant staining following impression-taking with fewer clinical complications.

To manage any clinical complications from using Tresident, the following advice is given:

- Provide lubricating drops post–impression.
- Review the ocular surface integrity 24 hrs later.
- Exclude dry eye patients and those with a comprised ocular surface, where possible.
- Consider prophylactic chloramphenicol treatment for patients with damaged or impaired ocular surface function.

This, combined with the favourable handling and excellent physical properties, makes Tresident a superior material for taking ocular impressions. For the first time using clinical grading scales, the effects of Orthoprint and Tresident have been evaluated to determine the ocular tissue complications following ocular impression procedures, providing comparative evidence and allowing practitioners to make an informed choice when deciding which material to use. The incidental adherent properties of polyvinylsiloxane materials to cells of the AOS may offer a novel collection technique to study cytology.

Chapter 6

The Cardiff Eyeshape Protocol – converting the ocular impression to a digital representation of the anterior ocular surface

The most favourable impression material for rendering an accurate and highly detailed structural representation of the AOS was examined in Chapter 5. The chosen material, an addition-polymerising, polyvinylsiloxane with hydrophilic properties, provided excellent elastic recovery and minimal linear dimensional change enabling the investigator to remove the material from the delicate anterior ocular surface (AOS) without damage, thus maintaining optimal feature representation and dynamic stability. The Cardiff Eyeshape Protocol (CEP) was developed to provide anatomical registration of the AOS impression and deliver a precise and repeatable model of the AOS that could then be scanned using active laser triangulation methods.

6.1 Introduction

The first plaster casts from human cadaver eyes to be employed were used by glass blowers to make pioneering scleral contact lenses (Fick, 1888): the plaster of Paris surface was used to mould trial glass lenses. Ocular impressions were later used to make a brass mould, which were used similarly to make glass scleral shells (Dallos, 1936). Fig 6.1 illustrates the method of production. The protocol described in Fig 6.1 does not include a description of any method of registration or orientation other than practitioner visualisation based on experience.

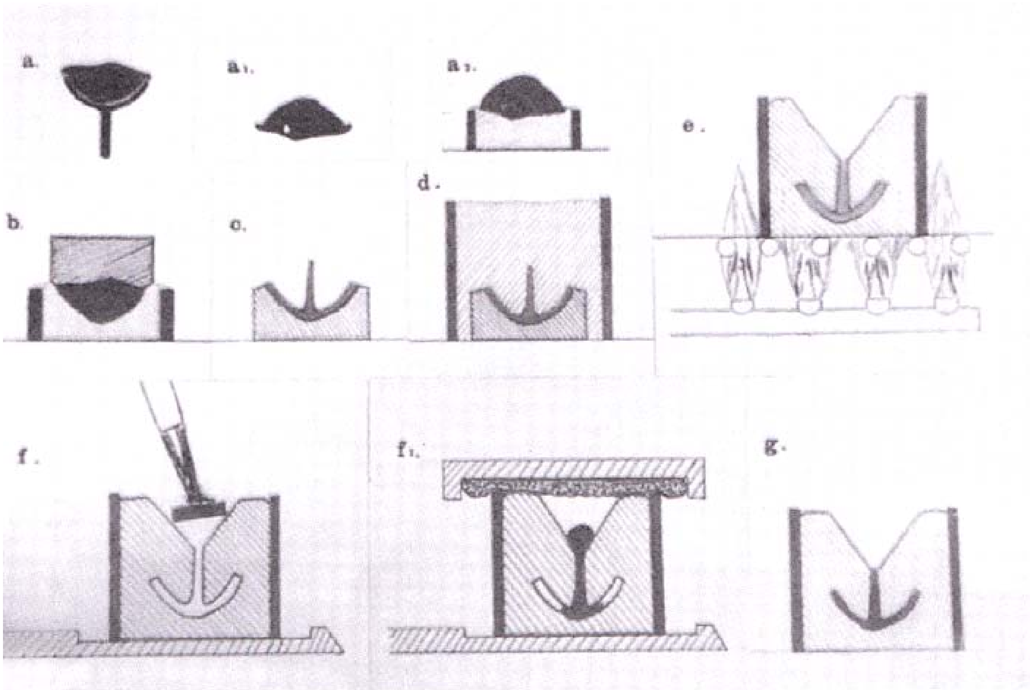

Figure 6.1: Schematic showing the lens making sequence; (a.) An impression is taken of the eye,(a_1.) From which a cast is taken of that, (a_2.) which is then set on a block. (b.) A female mould is taken from the cast in a low melting point material. (c.) A spigot is attached. (d.) The complete cast is enclosed in moulding material. (e.) The moulding material is removed to create a funnel and the whole mould is heated to remove the low melting point material. (f.) A small quantity of hot brass is placed within the funnel, (f_1) The lid of the moulding device is closed. With added heat and pressure, the hot brass is drawn into the mould. (g.) The brass mould is removed from the casting apparatus (Bowden, 2009).

Modern casting methods used a modified version of this protocol in the production of gas permeable scleral contact lenses. Small quantities of gypsum plaster are poured into the ocular impression, which is housed in an impression tray supported by a narrow-necked bottle. This primary cast is marked with a graphite pencil to locate the position of the vertical meridian (12 o'clock position), most commonly in line with markings on the impression tray, which are aligned with the correct anatomical location whilst in contact with the AOS (Pullum, 2007). The base of the primary cast is added later to provide adequate support during the polymerisation process when constructing the rough polymer scleral lens blanks (illustrated in Fig 6.2)

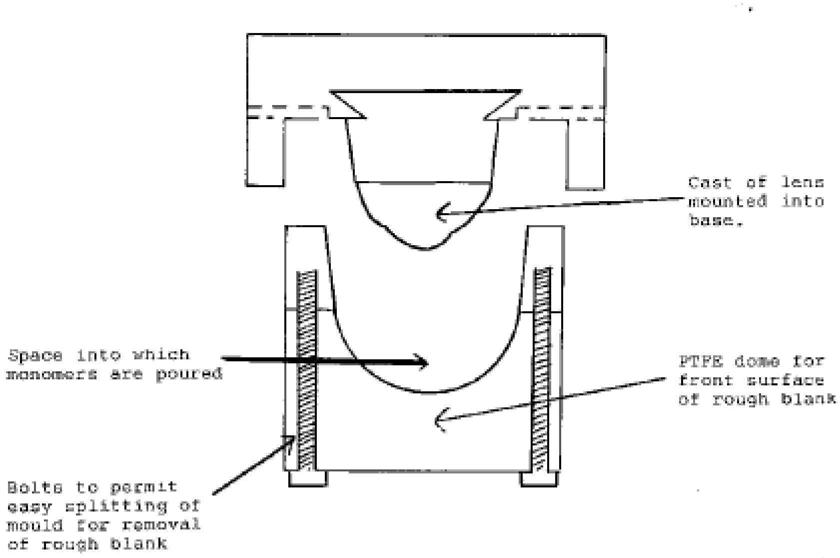

Figure 6.2: Construction of the mould required for rough rigid gas permeable scleral blanks (Pullum, 1987).

The remainder of this chapter describes the development of the Cardiff Eyeshape Protocol (CEP) and investigates a method of transferring the anatomical registration to the cast representation which was principally achieved by holding the resulting model in a bench vice for stability during the laser scanning process.

6.2 CEP Design and manufacture

6.2.1 Casting support and landmark registration device

An ocular impression casting tray (Cantor and Nissel Ltd, Brackley, Northamptonshire) was scanned using a touch-trigger probe installed on a co-ordinate measurement machine (CMM) Mitutoyo CMM machine – CRA Apex C Model (2005) (Mitutoyo (UK) Ltd, Andover, Hampshire). The digitised complex surface data was exported to CopyCAD 2010 (Autodesk, San Rafael, CA) and a casting support device designed to lock the impression tray position. The following series of diagrams (Fig 6.3-6.7) illustrate the design process undertaken which resulted in production of a casting support and landmark registration device.

.

Step 1:

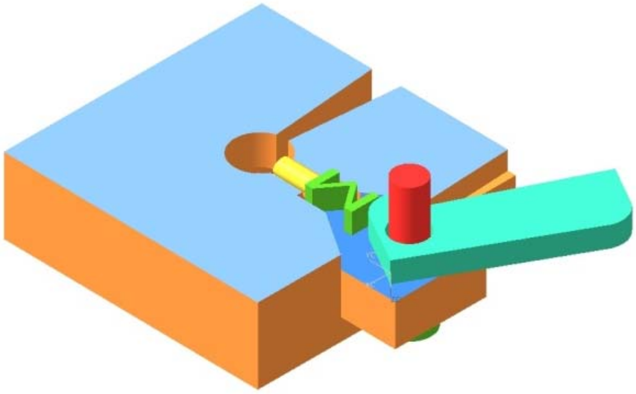

Figure 6.3: A non-uniform rational B-spline (NURBS) solid model of the locking mechanism used to position the impression tray (courtesy of Dr Hieu Le Chi, University of Greenwich).

Step 2:

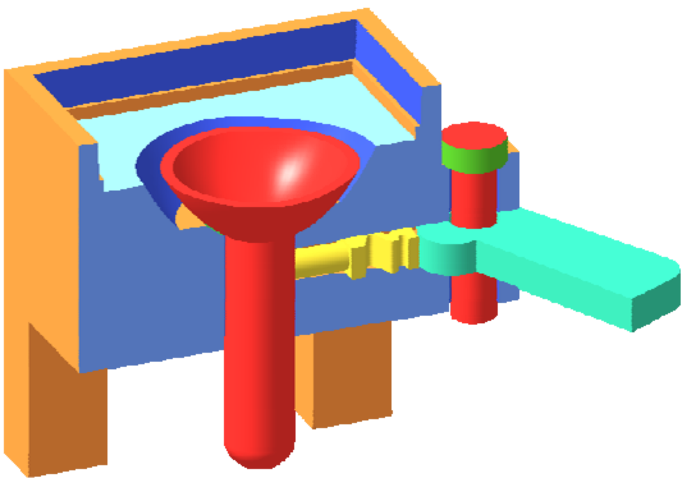

Figure 6.4: A NURBS solid model showing the position of the impression tray in the surrounding support structure (courtesy of Dr Hieu Le Chi, University of Greenwich)

Step 3:

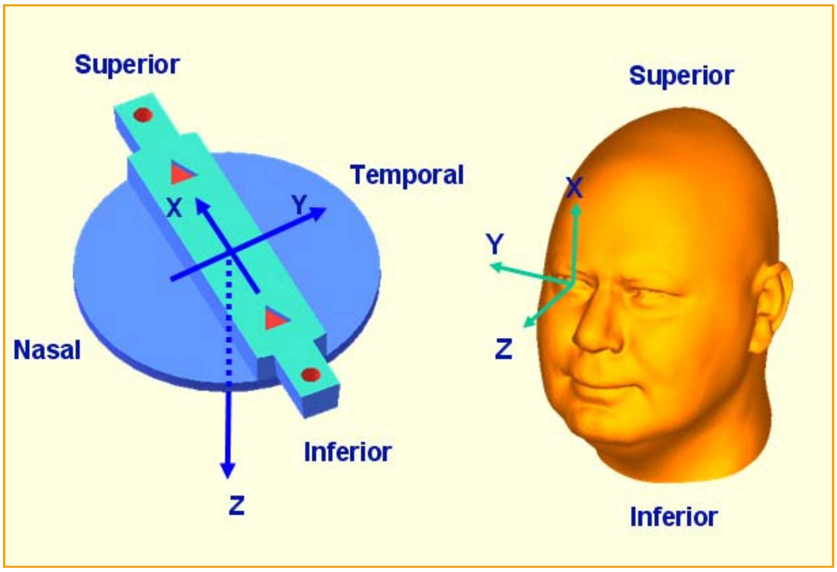

Figure 6.5: The mechanism to align the registration of the AOS was designed to be clamped into the bench vice positioned beneath the scanner. The arrows indicated the vertical meridian, which became an integral part of the AOS model as soon as the gypsum plaster had set and adhered to the polyamide material of the landmark device.

Step 4:

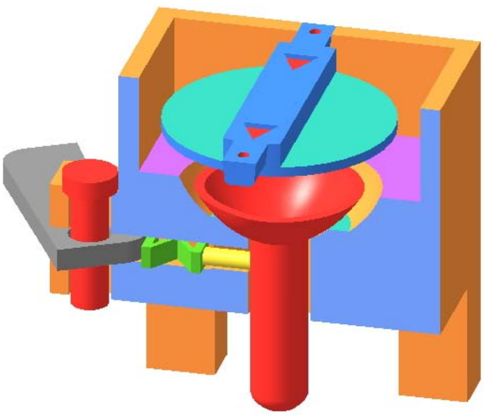

Figure 6.6: The landmark registration device was aligned with the impression tray registration dot(s), held in place by the locking mechanism.

Step 5:

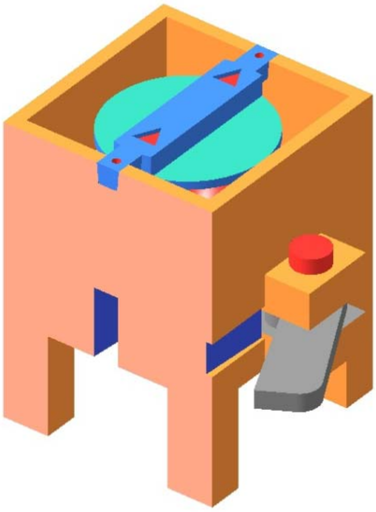

Figure 6.7: The final design was manufactured using selective laser sintering (SLS).

6.2.2 Prototype manufacture and testing

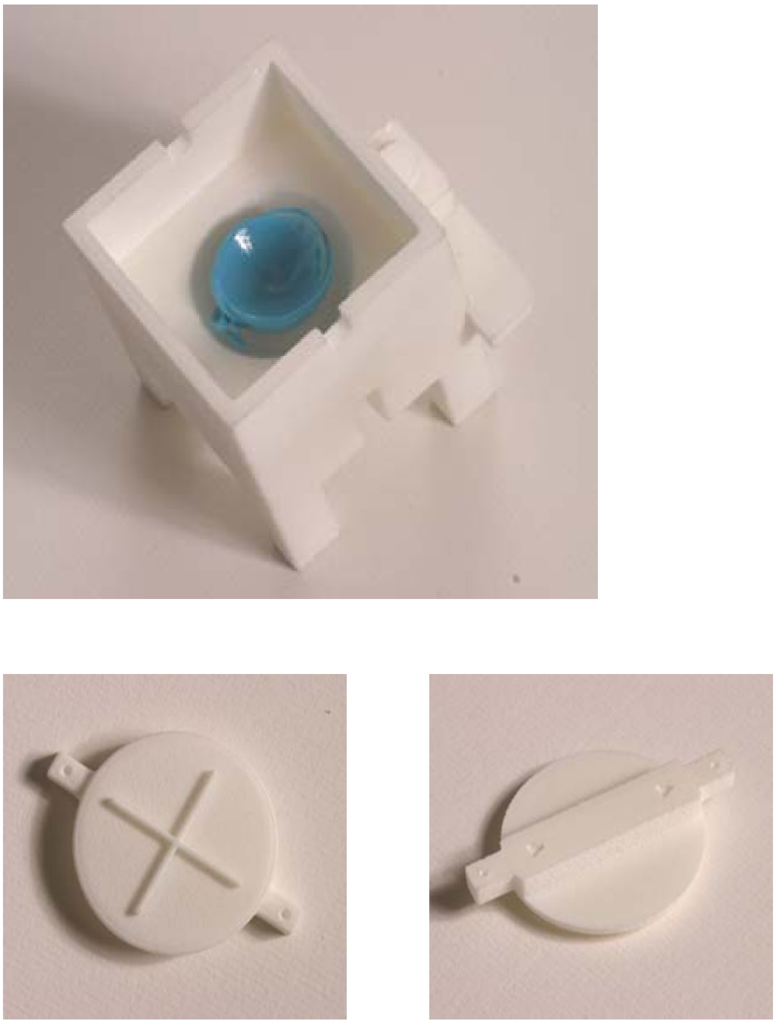

Figure 6.8: The final version of the casting support device (top) with an impression tray and ocular impression held in place, the landmark registration device (below) showing bottom (left) and top (right).

Extra-hard white plaster, Novadur (Ultima, Seiches-sur-Loir, France), a Type 4 Gypsum plaster, which conforms to BS 6873 (BSI, 2000), was identified as a suitable compound to be used in conjunction with Tresident (Shütz Dental Group GmbH, Germany). This product was found to have excellent adhesion to the polyamide powder used in the SLS process. The prototype was tested using the methods described in Chapter 8 (Section 8.3.2).

6.2.3 Model AOS

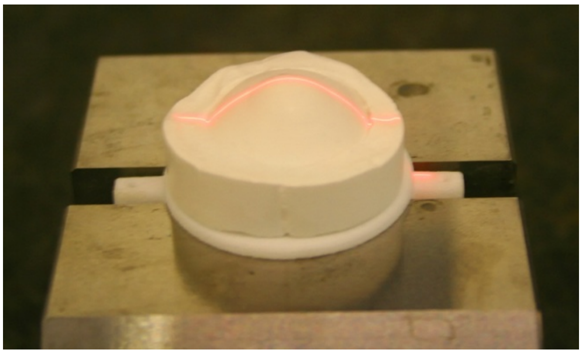

Figure 6.9: A model AOS with integral landmark registration device was tested using the bench vice for stabilisation and planar alignment (scanning laser showing as red line).

6.3 Investigating repeatability, reproducibility and stability of the model AOS

6.3.1 Aim

The aim was to validate the Cardiff Eyeshape Protocol, and to provide evidence that supports the use of the protocol for wide-field topographic data collection from the human anterior ocular surface *in-vivo*, to a standard acceptable to current industry and clinical requirements.

6.3.2 Introduction

A non-contact active laser triangulation system HYSCAN 45c, (Hymarc Ltd, Ontario, Canada) was selected for data acquisition from the model AOS. The advantages of this method where:

- No physical contact with the AOS model interface
- Fast digitising of substantial volumes
- Good accuracy and resolution for most common applications

- Excellent ability to scan highly detailed objects, where mechanical probes may be too large to access small intricacies

While this system was known to be less accurate than point-to-point sensing with touch-trigger probes, early experiments using the model prototypes suggested that the combined system error of using active laser triangulation amounted to ±0.065mm, which was comparable to repeatability of the modern methods of measuring the ocular surface reviewed in Chapter 2 and close to the manufacturing tolerance for contact lenses (in the region of ± 0.050mm British Standards 18369-2 (BSI, 2006)).

The published expansion of Novadur (Ultima, Seiches-sûr-Loir, France) was found to be 0.15% after 2 hours, but no data was available for stability during any period longer than this. It was envisaged that the model AOS casts might require storage for up to one month to allow data acquisition and analysis to be carried out.

6.3.3 Hypotheses

- Extra hard white plaster, Novadur (Ultima, Seiches-sûr-Loir, France), a Type 4 Gypsum plaster, which conforms to BS 6873 (BSI, 2000), can be used to cast a precise and reproducible model of the AOS that is stable and can be stored for an extended period of time.
- The accuracy of the Cardiff Eyeshape Protocol was within ±0.065mm.

6.3.4 Methods

6.3.4.1 Experimental procedure

A single 22mm steel ball-bearing was cast as a surrogate AOS using the procedure described in Chapter 8 (Section 8.3.2). The ball-bearing was supported to achieve a similar spatial orientation to the AOS in an upright individual. The model AOS was cast using the casting support and landmark registration device designed for the CEP. The model AOS was scanned using a touch-trigger probe installed on a co-ordinate measurement machine (CMM) Mitutoyo CMM machine – CRA Apex C

Model (2005) (Mitutoyo (UK) Ltd, Andover, Hampshire) to ensure the highest accuracy of measurements (±0.001mm) (Pham and Le Chi, 2008).

Repeatability
A single model AOS prototype (221_1) was measured at 3 different locations (z-1 to -3) with 3 different measurement set-ups.

Reproducibility
12 model AOS prototypes were measured once and compared at one location (z-4) to a reference prototype 221_1.

Stability
12 model AOS prototypes were measured at one location (z-4) twice, one month apart.

6.3.4.2 Data acquisition

The registration point or datum was set at the top of the cast of the 22mm steel ball bearing and located at the centre of a circle at sagittal depth of 1mm (z=-1mm). The circle was measured and located using 16 sampled points to define the location in order to ensure that the datum was located at the highest point at the centre of the circle (z=-1mm). The CMM software was prepared to automatically set up the datum and measuring the circumscribed locations at z=-1 to -5. The datum point and measurement locations were illustrated in Figure 6.10.

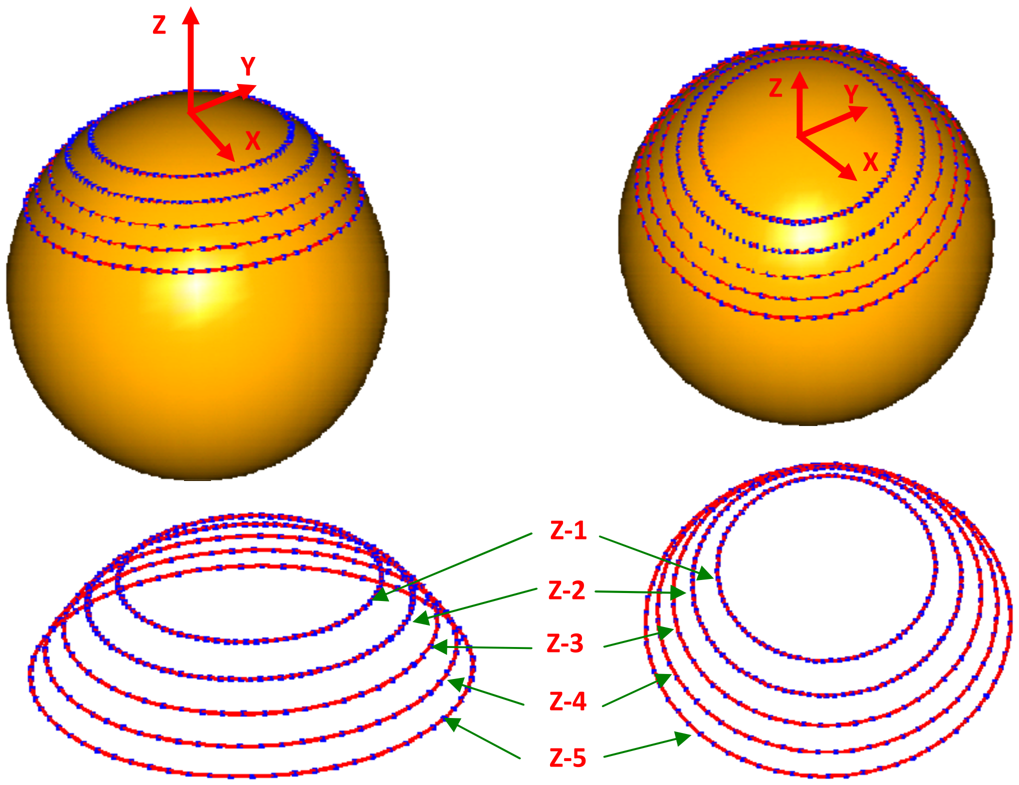

Figure 6.10: Diagram to show the measurement locations made by CMM and the datum point (courtesy of Dr Hieu Le Chi, University of Greenwich).

6.3.4.3 Data presentation and analysis

Measurements for the locations were presented as radial plots, using the least squares method, which determined the circle that makes the sum of the squares of the deviation between that circle and the measurement data a minimum. These plots were colour-coded to provide visualisation of hot colours (light green to red) as positive error and cold colours (dark green to dark blue) as negative error.

6.3.5 Results

6.3.5.1 Repeatability

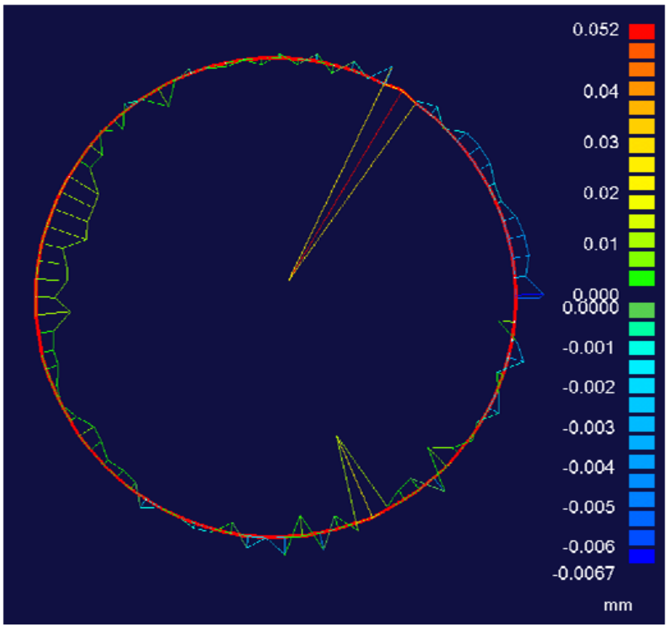

Figure 6.11: Comparison of the first and second measurement of prototype 221_1 at location z=-1 (100x magnification).

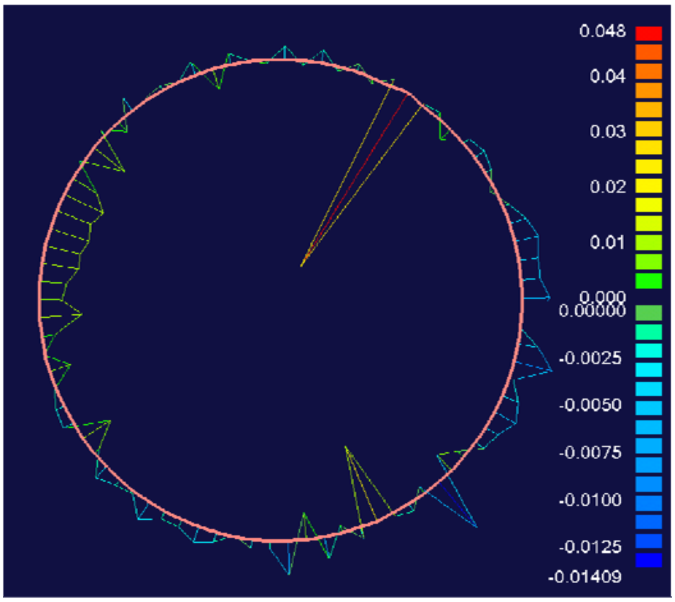

Figure 6.12: Comparison of the first and third measurement of prototype 221_1 at location z=-1 (100x magnification).

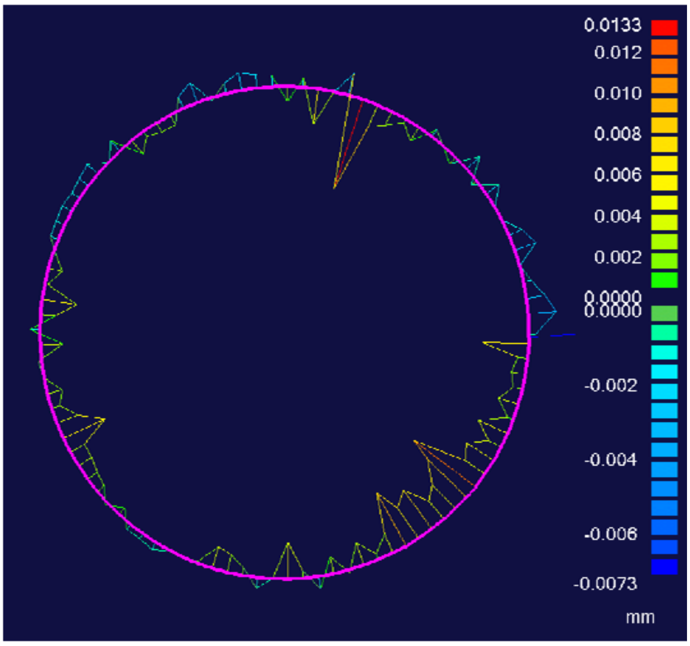

Figure 6.13: Comparison of the first and second measurements of prototype 221_1 at location z=-2 (200x magnification)

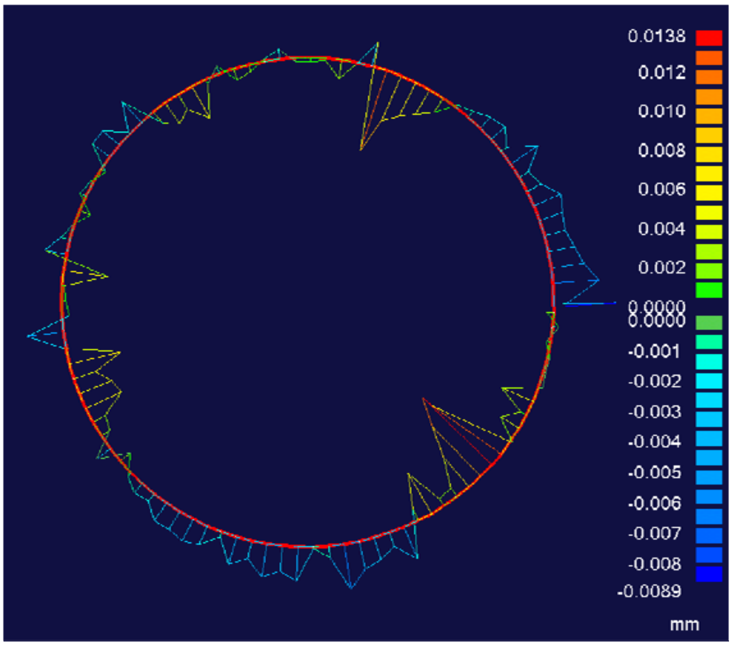

Figure 6.14: Comparison of the first and third measurement of prototype 221_1 at location z=-2 (200x magnification).

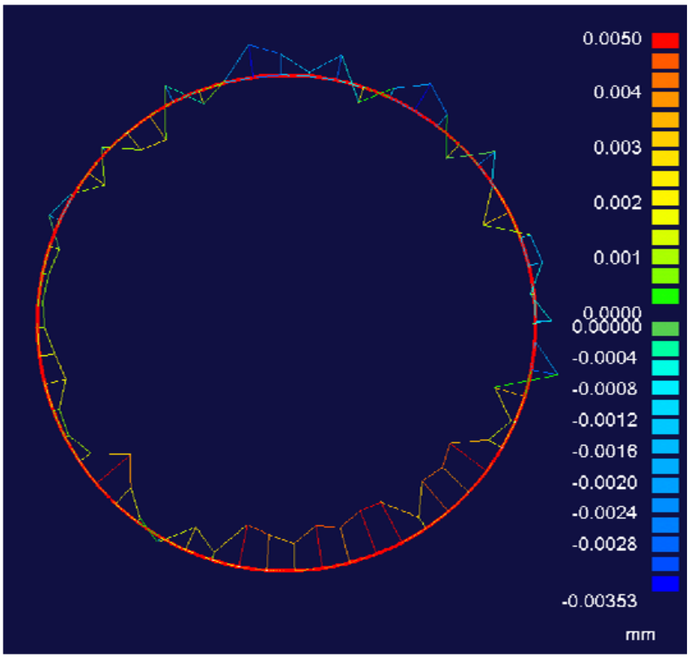

Figure 6.15: Comparison of the first and second measurements of prototype 221_1 at location z=-3 (300x magnification).

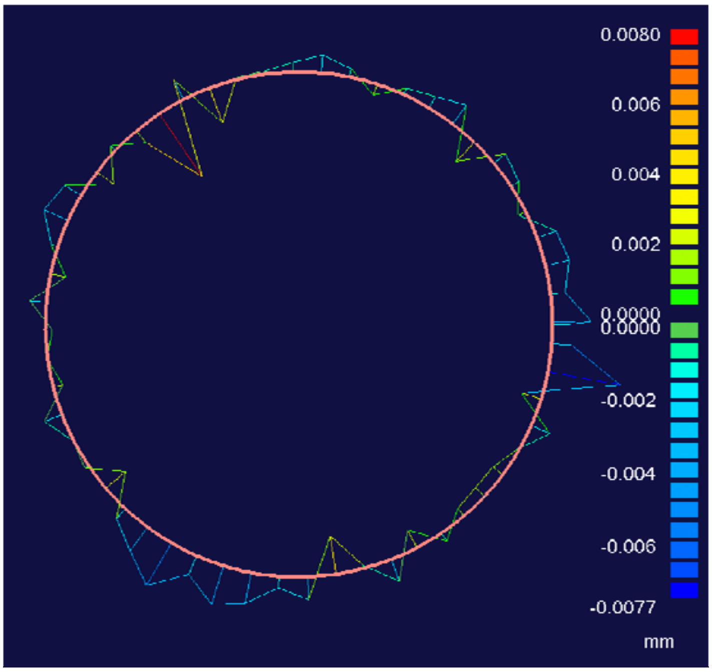

Figure 6.16: Comparison of the first and third measurements of prototype 221_1 at location z=-3 (300x magnification).

Measurements of prototype 221_1 were most accurate at z=-3 at 300x magnification, range +0.007 to -0.006mm (magnification here refers to the size and scale of the radial graph) The average value for differences between curvature measurements the 3 locations was +0.008mm ±0.021 [SD].

6.3.5.2 Reproducibility

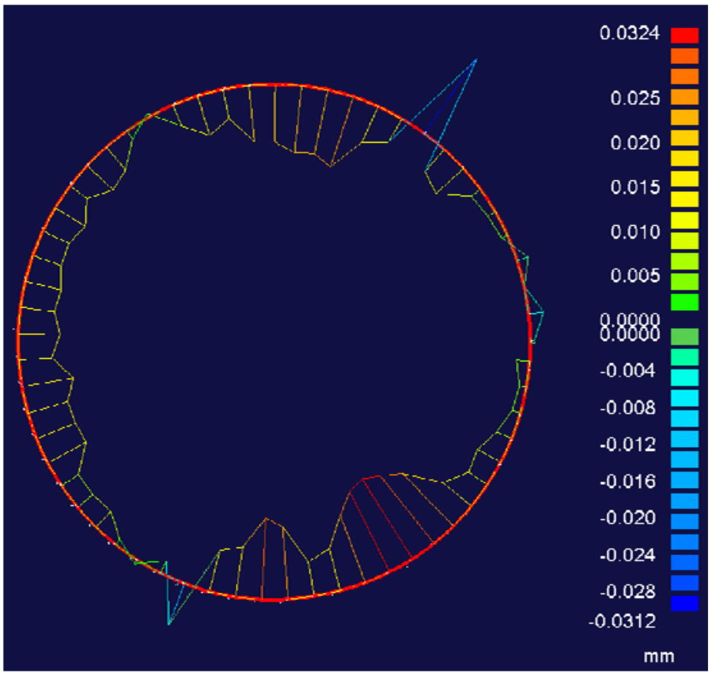

a)

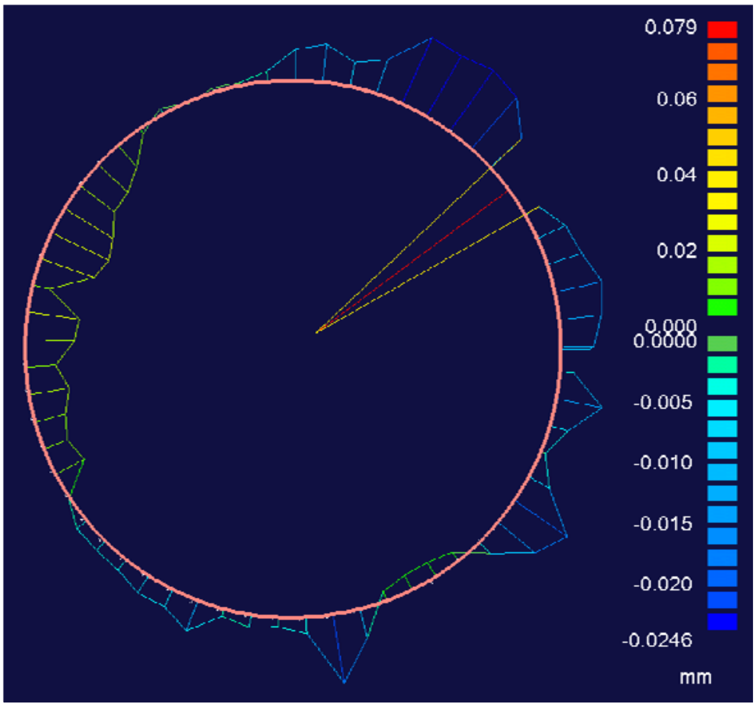

b)

Figure 6.17: Comparison of measurements taken at location z-4 for prototypes 221_ 2 to 221_12, using prototype 221_1 as the reference; a) prototype 221 _1 minus prototype 221_2, b) prototype 221_1 minus prototype 221_3.

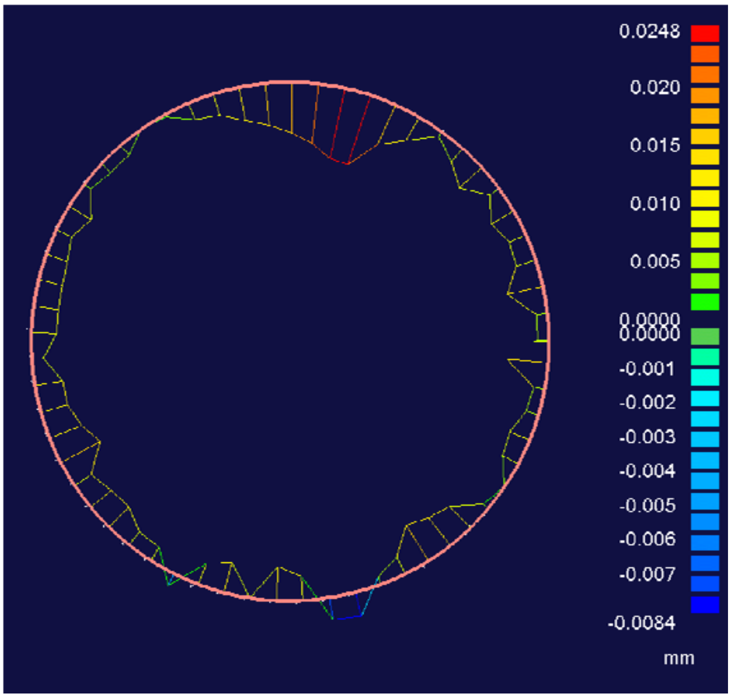

c)

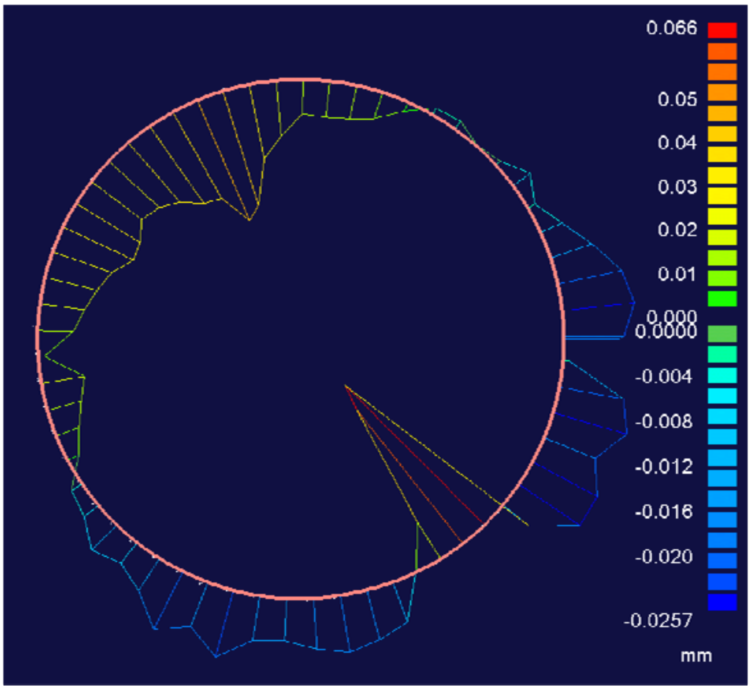

d)

Figure 6.18: Comparison of measurements taken at location z-4 for prototypes 221_ 2 to 221_12, using prototype 221_1 as the reference; c) prototype 221 _1 minus prototype 221_4, d) prototype 221_1 minus prototype 221_5.

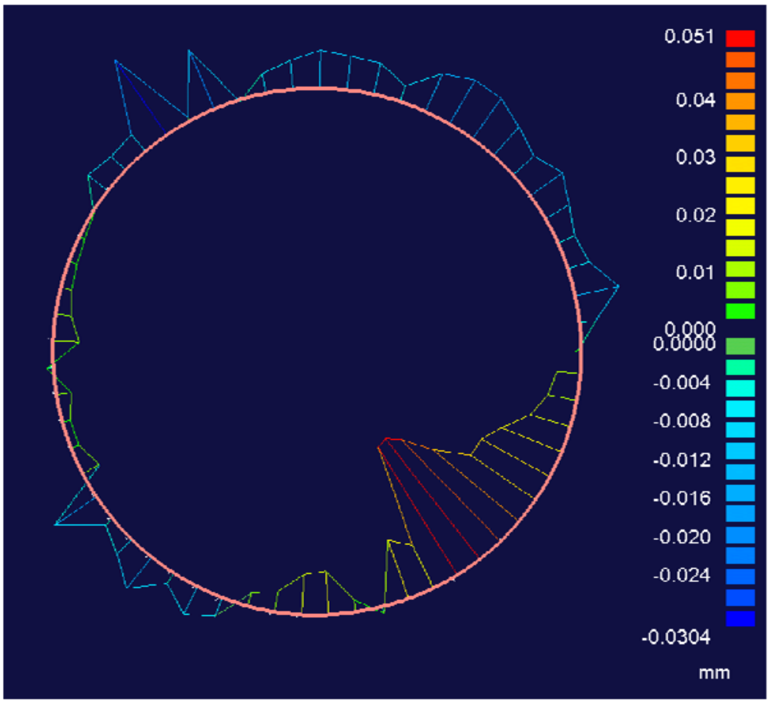

e)

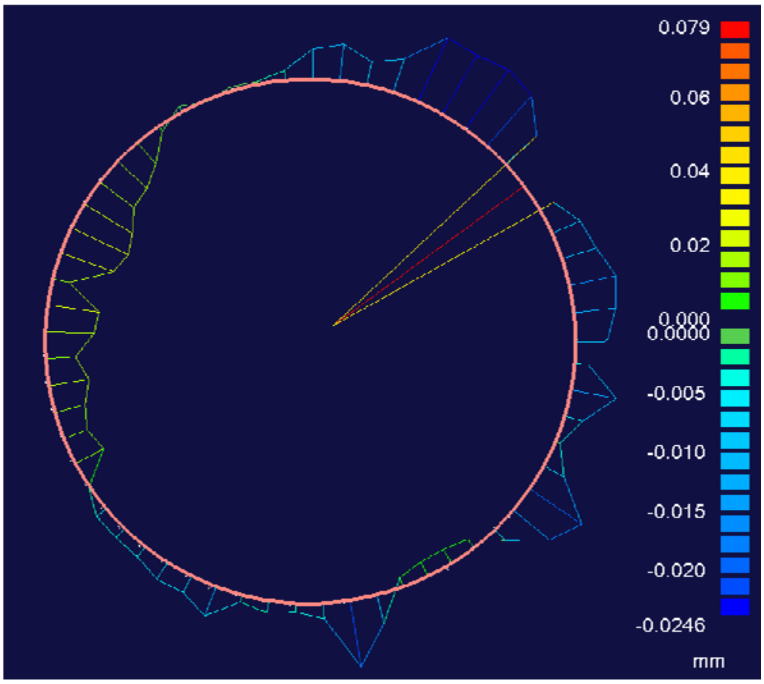

f)

<u>Figure 6.19</u>: Comparison of measurements taken at location z-4 for prototypes 221_ 2 to 221_12, using prototype 221_1 as the reference; e) prototype 221 _1 minus prototype 221_6, f) prototype 221_1 minus prototype 221_7.

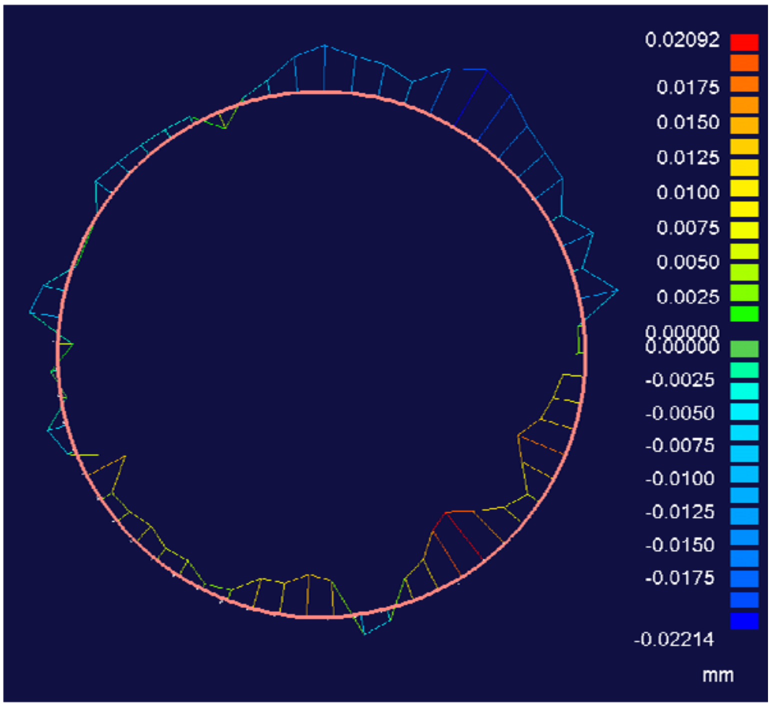

g)

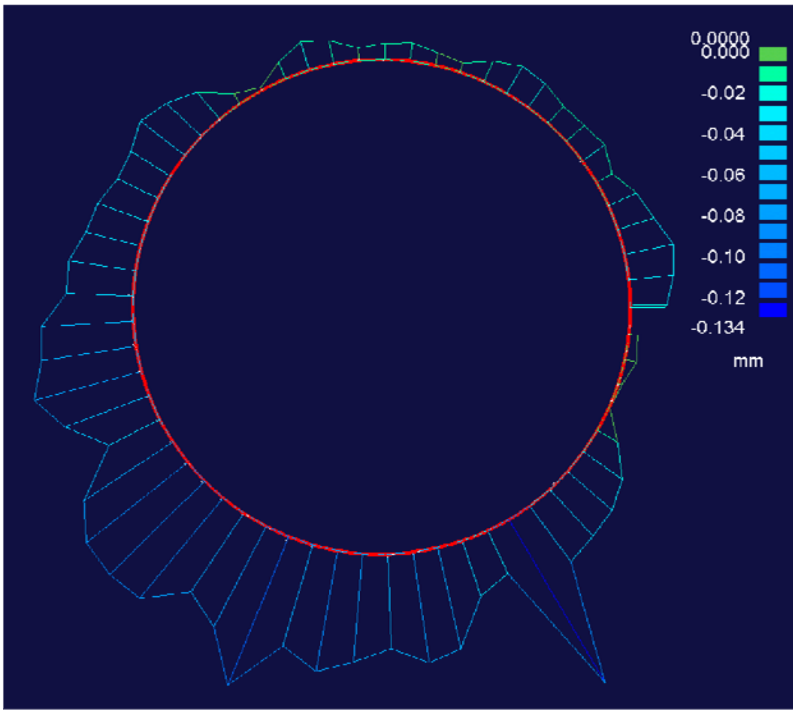

h)

Figure 6.20: Comparison of measurements taken at location z-4 for prototypes 221_ 2 to 221_12, using prototype 221_1 as the reference; g) prototype 221 _1 minus prototype 221_8, h) prototype 221_1 minus prototype 221_9.

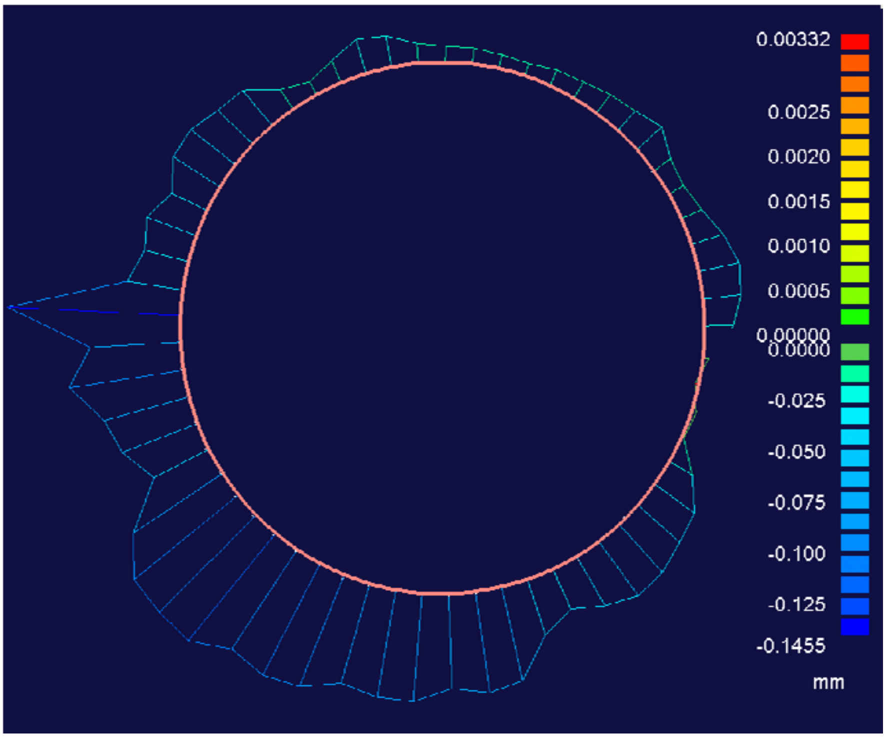

i)

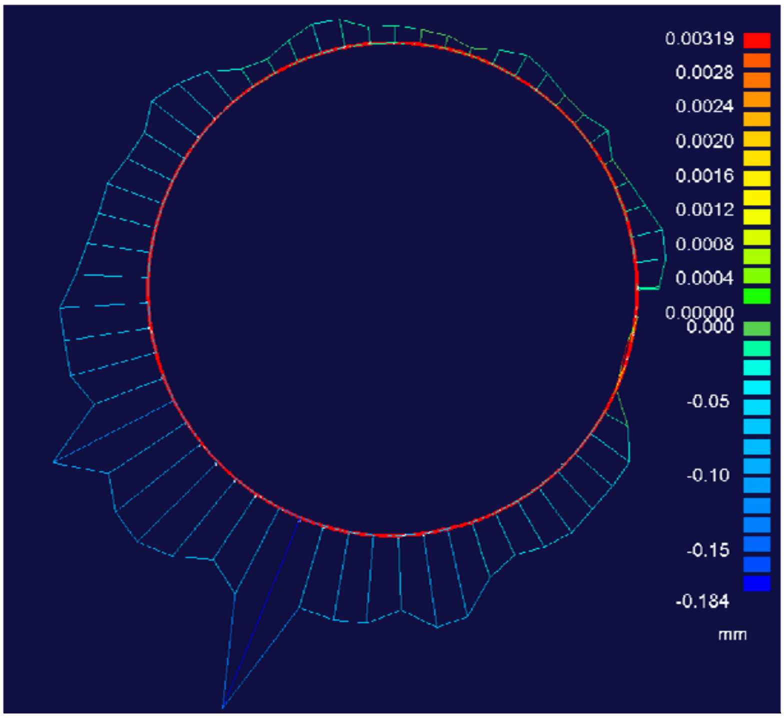

j)

Figure 6.21: Comparison of measurements taken at location z-4 for prototypes 221_ 2 to 221_12, using prototype 221_1 as the reference; i) prototype 221 _1 minus prototype 221_10, j) prototype 221_1 minus prototype 221_11.

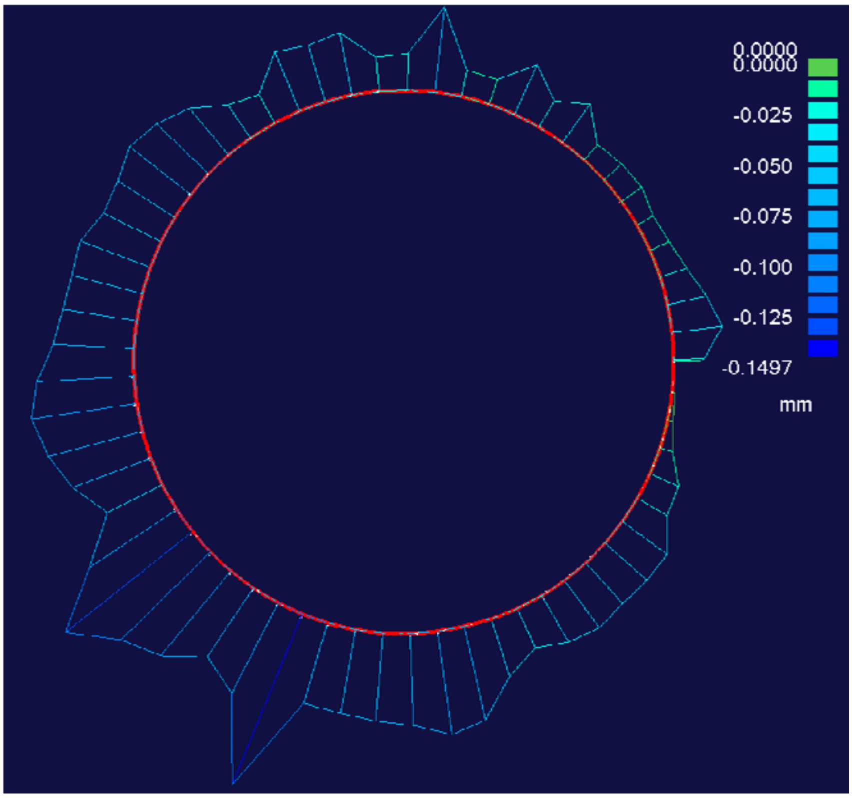

k)

Figure 6.22: Comparison of measurements taken at location z-4 for prototypes 221_ 2 to 221_12, using prototype 221_1 as the reference; k) prototype 221 _1 minus prototype 221_12.

When comparing measurements of z=-4 for each of 11 prototypes, the reproduced 22mm ball surface was found to be smaller than prototype 1, on average -0.0019±0.073 mm (range 0.033 to -0.071).

6.3.5.3 Stability

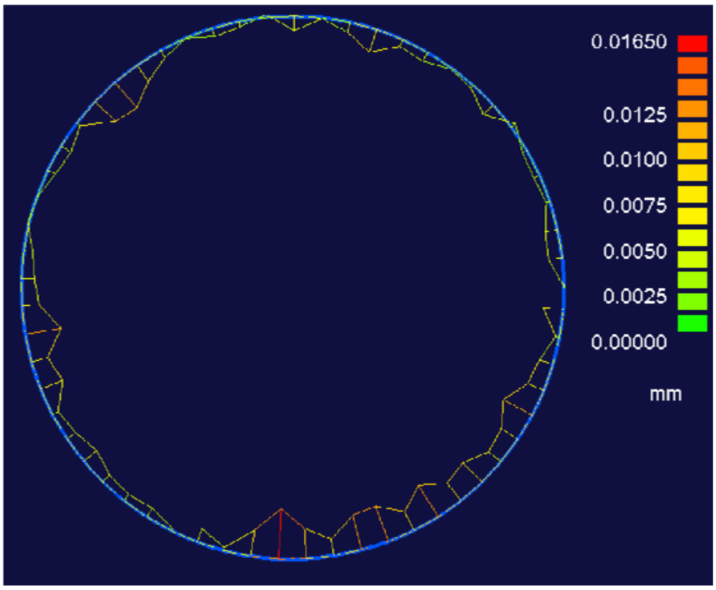

a)

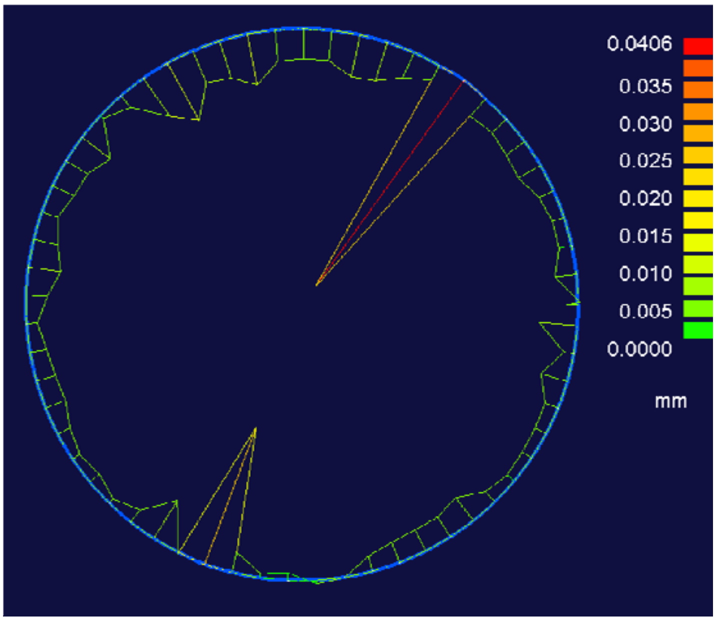

b)

Figure 6.18: Radial graphs showing comparison of measurements for prototypes 221_1 to 221 _12 at location z-4 at a one month interval apart: a) prototype 221_1, b) prototype 221_2.

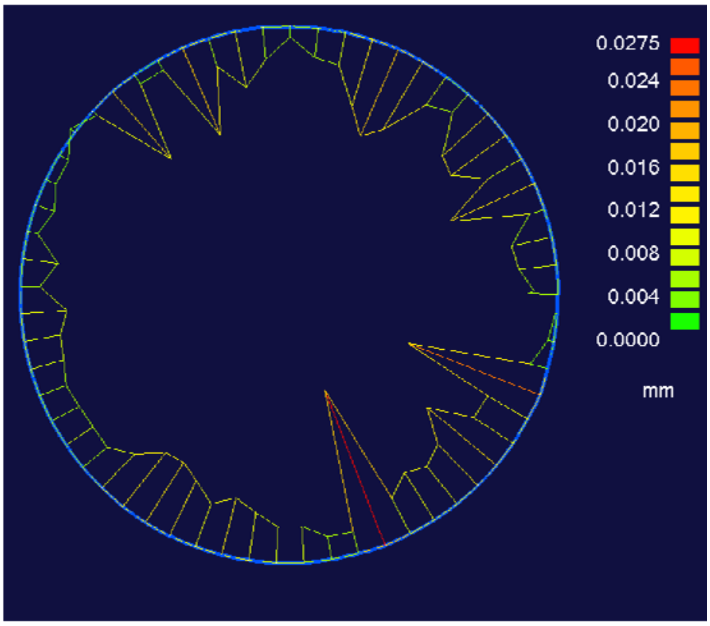

c)

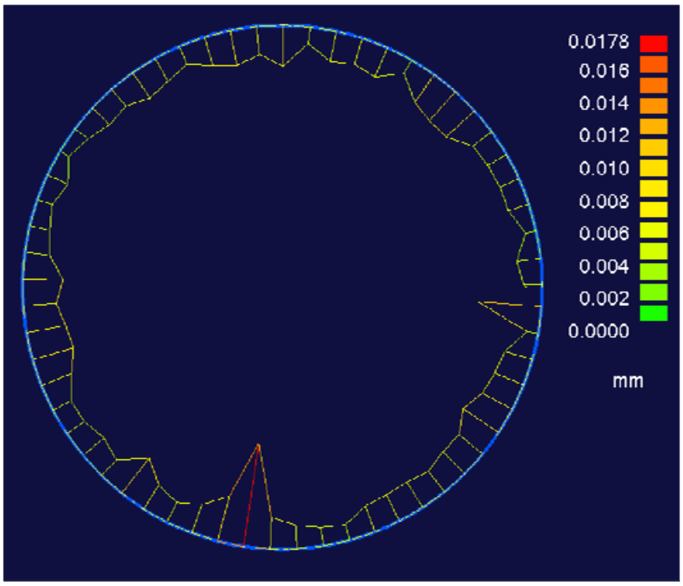

d)

Figure 6.18: Radial graphs showing comparison of measurements for prototypes 221_1 to 221 _12 at location z-4 at a one month interval apart: c) prototype 221_3, d) prototype 221_4.

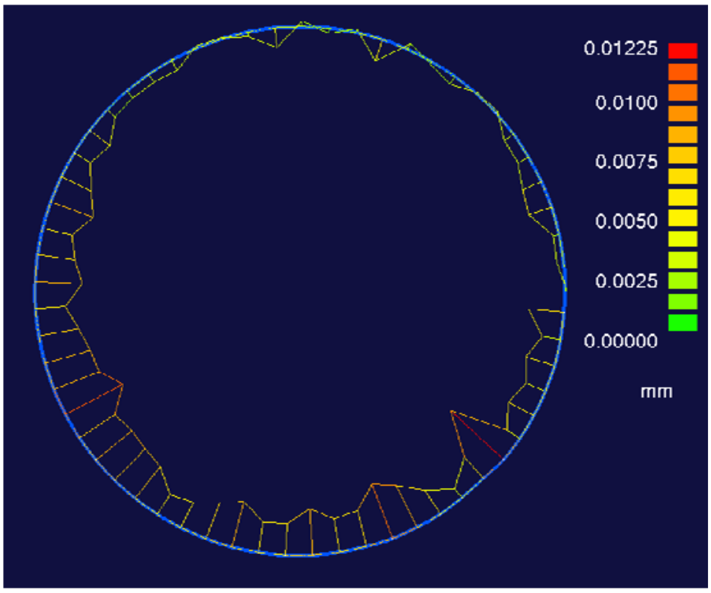

e)

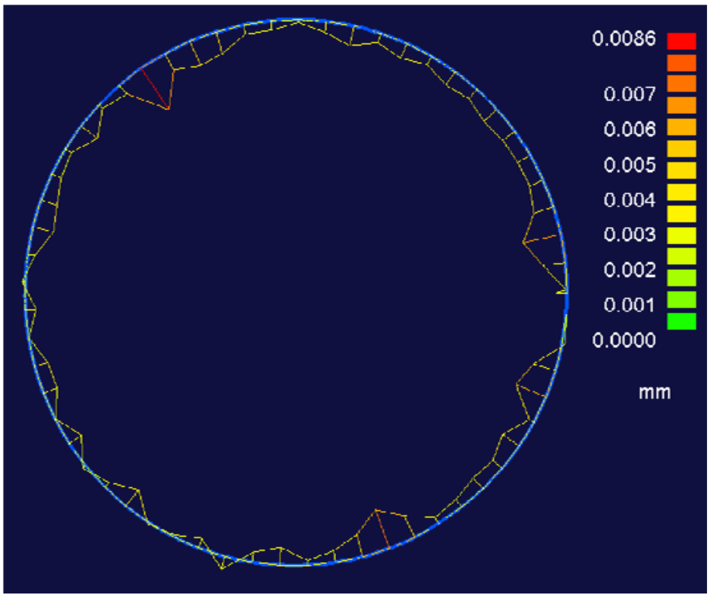

f)

Figure 6.18: Radial graphs showing comparison of measurements for prototypes 221_1 to 221 _12 at location z-4 at a one month interval apart: e) prototype 221_5, f) prototype 221_6

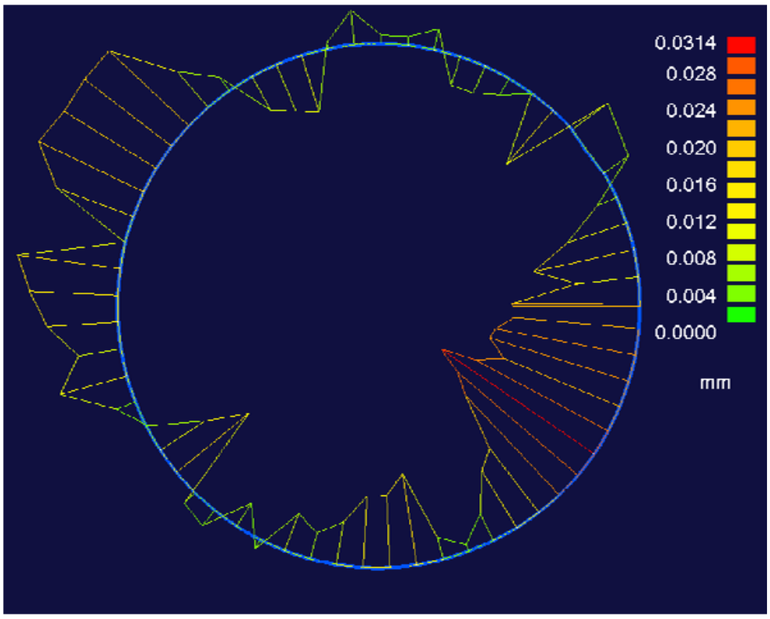

g)

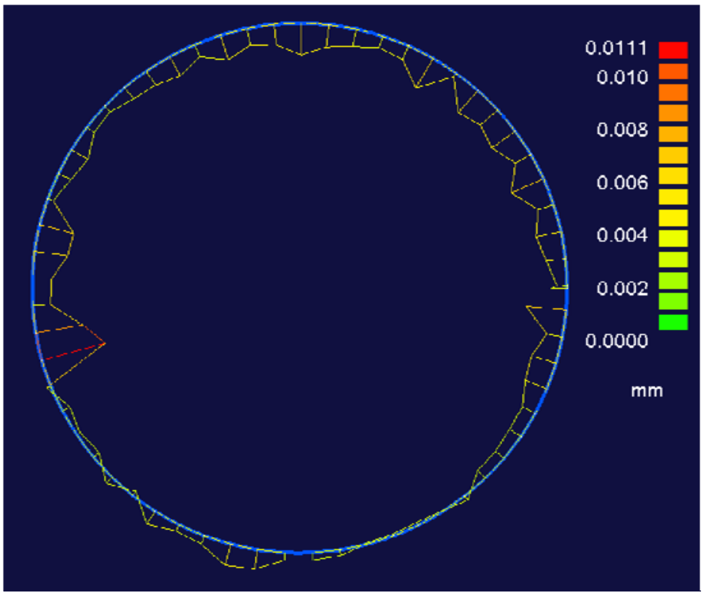

h)

<u>Figure 6.18:</u> Radial graphs showing comparison of measurements for prototypes 221_1 to 221 _12 at location z-4 at a one month interval apart: g) prototype 221_7, h) prototype 221_8

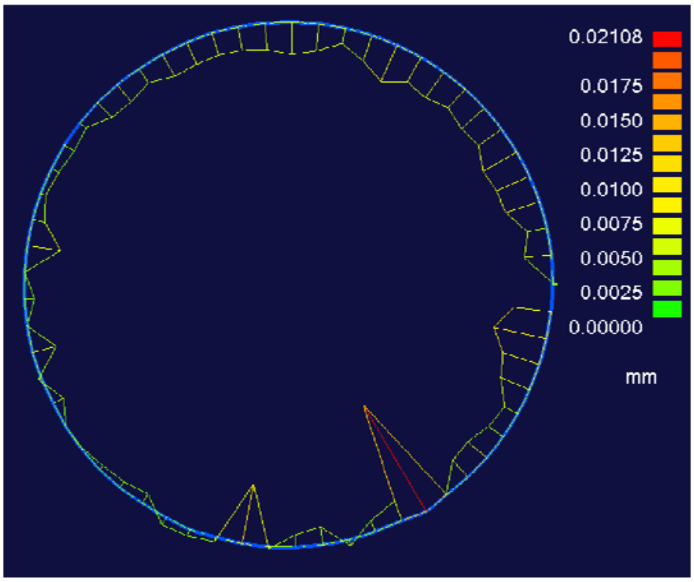

i)

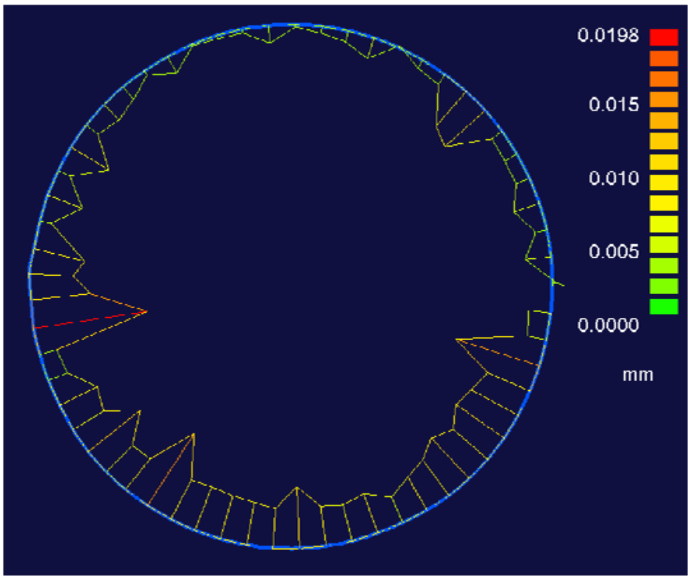

j)

Figure 6.18: Radial graphs showing comparison of measurements for prototypes 221_1 to 221 _12 at location z-4 at a one month interval apart: i) prototype 221_9, j) prototype 221_10

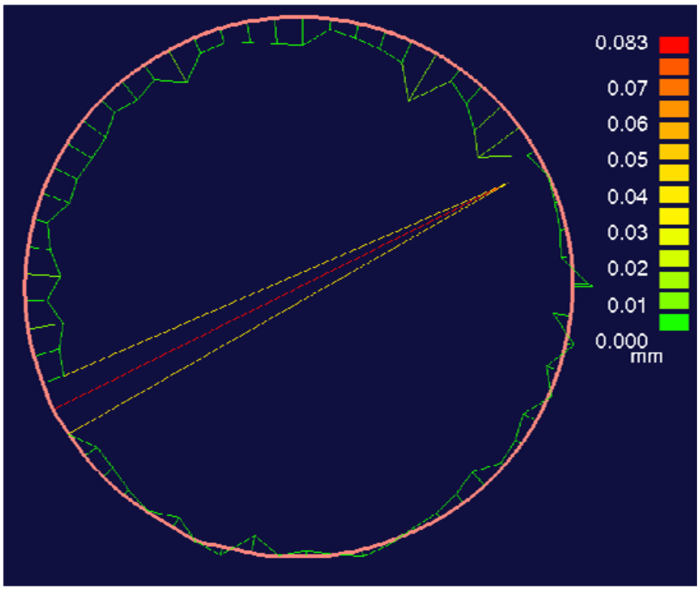

k)

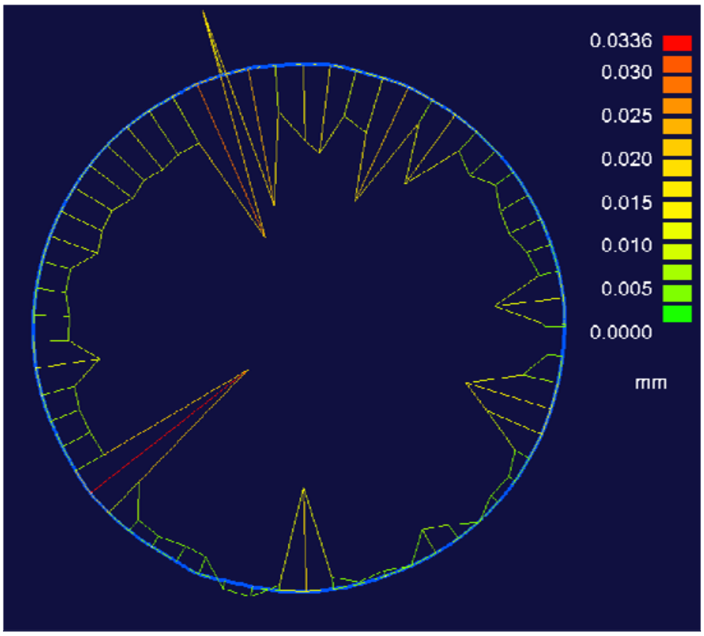

l)

Figure 6.23: Radial graphs showing comparison of measurements for prototypes 221_1 to 221 _12 at location z-4 at a one month interval apart: k) prototype 221_11, l) prototype 221_12

Measurements for all 12 prototypes were found to be larger, when measured on the second occasion; at a one month interval. The z-4 location was on average flatter 0.027mm ±0.020 [SD].

6.3.6 Discussion

This investigation has provided evidence to validate the combined use of ocular impression taking and CEP to provide a reliable system for collecting topographic data for a surrogate AOS (22mm ball bearing). Repeated measurements of a spherical 22mm diameter ball bearing cast according to the CEP, in the region 1-3mm below the datum were observed to be highly repeatable; +0.008mm ±0.021 [SD] . 12 castings of the same surrogate impression were also found to be reproducible to a high level of accuracy, the surface measurements were slightly smaller on average than the reference cast; -0.0019±0.073 (range 0.033 to -0.071). The AOS type IV gypsum casts were found to expand over a one month period by 0.027mm ±0.020 [SD], and allowances were made for any casts that required storage.

Further studies would be necessary to establish repeatability of anatomically accurate AOS surface models.

6.3.7 Conclusions

The Cardiff Eyeshape Protocol was found to meet all the requirements of a modern topographic data collection system:

- Repeatability: +0.008mm ±0.021 [SD]
- Reproducibility: -0.0019±0.073 (range 0.033 to -0.071)
- Stability: Extra-hard white plaster, Novadur (Ultima, Seiches-sûr-Loir, France) was found to expand by 0.027mm ±0.020 [SD] over a one month period.

Chapter 7

Does ocular impression taking cause distortion of the anterior ocular surface?

The previous chapter outlined the modernisation of the ocular impression taking procedure using the Cardiff Eyeshape Protocol. This protocol established a casting and scanning system that enabled the spatial registration of the AOS according to anatomical orientation and the creation of a stable platform to allow the accurate collection of up to 200,000 sample points per surface using non-contact active laser triangulation. The reliability of this protocol is assessed in the following series of experiments, which sought to identify whether the ocular surface topography is compromised by the invasive nature of the impression procedure.

The precise details of the technique used for the purposes of ocular impression taking were described previously (see Chapter 5: section 5.2.3.1). With the subject seated in an upright position, a silicone-based material was applied to an eye-shaped impression tray, which covered the AOS and was positioned beneath both upper and lower eyelids. The investigator supported the impression tray manually during the 2 mins 45 seconds required for the material to cure. During this procedure, there is an assumed amount of transient deformation of the AOS caused by the consistent contact of the material and tray, but the presence and extent of this deformation has not been previously reported or quantified.

7.1 Aims and Hypotheses

- The ocular impression technique used in the Cardiff Eyeshape Protocol does not deform the AOS to a clinically significant level.
- This system can be used to provide valid and reliable measurements of wide-field AOS morphometrics.

7.2 <u>Study 1</u>: To investigate the effect of ocular impression taking on the central cornea

7.2.1 Aims and Hypotheses

This study aimed to determine the topographic effect of modern ocular impression taking on the ACS, 10 minutes after the procedure.

The hypotheses proposed are:

- There is no significant lasting topographic deformation of the ACS in the principal meridians (horizontal and vertical) elicited by modern ocular impression taking.
- Orbscan IIz is a suitable instrument with which to image the ACS for comparison purposes.

7.2.2 Subjects

Measurements from the right eye only of 104 subjects were included in the study, (69 ♀ and 35 ♂). The mean age of the cohort was 24.65 ±6.64 years [SD] (range 17.61 to 42.55). Ethical approval for the study was obtained from the Cardiff School of Optometry and Vision Sciences Human Ethics Committee. All subjects were treated in accordance with the Tenets of the Declaration of Helsinki, and each provided informed, written consent. Volunteers were recruited from the staff and students of Cardiff University, and subjects were excluded if they were pregnant or breastfeeding, had any ocular or systemic condition known to affect the structure or characteristics of the anterior ocular surface, were taking any medication known to affect the ocular surface, had worn rigid lenses in the preceding 6 weeks or soft lenses in the preceding 2 weeks, and were not white European. This ethnic bias was chosen because it has been shown that ethnicity affects ocular surface morphometrics (Matsuda et al., 1992).

7.2.3 Experimental procedure

The right eye of each individual was scanned on two occasions using the Orbscan IIz (Bausch & Lomb, Orbtek Inc., Salt Lake City, UT) slit-scanning video-keratoscope (Fig 7.1), immediately before and then 10 minutes after impression taking. A previous study that compared the repeatability of axial radius of curvature for a single meridian using Orbscan IIz (Orb) technology found an insignificant difference in variability between 3 and 5 measures (Douthwaite and Parkinson, 2009). Ttherefore each scan was repeated 3 times and a mean value obtained. The subjects were instructed to blink twice and stare wide-eyed before each image acquisition. Measurements were made following the instructions from the Orbscan user manual, and subjects with poor tear break-up times were excluded from the study to minimise the influence of tear film variability on the reflected image quality.

Figure 7.1: Orbscan IIz (Bausch & Lomb, Orbtek Inc., Salt Lake City, UT)

7.2.4 Analysis

Mean axial curvature maps were sampled from the output screen (Fig 7.2) using an overlay grid with 0.5mm between each point. The transparent overlay was used to maximise the accuracy of cursor positioning. The radii of curvature were recorded along the extent of the vertical and horizontal meridians. The limit of the profile was determined by the available data for each subject, which was restricted by the reflective properties of the pre-ocular tear film and the extremities of the vertical palpebral aperture.

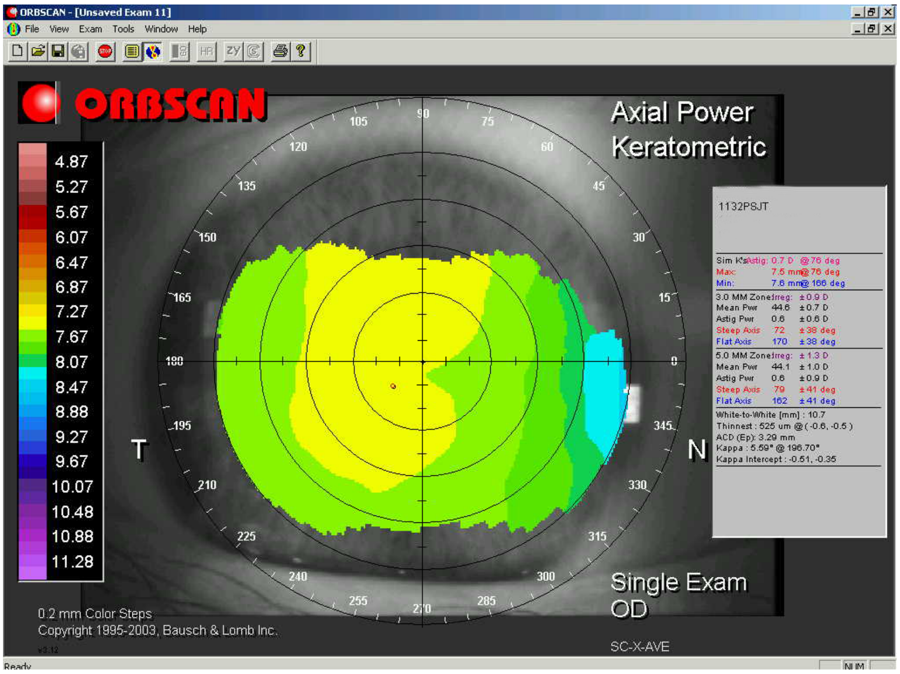

Figure 7.2: Orbscan IIz; Axial power keratometric output display (Scale bar set to radius of curvature).

7.2.5 Statistical analysis

All data was collated with Excel 2007 (Microsoft®, Redmond, DC), and analysed within SPSS v13 (SPSS Inc, Armonk, NY). Comparisons were made pre- and post-impression in the horizontal and vertical meridians. The profiles were aligned according to the instrument axis (designated 'Apex') and divided into annuli (Fig 7.3). A mean radius of curvature was calculated for each zone, with the length of each chord increasing in 1mm steps. After establishing a normal distribution of differences using the Kolmorogov-Smirnov test, paired sample t-tests were used to examine the variability between measurements.

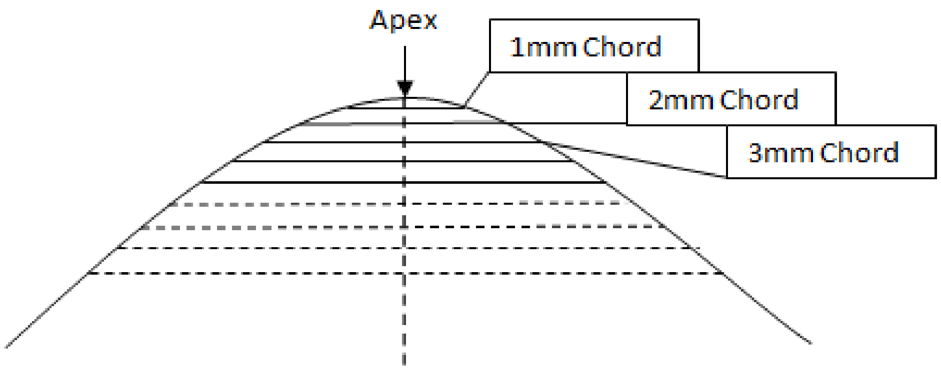

Figure 7.3: Diagram to show the area of profile included in each zone of cumulative mean radius of curvature.

The area of analysis was limited to 7mm horizontally and 4mm vertically, by the interference of the eyelids and eyelashes.

7.2.6 Results

7.2.6.2 Horizontal meridian

Area of interest	Mean radius of curvature (mm ±SD)		Mean difference in radius (mm±SD)	Paired-samples t-test Statistical significance (95% confidence interval)
	Pre Impression	Post Impression		
Apex	7.72 ± 0.31	7.73 ± 0.32	0.010 ± 0.28	P=0.713
1mm chord	7.73 ± 0.30	7.74 ± 0.32	0.013 ± 0.26	P=0.601
2mm chord	7.73 ± 0.30	7.75 ± 0.32	0.017 ± 0.26	P=0.510
3mm chord	7.74 ± 0.31	7.76 ± 0.32	0.019 ± 0.26	P=0.433
4mm chord	7.75 ± 0.31	7.77 ± 0.32	0.022 ± 0.26	P=0.372
5mm chord	7.76 ± 0.31	7.79 ± 0.32	0.024 ± 0.25	P=0.335
6mm chord	7.78 ± 0.31	7.80 ± 0.32	0.024 ± 0.26	P=0.338
7mm chord	7.79 ± 0.31	7.81 ± 0.32	0.023 ± 0.26	P=0.351

Table 7.1: Mean axial radius of curvature values measured using slit-scanning videokeratoscopy of the ACS, pre- and 10 minutes post-impression procedure in the horizontal meridian.

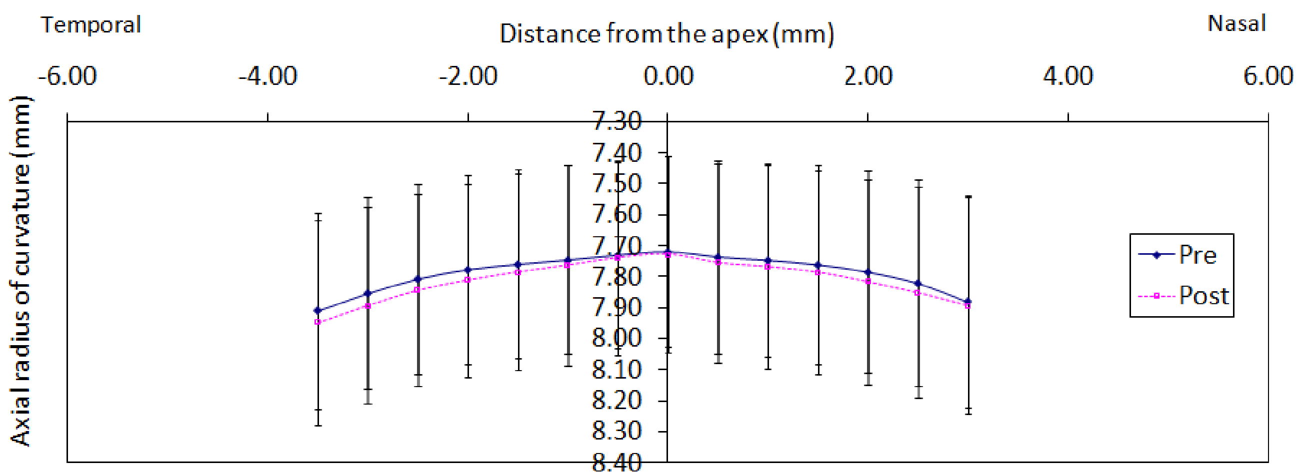

Figure 7.4: Comparison of corneal topography measured using Orb pre- and post-ocular impression procedure in the horizontal meridian (error bars indicate ± 1SD).

In the horizontal meridian (seen in Table 7.1 and Fig 7.4), small, but not statistically significant, increases in axial radii (overall flattening) occur post impression procedure. The flattening was found to be at a minimum at the apex 0.010± 0.28mm [SD] and maximum at 2.5-3.0mm either side of the apex at 0.024± 0.26mm.[SD] The mean difference for the complete data set horizontally was 0.018± 0.25mm [SD] was not statistically significance ($0.335<p<0.713$).

7.2.6.3 Vertical meridian

Area of interest	Mean radius of curvature (mm ±SD)		Mean difference in radius (mm±SD)	Paired-samples t-test Statistical significance (95% confidence interval)
	Pre Impression	Post Impression		
Apex	7.72 ± 0.29	7.72 ± 0.28	-0.003 ± 0.14	p=0.809
1mm chord	7.70 ± 0.29	7.70 ± 0.28	0.003 ± 0.13	p=0.817
2mm chord	7.68 ± 0.29	7.69 ± 0.28	0.009 ± 0.12	p=0.441
3mm chord	7.68 ± 0.29	7.69 ± 0.28	0.011 ± 0.11	p=0.317
4mm chord	7.68 ± 0.28	7.69 ± 0.28	0.013 ± 0.11	p=0.241

Table 7.2: Mean axial radius of curvature values measured using slit-scanning videokeratoscopy of the ACS, pre- and 10 minutes post-impression procedure in the vertical meridian.

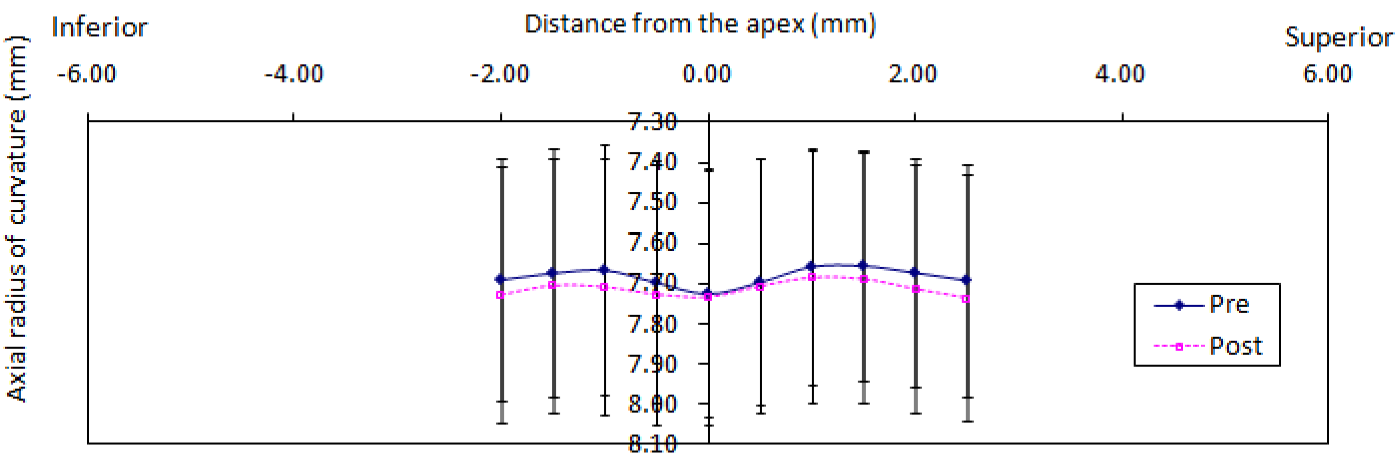

Figure 7.5: Comparison of corneal topography measured using Orb pre- and post-ocular impression procedure in the vertical meridian (error bar indicate ±1SD).

Similarly (as seen in Table 7.2 and Fig 7.5) in the vertical meridian, small, but not statistically significant, increases in axial radii (overall flattening) occurred post impression procedure. For example, at the apex the axial radius increased (flattened) by only 0.003± 0.14mm [SD]. The mean difference for the complete data set horizontally was 0.013± 0.11mm [SD], which was not statistically significance (0.209<p<0.809).

7.2.7 Discussion

This study examined the effect that ocular impression taking had on the ACS, 10 minutes after the procedure. The factors that affected the quality of scans were related to:

7.2.7.1 Instrument design

The Orbscan combines the advantages of placido-based curvature topography (Smolek and Klyce, 1997) and slit-scanning elevation triangulation (Snook, 1995). However, placido disc technology fundamentally suffers from image degradation when the surface measured deviates from spherical or aspheric curvature. It has been shown possible to create large, repeatable errors in the region of 200µm (Cairns and McGhee, 2005). Given that these errors affect the fidelity of the surface representation, the additional 40 Tyndall images collected as the Scheimpflug slit-beam strikes the reference plane, provide additional triangulated data which is faithful to complex surfaces (Cairns et al., 2003). In essence, the placido disc system provides the curvature data and the slit-scanning system provides the missing elevation data, at a total of 8,000 points per surface (Douthwaite, 2006). However, the Orbscan IIz software has no exact method of determining the ACS measurements at the site of light entering and leaving via slit-illumination (Cairns et al., 2003) and instead relies on low-order polynomial interpolation between slit slices (Douthwaite, 2006).

7.2.7.2 Technique

Errors in improper focusing or misalignment during image capture were found to be the most significant from the clinical standpoint using video-keratoscopy techniques (Mandell, 1992). However, since the introduction of slit-scanning with a Scheimpflug projection system in combination with videokeratoscopy, this issue has not been revisited. The reason for this may be the significant complexities brought about by combining the two systems. For example, the short focal length camera, which is used to image the s-shaped corneal optic sections of the cornea that joins at the centre of the placido disc reflected image (Fig 7.6), is optimally focused at a plane 1.0mm behind the corneal surface (Cairns and McGhee, 2005).

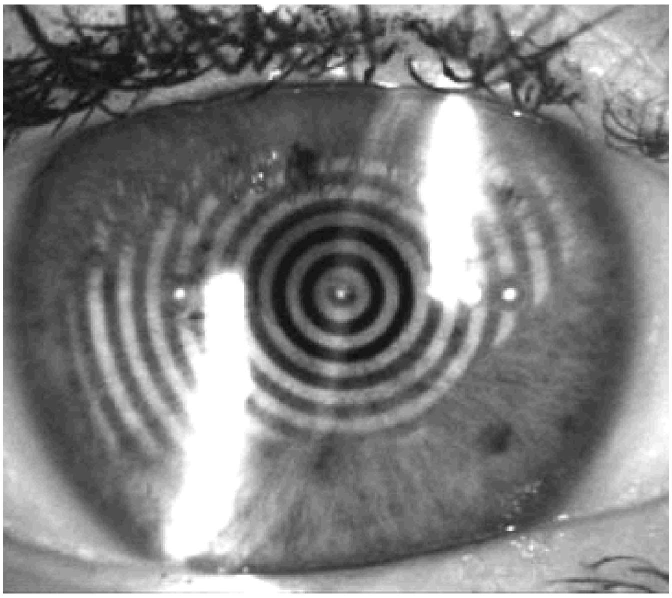

Figure 7.6: Correct alignment of the Orbscan IIz device with 2 half-slits converging at the centre of the placid disc image (Cairns and McGhee, 2005)

The image of the placido disc has been shown to be significantly posterior to this focusing plane (Applegate and Howland, 1995a), which leads to the question: how can both systems be focused adequately simultaneously, given that the relationship between the two planes of focus is dependent on the curvature of the corneal surface? This error may be partially responsible for the wide range of limits of agreement found when investigating Orbscan IIz intra-examiner repeatability for apical radius (+2.26 to -2.49D), and inter-examiner reproducibility (+3.72 to -3.39) (Cho et al., 2002). Given these limitations care was taken during this investigation to optimise the results by having a single experienced operator, who carried out all measurements.

7.2.7.3 Mechanical Effects

The results show that the action of applying polyvinylsiloxane to the ACS tear-film interface has a small, overall flattening effect, which increases with distance from the apex. This may be attributed to the pressure-release valve theory (Fig 7.7). The pressure exerted by the liquid silicone impression material applied to the ACS was reduced by the displacement of the material along the hollow stem of the impression tray, but the release holes in the tray cup were unable to function with equal efficiency since the lids offered opposing tension. This caused a movement of silicone towards the tray periphery, which combined with the pressure of the eyelids over the impression tray, caused an increasing compressive force over the measured ACS, and resulted in flattening curvature values.

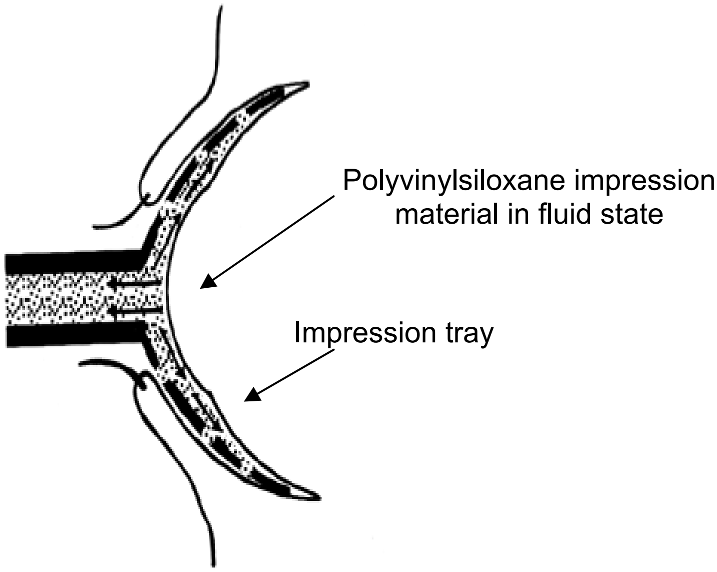

Figure 7.7: Position of the impression tray and fluid silicone impression material in contact with the AOS. Within the initial seconds of contact, the silicone near the apex is released via the hollow stem of the tray, while the silicone in the area adjacent to ACS is forced towards the eyelid fornices by the tension of the lid against the tray (adapted from (Pullum, 2007)).

7.2.7.4 Tear film stability

Rinsing the fornices with saline following the impression procedure, combined with the hydrophilic properties of the polyvinyl siloxane, may have caused disruption to the tear film structure, resulting in a loss of integrity and a reduction in thickness. Tear break-up time was assessed during this study and was found to be significantly reduced ($p<0.05$) by, on average, -6.65 ±3.25 seconds post-impression procedure. Further investigation would be necessary to determine the exact nature of the silicone-tear film interaction during ocular impression taking.

7.2.7.5 Repeatability

Excellent instrument repeatability was reported for anterior curvature for the Orbscan 0.0002±0.0007mm (SD) centrally on test surfaces (Cairns and McGhee, 2005). These measurements were taken across the central 3.5mm of inanimate test objects, and the values increased in the periphery (beyond 3.5mm) to 0.0007±0.0008mm (SD). Given that these values are significantly smaller than the axial radii of curvature differences recorded over the ACS, the observed differences are unlikely to be attributed to instrument variability.

7.2.7.6 Clinical implications

The Orbscan has been demonstrated to provide precise (Douthwaite and Parkinson, 2009) and highly accurate measurements of anterior surface elevation (Cairns et al., 2002). However, the fidelity of axial corneal topographic representation has been brought into question (Chapter 3). The method of representing corneal topography to date has been to use simplified, mathematical models based on experimental data. Assumptions have been made about the symmetry and rate of curvature change of the ACS, which have, no doubt, been reflected in the proprietary algorithms used in Orbscan IIz design. These factors render the Orbscan an exemplary machine with which to carry out comparative studies of the central 7mm of the human cornea.

7.2.8 Conclusion

There was no significant change to the topographic representation of the ACS recorded using Orbscan IIz technology in horizontal meridian, up to an annulus of 7mm or in the vertical meridian up to an annulus of 4mm, 10 minutes after the ocular impression procedure. The observed differences in radii of curvature found in this study fell within tolerances for contact lens fitting (0.05mm). Further investigation would be necessary to establish inter-examiner and intra-examiner variability.

7.3 <u>Study 2:</u> Comparison of the impression cast and the ocular surface *in-vivo* using AS-OCT Visante™

7.3.1 Introduction

Having examined the effects of the ocular impression taking procedure on the central cornea, the next step was to consider any effects on the peripheral topography and the corneo-limbal transition zone. The AS-OCT Visante™ (Carl Zeiss, Meditec Inc., Dublin, CA) utilises a 1310nm super luminescent LED laser source to provide anatomical location and anterior segment metrics. The scan dimensions are 16 x 6mm (transverse x axial), providing AOS surface profiles that span the entire cornea, corneo-limbal junction and a sector of the anterior sclera. The device has been used to scan inanimate objects, such as scleral contact lenses (Gemoules, 2008), teeth (Daniel et al., 2002) and bone surface (Pau et al., 2008). In this study, the device was used to examine the AOS *in-vivo* and compare it to the reflected light image of the positive cast made from an ocular impression of the same eye.

7.3.2 Aims and Objectives

This study aimed to determine the topographic effect of modern ocular impression taking on the shape of the AOS, by examining the eye surface *in-vivo* and comparing it to the cast made from an impression of the same.

The hypotheses proposed are:

- There is no significant difference between the curvature profiles sampled from AS-OCT Visante™ images in the principal meridians of the AOS *in-vivo* compared with that of its representative cast.
- AS-OCT Visante™ is a suitable instrument with which to image the AOS and representative cast surface for comparison purposes.

7.3.3 Subjects

Measurements from the right eyes only of 12 subjects were included in the study, (7 ♀ and 5 ♂), mean age of the group was 29.93±4.08 years [SD] (range 22.32 to 37.73). Ethical approval for the study was obtained from the Cardiff School of Optometry and Vision Sciences Human Ethics Committee. All subjects were treated in accordance with the Tenets of the Declaration of Helsinki, and each subject provided informed, written consent. Volunteers were recruited from the staff and students of Cardiff University, and subjects were excluded according to the same criteria used in Study 1.

The subject group (Table 7.3) was chosen to represent the range of corneal radii of curvature of the white European sample population (n=124), (obtained from the cohort sampled in Chapter 8), as measured using the 'traditional' Javal-Schiötz keratometer. The mean radius of curvature was found to be 7.75 ±0.28mm (Range 7.28-8.80)

Group	Mean Javal-Schiötz Keratometry (mm)	Number of individuals	Selection criterion
Steep	7.47	4	Mean + 1 Stdev
Average	7.75	4	Mean
Flat	8.03	4	Mean – 1 Stdev

Table 7.3: Selection criterion of individuals chosen for comparison of the impression cast with the ocular surface *in-vivo*.

7.3.4 Experimental Procedure

Repeated A-scans of the right eye were taken of the subject group using the AS-OCT VisanteTM (Carl Zeiss, Meditec Inc., Dublin, CA) (Fig 7.8).

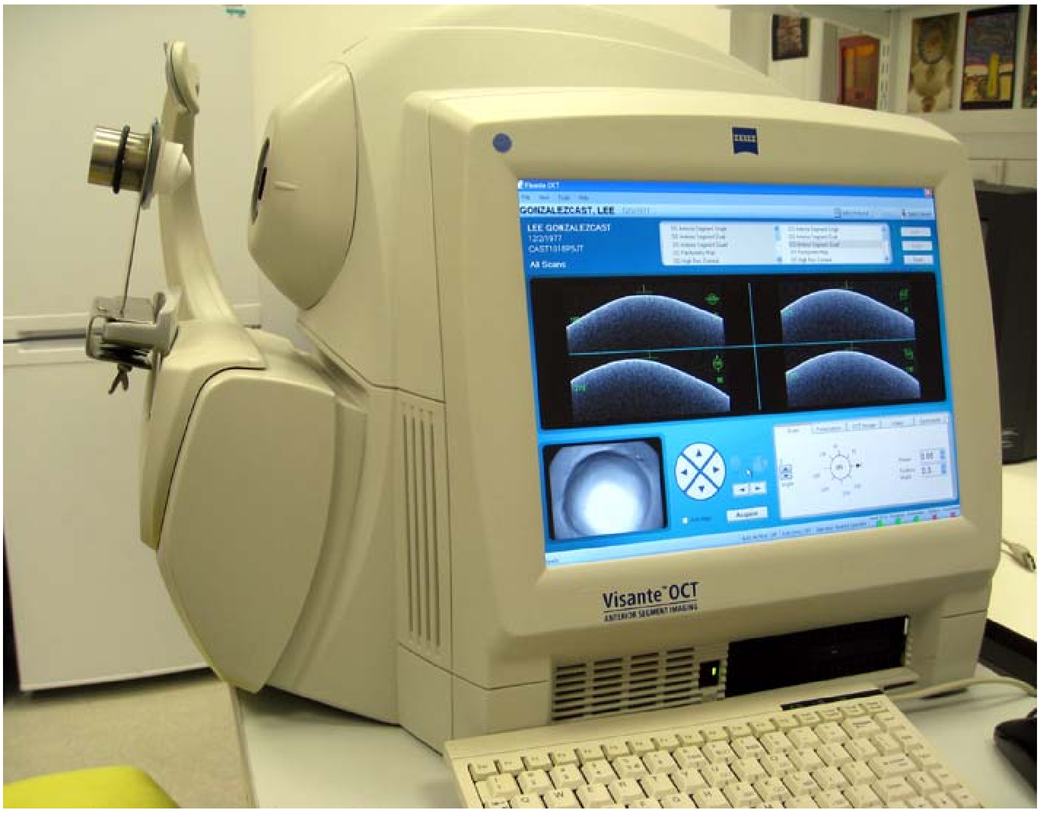

Figure 7 8: AS-OCT Visante™ (Carl Zeiss, Meditec Inc., Dublin, CA)

Three quad-scan sequences were collected of the eye *in-vivo*, followed by three quad-scan sequences of the impression cast. The cast was aligned with the instrument axis using an aluminium support bracket, which enabled the positioning and focusing systems of the machine to function in accordance with *in-vivo* scanning protocol (Fig 7.9). Cast centralisation was optimised visually.

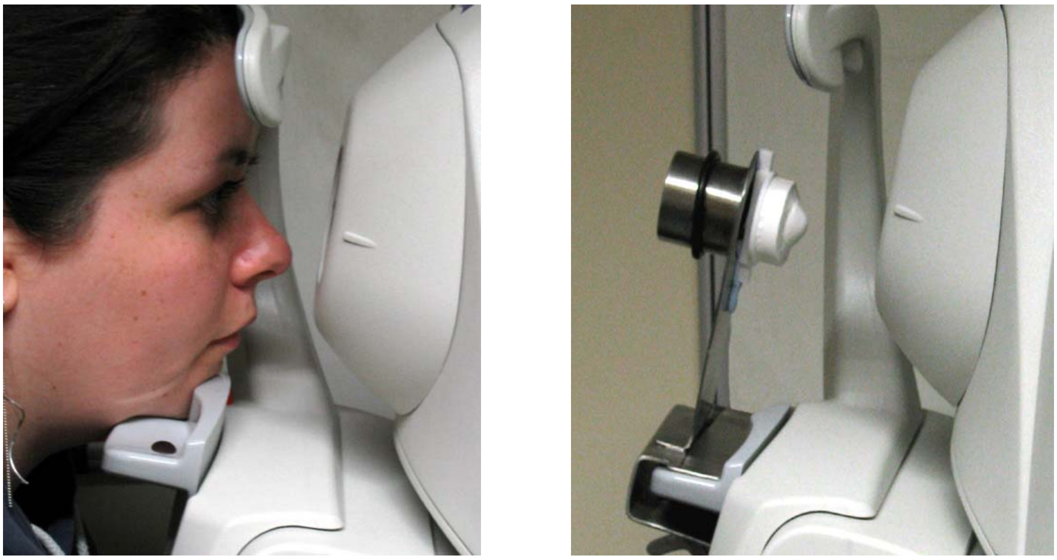

Figure 7.9: Position of the subject's right eye on the chin rest of the AS-OCT Visante™ (left), and the corresponding cast aligned for scanning using the aluminium support bracket (right).

Profiles from the horizontal and vertical meridians were extracted from the eye (Fig 7.10) and cast (Fig 7.11) quad-scan sequence, and the proprietary curvature correction software disabled (software version 1.0.12.1896).

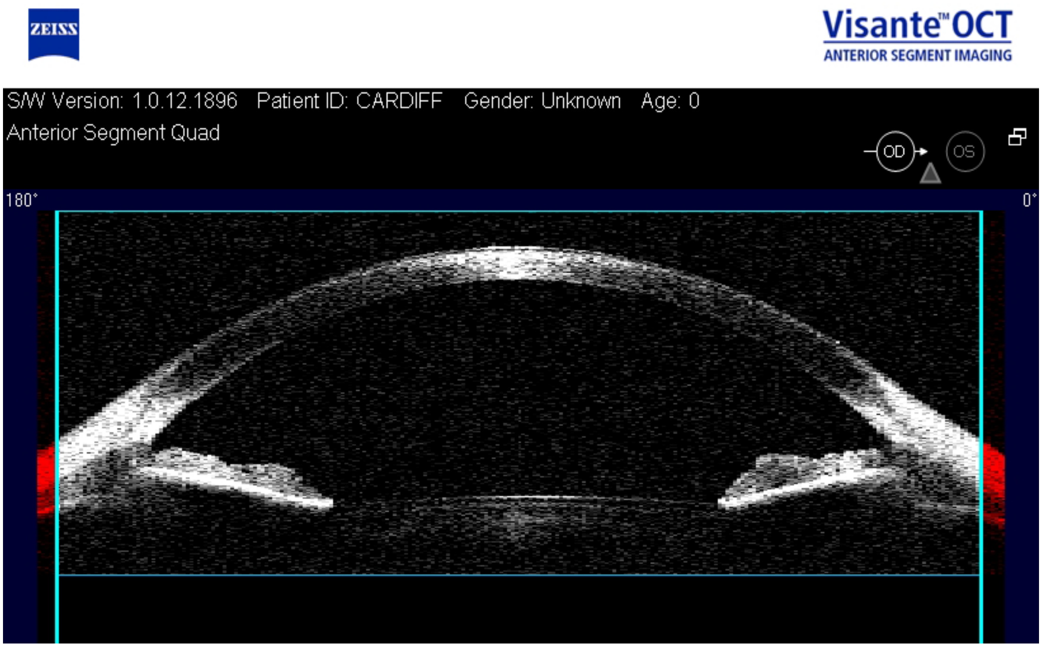

Figure 7.10: An example of an AS-OCT Visante™ image of an eye (1017PSJT) *in-vivo*, in the horizontal meridian.

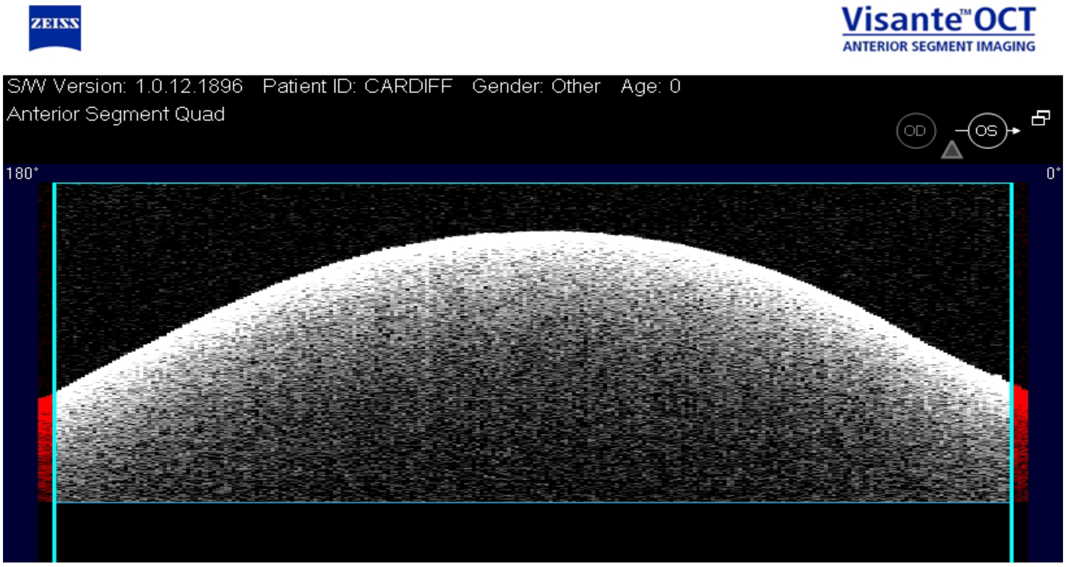

Figure 7.11: An example of an AS-OCT Visante™ image of a cast (1017PSJT) in the horizontal meridian

Eye and cast profiles were aligned using Adobe Photoshop v7 (Adobe Systems Inc., San Jose, CA). Merged profiles were sampled using a Liberty BASIC 4.0 (Shoptalk Systems, Framingham, MA) program developed to measure co-ordinates of the cornea to sub-pixel precision (Dunne et al., 2007). A screen overlay grid was used to sample surface co-ordinates (x,y) in units of 0.43mm (Fig 7.12)

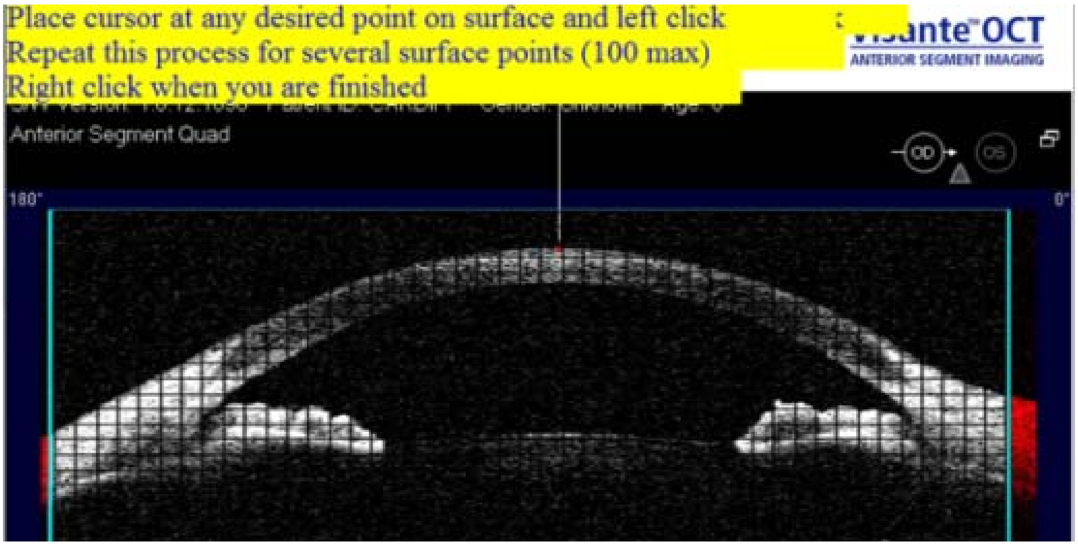

Figure 7.12: Screen shot to show the grid overlay used in conjunction with the custom-designed Liberty BASIC 4.0 curvature sampling program (Dunne et al., 2007).

7.3.5 Analysis

Comparative profiles were graphed using Excel 2007 (Microsoft®, Redmond, WA) and assigned 4th order polynomial functions as surface descriptors. These were used to calculate the area under each curve using GraphFunc (on-line java applet available at: www.seriesmathstudy.com). Areas under the curves were compared at a depth of 2mm from the highest point of elevation horizontally and 1mm vertically, to ensure that each profile could be compared in a controlled fashion. The smaller vertical areas (1mm depth) reflect the limited access to the surface curvature afforded by the eyelid position. Paired sample t-tests were carried out to examine the variability.

7.3.6 Results

7.3.6.1 Horizontal meridian

Cross-sectional profiles of mean eye and cast imaged using AS-OCT were represented in the horizontal meridian, both shown with error bars of ±1SD (Fig 7.13). The relative height differences (elevation) between the mean eye and cast surfaces are shown in the figure below.

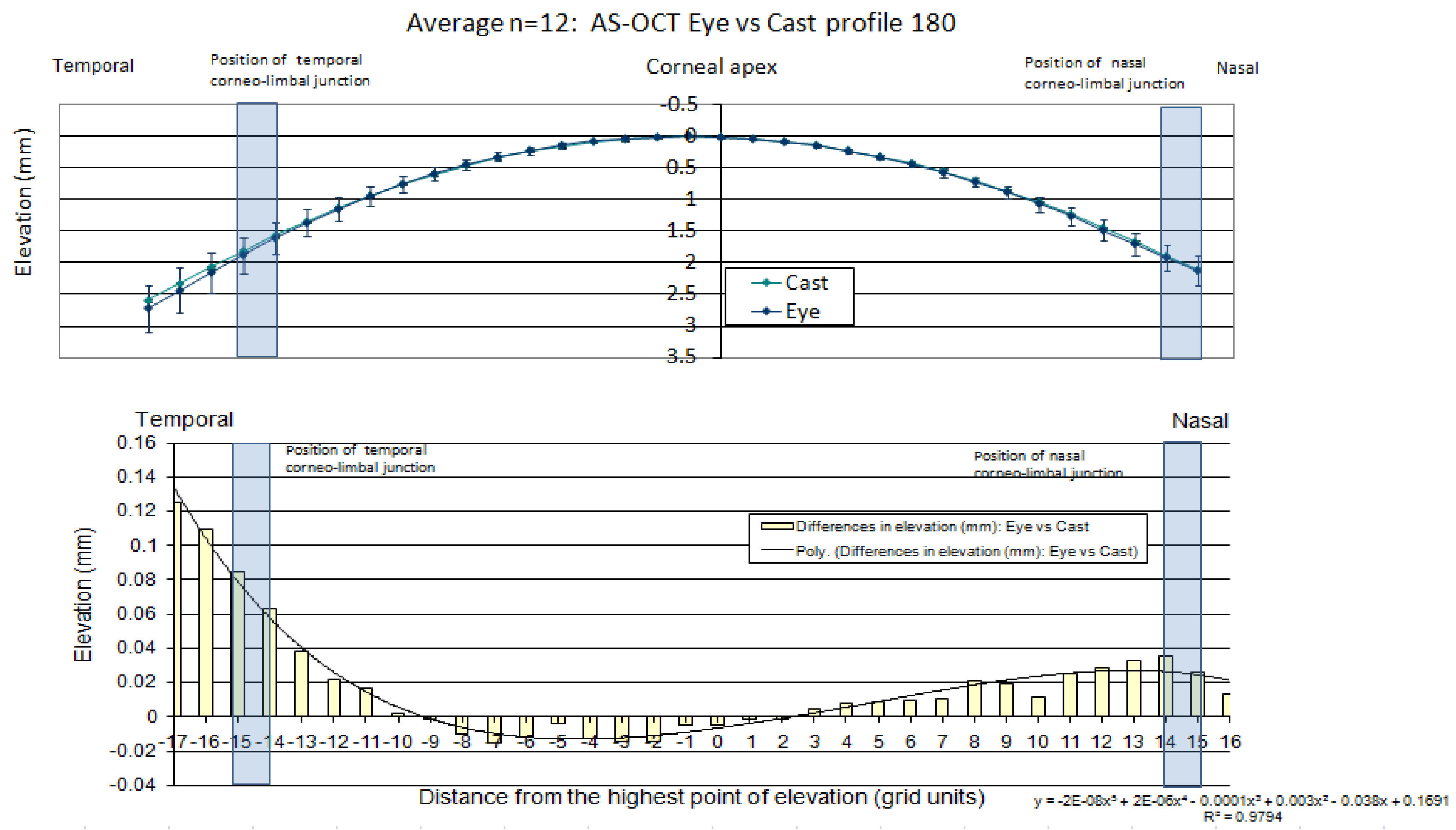

Figure 7.13: Horizontal 2-D profile comparison plots using AS-OCT Visante™ imaging to show the average eye *in-vivo* and its representative cast (top), with relative elevation differences between eye and cast shown below. Graphs have been scaled to match on the horizontal axis.

The mean difference in elevation found when comparing the average AOS *in-vivo* with its representative cast in the horizontal meridian was +0.018mm ±0.03 [SD] (range 0.125 to -0.015). The polynomial function shown in Fig 7.13 can be broken down into 3 distinct areas of interest:

- Temporal peripheral cornea to anterior sclera: region 3.87 to 7.31mm temporal to the designated apex. The cast became increasingly flatter than the eye contour moving from the nasal to temporal aspect. 0.001 – 0.125mm differences in elevation were found between the eye and cast, and the rate of change was optimally described by the 2nd order polynomial function:

$$y = 0.0013x^2 - 0.0301x + 0.1595, R^2 = 0.9925.$$

- Apex to central temporal cornea: region 0.86 nasal to 3.87mm temporal to the designated apex. The cast curvature was seen to dip, with the lowest point of inflection at 1.72mm from the apex. The differences in elevation were -0.001 to -0.015mm, and the curvature inflection trend was optimally described using the 4th order polynomial function:

$$y = -0.00001x^4 + 0.0003x^3 - 0.0021x^2 + 0.0042x - 0.0142, R^2 = 0.8429$$

- Central nasal cornea to nasal anterior sclera: region 0.86mm to 6.88mm nasal to the designated apex. The cast became increasingly flatter than the eye contour from temporal to nasal aspect, with a slower rate of change than measured on the temporal side. The differences in elevation were between 0.004 to 0.035mm, and the rate of change was optimally described using the 4th order polynomial function:

$$y = -0.000001x^4 + 0.00003x^3 - 0.0002x^2 + 0.0025x + 0.0028, R^2 = 0.9449$$

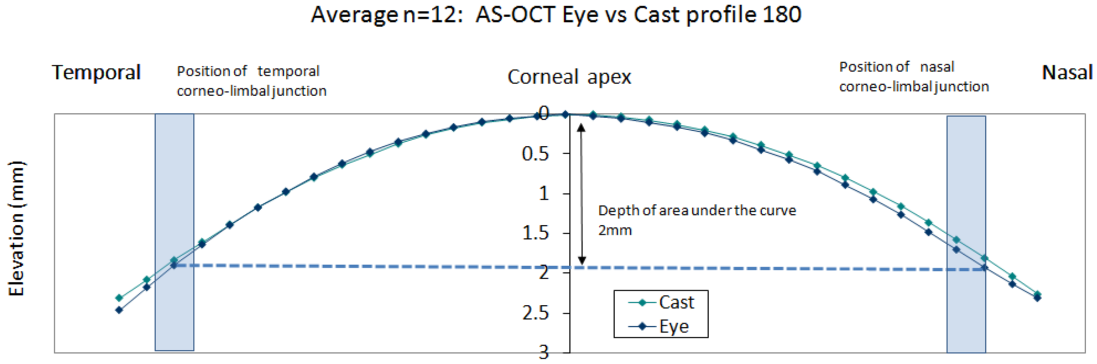

ID Number	AREA under the curve mm²	
	EYE180	CAST180
1009	32.98	33.49
1010	32.51	32.38
1017	32.49	33.17
1018	33.61	33.60
1019	33.73	33.74
1020	30.95	31.76
1021	30.48	30.58
1029	31.35	31.81
1035	32.02	31.94
1040	32.08	32.09
1052	30.41	30.52
1071	30.27	31.02
Average	31.25	31.47

Mean (SD) value for EYE180 31.86 ± 1.18
Mean (SD) value for CAST180 32.12 ± 1.11

Paired sample t-test **t(12)=-1.60 p= 0.138**

Figure 7.14: Comparison of the areas under the curve for the eye *in-vivo* and representative cast at 2mm below the corneal apex (highest point of elevation), measured from sampled horizontal AS-OCT Visante™ images for each subject.

The mean area under the curve in the horizontal meridian, measured 2mm from the designated corneal apex of the cast image group, was found to be marginally larger than the corresponding eye image group; difference 0.26mm ±0.33mm^2 [SD] (range -0.13 to 0.81mm^2). However, this difference between groups was not statistically significant (p=0.138).

7.3.6.2 Vertical meridian

Cross-sectional profiles of mean eye and cast imaged using AS-OCT were represented in the vertical meridian, both shown with error bars of ±1SD (Fig 7.15). The relative height differences (elevation) between the eye and cast surface are shown in the figure overleaf.

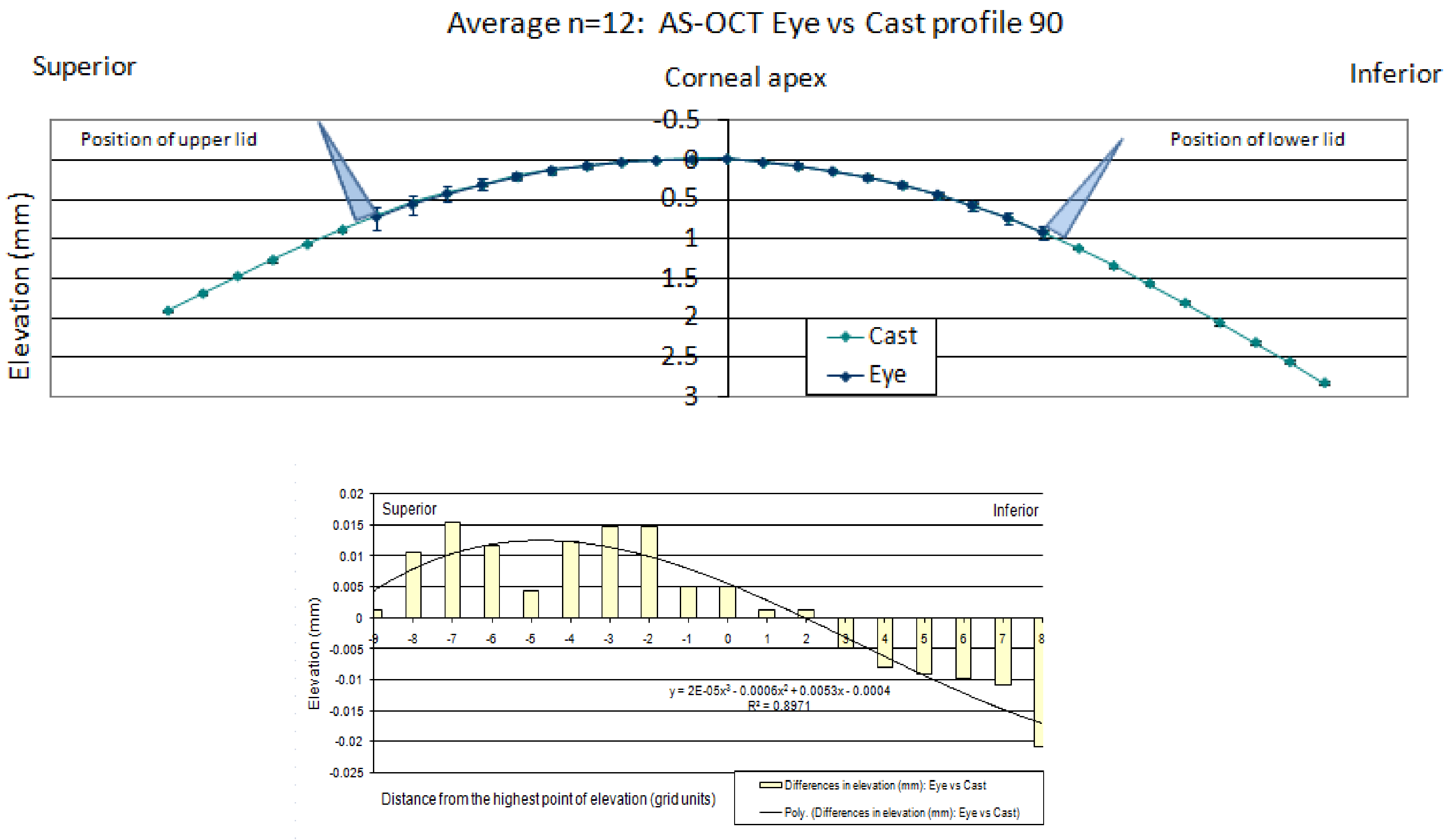

Figure 7.15: Vertical 2-D profile comparison plots using AS-OCT Visante™ imaging to show the average eye *in-vivo* and its representative cast (top), with relative elevation differences between eye and cast shown below, graphs have been scaled to match on the horizontal axis.

The mean difference in elevation found when comparing the average AOS *in-vivo* with its representative cast in the vertical meridian was +0.005 ±0.01mm [SD] (range 0.028 to -0.002). The data trend was best represented by a reverse-sigmoid curve with its inflection 0.86mm inferior to the designated corneal apex:

$$y = 0.00002x^3 - 0.0006x^2 + 0.0053x - 0.0004, R^2 = 0.8971$$

Superior to the inflection, the average cast becomes increasingly flatter than the eye contour. Differences of 0.001 to 0.015mm in elevation were found between the average eye and cast contours, and on the inferior aspect the differences were -0.004 to -0.020mm, with the cast contour becoming increasingly steeper than the average eye. These elevation differences are smaller than those found in the horizontal meridian by a 10-fold order of magnitude.

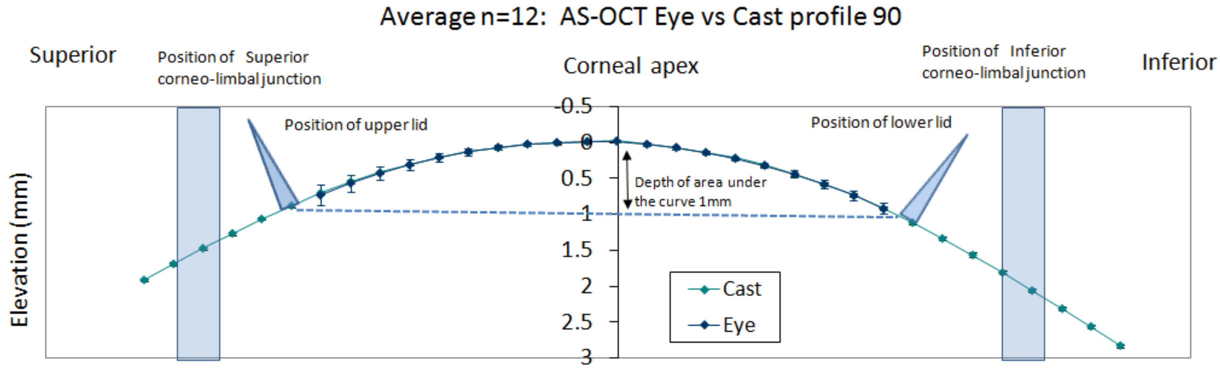

ID Number	AREA under the curve mm²	
	EYE90	CAST90
1009	6.28	6.17
1010	6.10	5.99
1017	6.36	6.31
1018	6.51	6.49
1019	6.72	7.10
1020	6.29	6.30
1021	6.80	6.58
1029	7.16	6.96
1035	6.03	6.16
1040	6.25	6.48
1052	6.43	6.53
1071	6.11	6.03
Average	6.39	6.40

Mean (SD) value for EYE 90   6.42 ± 0.32
Mean (SD) value for CAST 90   6.42 ± 0.33

Paired sample t-test   **t(12)=-0.114 p= 0.911**

Figure 7.16: Comparison of the areas under the curve for the eye *in-vivo* and representative cast at 1mm below the corneal apex (highest point of elevation), measured from sampled vertical AS-OCT Visante™ images for each subject.

The mean area under the curve in the vertical meridian, measured 1mm from the designated corneal apex of the cast image group, was found to be almost identical to the corresponding eye image group; difference 0.00 ±0.010mm^2 [SD] (range -0.11 to 0.01mm^2). The variability between groups was not statistically significant (p=0.911).

7.3.7 Discussion

To our knowledge, this study is the first attempt to compare a group of eyes imaged *in-vivo* with their representative casts, using AS-OCT Visante™ technology. The results show surprisingly little deformation of the AOS measured, this is a positive result and indicates that the impression/scanning method is reliable and able to produce a true representation of the anterior ocular surface. However, the methodology used in this study is limited by a number of complex control parameters, including a lack of anatomical registration and identical instrument alignment.

7.3.7.1 Errors of alignment

When imaging the AOS *in-vivo*, the scan should be centred on the corneal vertex reflex, which is seen on the AS-OCT instrument screen as a bright vertical flare line traversing the corneal profile (Fig 7.17). It has been suggested that it could be used as a reference for optical measurements (Huang and Izatt, 2008).

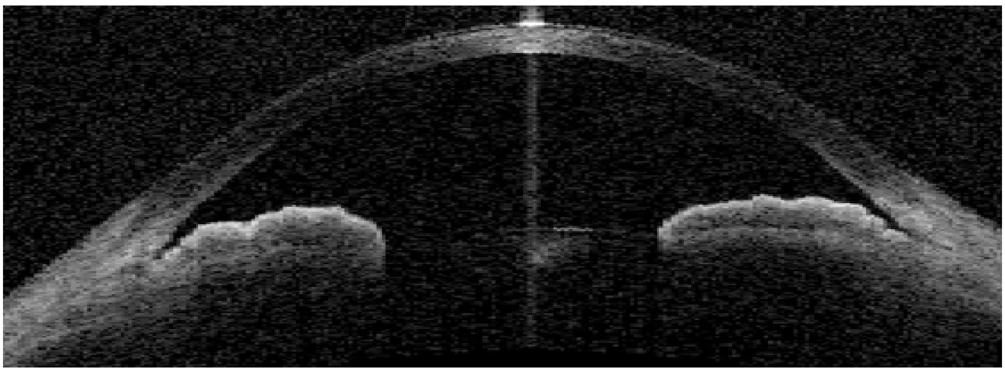

Figure 7.17: AS-OCT Visante™ corneal profile image illustrating the corneal vertex reflex.

However, the lack of transparency apparent in the gypsum plaster of the cast (Fig 7.14) meant that this vertical flare was not replicated, and this limited the comparison of the images to geometric visualisation. Furthermore, the lack of anatomical landmarks on the cast surface and the surface reflectivity may have facilitated further inaccuracies in the alignment process prior to quad-scan capture.

7.3.7.2 Repeatability of AS-OCT Visante™

Instrument repeatability for a small group (n=32) for the AOS was found to be poor 0.158mm (Huang et al., 2008) in comparison to other commercial topographic systems. The manufacturer states transverse accuracy is 0.217mm, it may be speculated that this is most likely to be the affect of a slow scan speed. Even at 2000 axial-scans per second, eye movement during the scans produces a noticeable error in the surface topography and subsequent corneal power measurements (Huang et al., 2008). Random motion artefacts may have been a contributing factor in the differences seen between the moving eye *in-vivo* and the stationary cast.

7.3.7.3 Averaging images

There was no available averaging facility for individual corneal profiles from the AS-OCT Visante™ quad-scan sequence. Three repeated scans were carried out for each subject; both eye and cast. The images which appeared to be the best resolution from each sequence where chosen for comparison purposes.

7.3.7.4 Clinical implications

The elevation comparisons taken during this study show that the cast profile increasingly flattened in the horizontal meridian from the nasal to temporal aspect across the peripheral cornea, traversing the limbus and on to the anterior sclera (Fig 7.18).

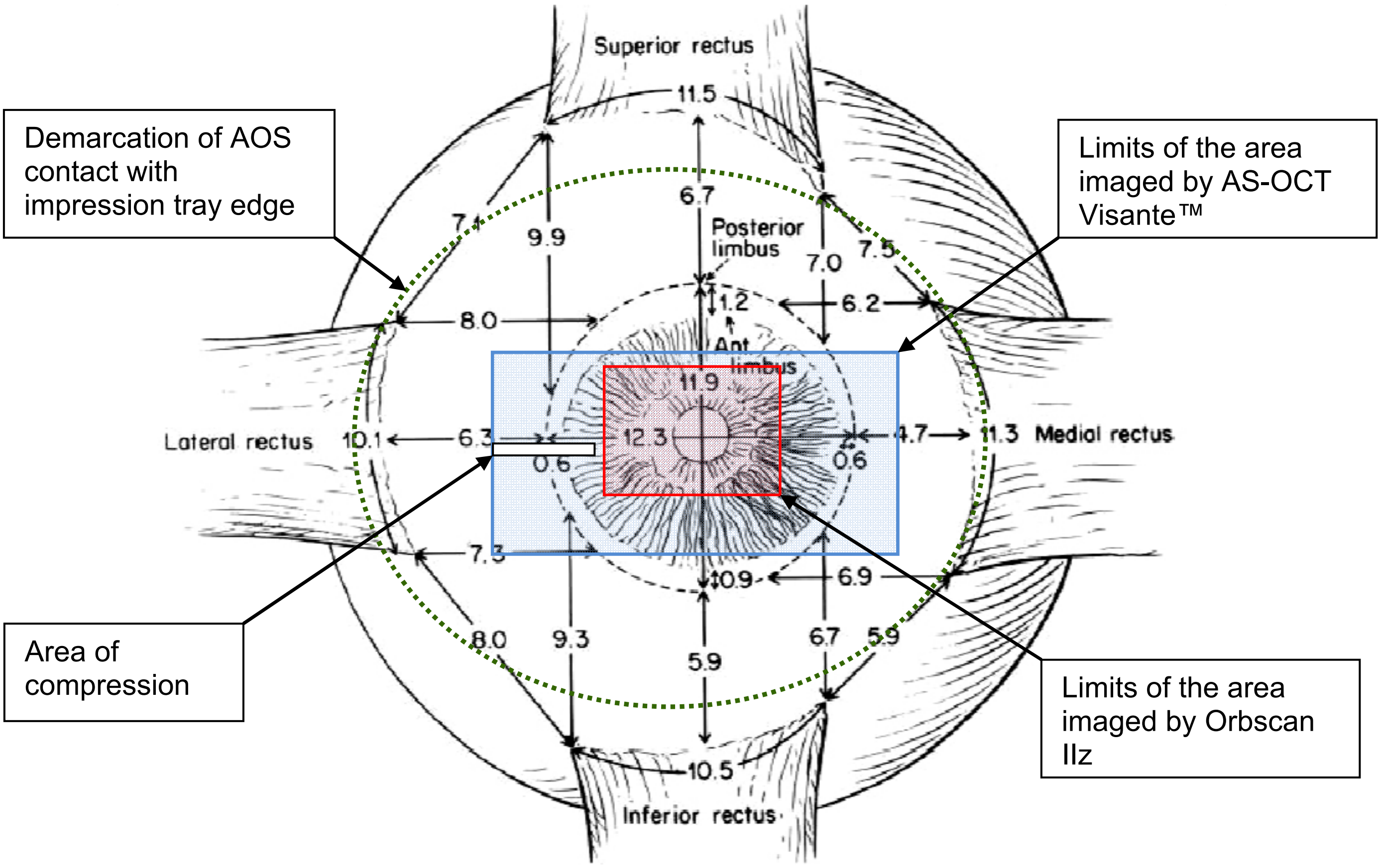

Figure 7.18: Diagram to show the features of the AOS and the areas imaged using AS-OCT Visante™ and Orbscan IIz (adapted from (Apt, 1980)). The green dotted line marks the position of the edge of the impression tray during impression taking, and the small white box, the area of possible compression.

This presents two questions: why does compression occur in this region only and does it have any clinical significance? Supporting evidence from scleral thickness studies shows that the sclera is thinnest temporally 4mm from the limbus, measuring in the region of 450µm thick (Norman et al.). When this is combined with the 6.3mm distance from the limbus to the lateral rectus insertion (Apt, 1980), the reduced physiological strength of the lateral rectus compared to the opposing medial rectus may render this region vulnerable to compression (Meredith and Goldberg, 1986). Thus the flattening of the cast surface may have been caused by:

- Localised pressure from the impression tray edge on the lateral rectus insertion causing the muscle to relax and release tension on the AOS (Vawda, Ranatunga and Geeves, 1995).
- Asymmetric impression tray design caused an uneven spread of silicone impression material, and the increased bulk of material was inclined to flatten the area where it collected.

The acceptable magnitude of error implicit in the cast production process is determined by its application. For example, the manufacturing of rigid gas permeable contact lenses requires high accuracy, in the region of ±0.05mm commensurate with the manufacturing tolerances of British Standards 18369-2 (BSI, 2006). However, this presents a problem, since, so far, the differences between AOS and cast have been described in terms of vertical height differences, but for application in contact lens manufacture however, radii of curvature are more appropriate. The tangential radius of curvature, sometimes referred to as local or instantaneous radius of curvature, is the curvature at each point on the surface with respect to neighbouring points (Corbett et al., 1999a). Methods of measurement are described in BS 19980 (BSI, 2005a). Tangential radii of curvature were therefore calculated for the average eye and cast surfaces for the group, and compared graphically in a similar fashion as described for the elevation comparison (Fig 7.19).

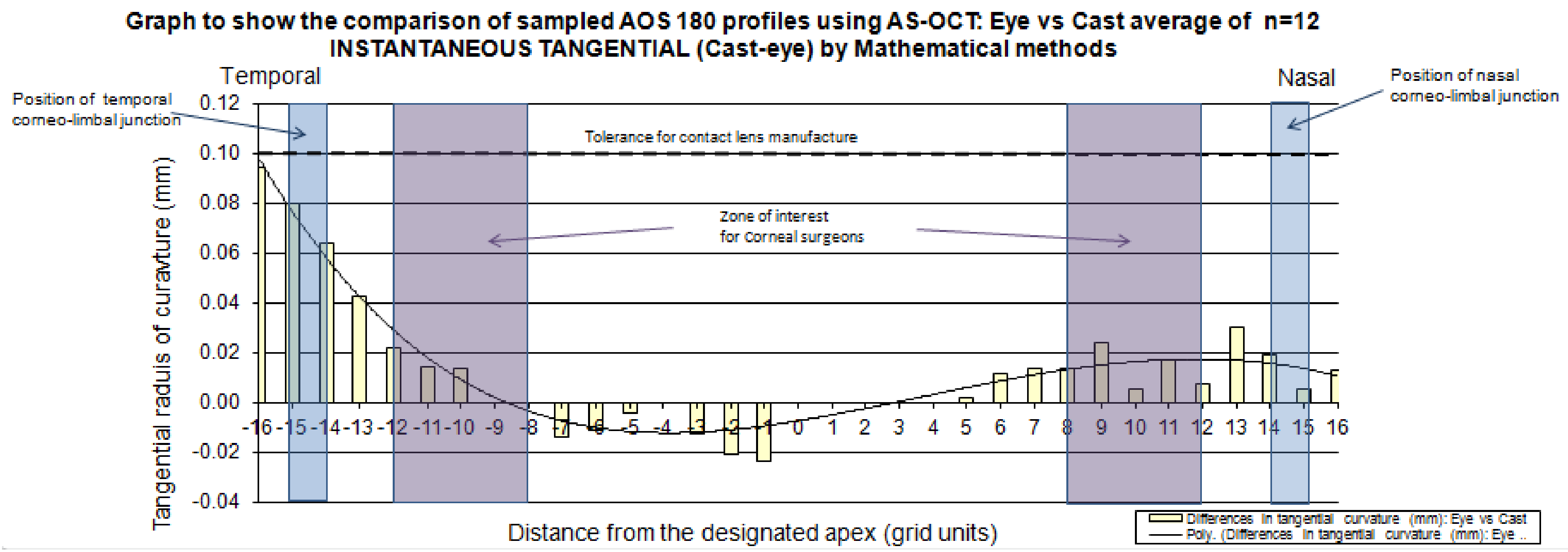

Figure 7.19: Comparison of tangential curvature values determined from AS-OCT Visante™ images of the average (n=12) AOS *in-vivo* and representative cast.

Focusing again on the peripheral cornea to anterior sclera (temporal aspect), all of the instantaneous radii measurements here were found to be within 100µm; that is ± 0.05mm (range 13.46 to 94.08µm), suggesting that the impression/scanning method would therefore be considered within clinically significant limits for rigid gas permeable contact lens manufacture.

7.3.8 Summary of results

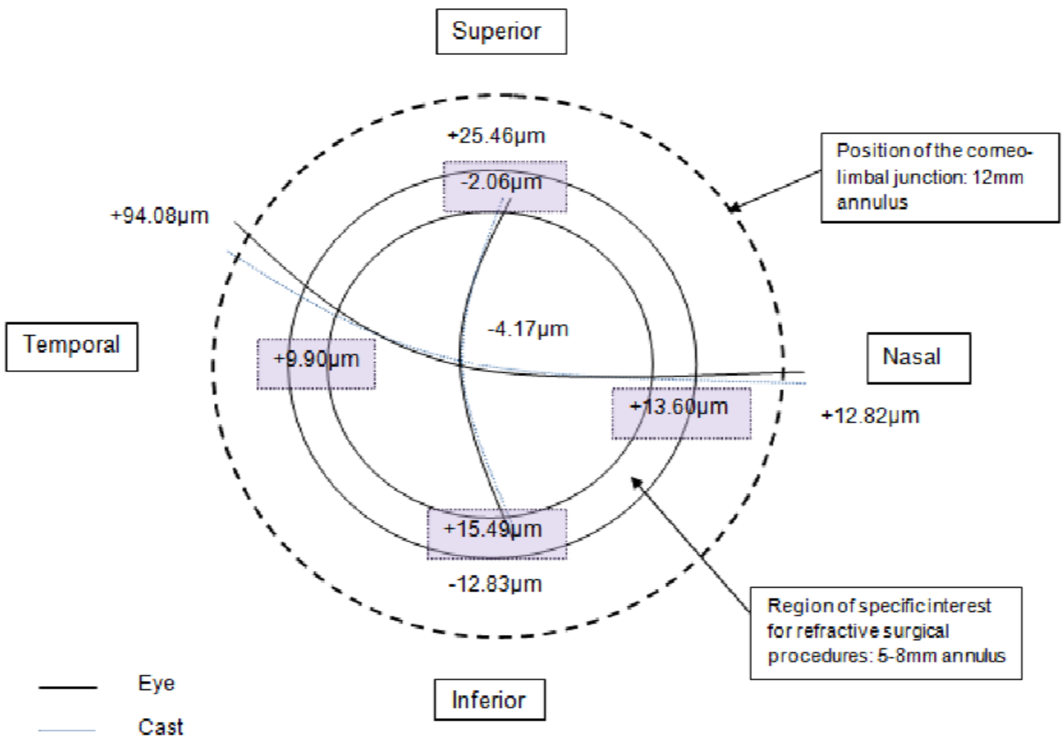

Figure 7.20: Diagram to show the instantaneous curvature differences (mm) between the ocular surface *in-vivo* and a representative cast (n=12) using AS-OCT Visante™ to image the surfaces. The position of the corneo-limbal junction is indicated, in addition regions of specific interest to refractive surgeons (5-8mm annulus).

The summary diagram highlights the suitability of the ocular impression/casting procedure for refractive surgical planning and as a model surface for designing contact lenses.

7.3.9 Conclusion

- There were minimal differences between the curvature profiles sampled from the AS-OCT Visante™ images in the principal meridians of the average AOS *in-vivo* compared with that of its representative cast.
- The region from the peripheral cornea to the anterior sclera in the horizontal meridian was flattened during ocular impression taking, but this was found to be within clinically significant limits and tolerance for rigid gas permeable contact lens manufacture. Further work is necessary to establish regional 3-dimensional topographic variation in representative cast contours, which may offer greater understanding of the interaction between AOS and the modernised ocular impression procedure.
- The AS-OCT Visante™ was found to be a suitable instrument with which to image the AOS and representative cast surface for comparison purposes, within the 16mm x 6mm (transverse x axial) scan limits.

7.4 Study 3: Comparison of the impression cast using laser triangulation and AS-OCT Visante™ imaging

7.4.1 Introduction

In the previous study in this series, the accuracy of the topographic representation of the cast surface using AS-OCT Visante™ imaging was brought into question. Motion artefacts caused by insufficient scan speed and proprietary 'de-warping' algorithms based on Fermat's principle (Huang et al., 2008) are likely contributing factors. If the suspected distortion of the cast surface contour caused by AS-OCT Visante™ imaging affected the output in an uneven distribution, this may partially explain the differences in elevation and tangential curvature seen in Study 2. The fidelity of the cast surface representation provided by the AS-OCT Visante™ requires further investigation. Chapter 6 outlined the Cardiff Eyeshape Protocol, which was designed to provide a wide-field morphometric data sampling system using a non-contact active laser triangulation system HYSCAN 45c (Hymarc Ltd, Ontario, Canada) capable of scanning more than 200,000 point per cast surface to a accuracy of 0.060 ±0.025mm [SD] unpublished (Le Chi, 2008). The casts used in Study 2 were sampled using the scanning system and the anterior surfaces compared to the AS-OCT Visante™ images.

7.4.2 Aims and objectives

This study aimed to establish the fidelity of AOS representation by AS-OCT Visante™ imaging by comparing the 2-D digital output to images sampled from scanning the cast using non-contact laser triangulation. The cast surface representation provided by the laser triangulation was used as the reference surface.

The hypotheses proposed are:

- Images of the cast moulded from modern ocular impression taking, and captured using AS-OCT Visante™ technology, are not a true representation of the surface profile.

- The differences found between digital images acquired of the cast surface using AS-OCT Visante™ and Hyscan 45c Laser triangulation are not clinically significant.
- The differences found between digital images acquired of the cast surface using AS-OCT Visante™ and Hyscan 45c Laser triangulation are not consistent across the surface profile or orientation.

7.4.3 Subjects

The same subjects were used for this investigation as described in Study 2.

7.4.4 Experimental procedure

The AS-OCT Visante™ scans of the 12 casts were retrieved from the quad-scan sequences imaged using the procedure described in Study 2. The casts were imaged using the Hyscan 45c scanning protocol outlined in Chapter 6.

7.4.5 Sampling

The AS-OCT Visante™ images of the cast were extracted from the quad scan sequences using proprietary software. Horizontal and vertical profiles were annotated using digital callipers provided (software version 1.0.12.1896) and converted to bitmap image format (Fig 7.21).

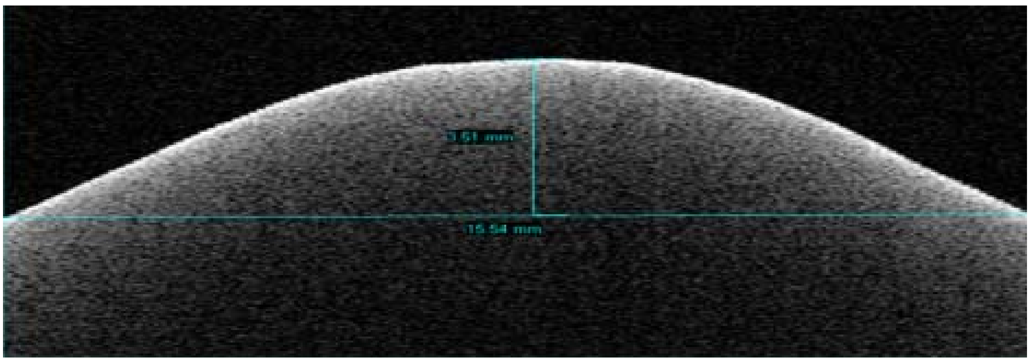

<u>Figure 7.21:</u> A processed AS-OCT Visante™ image of the cast in horizontal profile showing dimensions provided by proprietary digital callipers.

2-dimensional profiles, captured using laser triangulation, were extracted from the 3-dimensional surface plots using a purpose-designed OPTOMRC Visual Basic 6.0 (Microsoft®, Redmond, WA) program imbedded in AutoCAD 2010 (Autodesk®, St Rafael, CA). 2-dimensional drawing outputs were annotated with linear dimension bars (Fig 7.22).

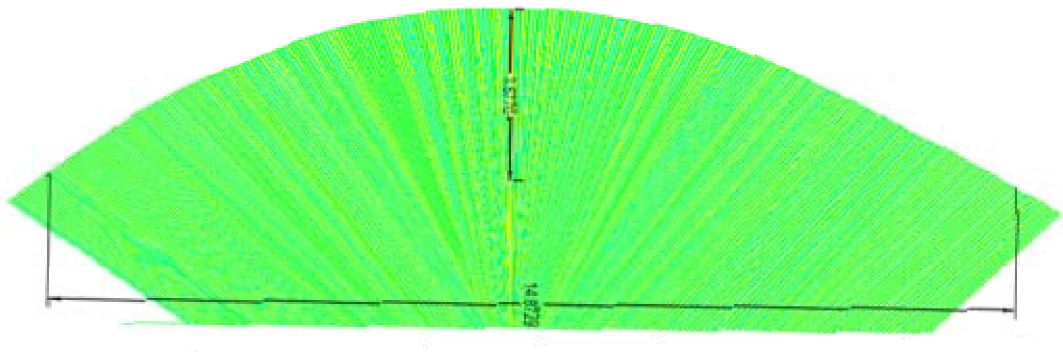

Figure 7.22: A processed Hyscan 45c image of the cast in horizontal profile showing dimensions annotated using AutoCAD linear dimension bars.

7.4.6 Analysis

The images from each system were scaled to match and visually aligned using Adobe Photoshop v7 (Adobe Systems Inc., San Jose, CA). Profiles were graphed and analysed using the techniques described in Study 2.

7.4.7 Results

7.4.7.1 Horizontal meridian

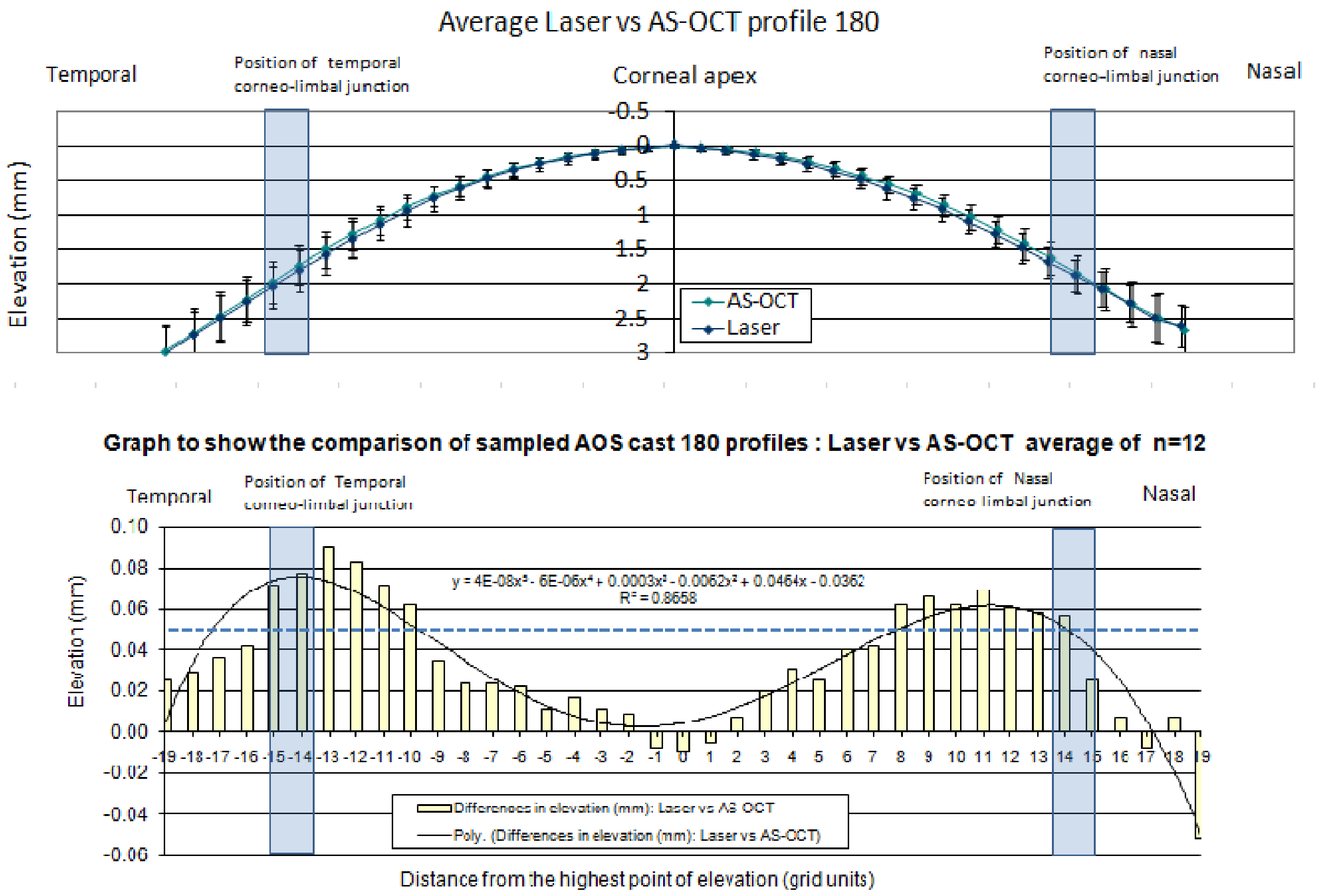

Figure 7.23: Horizontal 2-dimensional profile comparison plots of the representative cast of the average AOS using AS-OCT Visante™ imaging and Hyscan 45c laser scanning technology, with relative elevation differences between aligned digital profiles shown below. The graphs have been scaled to match on the horizontal axis.

The mean difference in elevation found when comparing the average AOS representative cast scanned by AS-OCT Visante™ and Hyscan 45c laser technology in the horizontal meridian was +0.033 ±0.03mm [SD] (range 0.090 to -0.052) with the laser representation as the reference (Fig 7.23). The data trend was best represented by a double hump curve with its central dip 0.86mm temporal to the designated corneal apex:

$$y = 0.00000004x^5 - 0.000006x^4 + 0.0003x^3 - 0.0062x^2 + 0.0464x - 0.0362,$$

$$R^2 = 0.8658$$

On the temporal aspect the AS-OCT representation becomes increasing flatter reaching a maximum of 0.090mm at 5.90mm from the apex, (range of values from 0.090 to -0.007). This is reflected in a similar fashion on the nasal aspect reaching a maximum of 0.070mm flatter than the Hyscan 45c radii measurements at 4.73mm from the apex. The AS-OCT image was steeper by -0.052mm at the furthest nasal sample location.

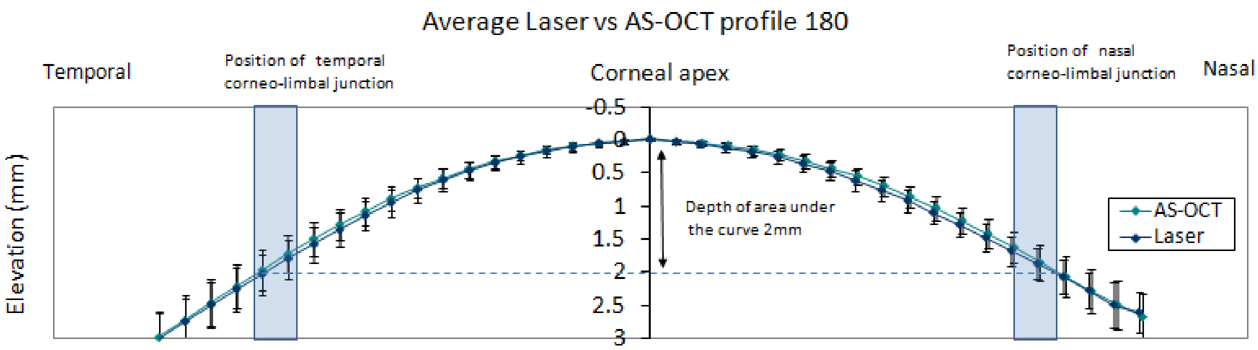

ID Number	AREA under the curve mm^2	
	AS-OCT180	LASER180
1009	18.07	17.89
1010	17.64	17.30
1017	18.16	17.19
1018	18.41	17.33
1019	18.32	18.96
1020	18.19	19.34
1021	16.76	16.30
1029	17.24	16.64
1035	17.22	16.56
1040	17.73	16.94
1052	16.65	15.86
1071	17.06	16.39
Average	17.52	17.02

Mean (SD) value for AS-OCT180 17.62 ± 0.62
Mean (SD) value for LASER180 17.23 ± 1.05

Paired sample t-test **t(12)=2.07 p= 0.062**

Figure 7.24: The areas under the curve at 2mm below the corneal apex (highest point of elevation) were measured from sampled horizontal AS-OCT Visante™ and Hyscan 45c laser scanned images for each subject; comparing cast surface representation between the 2 techniques.

The mean area under the curve in the horizontal meridian (Fig 7.24), measured 2mm from the designated corneal apex of the AS-OCT image group, was found to be slightly larger than the corresponding Hyscan 45c image group; 0.390 ±0.84mm [SD] (range -1.15 to 1.08mm). The variability between groups was not statistically significant ($p=0.062$).

7.4.7.2 Vertical meridian

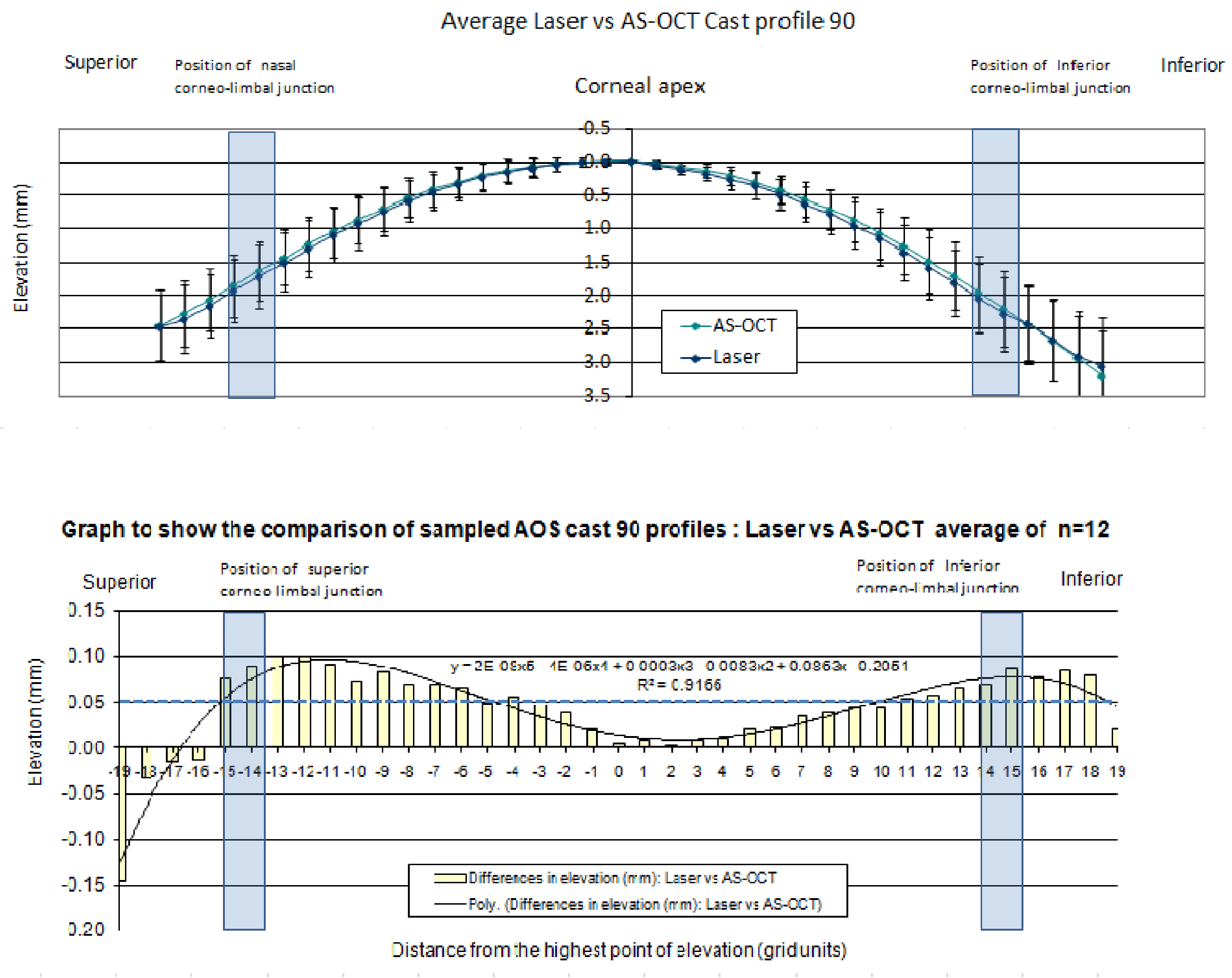

Figure 7.25: Vertical 2-dimensional profile comparison plots of the representative cast of the average AOS using AS-OCT Visante™ imaging and Hyscan 45c laser scanning technology, with relative elevation differences between aligned digital profiles shown below. Graphs have been scaled to match on the horizontal axis.

The mean difference in elevation found when comparing the average AOS representative cast scanned by AS-OCT Visante™ and Hyscan 45c laser technology in the vertical meridian was +0.045 ±0.05mm [SD] (range 0.101 to -0.144) with the laser representation as the reference (Fig 7.25). The data trend was best represented by a double hump curve (as with the horizontal data) with its central dip 0.86mm inferior to the designated corneal apex:

$$y = 0.00000002x^5 – 0.000004x^4 + 0.0003x^3 - 0.0083x^2 + 0.0863x - 0.2051,$$

$$R^2 = 0.9166$$

On the superior aspect the AS-OCT representation becomes increasing flatter reaching a maximum of 0.101mm at 5.59mm from the apex, (range of values from 0.100 to -0.144). This is reflected in a similar fashion on the inferior aspect reaching a maximum of 0.086mm flatter than the Hyscan 45c radii measurements at 6.45mm from the apex. The AS-OCT image was steeper by -0.144mm at the furthest superior sample location.

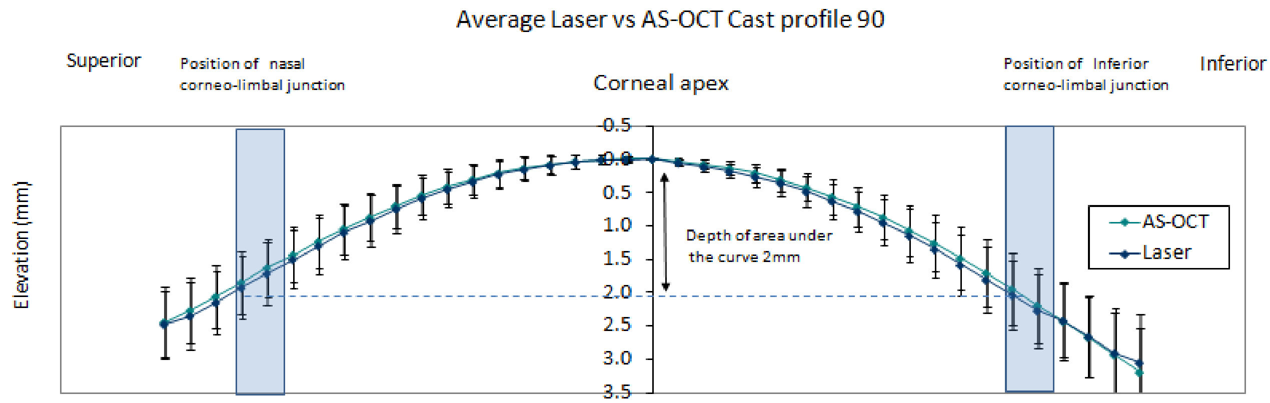

ID Number	AREA under the curve mm²	
	AS-OCT90	LASER90
1009	17.52	17.35
1010	16.92	17.25
1017	17.97	17.23
1018	18.56	17.76
1019	18.73	17.75
1020	17.64	17.01
1021	16.82	17.81
1029	18.89	18.55
1035	17.91	17.79
1040	17.69	17.98
1052	17.23	17.80
1071	16.86	16.49
Average	17.14	17.05

Mean (SD) value for AS-OCT90 17.68 ± 0.53
Mean (SD) value for LASER90 17.52 ± 1.05

Paired sample t-test **$t(12)=0.99$ $p= 0.343$**

Figure 7.26: Areas under the curve at 2mm below the corneal apex (highest point of elevation) were measured from sampled vertical AS-OCT Visante™ and Hyscan 45c laser scanned images for each subject; comparing cast surface representation between the 2 techniques.

The mean area under the curve in the vertical meridian, measured 2mm from the designated corneal apex of the AS-OCT image group (Fig 7.26), was found to be slightly larger than the corresponding Hyscan 45c image group; 0.160 ±0.76mm [SD] (range -0.99 to 0.98mm). The variability between groups was not statistically significant (p=0.343).

7.4.8 Discussion

During the course of this investigation the Hyscan 45c laser scanned image was presented as the gold standard representation of the ocular cast surface. These images were compared to those scanned using AS-OCT Visante™ technology to determine whether the changes in curvature observed in Study 2 were influenced by proprietary curvature correction factors. It has been demonstrated that there were clinically significant differences between the two methods in some areas (>0.050mm for contact lens fitting and >0.100mm tolerance for contact lens manufacture) found along both horizontal and vertical meridians. As in study 2, limitations of the investigation were:

7.4.8.1 Errors in alignment

The Hyscan 45c images were obtained initially in 3-dimensional format. The corneal apex was identified using the methods stipulated by BS EN ISO 19980 (BSI, 2005b). The AS-OCT Visante™ apex registration relied on lining up the cast apex with the machine instrument axis, due to lack of transparency of the gypsum plaster this relied on the operator visualising this alignment and further refinement of registration during image overlaying. The success of this process was influenced by the asymmetric nature of the 2-dimensional profile, however the exact influence of this parameter requires further investigation.

7.4.8.2 Repeatability of AS-OCT Visante™

This has been discussed in Study 2.

7.4.8.3 Repeatability of Hyscan 45c

Chapter 6 outlined a study that provided for a small group (n=12) of 22mm ball bearing casts (AOS surrogates) using the active laser triangulation system (±0.008 ±0.021mm [SD]).

7.4.8.4 Averaging images

Each cast was scanned once using the Hyscan 45c laser device, the profiles extracted were compared to the best quality AS-OCT image profile from a series of 3. There were no available systems for averaging for either technology. Further investigation would be required here to optimise accuracy of both scans.

7.4.8.5 Contact lens fitting with AS-OCT Visante™

AS-OCT Visante™ has been used as part of a novel scleral lens fitting system (Gemoules, 2008), the practitioner calculated fitting base curve values using AS-OCT images and concluded that they were, on average, -0.110mm steeper than the base-curve values measured using a radiuscope. This concurs with the findings of this study that the AS-OCT representation is flatter than the ‘true’ surface shape hence the scleral lens that will align best with the surface shape will be steeper than the calculated measurements from the AS-OCT images. Using AS-OCT sagittal and chord measurements from the AOS, combined with corneal topography from another instrument, the accuracy and efficiency of scleral contact lens fitting has been improved.

7.4.8.6 Correcting the curvature

A study assessing the accuracy of the AS-OCT Visante™ for corneal and lens biometry using a model eye, found that the AS-OCT overestimates anterior corneal surface radii within clinically acceptable limits over the central 6mm annulus (region) by +0.020mm (Dunne et al., 2007). However the authors observed that the x-coordinate error increased towards the periphery (Fig 7.27)

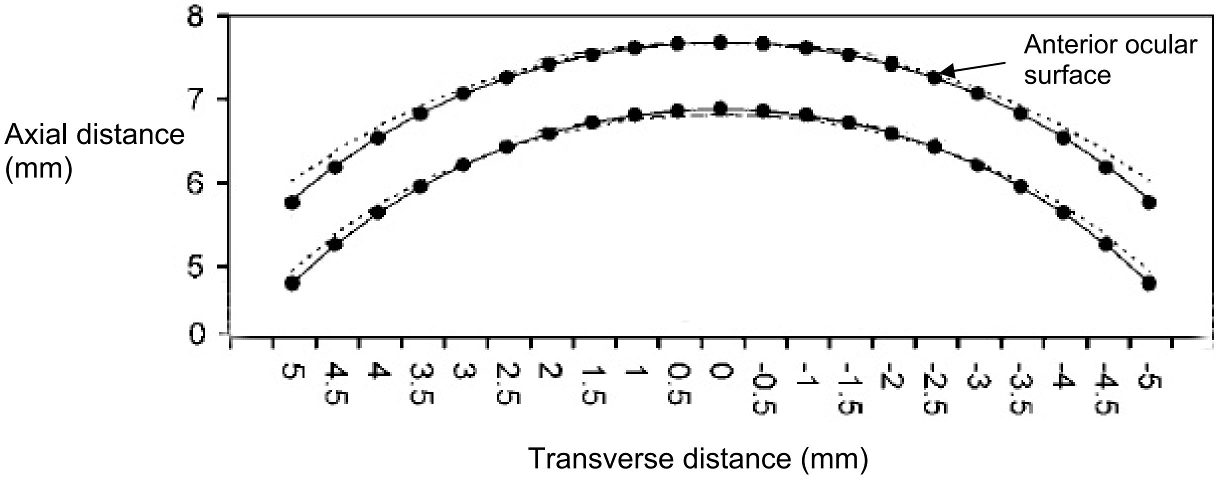

Figure 7.27: AS-OCT Visante™ representation of the AOS (top) using built-in software (indicated as dotted line) compared to improved computing scheme (indicated as thick line with large circles) adapted from (Dunne et al., 2007).

This finding agrees with the present study and offers a possible solution to improving the fidelity of AS-OCT AOS representation. However the model eye anterior surface curvature radii used in Dunne's study were simplified monocurve or bicurve designs which may not provide the most accurate solution in light of the 'true' surface asymmetry observed in human eyes. Further work is required to factor out this parameter.

7.4.8.7 Summary of Results

	Study 1	Study 2	Study 3
Question	Does impression taking deform the cornea, 10 mins after the procedure?	Is the cast scan as good as the eye scan?	Is the AS-OCT providing an accurate cast representation?
Instruments	Orbscan IIz	AS-OCT Visante™	AS-OCT Visante™ and Hyscan 45C laser
Horizontal meridian (180°)	No significant change up to 7mm annulus – limited by reflective surface	No - peripheral cornea to the anterior sclera was flattened during ocular impression taking influenced by AS-OCT AOS infidelity.	No, pattern of increasing flattening up to corneo-limbal transition
Vertical meridian (90°)	No significant change up to a 4 mm annulus – limited by eyelids	Yes – but access to AOS limited by eyelids	No pattern of increasing flattening of lower magnitude than horizontal profile
Area under the curve	Not done	Not significantly different	Not significantly different

7.4.9 Conclusions

Images of the AOS cast moulded from modern ocular impression taking, and captured using AS-OCT Visante™ technology, are not a true representation of the surface profile. Refinement of curvature correction algorithms may improve the fidelity, and further investigation is required to establish the optimal approach.

The differences found between digital images acquired of the cast surface using AS-OCT Visante™ and Hyscan 45c Laser triangulation are clinically significant at one point sampled on the horizontal profile. Further work is required to improve sample density and location to clarify these initial findings since curvature variation trend was not found to be consistent across the sampled surface profiles.

7.5 General Conclusions

- The AS-OCT Visante™ can be used to image ocular casts poured from Novadur Type IV Gypsum plaster.
- Ocular impression/casting procedures used for these studies flatten the peripheral cornea, corneo-limbal transition and anterior sclera located on the temporal aspect of the horizontal meridian, this surface alteration was found to be within tolerance for gas permeable lens manufacture.
- The changes observed are influenced to some extent by the inaccurate representation of the AOS by AS-OCT Visante™ and the expansion of the Novadur type IV gypsum plaster (Chapter 6). Nevertheless this system of quantification and representation of the human AOS *in-vivo* is suitable and satisfies the requirements of wide-field AOS exploration for this study in the absence of any less invasive method.

Chapter 8

Defining the entire anterior ocular surface shape using ocular impression techniques

'The eye, being an anatomical structure, is so complex that it can only be quantified if certain assumptions are made about its anatomy. This simplifies the construction of the model, but reduces the exactness.'
(Saunders, 1982)

8.1 Introduction

During the course of investigations for this thesis, the ocular impression-taking technique used primarily in modern clinical practice for the fabrication of scleral and cosmetic lens shells has been modernised and undergone rigorous scrutiny. Chapter 7 has provided evidence to support the use of this procedure in the absence of any other less invasive method to explore the uncharted topographic regions of the human AOS *in-vivo*, those areas of interest which are ordinarily covered by the eyelids and beyond the peripheral cornea, and thus inaccessible to optical imaging techniques.

The Cardiff Eyeshape protocol, outlined in Chapter 6, has extended the ocular impression technique by including a system of casting that provides an anatomical reference, along with platform stability, to facilitate the collection of a digital 3-D representation of the AOS by non-contact active laser triangulation. A database of ocular impressions was compiled that is thought to be representative of the white European population. For the first time wide-field AOS morphometric descriptors were assigned to anatomical regions previously only viewed by shadow photography of impression casts (Marriott, 1966), (Pullum, 2007) or measured ex-vivo (Apt, 1980) in a physiologically compromised state. Using this database, this chapter outlines the topographic characteristics of the human AOS *in-vivo* in relation to anatomical location, refractive error and gender.

8.2 Background

Customised treatments and increasingly higher patient expectations after anterior ocular surgical procedures have intensified the demand on technology to provide reliable, repeatable and highly accurate ocular surface contour measurements (Wang et al., 2006). The advent of femtosecond laser-assisted refractive surgery has enabled flaps of corneal tissue to be cut as thin as 0.09mm (Soong and Malta, 2009), with an accuracy of 0.001mm (Jonas and Vossmerbäumer, 2004). These procedures are reliant on measurements that preserve topographic fidelity of the AOS, as also are the designs for comfortable, clinically viable contact lenses used for optical or cosmetic rehabilitation. Chapter 3 presented the problem that arises from an increasingly uncertain reliability of AOS representation beyond the 3mm apical region using slit-scanning placido disk technology and Schiempflug photographic methods. Yet both systems are currently used to provide topographic data for refractive surgical planning. It follows then that a gold standard topographic representation of the human AOS *in-vivo* would offer invaluable insights, for the implementation of improved curvature correction algorithms for current technologies, extended topographic profiles with which to design contact lenses with optimal apposition to AOS contour, particularly those with larger diameters, and baseline data with which to study structural AOS abnormality and pathological change. This data could be used to provide further accuracy to finite element analysis of the AOS, modelling physical changes and predicting behaviour of the structures. Stresses in the cornea due to posterior pressure have also been found to be dependent on topography (Elsheikh, 2010), which has implications for studies relating to the measurement of raised intraocular pressure and treatment of glaucoma.

The topography of the ACS has previously been studied using a two-part polyvinylsiloxane material to assess ablation rates, profiles and volumetry when Er:YAG laser was used to photoablate the cornea of rabbits (Bachmann et al., 1992) and human subjects (Bachmann et al., 1993). The authors reported a cast accuracy of less than 1µm and that the silicone did not appear to interfere with the wound healing mechanisms of the corneal epithelium. These studies support the choice of ocular impression material used here and the suitability of the modern ocular impression-taking procedure for evaluation of a detailed, accurate representation of the AOS.

8.3 Aims and Objectives

This study used a modernised ocular impression procedure and the Cardiff Eyeshape protocol to obtain topographic data from the cornea, limbus and anterior sclera of human subjects' *in-vivo*. The hypotheses proposed were:

- AOS data collected by scanning casts of ocular impressions can be used to describe changes in the surface profile related to:
    1. Anatomical location
    2. Refractive error in myopia
    3. Gender
- This process may be presented as the 'gold standard' for wide-field topographic validation of the AOS surface characteristics in human *in-vivo* subjects.

8.4 Methods

8.4.1 Subjects

Ocular impressions were carried out on 124 white European subjects recruited for the investigation. Subsequently 5 casts were excluded due to unacceptable surface irregularities, and therefore 119 were included in the final analysis (76 ♀ and 42 ♂), mean age of the cohort was 25.43±5.34 years [SD] (range 17.61 to 42.55). Ethical approval for the study was obtained from the Cardiff School of Optometry and Vision Sciences Human Ethics Committee. All subjects were treated in accordance with the Tenets of the Declaration of Helsinki, and each provided informed, written consent. Volunteers were recruited from the staff and students of Cardiff University, and were excluded if they were pregnant or breastfeeding, had any ocular or systemic condition known to affect the structure or characteristics of the anterior ocular surface, were taking any medication known to affect the ocular surface, had worn rigid gas permeable lenses in the preceding 6 weeks or soft lenses in the preceding 2 weeks, and were not white European. This ethnic bias was chosen because it has been shown that ethnicity affects ocular surface morphometrics (Matsuda et al., 1992), (Ip et al., 2007), (Logan et al., 2004).

8.4.2 Experimental procedure

The method used to obtain an ocular impression of the AOS has been described in detail in Chapter 5 (Section 5.2.2). The cast was poured using extra-hard white plaster, Novadur (Ultima, Seiches-sûr-Loir, France), a Type 4 Gypsum plaster which conforms to BS 6873 (BSI, 2000). The impression tray and material were placed into the casting support device (Fig 8.1) lined up with the cut-out slot and locked in place.

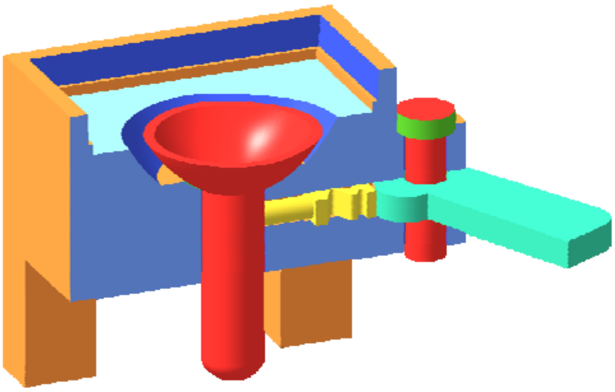

Figure 8.1: Cross-sectional view of the casting support device showing the position of the impression tray and the mechanism used to lock the tray in place (courtesy of Dr Hieu Le Chi, University of Greenwich).

A PVC ring (die cavity) was positioned to align the opening with the registration marks on the casting support device, and temporarily secured using adhesive tape (Fig 8.2).

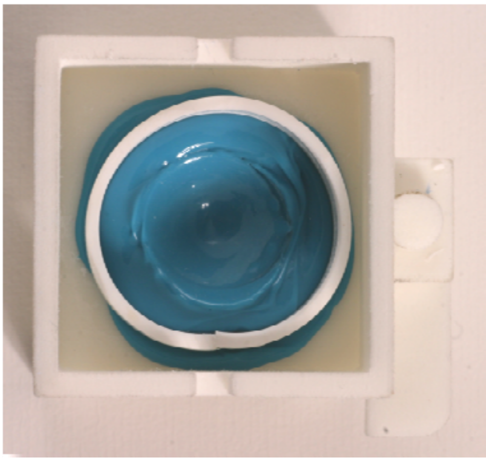

Figure 8.2: Casting support device photographed from above, showing the PVC ring positioned within the impression tray, and the impression material in-situ in preparation for casting.

The PVC ring was removed and Tresident were introduced to the device around the edge of the acrylic tray to support and stabilise the impression. Thereafter, the PVC ring was repositioned and left for 5 minutes to ensure the silicone had cured. Then 37.5cc of tap water was added to 150g of Novadur and mixed using a metal spatula in a rubber plaster bowl. The mixture was poured uniformally into the die cavity and tapped to remove any air trapped in the plaster body (Fig 8.3).

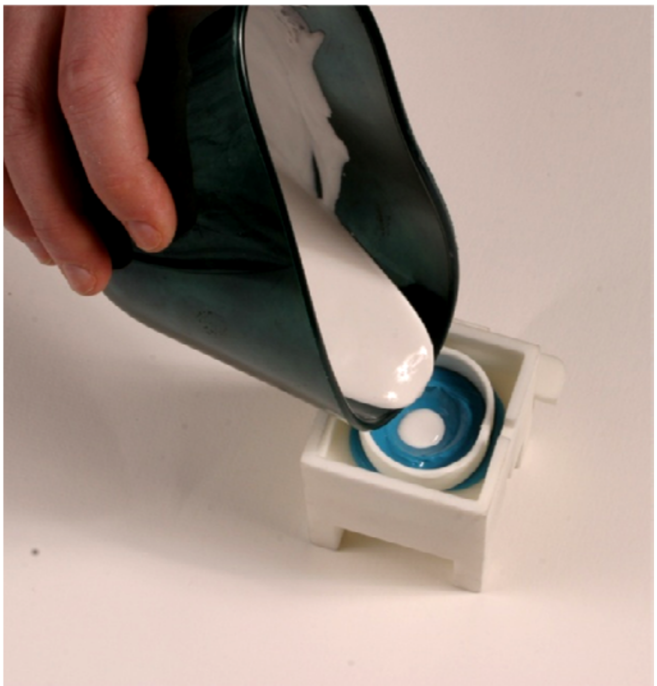

Figure 8.3: Photograph showing wet plaster being poured into the die cavity (courtesy of Benjamin Jones).

The working time for the material was 5-6 mins, and within this time a landmark registration disc was floated onto the wet plaster, lining up with the slots in the casting support device (Fig 8.4).

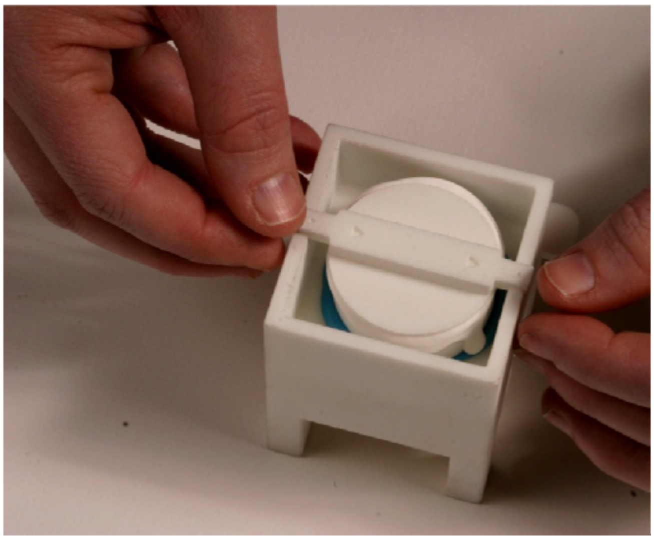

Figure 8.4: Photograph showing the landmark registration disc positioned and floated onto the wet plaster (courtesy of Benjamin Jones).

The plaster was set after 11-15 mins, but, following manufacturer's instructions, the cast was not removed for 45 mins. The excess plaster was removed using a paring-off scalpel and the combined cast and registration disc stored with a duplicate cast to be transported to the scanning facility.

The cast was scanned using a non-contact, active, laser triangulation system HYSCAN 45c, (Hymarc Ltd, Ontario, Canada). A 25μm infra-red laser beam collected the surface data at up to 2000 points per second (Fig 8.5). The cast was connected, via optoisolator electronics, to the DEA IOTA 1102 scales (CMM Technology Inc, CA, USA), allowing synchronisation of cast movement with the laser beam to determine XYZ coordinates and intensity data. A dedicated ethernet link was used to transmit the points to a Windows NT Workstation computer running XhyscanNT (Hymarc Ltd, Ontario, Canada).

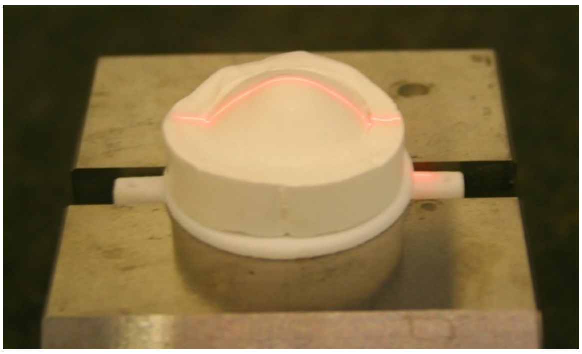

Figure 8.5: Photograph to show the cast held in the scanner vice, with the laser beam shown as a red line crossing the surface collecting co-ordinate data in digital format.

The data collected by the scanner was processed by isolating the surface of interest, establishing registration in the x, y and z planes, smoothing, and finally producing a NURBS model (non-uniform rational B-splines), which is a 3-D representation that was used for analysis (Fig 8.6).

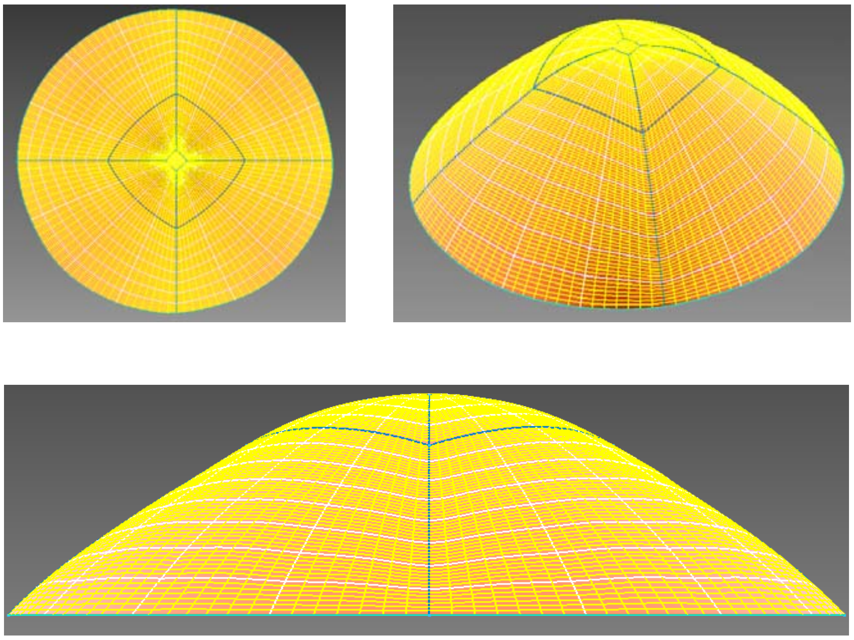

Figure 8.6: A NURBS 3-D model of the anterior ocular surface topography from ocular impression cast (Courtesy of Dr Hieu Le Chi, Greenwich University)

8.4.3 Data extraction

This section describes the methods that were used to locate and separate the specific data subsets from the 200,000 point cloud obtained by scanning the eye cast with a laser system.

8.4.3.1 2-dimensional contour profiles

Data clouds from the NURBS 3-dimensional array were allocated an stl (stereolithography) file format generated by the proprietary computer-aided design (CAD) software system XhyscanNT. These files described the surface geometry of the cast without any other CAD attributes; for example, texture and colour. These files were transcoded to text file format of x,y,z co-ordinates and 2-dimensional profiles, sampled using a custom-designed Visual Basic for applications (VBA) module (Microsoft®, WA, USA). The module OPTOMRC (Fig 8.7) was embedded in AutoCAD 2010 (Autodesk® Inc, CA, USA) enabling profiles to be sampled every 5 degrees, and the output stored as a text file containing sagittal radius of curvature measurements at 800 points along the profile and the associated x,y co-ordinates to locate the positions.

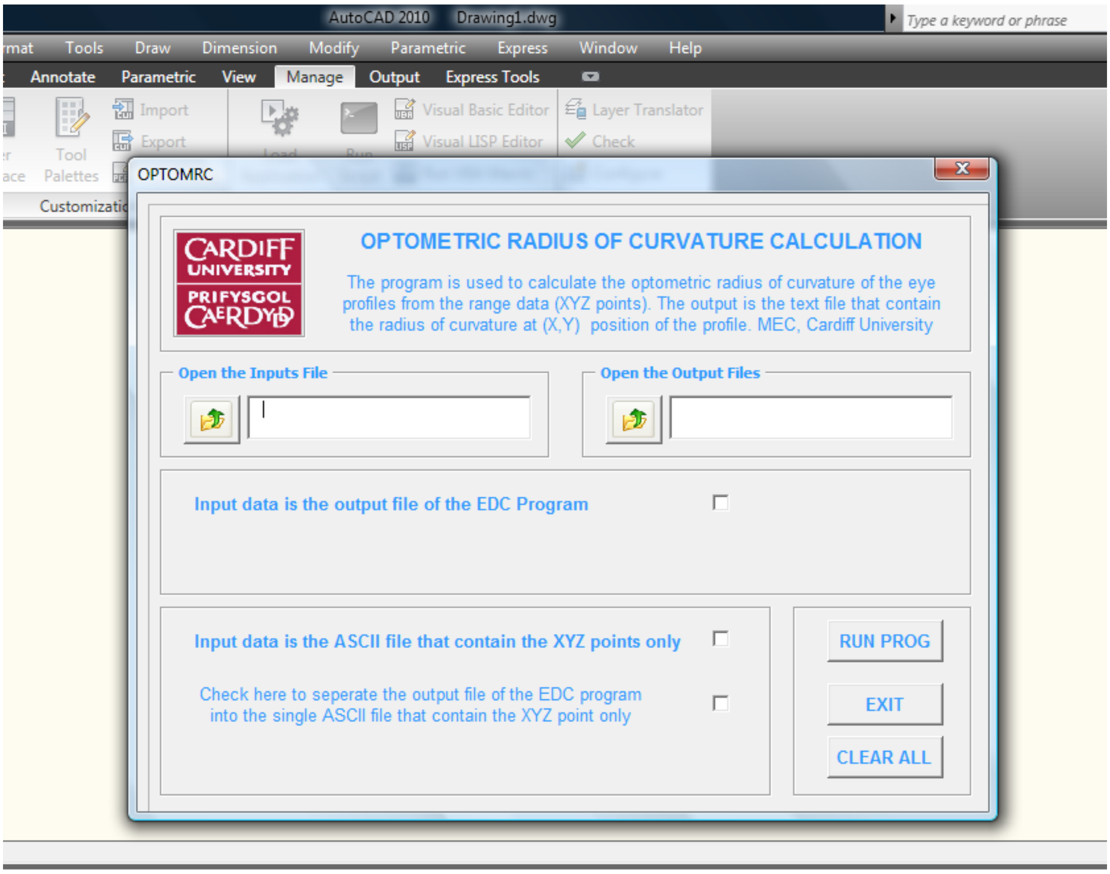

Figure 8.7: Screen grab to show the Visual Basic for Applications module (OPTOMRC) interface with AutoCAD 2010.

The profile orientation was standardised in Cartesian convention, from positive to negative. The arrangement of profiles is seen in Fig 8.8 (below).

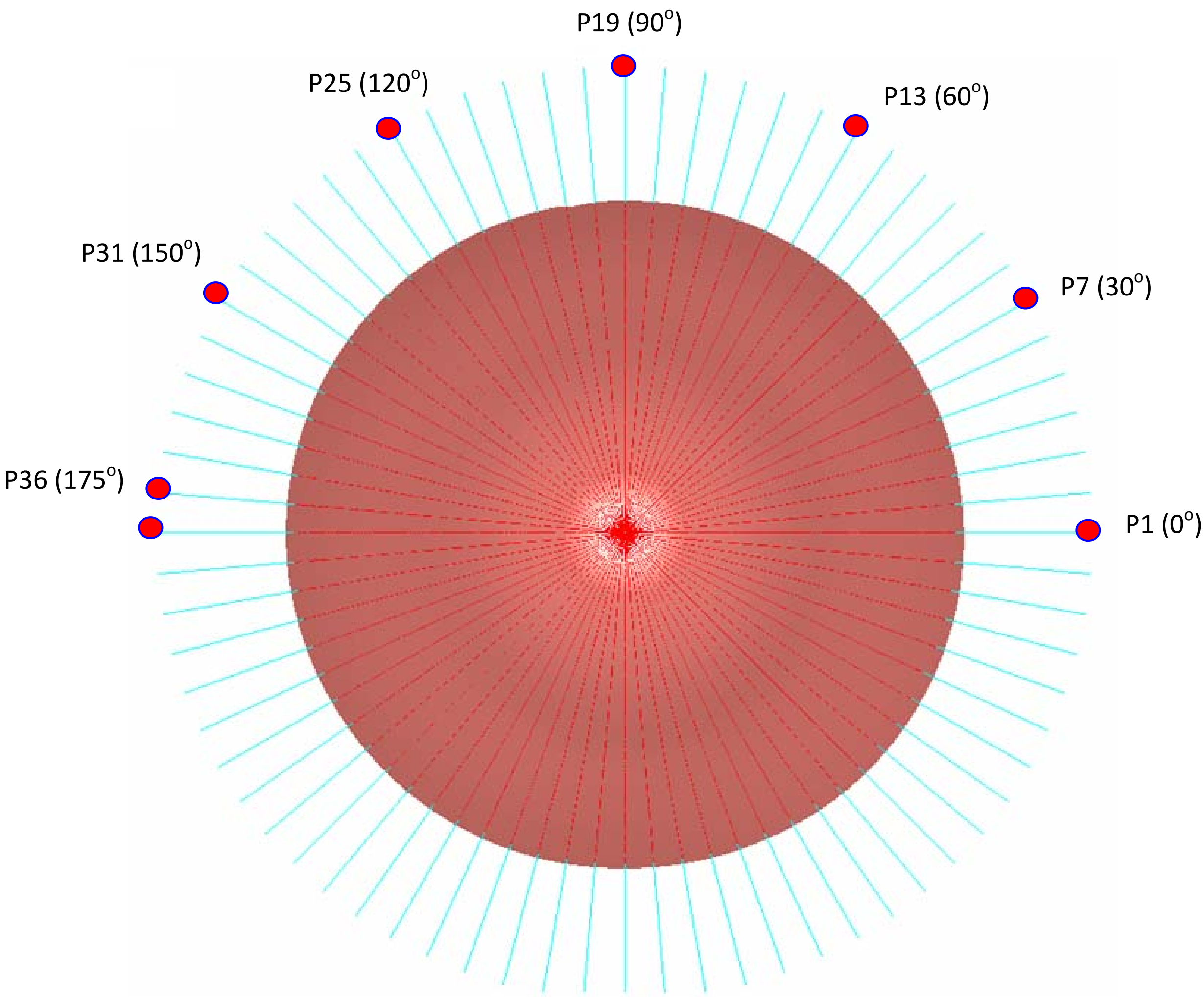

Figure 8.8: The arrangement of 2-dimensional AOS profiles from P1 to P36; angle between consecutive profiles was 5° (Courtesy of Dr Hieu Le Chi, Greenwich University).

2-dimensional data sets were exported to macro-enabled Excel 2007 spreadsheets (Microsoft®, WA, USA), within which the 800 point profiles were sampled at 0.25mm and 0.50mm intervals (linear grid measurements), from the highest point of elevation or designated apex. These profiles were plotted for initial visualisation and anatomical locations assigned. These locations were determined, in part, by examining the AS-OCT Visante™ images of a number of individuals from the studies carried out in Chapter 7.

8.4.3.2 Cast volume

3-dimensional volume measurements from cast surface plots were extracted from the XhyscanNT files viewed in AutoCAD 2010. Using 1:1 scalar representation, the z-plane 4mm below the corneal apex of the cast was identified and the volume calculated (Fig 8.9)

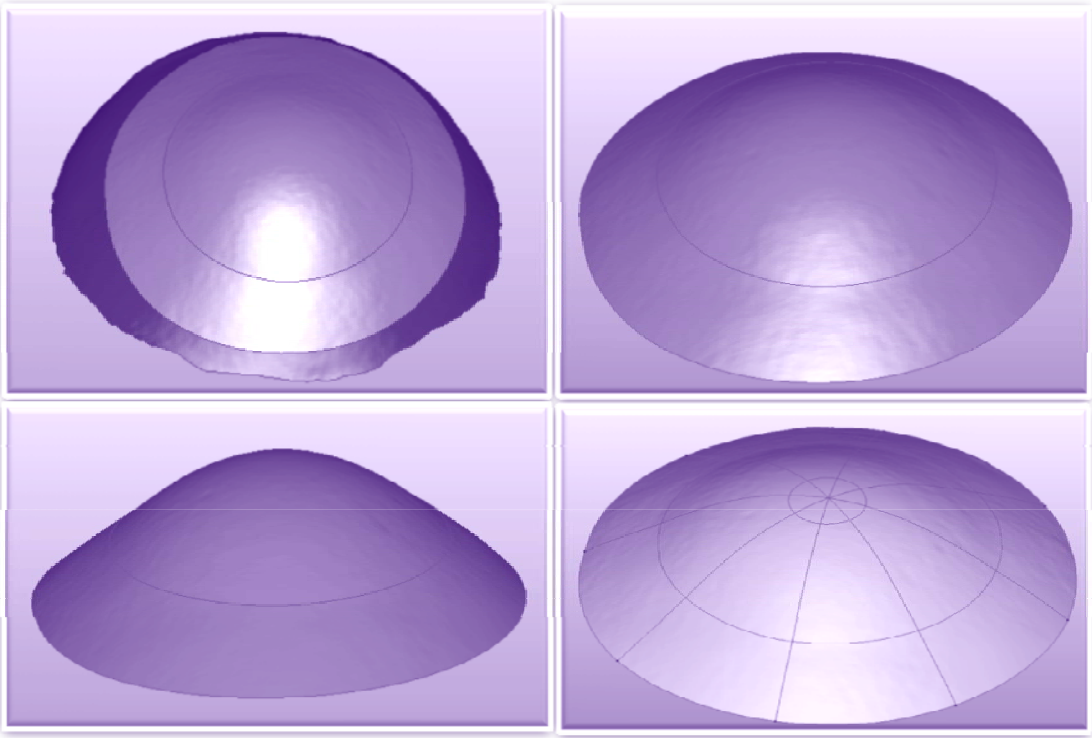

Figure 8.9: Screen grabs of the cast surface plots in AutoCAD 2010, showing delineation of the z-plane (4mm below corneal apex), and preparation for volume tool quantification (courtesy of Dr Hieu Le Chi, Greenwich University).

8.4.4 Data management

This section provides definitions of the topographic descriptors, along with the system adopted to optimise the nomenclature of orientation and location used during this investigation and which outlines categorisation of the cohort by means of refractive error group. The method of cleansing unreliable central corneal data clustered at the apex is reported.

8.4.4.1 Definition of axial (sagittal) curvature

a) **Corneal apex (C)**

The location on the cast surface, where the mean of the local principal curvature is greatest.

b) **Instrument axis (I)**

The line perpendicular to the plane of tangency to the designated corneal apex of the cast surface.

c) **Axial (sagittal) radius of curvature (r_a)**

The distance in mm from a point (B) on the cast surface to the instrument axis, along the anterior ocular surface meridian normal at the point (Fig 8.10).

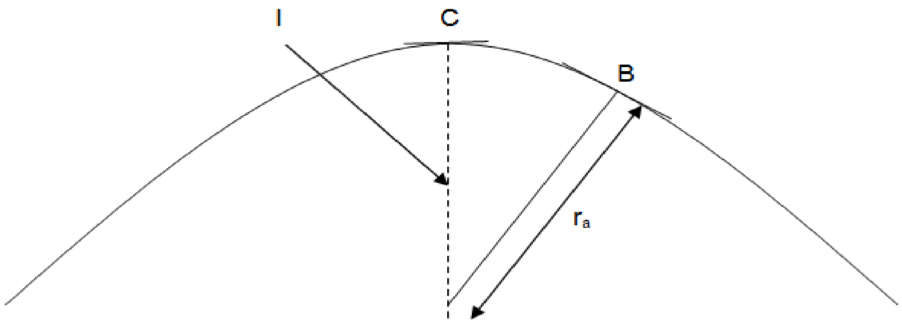

Figure 8.10: Illustration of the axial radius of curvature (r_a) showing the instrument axis and corneal apex.

8.4.4.2 Meridional profile descriptors

Using the standard optometric axis notation to ascertain orientation, 2-dimensional meridional topographic profiles were extracted and assigned anatomical regions of interest (Fig 8.11). The sampled sections were horizontal (180°), positive oblique (45°), vertical (90°) and negative oblique (135°).

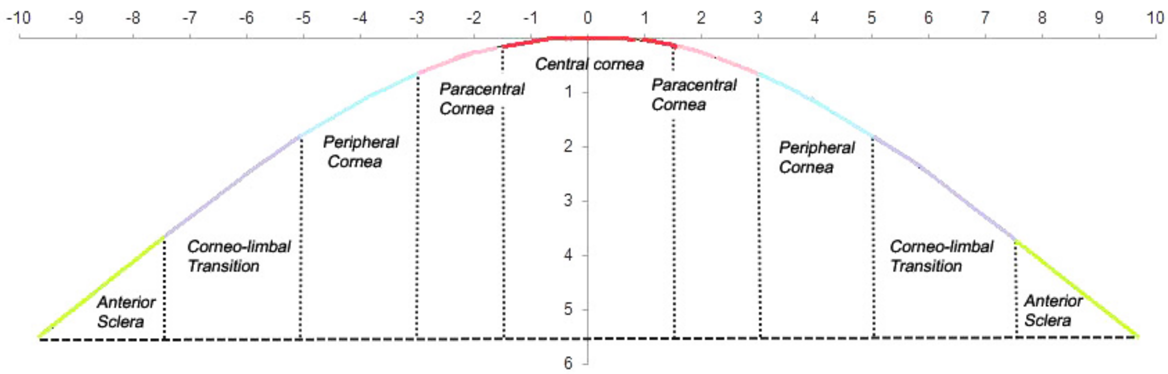

Figure 8.11: Diagram to illustrate the anatomical descriptors assigned to the 2-dimensional AOS profiles.

The majority of studies of corneal topography have investigated the central 6mm, a diameter limited by the method of data collection (Read et al., 2006a). In the earlier studies, morphometrics of the central cornea, often described as the corneal 'cap', were found to be affected by an artefact of the measurement methods (Mandell, 1992), principally that the criterion for the diameter of the central area was given an arbitrary value of 3-4 mm. For comparison, this study chose to represent the central cornea as a 3mm chord centred on the apex value, but the mean values of all radii of curvature along each profile section were instead calculated following removal of spurious radii values calculated by OPTOMRC VBA data extraction module close to the instrument axis. (If more than 40 sample points (>1mm of the profile contour) were removed from the data string, the curvature values were interpolated using a 4th order polynomial function). In this way, the measurement accuracy of the 'central cap' was improved.

The table below (Table 8.1) illustrates the working methods used to establish this precedent, all measurements in millimetres.

Method	Mean axial radius of curvature n=119	Standard deviation [SD]	Comment
CC Raw	38.38	±359.57	Spurious numbers
CC Outliers removed	7.59	±0.51	
CC Apical zone removed	7.80	±0.32	Flatter than expected
CC Removal <40 pts and interpolate >40 pts	7.23	±0.44	Steeper than expected
CC Interpolated n=50	7.24	±0.43	15 mins per subject
CC J-S Vertical	7.67	±0.29	2 sample points
CC J-S Vertical (Daily and Coe, 1962)	7.51		Steepest vertical K's in the literature
CC Vertical Orbscan	7.68	±0.29	Central dips causes flatter values
CC Vertical Pentacam	7.77	±0.29	Same dip

Table 8.1: Table documenting the approach to data cleansing of central corneal (CC) radii.

Sampled central corneal (CC) radii using the OPTOMRC VBA calculation yielded unexpected results clustered around the apex. The raw data (Table 8.1) gave a value of 38.38±359.57mm [SD] as the mean for the cohort. Removing the outliers by visual inspection (CC Outliers removed) produced a mean of 7.59 ±0.51mm [SD]. Going a further step (CC Apical zone removed) and removing 80 sampled radii centred on the apex, the figure was flatter than anticipated at 7.80±0.32mm [SD]. In comparison, the J-S keratometry in the near vertical meridian was 7.67±0.29mm [SD], indicating that the 'CC Apical zone removed' method was too much.

Given that this measurement (CC Apical zone removed) was, in effect, the recorded value of the slope at a linear distance of 1.5-1.75mm from the apex, and that the gradient was expected to increase further, the predicted mean radii will be steeper than the value recorded. Therefore, a systematic approach was adopted to remove or interpolate data dependant on the number of rogue values (CC Removal <40 pts and interpolate >40 pts). If more than 40 sequential data points (>1mm profile curvature or 0.5% of the data string) required removal, a 4th order polynomial curve function was used to interpolate the missing data. If less than 40 rogue values were identified in the data string these were removed. To check the validity of this method, a sample of 50 individuals underwent CC interpolation (CC Interpolated n=50) to quantify the effect of the lack of interpolation, and the difference in cumulative mean radius of curvature between the two methods was found to be only 0.019 mm, which was considered as being not clinically significant. As a result, the CC removal or interpolated technique was used for all data sets.

8.4.4.3 Anatomical regions of interest

The areas of interest beyond the central cornea are shown in the diagram Fig 8.12; paracentral cornea (PAC) from 3-6mm chord, peripheral cornea (PEC) from 6-10mm chord, corneo-limbal transition (CLT) from 10-15mm (Van der Worp, Graf and Caroline, 2010), and anterior sclera (ASC) from 15-20mm.

These anatomical descriptors were extended to encompass annuli (regions of interest) centring on the corneal apex, each defined by the two diameters equal to the chords used in Fig 8.11.

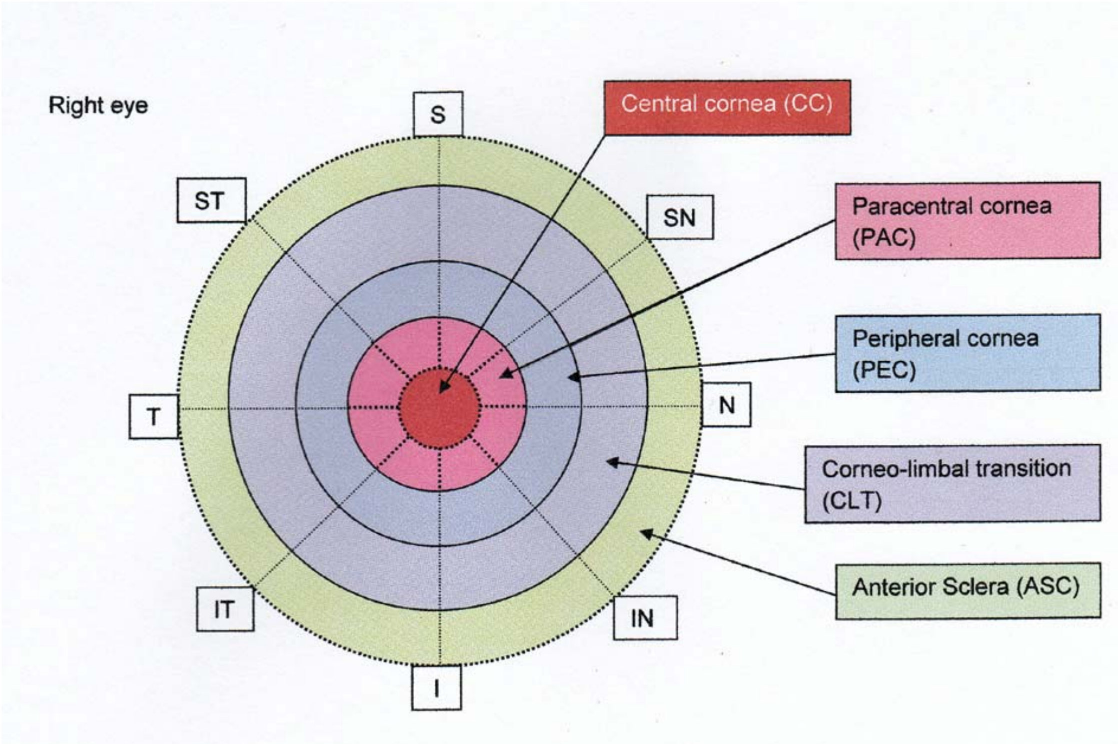

Figure 8.12: Diagram of the anterior aspect of the eye, to show the anatomical regions of interest used during analysis of the AOS (right eye), indicating the sampled meridians.

8.4.4.4 Refractive error groups

The data was categorised according to the mean spherical equivalent (MSE), and any individuals with astigmatism greater than ±1.75DC or hypermetropia greater than +2.00DS were excluded.

Group	Mean spherical equivalent	Number of individuals
GP1	Plano to +2.00DS	20
GP2	-0.25DS to -2.00DS	26
GP3	-2.25DS to -4.00DS	21
GP4	-4.25DS to -6.00DS	26
GP5	-6.25DS to -8.00DS	21
	Total	114

Table 8.2: Numbers of subjects within each refractive error sub-group.

8.4.5 Data analysis

Statistical analysis was performed using SPSSv13 (SPSS Inc., IL, USA). Average values were derived for radii found along the designated profile locations (meridians) in the regions of interest (annuli). Variation in the mean axial radius of curvature measurements were compared across 4 meridians; 180°, 45°, 90° and 135° with respect to location, refractive error and gender. Kolmorogorov-Smirnov tests were carried out to assess the normality of the data. One-way, between-groups ANOVA was used to examine regional variations in axial curvature, in addition further comparisons were made between a reference group (GP1; Plano to +2.00DS) and the myopic refractive error groups (GP2 to GP5). A mixed-between, within-subjects ANOVA was used to test for effects of gender and refractive error groups on regional variations. P-values were reported following post hoc test using Bonferroni adjustment.

Further one-way, between-groups ANOVA investigated the effect of myopic refractive error on volumetric measures of the AOS, comparing a reference group (GP1: Plano to +2.00DS) and the myopic refractive error groups (GP2 to GP5), and a mixed between-within-subjects ANOVA was used to test for effects of gender and refractive error groups on volume. P-values were reported following post hoc test using Bonferroni adjustment.

Visual comparisons were made of cast topography compared to data collected from the Javal-Schiötz Keratometer, Orbscan IIz and Pentacam in the horizontal and vertical meridians (Chapter 3) and symmetry of radii within the area of interest

8.5 Results

8.5.1 Regional curvature map of the entire anterior ocular surface

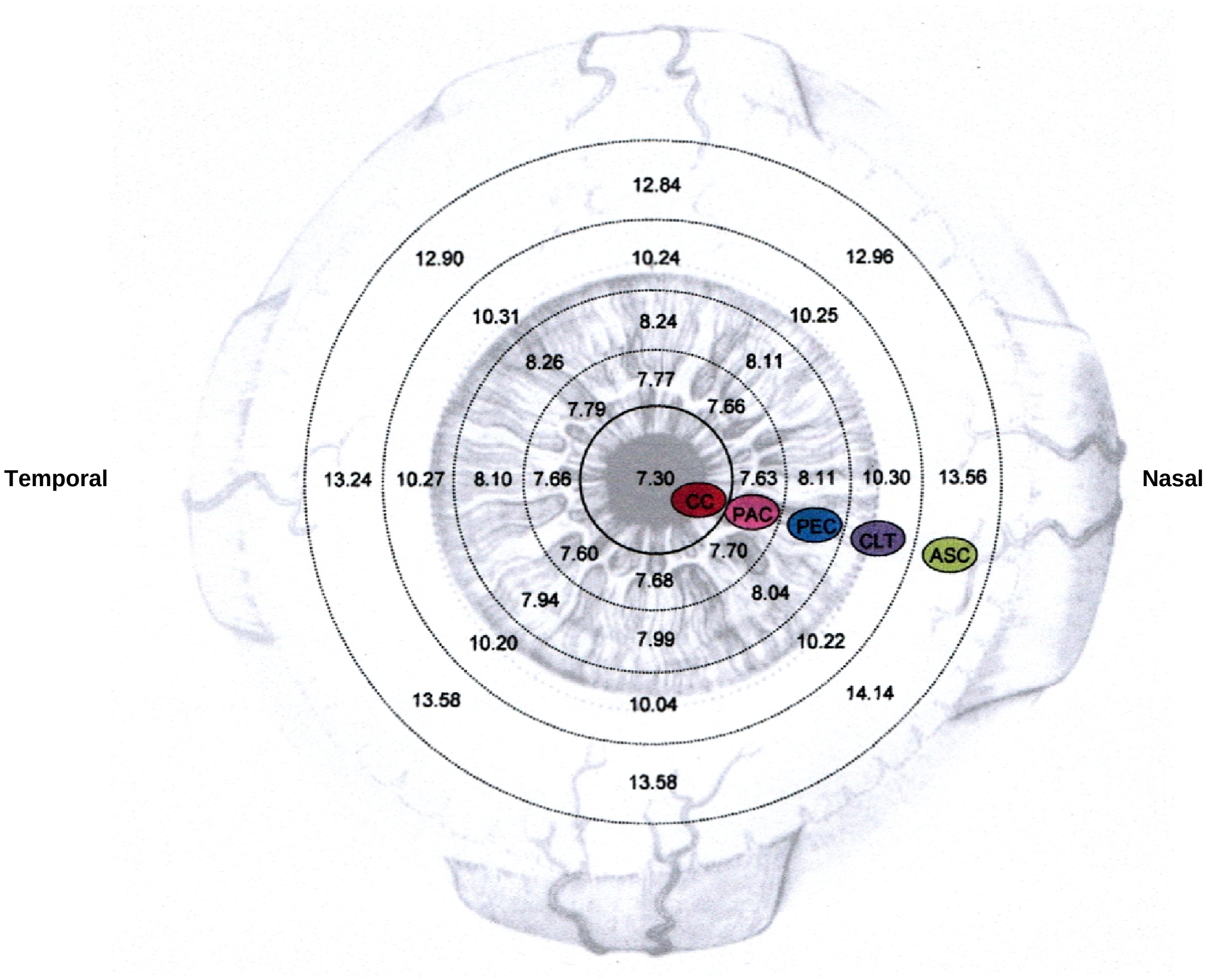

Figure 8.13: Diagram of the anterior ocular surface anatomy, adapted from (Hogan et al., 1971), showing the regions of anatomical interest and mean axial radii of curvature by location (each specified radius represents a mean of the curvature measurements taken along the section of meridian at the particular location).

a) <u>Central cornea</u>

This map (Fig 8.13) was used to describe the variation of mean axial radii of curvature values that correspond to particular anatomical location – a section of the 2-dimensional meridional profile. Average radii values within the 3mm annulus of the central cornea (CC) were 7.30±0.46mm [SD]. There was no statistically significant difference found between the curvatures of the eight profile sections in this region (1.00>p>0.336).

b) <u>Paracentral cornea</u>

The paracentral cornea (PAC) was found to have curvature values ranging from 7.53 to 7.85, with a mean of 7.69±0.37mm [SD]. The steepest values were found at the IT and T locations (IT 7.60±0.35mm [SD], T 7.63±0.37mm [SD]). These locations were statistically steeper than the flattest locations in the region S (7.78±0.36mm [SD], p=0.03) and ST (7.79±0.36mm [SD], p=0.020). The paracentral cornea had a regular mean curvature across all profiles in the nasal aspect.

c) <u>Peripheral cornea</u>

The peripheral cornea (PEC) was found to have a wider range of variation in curvature than PAC, 7.94 to 8.26, mean of 8.10±0.45mm [SD], and flatter values in the superior aspect (SN 8.12±0.49mm [SD], S 8.24m±0.49mm [SD], ST 8.26±0.46mm [SD]), compared to the inferior aspect (IT 7.94±0.41mm [SD], I 7.99±0.38mm [SD], IN 8.04±0.38mm [SD]). The superior aspect of the peripheral cornea was found to be significantly flatter than the inferior aspect (SN-IT p=0.04, S-I p=0.00, ST-IN p=0.006). The horizontal meridian was the only profile to demonstrate symmetry in this region (N 8.11±0.45mm [SD], T 8.11±0.46mm [SD], p=1.00).

d) <u>Corneo-limbal transition</u>

The range of values found in the corneo-limbal transition (CLT) region was 9.92 to 10.50, mean of 10.22±0.97mm [SD]. This region was shown to be symmetrical with no statistical difference between locations (1.00>p>0.061).

e) <u>Anterior sclera</u>

The flattest region corresponding to the anterior sclera (ASC) provided the widest range of values 12.84 to 14.14, mean of 13.36±0.93mm [SD]. Steeper radii were found on the superior aspect (ST 12.90±1.03mm [SD], S 12.79±0.93mm [SD], SN 12.96±0.96mm [SD]) compared to the inferior aspect (IT 13.59±1.25mm [SD], I 13.58±1.10mm [SD], IN 14.14±1.22mm [SD]). The superior aspect of the ASC was steeper than the inferior aspect and this was statistically significant (SN-IT p=0.00, S-I p=0.00, ST-IN p=0.00). This region demonstrated the greatest asymmetry, the flattest radius of curvature was found in the infero-nasal location under the lower lid (IN 14.14±1.22mm [SD]), and the steepest under the upper eyelid in the superior location (S 12.84± 0.92mm [SD]).

8.5.2 Symmetry of surface curvature within regions of interest (annuli)

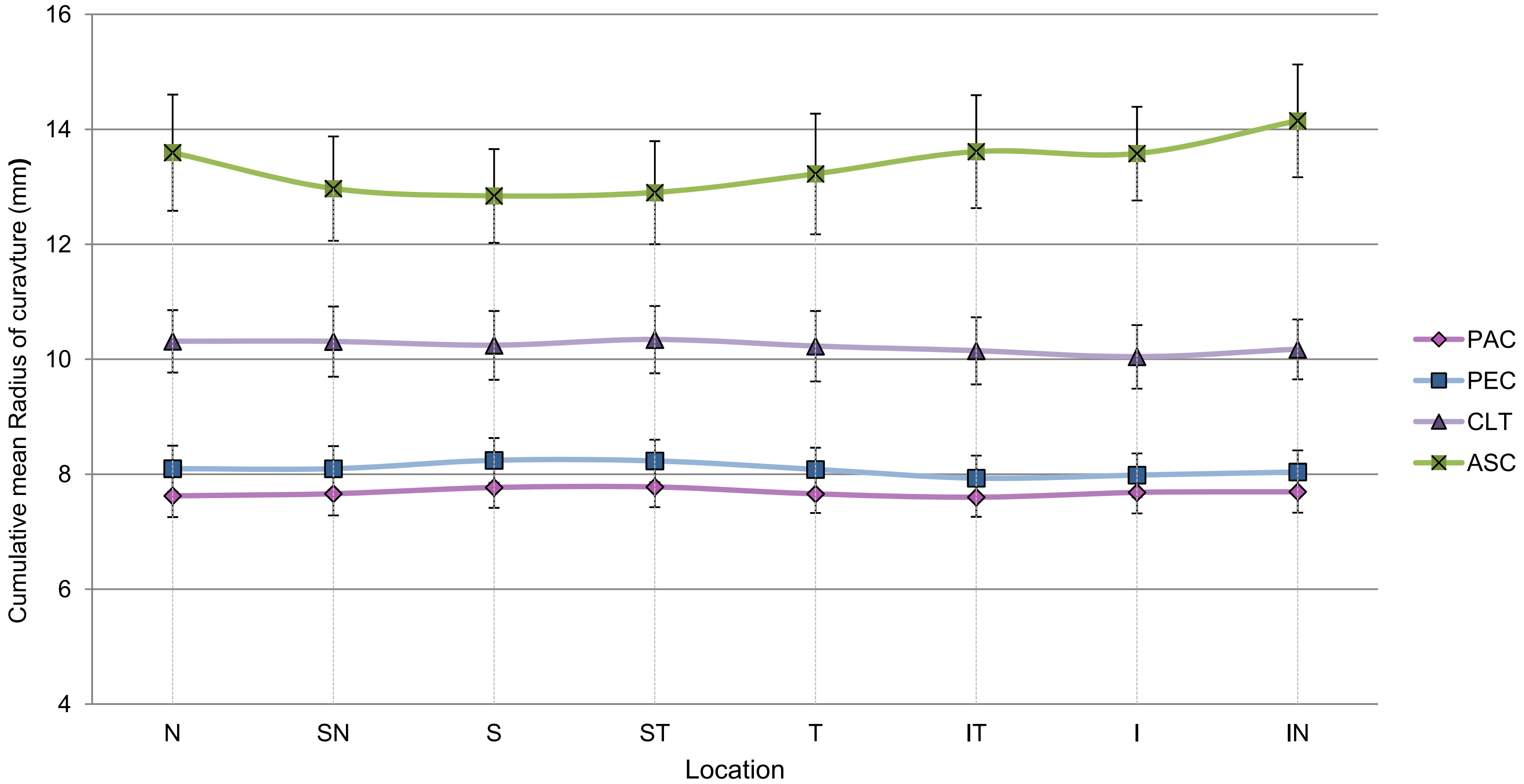

Figure 8.14: Graph to show the changes in curvature of the AOS by anatomical region of interest, showing each meridional location.

Further quantification of regional variation was shown in graphical form (Fig 8.14). The change in curvature values can be seen to be similar across locations for the PEC and PAC annuli, exhibiting identical profile contours. The ASC region, however, was shown to alter radically from this, with steeper radii in the superior aspects and flatter radii inferiorly.

Section summary: 8.5.1 and 8.5.2

Region	Mean axial radius of curvature (mm [SD])	Range of radius of curvature values (mm)	Symmetry
Central cornea	7.30 ±0.46	7.37-7.71	Yes
Paracentral cornea (PAC)	7.68 ±0.37	7.53-7.85	No, regular curvature on the nasal aspect, steepest and flattest values on temporal aspect
Peripheral cornea (PEC)	8.10 ±0.45	7.86-8.35	No, flatter on the superior aspect than corresponding locations on the inferior aspect
Corneo-limbal transition (CLT)	10.22 ±0.97	9.92-10.50	Yes
Anterior sclera (ASC)	13.34 ±1.19	12.62-14.34	No, greatest asymmetry of all regions, superior aspect steeper than corresponding locations on inferior aspect

8.5.3 Profile descriptors

8.5.3.1 Horizontal (180°) meridian

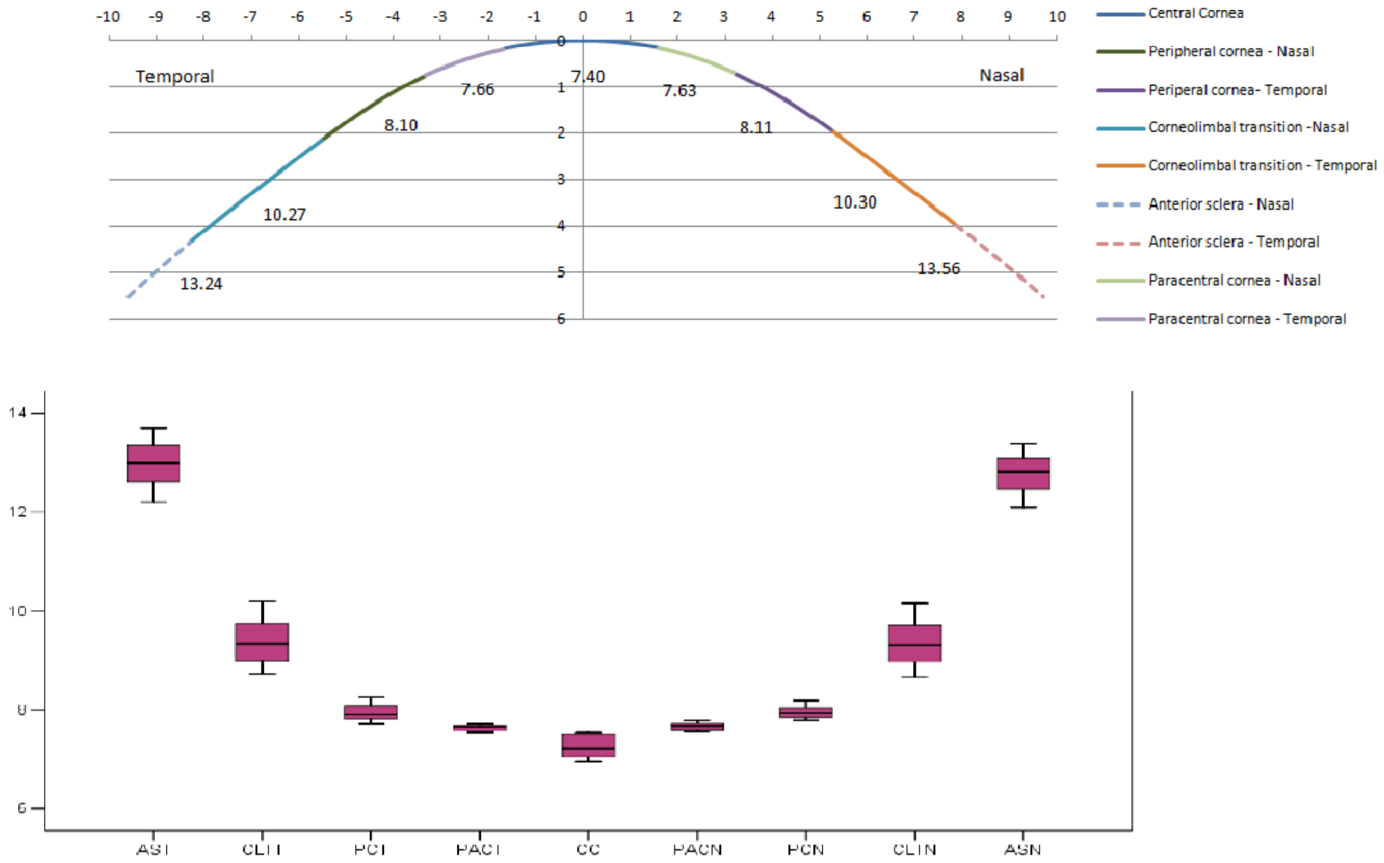

Figure 8.15: Horizontal profile of the average eye (n=119) with mean axial radius of curvature values for each location along the profile (top), the degree of dispersion of the values for each location (below) shown by median value, the interquartile range (Q1-Q3), and maximum and minimum radius values

The data distribution for the anatomical locations chosen along each profile showed a considerable amount of variation at CC (Fig 8.15). This was found to be at a minimum along the horizontal profile interquartile range (IQR) of 0.61mm, (minimum 6.44 and maximum 8.71mm), with a median value of 7.29mm. The range of mean radius of curvature for this region, within 95% confidence interval (CI), was 7.30 to 7.46mm.

The data distribution for the PAC and PEC regions was found to be significantly narrower: PACN IQR 0.41mm (minimum 6.62 and maximum 8.55), PACT IQR 0.40mm (minimum 6.64 and maximum 8.76mm) and PCN IQR 0.52mm (minimum 6.67 and maximum 9.20), PCT IQR 0.53mm (minimum 7.30 and maximum 9.35mm). The range of mean radius of curvature for PACN was 7.55 to 7.68 (95% CI) steeper than the corresponding PACT 7.50 to 7.70 (95% CI).

Radii measured in the CLT region of the profile were similar in both aspects with a wider IQR than CC, PAC or PEC (CLTN IQR 0.69mm (minimum 9.30 and maximum 11.61mm) and CLTT IQR 0.74mm (minimum 9.17 and maximum 12.41mm)). The range of mean radius of curvature CLTN was 10.24 to 10.43 (95% CI) compared to CLTT 10.12 to 10.35 (95% CI).

The ASC region was found to have the greatest variation curvature and data distribution; ASN range of mean radius of curvature 13.44 to 13.81 (95%CI), IQR 1.20mm (minimum 11.62 and maximum 18.41mm) and AST range of mean radius of curvature 13.04 to 13.44 (95%CI), IQR 1.10mm (minimum 10.34 and maximum 19.65mm)

8.5.3.2 Positive oblique (45˚) meridian

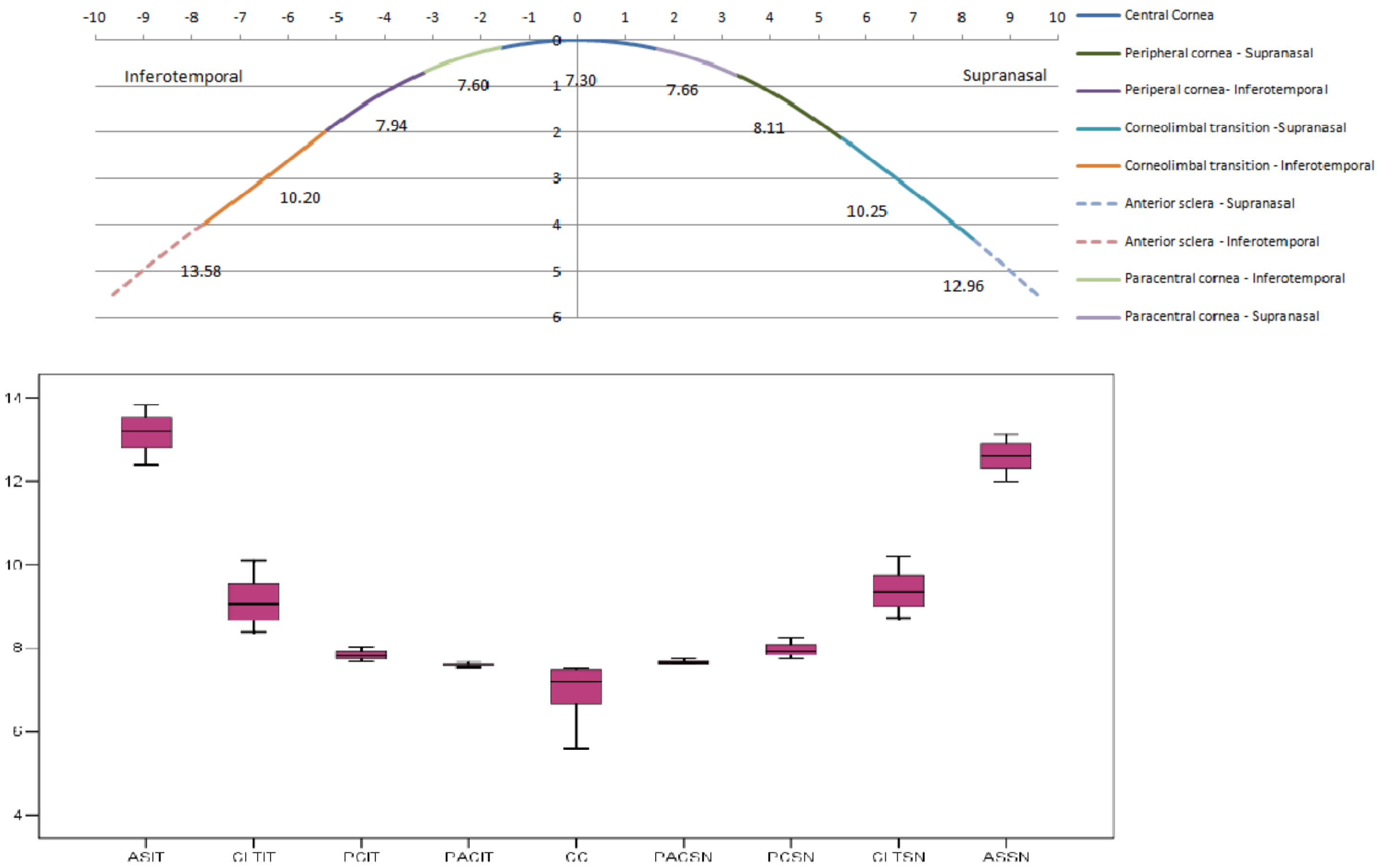

Figure 8.16: Positive oblique profile of the average eye (n=119) with mean axial radius of curvature values for each location along the profile (top), the degree of dispersion of the values for each location (below) shown by median value, the interquartile range (Q3-Q1) and maximum and minimum radius values.

Along the positive oblique profile (Fig 8.16), CC measurements were found to steepen and the data distribution increased compared to the horizontal profile; CC45 range of mean radius of curvature 7.18 to 7.36 (95%CI), IQR 0.67mm (minimum 5.59 and maximum 8.49mm) and CC180 range of mean radius of curvature 7.30 to 7.46 (95%CI), IQR 0.61mm (minimum 6.44 and maximum 8.71mm).

The radii measured in the PAC, PEC and CLT regions of the positive oblique profile exhibited an identical trend to the horizontal profile with respect to curvature values and data distribution.

For the anterior scleral region, ASIT was found to be flatter than AST, and ASSN steeper than ASN; range of mean radius of curvature ASIT 13.42 to 13.80 (95% CI) compared to AST 13.04 to 13.44 (95% CI) and ASSN 12.80 to 13.14 (95% CI) compared to AST 13.44 to 13.81 (95% CI).

8.5.3.3 Vertical (90˚) meridian

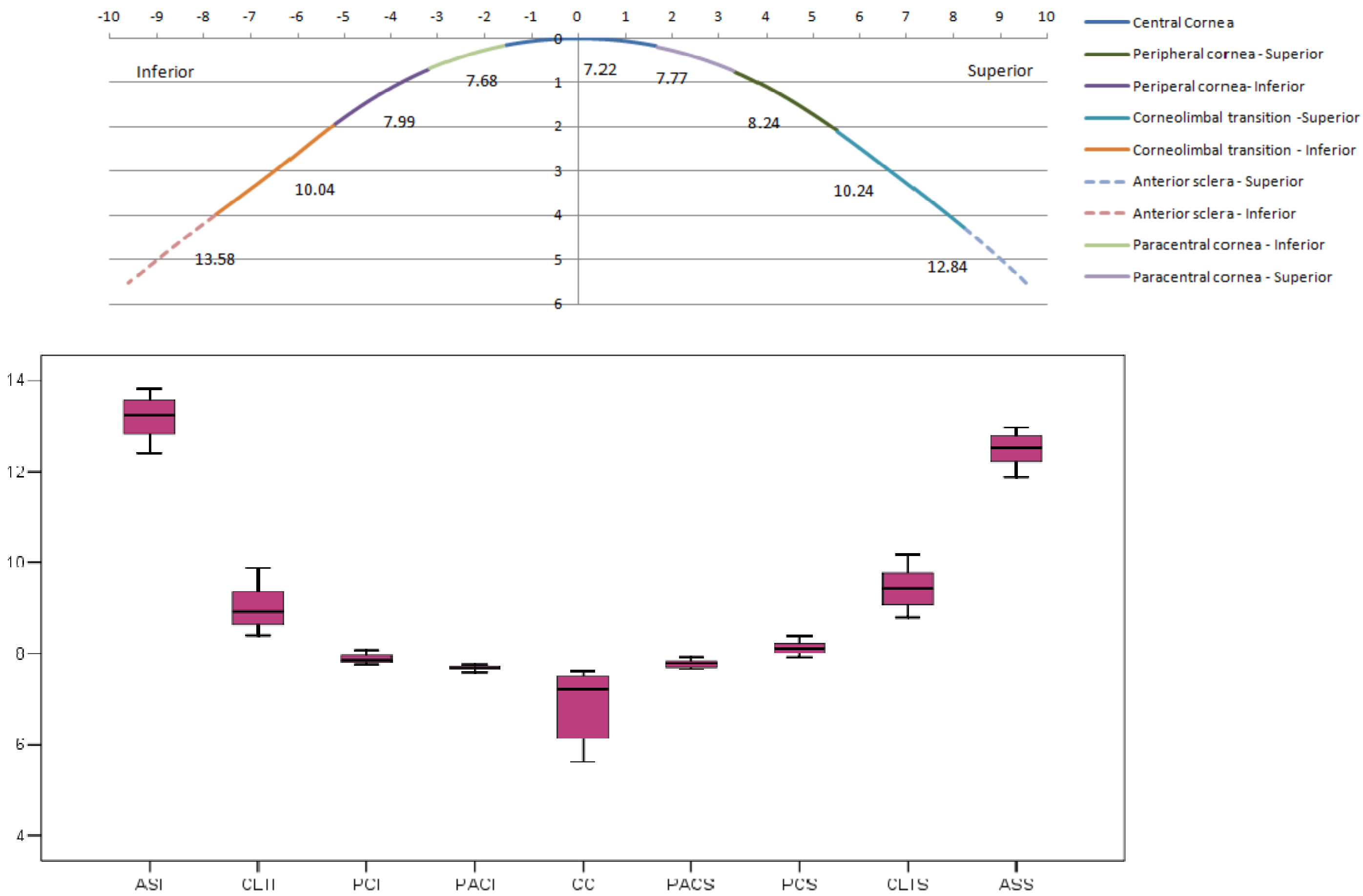

Figure 8.17: Vertical profile of the average eye (n=119) with mean axial radius of curvature values for each location along the profile (top), the degree of dispersion of the values for each location (below) shown by median value, the interquartile range (Q3-Q1) and maximum and minimum radius values.

The vertical profile was found to have the steepest CC values (Fig 8.17), compared to the other 3 profiles; range of mean radius of curvature CC90 7.02 to 7.28mm (95% CI) compared to CC180 7.30 to 7.46mm (95% CI), CC45 7.14 to 7.36mm (95% CI) and CC135 7.12 to 7.39mm (95% CI).

This profile exhibited a flatter range of values for radii in the remaining superior corneal and transition regions when compared to the same locations on the inferior aspect of the profile; PACS 7.69 to 7.82mm (95% CI), PCS 8.15 to 8.30mm (95% CI), CLTS 10.12 to 10.35mm (95% CI) compared to PACI 7.60 to 7.74mm (95% CI), PCI 7.90 to 8.05mm (95% CI), CLTI 9.94 to 10.14mm (95% CI).

The steepest scleral radii on the sampled AOS were found along the superior aspect of the vertical profile; ASS 12.67 to 12.97mm (95% CI). However, the corresponding location on the inferior aspect was not symmetrical; ASI 13.40 to 13.71mm (95% CI).

The data distribution along the vertical profile was most variable at the CC location; CC90 IQR 0.86mm (minimum 5.58 and maximum 8.35mm), with the majority of values within the 25th percentile, curvature less than 7.30mm, but greater than 6.23mm, compared to CC135 IQR 0.77mm (minimum 5.61 and maximum 8.80mm), CC45 IQR 0.67mm (minimum 5.59 and maximum 8.49mm), and CC180 IQR 0.61mm (minimum 6.44 and maximum 8.71mm).

The distribution trend across the locations was similar to that of the previous horizontal and positive oblique profiles, with PAC and PEC values for the whole cohort characterised by small IQR values; PACS IQR 0.35mm (minimum 6.31 and maximum 8.75mm), PACI IQR 0.42mm (minimum 6.90 and maximum 8.98mm), and PCS IQR 0.47mm (minimum 7.19 and maximum 9.70mm), PCI IQR 0.48mm (minimum 7.23 and maximum 9.32mm).

8.5.3.4 Negative oblique (135˚) meridian

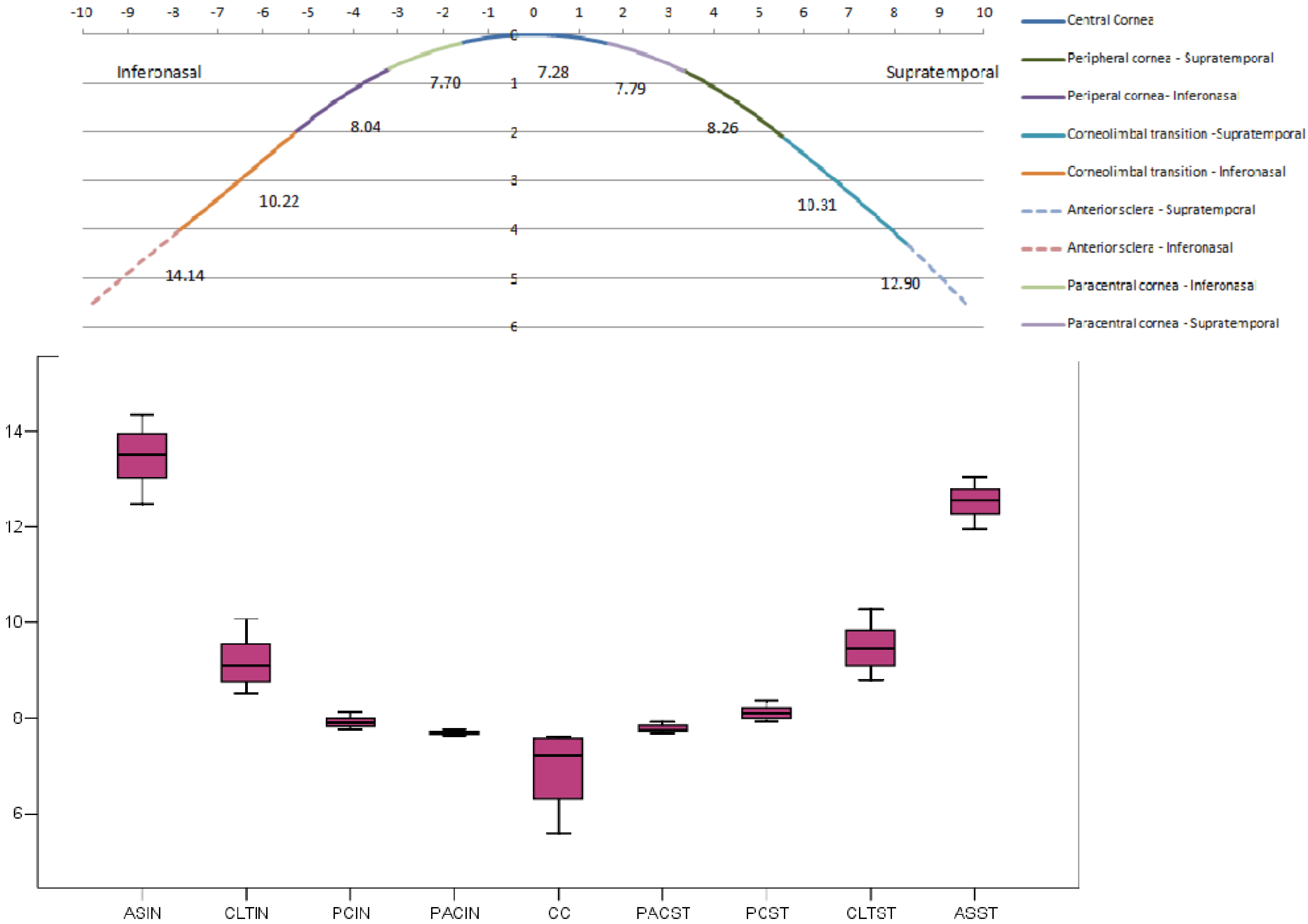

Figure 8.18: Negative oblique profile of the average eye (n=119) with mean axial radius of curvature values for each location along the profile (top), the degree of dispersion of the values for each location (below) shown by median value, the interquartile range (Q3-Q1) and maximum and minimum radius values.

The PAC and PEC regions of the negative oblique profile (Fig 8.18) were found to have a flatter range of radii of curvature when compared to the corresponding locations on the positive oblique profile; PACST 7.71 to 7.84mm (95% CI), PACIN 7.60 to 7.76 mm (95% CI) compared to PACSN 7.57 to 7.72mm (95% CI), PACIT 7.52 to 7.65mm (95% CI) and PCST 8.16 to 8.30mm (95% CI), PCIN 7.97 to 8.11mm (95% CI) compared to PCSN 8.02 to 8.17mm (95% CI), PCIT 7.85 to 8.00mm (95% CI).

The flattest location of anterior scleral curvature on the sampled AOS was found to be the infero-nasal aspect of the negative oblique profile; ASIN 13.96 to 14.33mm (95% CI), the corresponding ASST was not symmetrical; ASST 12.74 to 13.08mm (95% CI) and considerably steeper.

The data distribution trend across locations was found to reflect a similar pattern as the previous horizontal, vertical and positive oblique profiles.

Section summary: 8.5.3

Region	Steepest radius of curvature (mm)	Flattest radius of curvature (mm)	Data distribution	Comments
Central cornea (3mm chord)	Vertical profile 7.02-7.28	Horizontal profile 7.30-7.46	Vertical>negative oblique>positive oblique>horizontal profile IQR 0.66-0.86	Similar range of radii found along positive and negative oblique profiles
Paracentral cornea (3-6mm chord)	Nasal location 7.63	Supero-temporal location 7.79	Least variable of all regions IQR 0.35-0.45	Asymmetric Most robust metric
Peripheral cornea (6-10mm chord)	Infero-temporal location 7.94	Supero-temporal location 8.26	Tight distribution IQR 0.45-0.53	Asymmetric
Corneo-limbal transition (10-16mm chord)	Infero-temporal location 10.04	Supero-temporal location 10.31	IQR 0.67-0.84	
Anterior sclera (16-20mm chord)	Superior location 12.84	Infero-nasal location 14.14	IQR 0.87 – 1.46 Most variable of all regions	Most asymmetric of all regions

8.5.4 Comparison with other topographic devices; Orbscan IIz and Pentacam

8.5.4.1 Horizontal profile

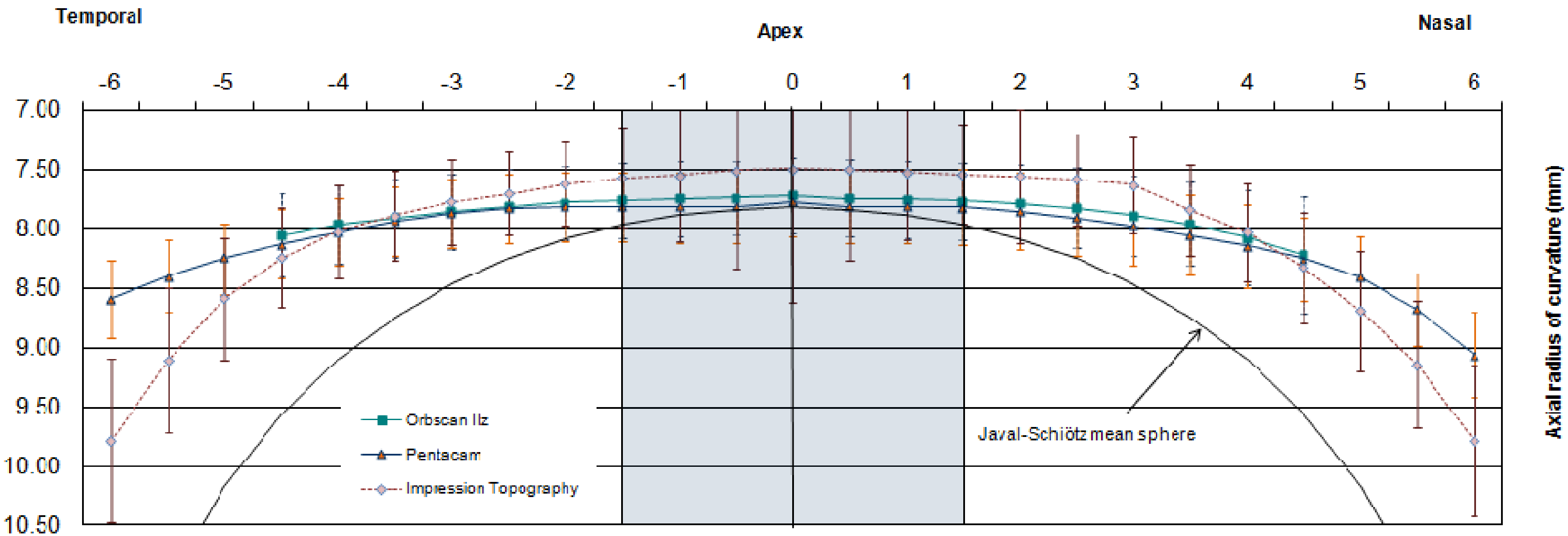

Figure 8.19: Comparison of the shape of the 180˚ meridian of the right eye (n=119) using a Javal-Schiötz Keratometer, Orbscan IIz, Pentacam and ocular impression methods

Data sampled for the investigation in Chapter 3 was used to provide a visual comparison of the AOS topography of the white European cohort (n=119) using slit-scanning technology (Orbscan IIz), Scheimpflug photography (Pentacam), and the ocular impression-taking methods (Fig 8.19). The topographic profiles were aligned using the instrument axis for the 2 commercial instruments and the designated apex (described in 8.4.4.1).

The horizontal profiles are shown scaled at 1:1 ratio. The mean axial radii values were found to have no statistical difference compared to the gold standard Javal-Schiötz measurements (Chapter 3, Section 3.4) for the CC (Orb p=0.080, Pent p=1.000). The findings for impression topography indicated notably steeper values CC180 7.38±0.04mm [SD], compared to the Orb CC180 7.75±0.31mm [SD] and Pent CC180 7.81±0.30mm [SD]. These radii were steeper than the Orb and Pent profile on both the nasal and temporal aspects of the profile until the 8mm chord, at which point the impression profile was found to intercept and rapidly steepen in both aspects of the CLT region.

8.5.4.2 Vertical profile

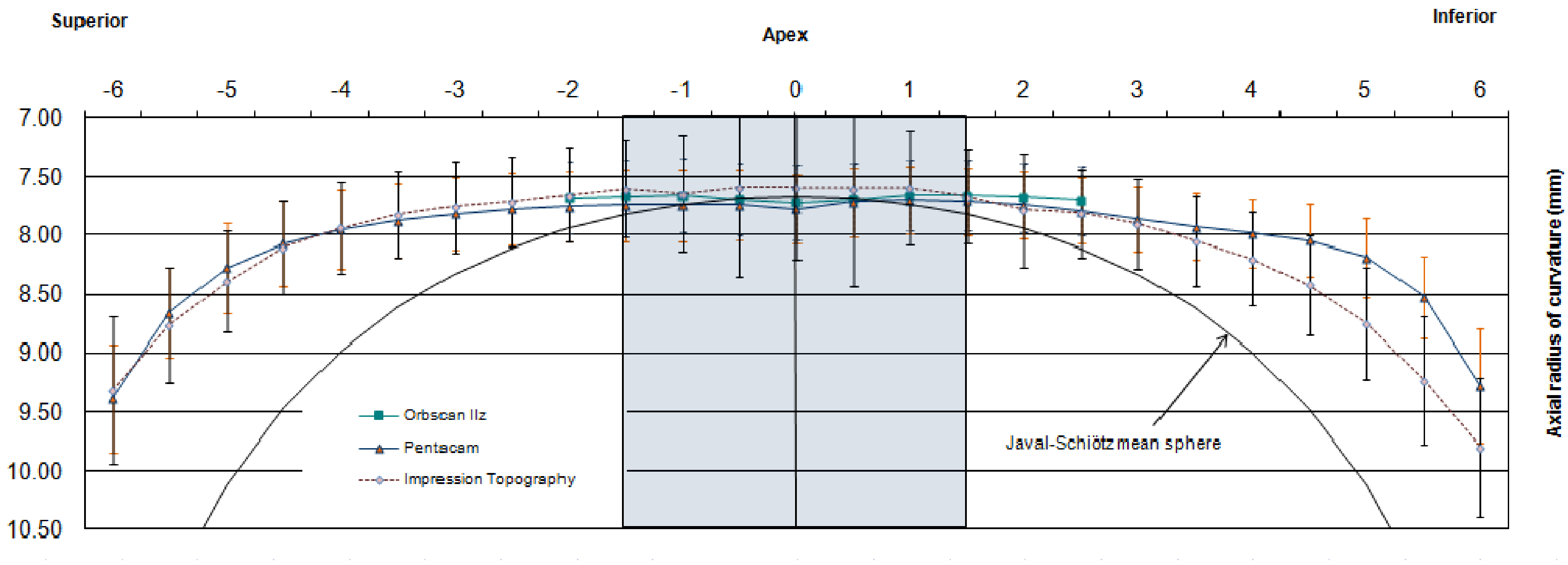

Figure 8.20: Comparison of the shape of the 90˚ meridian of the right eye (n=119) using a Javal-Schiötz Keratometer, Orbscan IIz, Pentacam and ocular impression methods

The vertical profiles are shown scaled at 1:1 ratio. The mean axial radii values were found to have a statistical difference compared to the gold standard Javal-Schiötz measurements (Chapter 3, Section 3.4) for the CC90 Orb ($p<0.001$). but not for the Pent ($p=0.231$). The findings for impression topography indicated notably flatter values CC90 7.15mm ±0.07 [SD], compared to the Orb CC90 6.67±0.42mm [SD] and steeper than the Pent CC90 7.73±0.29mm [SD].

The impression profile curvature was not found to follow the negative curvature inflection (dip) seen for Orb and Pent, centred on the apex (Fig 8.20). The three profiles were found to be similar beyond this region until the 6mm chord, at which point the impression profile can be seen to intercept the Pent profile and rapidly steepen in the inferior aspect. Along the superior aspect the impression profile was marginally steeper, but mimicked the curvature variation of the Pent profile.

8.5.5 The effect of increasing myopic refractive error on AOS shape

8.5.5.1 Comparison by meridional profile

a) Horizontal (180˚) Meridian

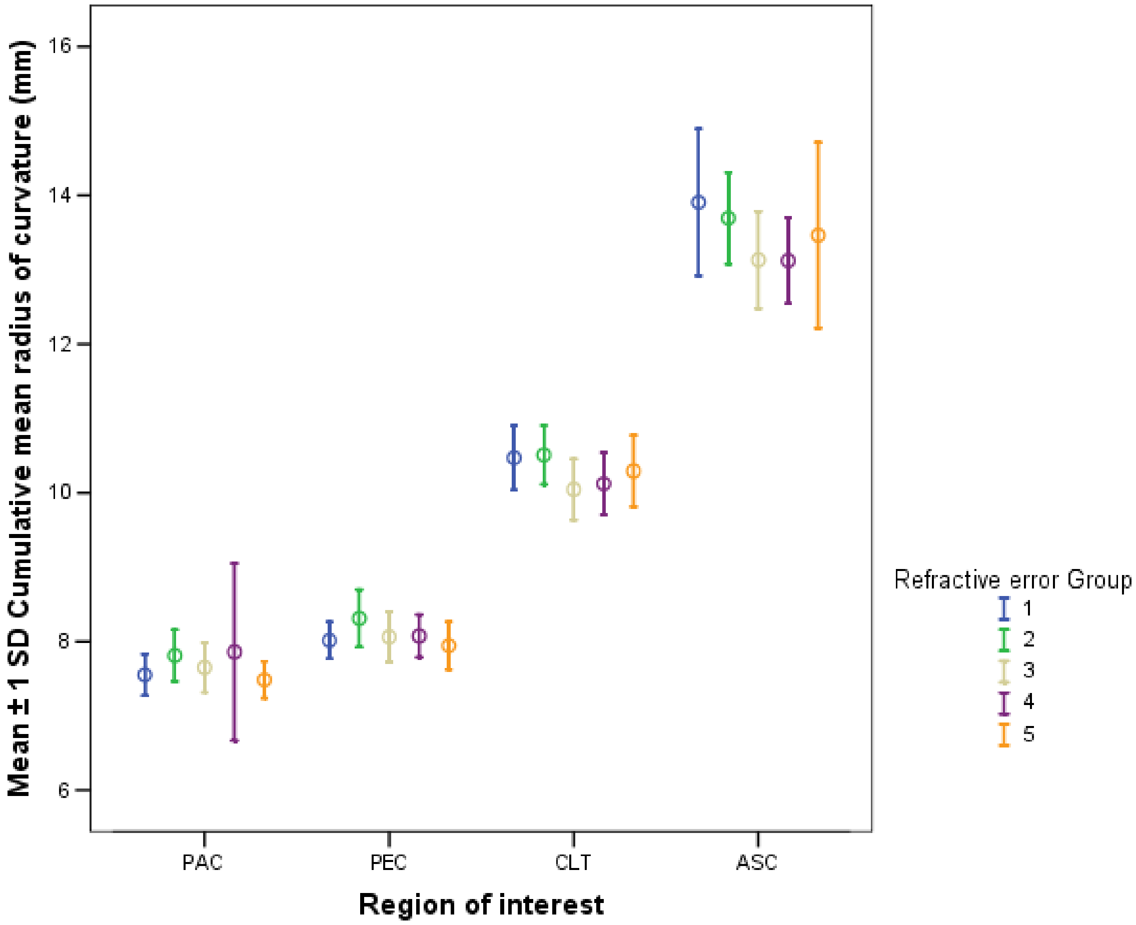

Figure 8.21: Comparison of mean regional radius of curavture changes related to myopic refractive error: horizontal (180˚) profile

Comparison of regional curvature with increasing myopic refractive error *Horizontal (180) Profile*						
	Location	GP1	GP2	GP3	GP4	GP5
Number of eyes		20	26	21	26	21
Mean radius of curvature ± [SD] (mm)	PAC	7.550 ±0.28	7.809 ±0.35	7.649 ±0.34	7.634 ±0.26	7.483 ±0.25
	PEC	8.012 ±0.25	8.310 ±0.39	8.060 ±0.34	8.073 ±0.29	7.944 ±0.32
	CLT	10.469 ±0.43	10.508 ±0.40	10.044 ±0.41	10.120 ±0.41	10.292 ±0.48
	ASC	13.805 ±0.75	13.692 ±0.61	13.130 ±0.65	13.143 ±0.58	13.320 ±0.71

Table 8.3: Comparison of mean regional curvature with increasing refractive error group; horizontal (180˚) profile

Statistically significant differences in the regional radii of curvature across the refractive error groups along the horizontal profile were found between:

- PAC: GP1 - GP2; -0.26±0.09mm [SEM] (p=0.034) flatter
- PEC: GP1 - GP2; -0.30±0.10mm [SEM] (p=0.021) flatter
- CLT: GP1 – GP3; 0.42±0.13mm [SEM] (p=0.015) steeper
- ASC: GP1 – GP3; 0.67±0.21mm [SEM] (p=0.012) steeper
- ASC: GP1 – GP4; 0.66±0.20mm [SEM] (p=0.009) steeper

b) Positive oblique (45) Meridian

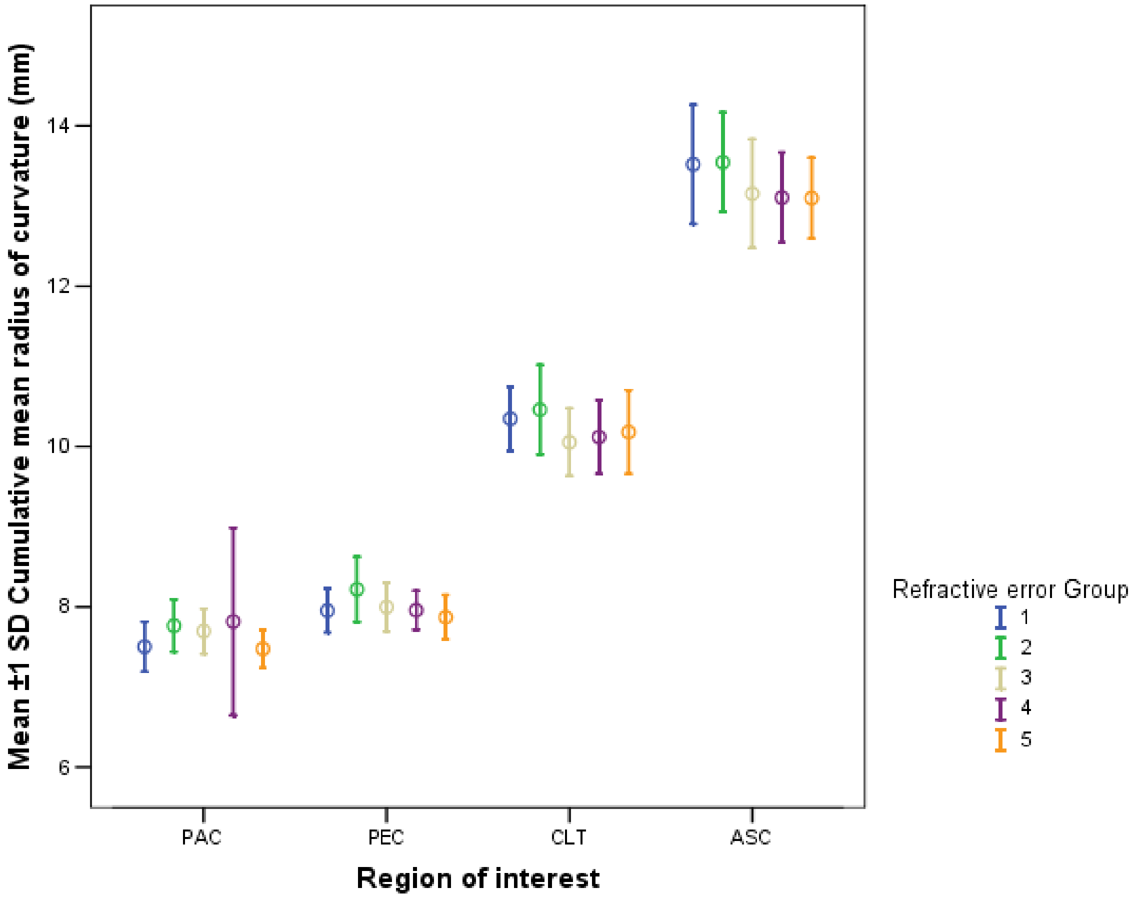

Figure 8.22: Comparison of mean regional radius of curvature changes related to myopic refractive error: positive oblique (45˚) profile

Comparison of regional curvature with increasing myopic refractive error *Oblique (45) Profile*						
	Location	GP1	GP2	GP3	GP4	GP5
Number of eyes		20	26	21	26	21
Mean radius of curvature ± [SD] (mm)	PAC	7.503 ±0.31	7.766 ±0.33	7.648 ±0.28	7.596 ±0.25	7.477 ±0.24
	PEC	7.954 ±0.27	8.160 ±0.32	7.998 ±0.30	7.959 ±0.24	7.871 ±0.28
	CLT	10.469 ±0.43	10.508 ±0.40	10.044 ±0.41	10.120 ±0.41	10.292 ±0.48
	ASC	13.520 ±0.74	13.546 ±0.62	13.155 ±0.68	13.123 ±0.56	13.099 ±0.50

Table 8.4: Comparison of mean regional curvature with increasing refractive error group; positive oblique (45˚) profile

Statistically significant differences in regional radii of curvature across refractive error groups were only found between:

- PAC: GP1 - GP2; -0.26±0.08mm [SEM] (p=0.020) flatter

c) Vertical (90˚) Meridian

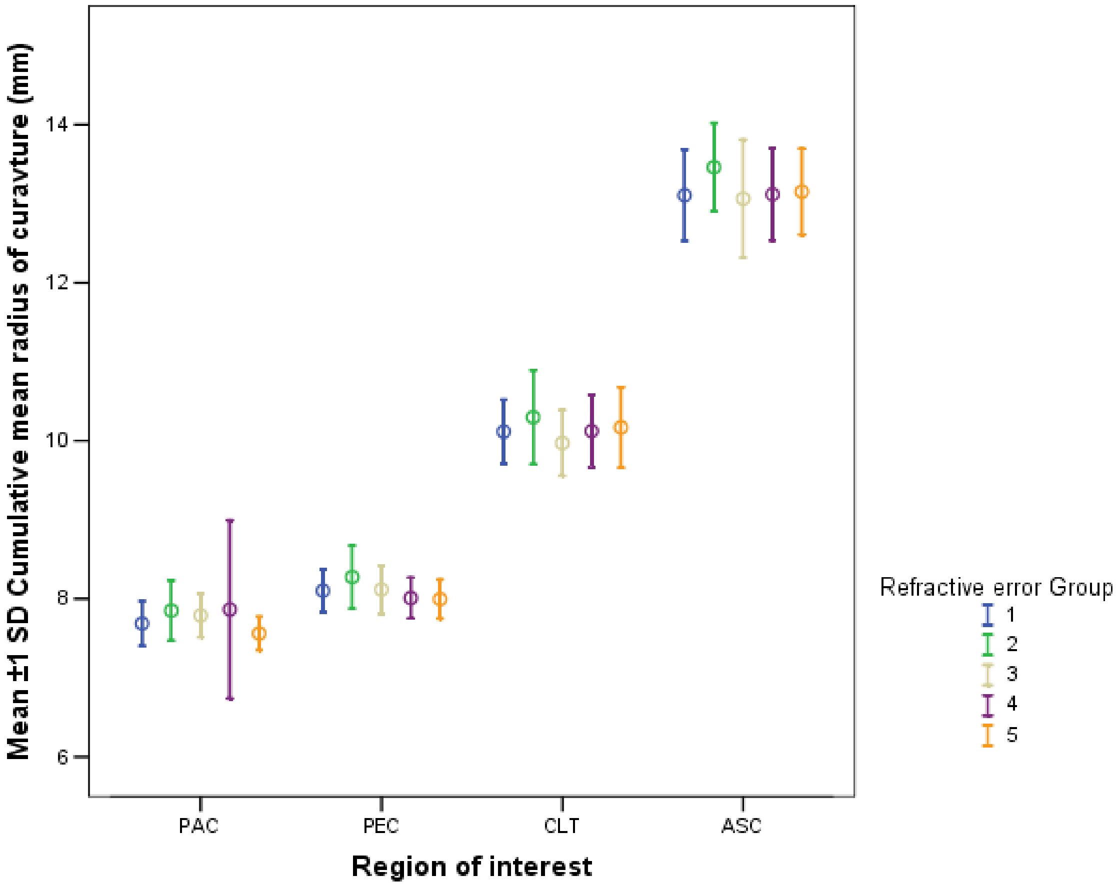

Figure 8.23: Comparison of mean regional radius of curvature changes related to myopic refractive error: vertical (90˚) profile.

Comparison of regional curvature with increasing myopic refractive error *Vertical (90) Profile*						
	Location	GP1	GP2	GP3	GP4	GP5
Number of eyes		20	26	21	26	21
Mean radius of curvature ± [SD] (mm)	PAC	7.688 ±0.28	7.851 ±0.38	7.789 ±0.28	7.655 ±0.27	7.561 ±0.21
	PEC	8.102 ±0.27	8.275 ±0.40	8.117 ±0.31	8.009 ±0.26	7.996 ±0.25
	CLT	10.114 ±0.41	10.297 ±0.59	9.971 ±0.41	10.122 ±0.46	10.168 ±0.51
	ASC	13.106 ±0.58	13.461 ±0.56	13.064 ±0.75	13.126 ±0.57	13.152 ±0.54

Table 8.5: Comparison of mean regional curvature with increasing refractive error group; vertical (90˚) profile

No statistically significant differences in regional cumulative radii of curvature across refractive error groups were found for the vertical profile.

d) Negative oblique (135˚) meridian

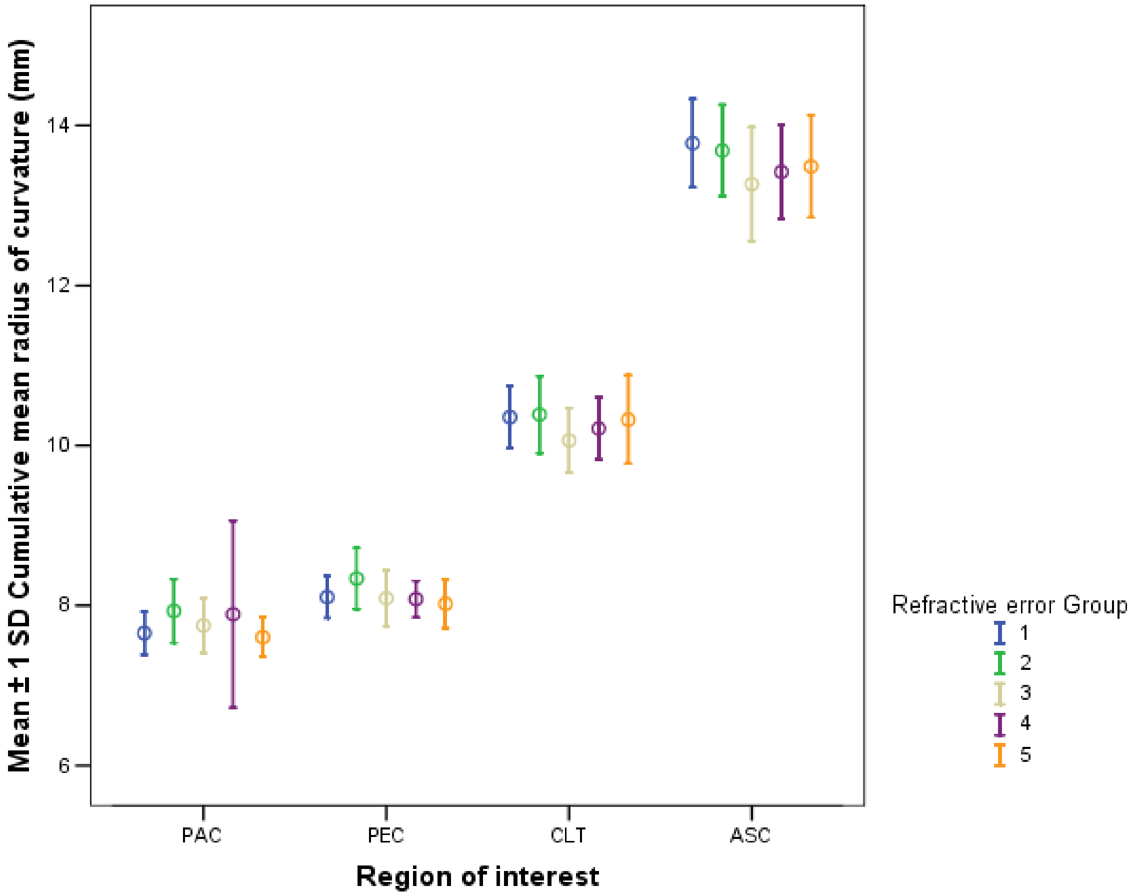

Figure 8.24: Comparison of mean regional radius of curvature changes related to myopic refractive error: negative oblique (135˚) profile.

Comparison of regional curvature with increasing myopic refractive error *Oblique (135) Profile*						
	Location	GP1	GP2	GP3	GP4	GP5
Number of eyes		20	26	21	26	21
Mean radius of curvature ± [SD] (mm)	PAC	7.654 ±0.27	7.932 ±0.40	7.749 ±0.34	7.670 ±0.24	7.604 ±0.25
	PEC	8.105 ±0.26	8.337 ±0.38	8.091 ±0.35	8.081 ±0.23	8.022 ±0.30
	CLT	10.354 ±0.39	10.387 ±0.48	10.063 ±0.40	10.213 ±0.39	10.324 ±0.55
	ASC	13.779 ±0.55	13.686 ±0.57	13.267 ±0.71	13.427 ±0.58	13.488 ±0.64

Table 8.6: Comparison of mean regional curvature with increasing refractive error group; negative oblique (135°) profile.

Statistically significant differences in regional radii of curvature across refractive error groups were only found between:

- PAC: GP1 - GP2; -0.27±0.09mm [SEM] (p=0.026) flatter

Section summary: 8.5.5.1

The majority of changes in regional curvature between refractive error groups were observed along the horizontal profile, when compared to the average refractive error group (GP1) radii were:

- At PAC and PEC: flatter in low myopes (up to -2.00DS)
- At CLT and ASC: steeper in moderate myopes (-2.25 to -4.00DS)
- At ASC: steeper in moderate myopes (-4.25 to -6.00DS)
- PAC was found to be flattened along the positive and negative oblique meridians (GP1-GP2).
- No significant changes were found along the vertical profile.

The following section maps these changes in relation to location (taking into consideration profile aspect) and refractive error group.

8.5.5.2 Anatomical location comparison

The influence of increasing myopic refractive error on AOS curvature, comparison with GP1 (Plano to +2.00DS).

a) Low Myopes (-0.25DS to -2.00DS)

GP1 compared to low myopes (-0.25DS to -2.00DS); GP1 minus GP2.

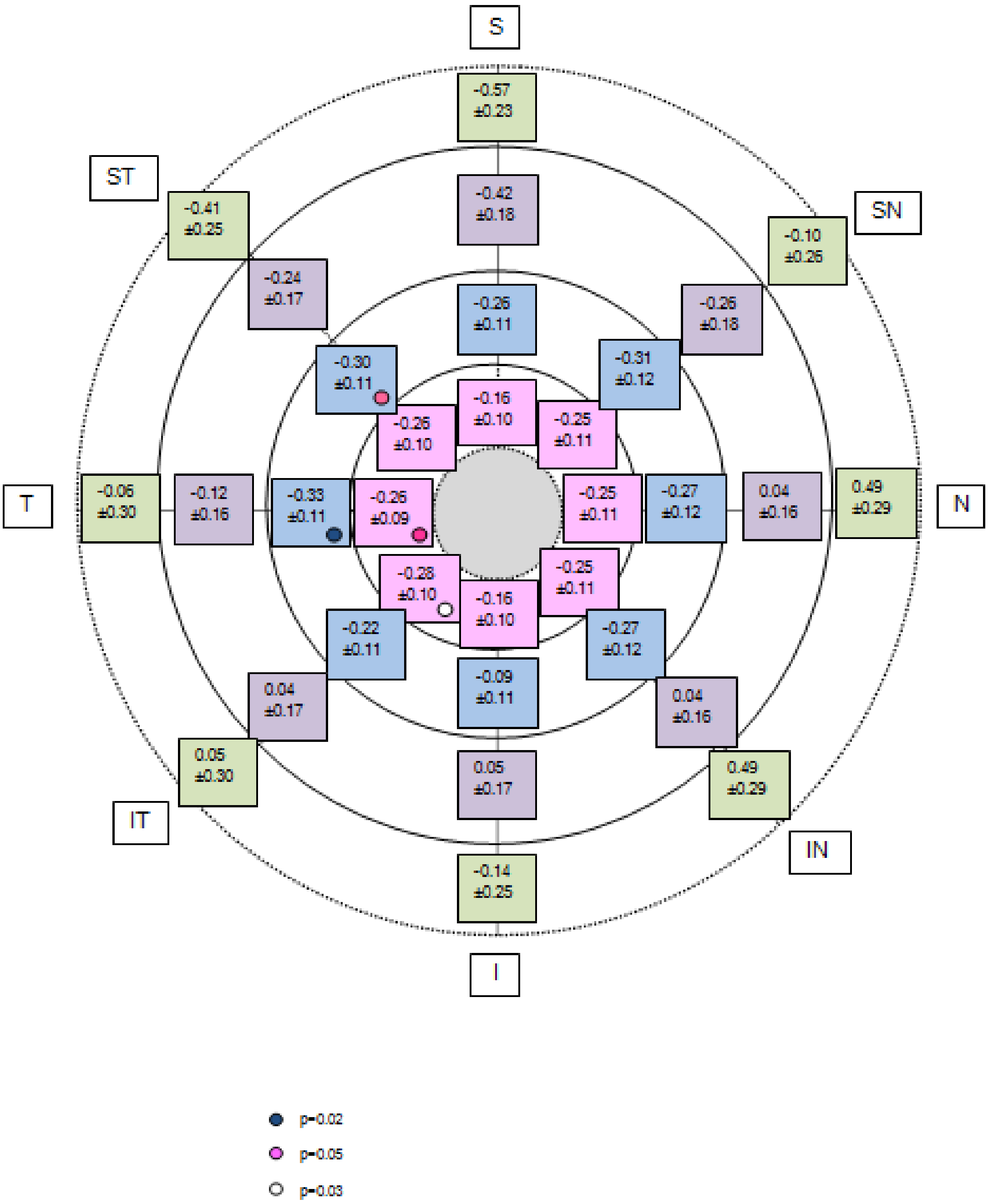

Figure 8.25: Comparison map of AOS curvature between GP1 and GP2 (GP1 minus low myopes), the numerical values displayed in each box are the $\overline{x}$ difference in mean radii of curvature ± [SEM], the small coloured circles indicate statistical significances found.

Significant flattening of the radii of curvature in low myopes was observed at locations:

- PACT (-0.26mm ±0.09 ,p=0.05) and PACIT (-0.28mm ±0.10, p=0.03)
- PCST (-0.30mm ±0.11,p=0.05) and PCT (-0.33mm ±0.11, p=0.02)

b) Moderate myopes (-2.25DS to -4.00DS)

GP1 compared to moderate myopes (-2.25DS to -4.00DS): GP1 minus GP3

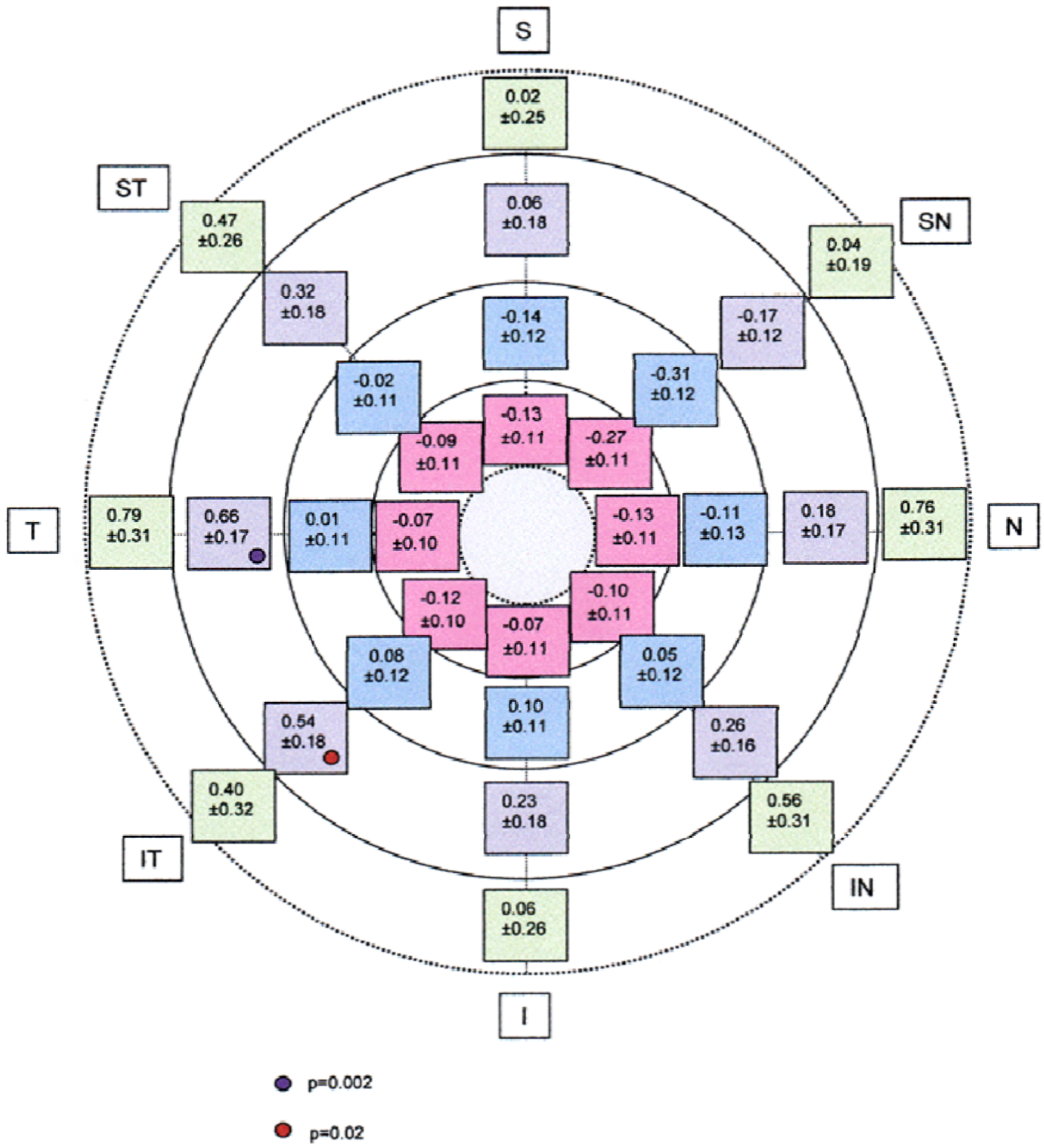

Figure 8.26: Comparison map of AOS curvature between GP1 and GP3 (GP1 minus moderate myopes), the numerical values displayed in each box are the $\bar{x}$ difference in mean radii of curvature ± [SEM], the small coloured circles indicate statistical significances found.

Significant steepening of the radii of curvature in moderate myopes (-2.25 to -4.00DS) was observed at locations:

- CLTT (0.66mm ±0.17 ,p=0.002) and CLTIT (0.54mm ±0.18, p=0.02)

c) Moderate myopes (-4.25DS to -6.00DS)

GP1 compared to moderate myopes (-4.25DS to -6.00DS) ; GP1 minus GP4

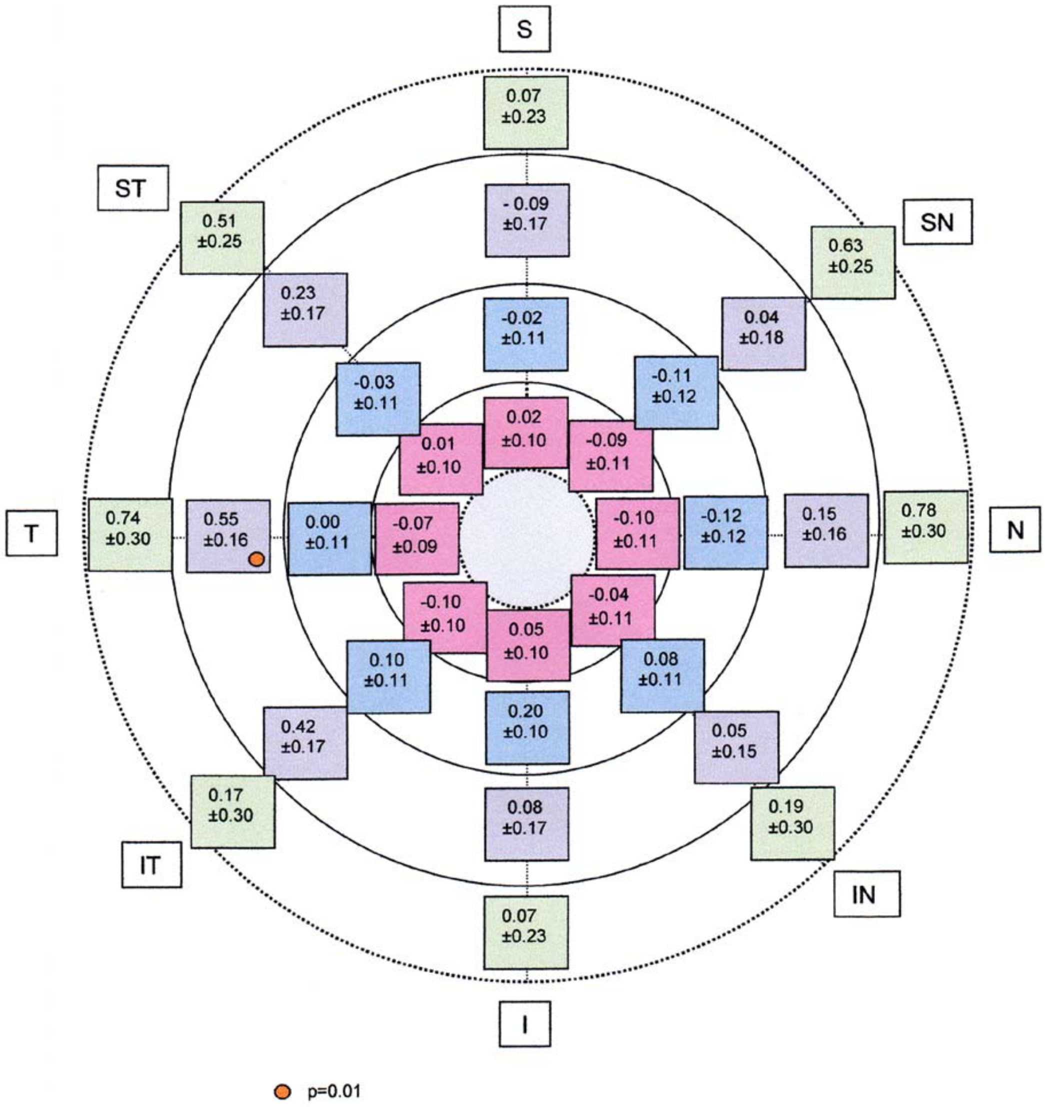

Figure 8.27: Comparison map of AOS curvature between GP1 and GP4 (GP1 minus moderate myopes), the numerical values displayed in each box are the $\overline{x}$ difference in mean radii of curvature ± [SEM], the small coloured circle indicates statistical significance found.

Significant steepening of the radii of curvature in moderate myopes (-4.25 to -6.00DS) was observed at location:

- CLTT (0.55mm ±0.16 ,p=0.01)

d) High myopes (-6.25DS to -8.00DS)

GP1 compared to high myopes (-6.25DS to -8.00DS) ;GP1 minus GP5

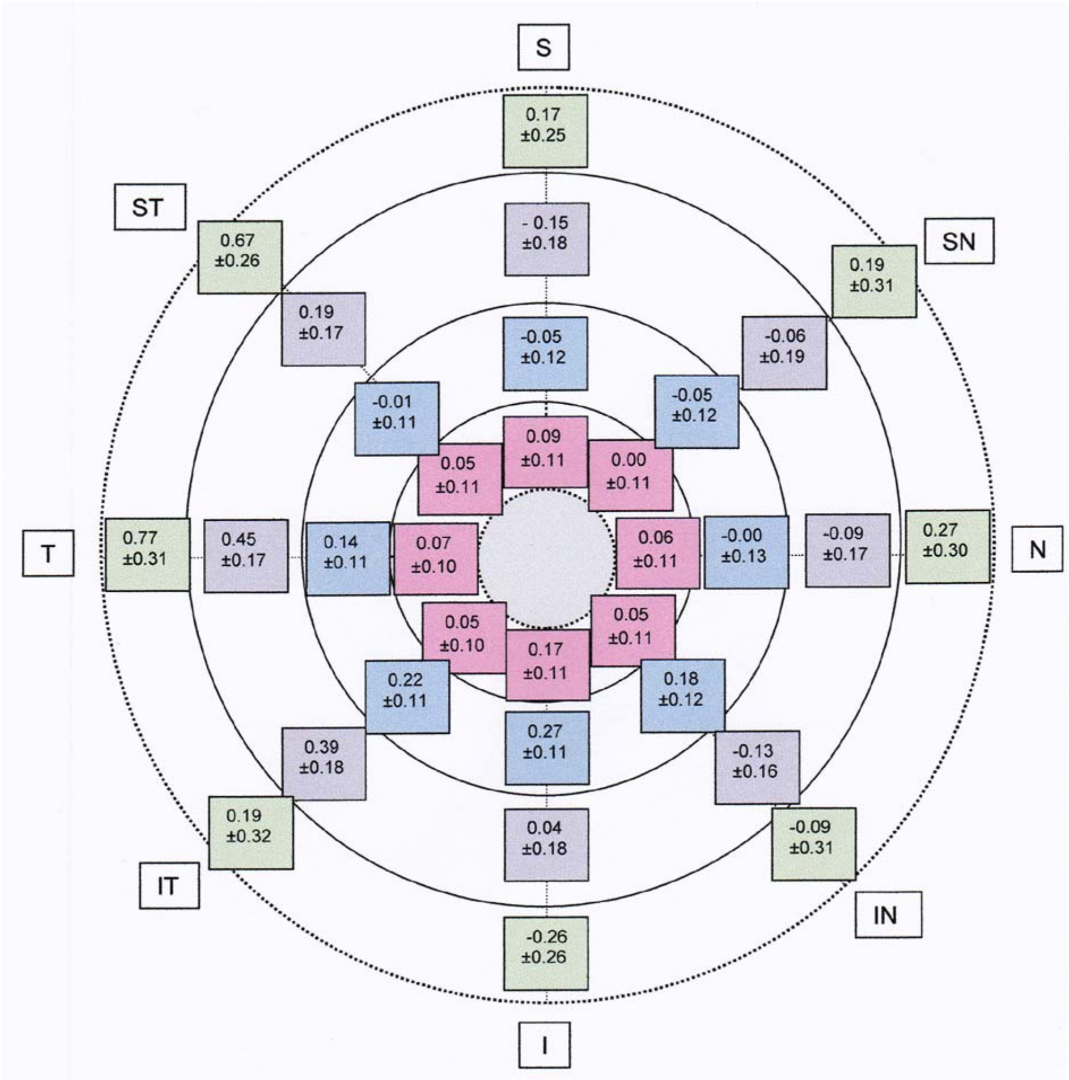

Figure 8.28: Comparison map of AOS curvature between GP1 and GP5 (GP1 minus high myopes), the numerical values displayed in each box are the $\bar{x}$ difference in mean radii of curvature ± [SEM], there were no statistical significances found.

No curvature changes were found comparing GP1 to high myopes (-6.25 to -8.00DS).

e) The effect of increasing myopia group on overall AOS profile

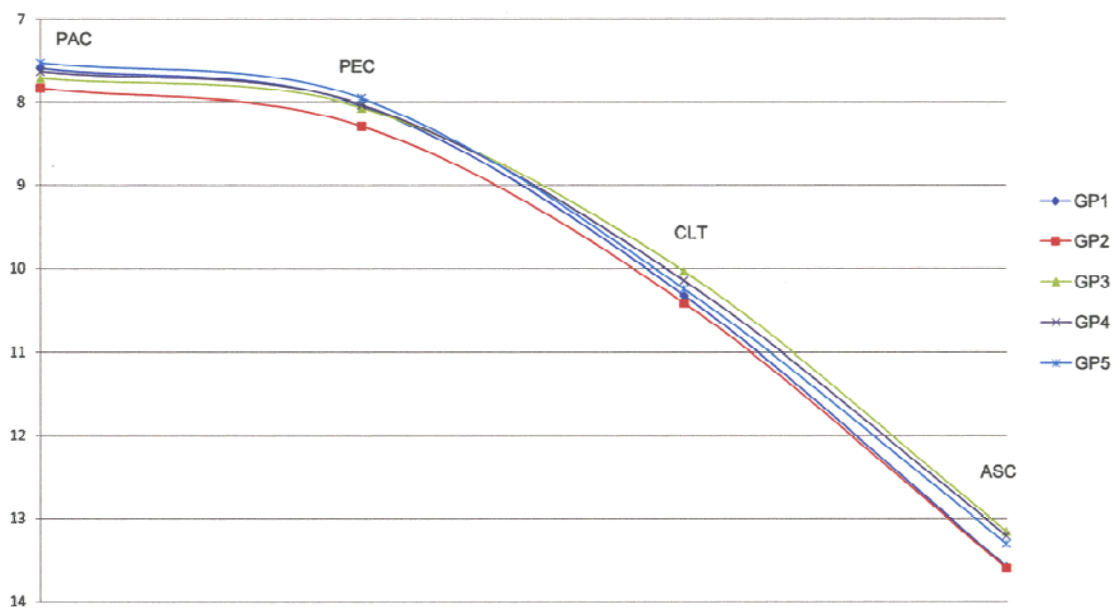

Figure 8 29: Graph to show the average profile for each refractive error group.

Regional profiles with respect to refractive error group were compared for visual comparison (Fig 8.23). GP2 (low myopes) were observed to have flatter corneal radii than the average refractive error group, GP1. GP3 (moderate myopes -4.25 to -6.00DS) were observed to have the steepest CLT radii of all the groups.

Section Summary: 8.5.5.2

Changes in mean radii of curvature along specific profile locations were observed when comparing GP1 to groups of increasingly myopic individuals following post hoc testing, specifically:

1. Low myopes (up to -2.00DS) flattening to the cornea:

PACT (-0.26mm ±0.09 ,p=0.05) and PACIT (-0.28mm ±0.10, p=0.03)
PCST (-0.30mm ±0.11,p=0.05) and PCT (-0.33mm ±0.11, p=0.02)
Flattest changes in radii to the peripheral cornea.

2. Moderate myopes (-2.25 to -4.00DS) steepening to the corneo-limbal transition:

CLTT (0.66mm ±0.17 ,p=0.002) and CLTIT (0.54mm ±0.18, p=0.02)

3. Moderate myopes (-4.25 to -6.00DS) steepening to corneo-limbal transition:

CLTT (0.55mm ±0.16 ,p=0.01)

4. High myopes (-6.25 to -8.00DS) no changes to AOS curvature observed.

8.6 Discussion

8.6.1 Description of the AOS – profile variation and symmetry

8.6.1.1 Central corneal enigma

Horizontal Keratometry (mm)	Vertical Keratometry (mm)	Range	Measurement method	Reference
7.40 ± 0.22 [SD]	7.22 ± 0.68 [SD]	5.62 to 7.70	Impression topography	This study
7.91 ± 0.26 [SD]	7.76 ± 0.26 [SD]	7.30 to 8.55	Javal-Schiötz	This study
7.86	Not reported	7.30 to 8.40	Javal-Schiötz	(Gullstrand, 1924)
7.78 ± 0.29 [SD]	7.63 ± 0.29 [SD]	7.28 to 8.80	Javal-Schiötz	This study
7.80	Not reported	7.12 to 8.49	Javal-Schiötz	(Gullstrand, 1924)
7.82 ± 0.29 [SD]	7.67 ± 0.30 [SD]	7.28 to 8.80	Javal-Schiötz	This study
7.86	Not reported	7.00 to 8.65	Javal-Schiötz	(Stenström, 1948)
7.65	7.51	Not reported	Javal-Schiötz	(Daily and Coe, 1962)
7.80	Not reported	7.20 to 8.40	Javal-Schiötz	(Ruben, 1975)
7.69 ± 0.26 [SD]	Not reported	7.10 to 8.55	Javal-Schiötz	(Davies et al., 2003)

Table 8.7: Central corneal curvature measurements and comparisons (blue shading indicates male gender, pink shading indicates female gender, no shading indicates mixed gender).

This study has shown that the paracentral cornea locations had the least variable morphometric examined across the 5 anatomical regions described and had average radii 7.67±0.03mm [SEM] (range 6.31 to 8.66). This finding supports the current use of keratometry to evaluate the central corneal curvature. The Javal-Schiötz keratometer has been designed to measure the spherical curvature of a reflected surface at a distance close to 1.47 mm either side of the instrument axis (in this case the line of fixation) (Bennett and Rabbetts, 1991). This positions the mires on opposite sides of the corneal apex and so even if one aspect is steeper than the other, it results in an average value of the two sides (Smith, 1977). However, this is unlikely to happen, since impression topography has revealed that this cohort exhibits a degree of asymmetry throughout this region, with the greatest curvature variation between the superior and inferior aspects and supra-temporal and infero-nasal aspects, questioning the accuracy of the vertical keratometry metric.

The Javal-Schiötz design assumes that the corneal apex was centred on the instrument axis, but studies have shown that the apex positions are seldom found coincident with the line of fixation, with no directional trend (Mandell, 1969). Angular misalignment greater than 2-3° of the corneal surface has been found to underestimate the 3rd and 4th order corneal surface aberrations (Salmon and Thibos, 2002) affecting the outcome of corneal refractive surgery. Crucially, these procedures require an accurate representation of the central cornea within 6-7 mm of the apex, enabling tissue restructuring to influence refractive error. However, the conclusions drawn in Chapter 3 provide evidence to suggest that the algorithms employed by the Orbscan IIz and Pentacam topographic systems (often used during surgical planning) have been influenced by traditional keratometric corneal values, which, although longstanding and accepted by the ophthalmic and optometric community, appear to compromise the fidelity of the AOS contour representation.

This conclusion finds support from a small mire keratometry study of 26 individual corneal profiles, found to be accurate and repeatable (± 0.25mm), and which postulated that every corneal was ‘as unique as a fingerprint’ (Mandell, 1992) (Fig 8.30). Furthermore, Fig 8.31 exemplifies the use of wave front aberrometry, showing the highly individual nature of each AOS.

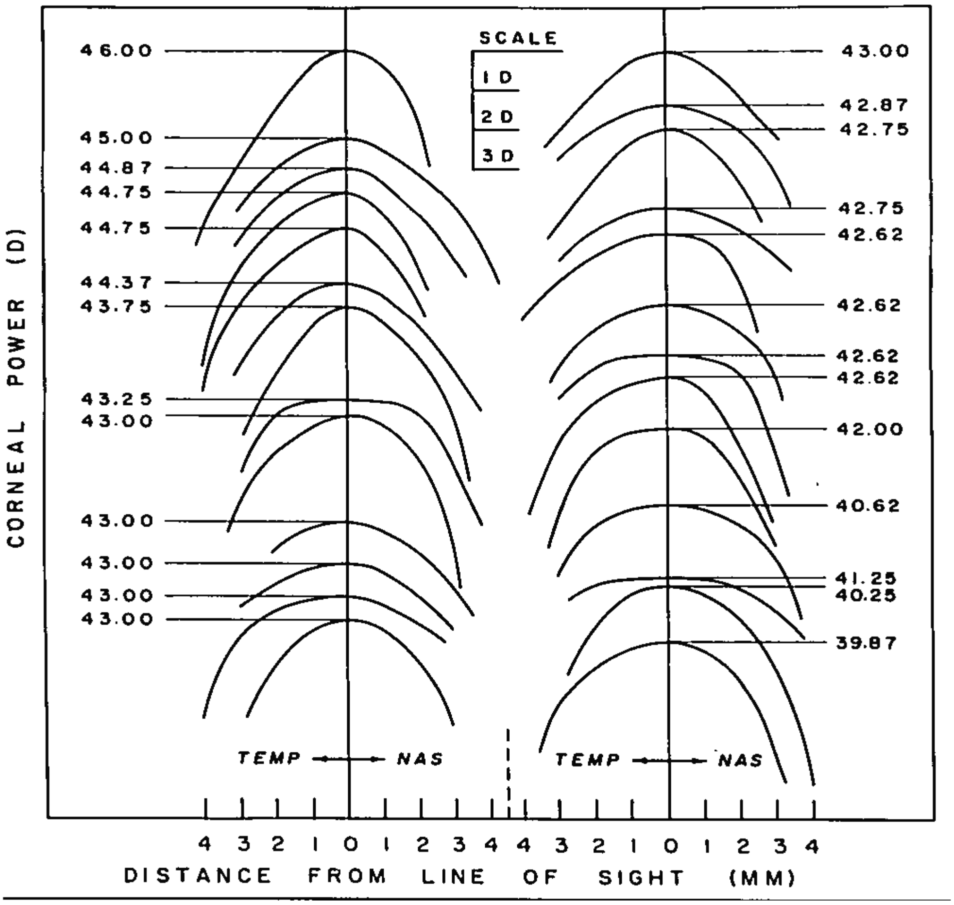

Figure 8.30: Central corneal profiles (n=26) along the horizontal meridian measured using small mire keratometry (Mandell, 1992).

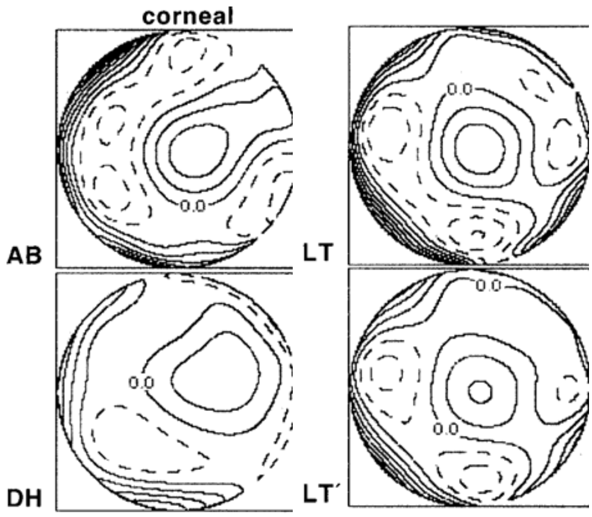

Figure 8.31: Diagram to show the higher-order, wave-front aberration contour plots of the AOS of 4 individuals (Salmon and Thibos, 2002).

However, while the Cardiff Eyeshape protocol avoids this error, the central corneal morphometric provided by impression methods was affected by a lack of precise apical registration, and by errors inherent in the mathematical function used as angles become small close to the instrument axis (approaching zero). The values seen in Table 8.7 reflect the steeper radii found in the vertical meridian 7.22±0.68mm [SD] compared with 7.40±0.22mm [SD] in the horizontal meridian as previously measured. These were steeper than the traditional keratometry values due the nature of the unique surface topography and mean radii method used to establish them.

The mean J-S keratometry values for the cohort 7.75±0.28mm [SD] compared favourably with those in a similar university population in the United Kingdom (n=198) aged 16-60, 7.69±0.26mm [SD], although ethnicity was not stated and may account for the slightly steeper value (Davies et al., 2003).

Comparative measurements of J-S between genders were shown to be similar to values taken during early usage of the J-S keratometer (ophthalmometer) (Gullstrand, 1924). This suggested that the central corneal keratometry measurements for the white European population have not altered significantly during the last 87 years; females were found to have steeper than average keratometry measurements than the males by 0.13±0.23mm [SD]. This difference undoubtedly has clinical implications for both contact lens fitting and refractive surgery.

The PAC and PEC regions of the cornea were shown to maintain asymmetric integrity and the least variability across the regions for the cohort investigated. These regions were characterised by the area of highest predictability and regularity, which may attribute to the success and stability of gas permeable contact lenses covering up to a 10mm diameter (5mm either side of the apex) (Worp et al., 2002), (Gill, 2010)

8.6.1.2 Wider horizons

Anterior scleral radius of curvature (mm)	Measurement method	Reference
About 12mm	Anatomical callipers	(Hogan et al., 1971)
Temporal curves 14-18mm (57%)	Shadow photography asymmetry observed	(Marriott, 1966)
Nasal curves Over 40 mm		
Vertical curves 15.30 to conical		
11-12 mm assuming globe is spherical	Scleral lens fitting	(Watson et al., 2004)
12.40mm (range 10.10 to 16.60)	Best fit sphere using AS-OCT Visante™ images	(Worp, Graf and Caroline, 2010)
14 to 19 mm	Moiré interferometry	(Jongsma et al., 1998)
Steepest superior aspect 12.84mm, flattest inferonasal aspect 14.14mm, wide variation (range 10.34 to 18.41)	Non-contact active laser triangulation of ocular impression cast surface	This study

Table 8.8: Anterior scleral curvature review

Studies using the Eye surface shape profiler prototype (Meye Optics, Eindhoven, Netherlands) have been able to measure the AOS of the open eye up to 18mm (Fig 8.32) in the horizontal meridian in a similar point-to-point curvature evaluation method (Fig 8.33) (Worp et al., 2010).

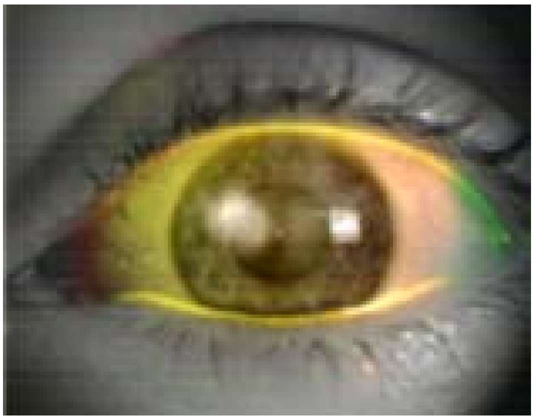

Figure 8.32: Photograph of the anterior eye indicating the area measured using Moiré interference techniques employed by the Eye surface shape profiler (Snepvangers, 2010).

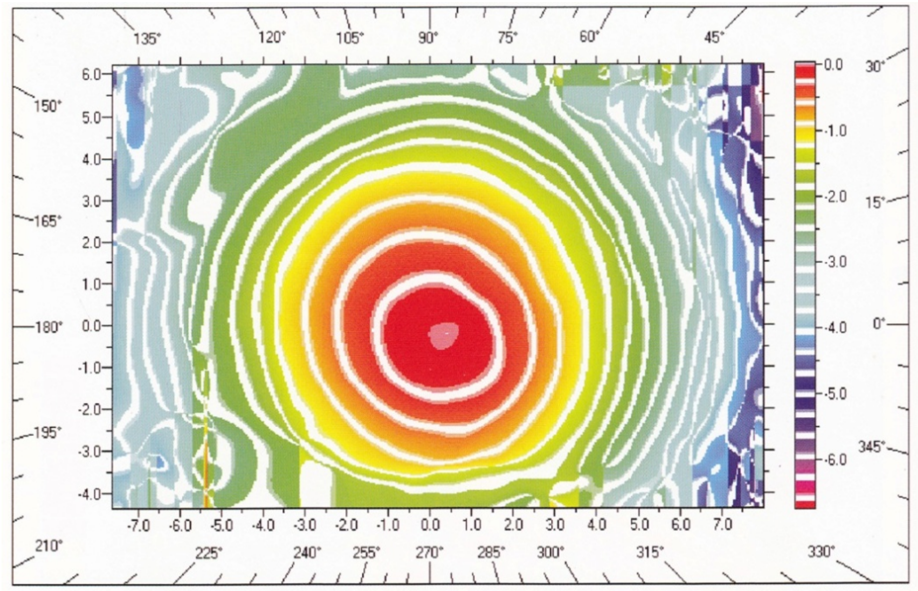

Figure 8.33: A 2-dimensional plot of corneal contour displaying areas of equal elevation by false colour representation measurements obtained by Moiré interferometry (Corbett, Rosen and O'Brart, 1999c).

A study using Moiré interferometry as a source of AOS morphometrics to aid contact lens fitting showed that the optimisation of rigid lens fitting required further data relating to the mid-peripheral (or PEC) region in 88% of cases (Worp et al., 2002). Improvements in scleral lens fitting have been described using AS-OCT techniques (Gemoules, 2008), although these were also limited by accessibility to anatomical regions particularly in the vertical meridian. It therefore follows that larger diameter semi-limbal and scleral contact lens fitting processes would benefit from enhanced AOS metrics provided by this study.

This investigation has extended the limit of AOS morphometrics to encompass regions covered by both eyelids and is presented here as the new ‘gold standard’ for wide-field AOS topographic representation. For the first time, the quantification of surface characteristics of the entire anterior scleral region have been demonstrated, and these locations were found to display significant asymmetry and regional variability. The steepest radii were found in the vertical meridian beneath the upper lid and flattest in the infero-nasal aspect beneath the lower lid.

8.6.1.3 The influence of myopic refractive error on AOS topography

a) Low myopes (Up to -2.00DS)

The AOS was found to be flatter at the temporal PAC and PEC (along the horizontal meridian) and at the supra-temporal PEC and infero-temporal PAC. All changes were found in the temporal aspect, suggesting some resistance to deformation on the opposing nasal side. These changes may be attributed to:

- Corneal thickness; found to be thinnest in the temporal aspect (Liu, Huang and Pflugfelder, 1999).
- Tensile differences within the lamellar structure; preferential orientation of stromal lamellae (Fig 8.34) provides mechanical stiffness highest in preferred directions of lamellae (Boote et al., 2006). This produces areas of structural vulnerability to localised change, i.e. flattening during an active global expansion process

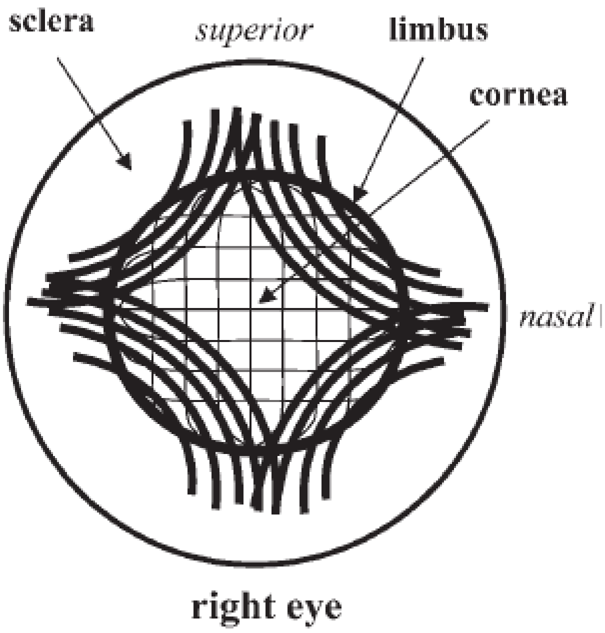

Figure 8.34: Idealised theoretical model showing directions of preferential alignment, reinforcing collagen fibrils in cornea, limbus and adjacent sclera of the right eye (Boote et al., 2006).

- Tensile differences in a secondary tension ring; afforded by the extraocular muscle insertions; shorter distance to nasal medial rectus insertion (5.50mm) than the temporal lateral rectus insertion (6.90mm), together with stronger muscle action than opposing lateral rectus (Hogan et al., 1971), providing increased tension to the nasal aspect limiting expansion deformability. Resistance to indentation was found to be lowest at the supra-temporal aspect of the anterior sclera (Patel et al., 2011).

Flattening of the peripheral cornea has been reported with increasing myopia using TMS-1 computerised video-keratoscopy, this is associated with increasing vitreous chamber depths and axial elongation (Carney, Mainstone and Henderson, 1997). The present study found that this only occurred in the low myope group. It is possible that deformation of the AOS by impression techniques had obscured this observation, and further investigation is necessary to evaluate the precise effect in order to factor it out.

b) Moderate myopes (-2.25 to -6.00DS)

The AOS was found to be steeper in the temporal and infero-temporal aspects of the CLT. This may be due to:

- Compression of the apex by ocular impression taking; regional pressure at the apex combined with unloading behaviour of the cornea (Elsheikh, 2010) resulting in ‘bulging’ at the CLT.
- Vulnerability to localised deformation during global expansion; as discussed for low myopes.
- A different target tissue for the expansion mechanism: higher levels of retinal defocus may drive changes to different areas of the globe, hence no corneal changes measured for this group compared to GP1
- A combination of some or all of the above.

<u>c) High Myopes (-6.25 to -8.00DS</u>)

There were no significant differences found in AOS locations comparing high myopes to GP1. This suggested that:

- The target tissue for global expansion mechanism during myopic progression in high myopia may be situated beyond the AOS investigated in this study.
- High myopes have AOS topography similar to GP1

<u>Type 1 statistical errors:</u> 128 statistical comparisons have been made across 4 merdians, to ensure against type 1 statistical errors, p-values of less than 0.008 should only be considered significant. According to these criteria, only one of the curvature comparisons made between locations for increasing myopic refractive error groups are significant (p=0.002)

8.6.1.4 The influence of Gender on AOS topography

This study found that the volume of the AOS measured in females was significantly larger than males, yet this decrease in volume was not observed to effect uniform changes in surface curvature. Volumes of the AOS (4mm below the origin) were found to be larger in the male group, on average 10.55± 3.87mm^3 [SEM] (F=0.152 t=-2.724), this was found to be statistically significant p<0.01.

As expected, the curvature steepened, but only to significant levels in the vertical and negative oblique meridians (p=0.026 and p=0.032). This may be explained by an asymmetric growth pattern favouring the near horizontal meridian (12.5°) along the palpebral aperture as the 'path of least resistance', which, on further expansion to reach male dimensions, has flattened in the near vertical meridian accordingly.

8.7 Conclusions

- Impression techniques can be used to provide wide-field topographic point-to-point curvature morphometrics of some areas of the AOS which have not previously been quantified. This technique is presented as the new 'gold standard'.

- Changes to the AOS with increasing myopia have been documented revealing flattening of the paracentral and peripheral cornea in low myopes, steepening of the corneo-limbal transition in moderate myopes, and no changes in high myopes.
- Females have been found to have smaller ocular volume measurements than males, although smaller eyes are not uniformly symmetrical, vertical and negative oblique meridians were found to be steeper, suggesting an asymmetric growth pattern favouring the near horizontal meridian.
- Impression topography has the potential to provide improved AOS fidelity to customise refractive surgery protocols, improve contact lens and scleral shell design stability and comfort, and establish a baseline for the further understanding of AOS abnormality. It is acknowledged that for measurement of areas of the AOS accessible by reasonable adjustments of fixation, non-invasive techniques such as AS-OCT imaging should be considered preferable. Further work would be necessary to provide a robust statistical sample size of wide-field AOS topography and additional age-related white European population data.

Chapter 9

Overall Summary

The quality of optical, surgical or mechanical rehabilitation of a compromised AOS depends, to a significant extent, on the anatomical accuracy of the model used to represent it. Access to the *in-vivo* surface is limited by the size of the palpebral aperture, since the upper and lower eyelids cover most of the vertical aspect, and also by the micro-saccadic eye movements which characterise fixation. Nonetheless, recent developments to improve the outcome of such treatments have driven the need to provide reliable and highly accurate morphometrics of the AOS.

The overall aim of this thesis was:

- To review the current knowledge of the AOS topography and its limitations
- To establish a system of accurate and reliable data acquisition for the entire topographic profile of the human AOS *in-vivo*, represented as a virtual 3-dimensional model.
- To ensure that the methods used were optimised to maintain minimal discomfort and inconvenience to the patient.
- To provide an acceptable descriptor of the AOS topography with which to communicate curvature variability to professionals working within the field.

Therefore, with a view to improving patient care, this series of investigations attempted to find a non-invasive method of collecting fast, accurate, reliable and easily interpreted data for the entire AOS.

The aim of the comparison study in Chapter 3 was to establish the influence of 'traditional' keratometry on the design of 2 modern instruments that provide topographic data beyond the central cornea. It was found that the 3 devices can be used interchangeably to provide biometry for intraocular lens replacement procedures; however Pentacam topographic measurements were significantly flatter than Orbscan, excluding the use of Pentacam data with the Orbscan Fitscan RGP fitting software. The fidelity of the vertical AOS representation by Orbscan and

Pentacam appears to have been compromised by interpolation and image collection methodology, revealing that the corneal ‘dip’is an artefact.

In Chapter 2, the available technologies for data collection were reviewed and magnetic resonance imaging identified as the most likely system to fit the study requirements. However, after experimentation with different T-1 and T-2 weighted spin-echo sequence protocols, using a 3-Tesla MRI scanner with a blink artefact reduction device (Chapter 4), the optimal protocol yielded too few axial sections through the globe to procure sufficiently resolute data with which to differentiate the AOS and reconstruct digital 3-D representations. Further work using additional eye surface radio frequency coils and a 7-Tesla external magnetic field offers the best opportunity to achieving this goal.

In the absence of any less invasive technique, ocular impression taking was revisited as the next most viable opportunity, during the course of this study, to collect data for the entire AOS. Chapter 5 outlines a study to determine the clinical safety of 2 available impression taking materials. Few studies have been carried out to ascertain the effects of polyvinylsiloxane on the AOS, although it has been adopted by Optometrists and Ocularists as the industry standard. This randomised control trial found that the alginate, Orthoprint, caused an abnormal hyperaemic response to the bulbar conjunctiva, accompanied by significant superficial corneal staining. This may be attributed to a toxic reaction between the material and the eye surface, exacerbated by mechanical abrasion caused by eyelid movement and granular material apposition. Tresident, the polyvinylsiloxane, was considered the material of choice with fewer clinical complications and more stable, convenient handling properties. Clinical advice was offered here regarding management of patients having ocular impressions with Tresident. The incidental adherent properties of polyvinylsiloxane materials to cells of the AOS may offer a novel collection technique to study cytology.

Modernisation of the ocular impression procedure and casting protocol (CEP) was outlined in Chapter 6. The opportunity to design and manufacture using reverse engineering facilities allowed for the development of a system of casting support and registration. Devices for anatomical registration and scanning stabilisation of the eye-shaped cast enabled an active laser triangulation technique to be validated for the collection of 200,000 data points in a digital 3-dimensional format. The CEP was found to be repeatable (±0.008 ±0.021mm [SD]), reproducible (-0.0019 ±0.073mm) and the casts were stable for storage for up to a month (expanded by 0.027mm ±0.020 [SD]).

The modernised impression taking/casting procedure was scrutinised in Chapter 7 in a series of experiments with the aim of identifying whether the ocular surface topography is compromised by the invasive nature of the procedure. The Orbscan IIz and AS-OCT Visante™ were used to image the AOS and provide comparative topographic data. AS-OCT Visante™ was used to image the eye-shaped cast, which was compared to the AOS *in-vivo*, and identified a region from the peripheral cornea to the anterior sclera in the horizontal meridian which was flattened during ocular impression taking. This was found to be within clinically significant limits for contact lens fitting and within tolerance for lens manufacture. However, the imaging techniques were limited to the exposed AOS within the palpebral aperture, and further work would be required to expand the locations that were analysed and increase the sample size. This would provide a full 3-dimensional difference map.

Once the impression/casting process had been designated fit for purpose, a database of normal white European eyeshape was established (n=119). Individuals aged 18-40 years had ocular impressions taken and 3-dimensional virtual representations of the cast were obtained. Volumetric and 2-dimensional topographic profiles were extracted allowing for the analysis of point-to-point curvature morphometrics of some areas of the AOS which have not previously been quantified. Changes to the AOS with increasing myopia, in comparison to an emmetropic reference group, were documented, revealing flattening of the paracentral and peripheral cornea in low myopes, steepening of the corneo-limbal transition in moderate myopes, and no changes in high myopes. Females were found to have smaller ocular volume measurements than males, although smaller eyes are not uniformly symmetrical, the vertical and negative oblique meridians were found to be steeper, suggesting an asymmetric growth pattern favouring the horizontal meridian.

The new ocular impression/casting technique has been presented here as the 'gold standard' for wide-field anterior ocular surface data collection. The improved AOS fidelity can be used to provide enhanced morphometrics (Fig 9.1) to ophthalmic surgeons, ocularists, contact lens practitioners, vision scientists and researchers.

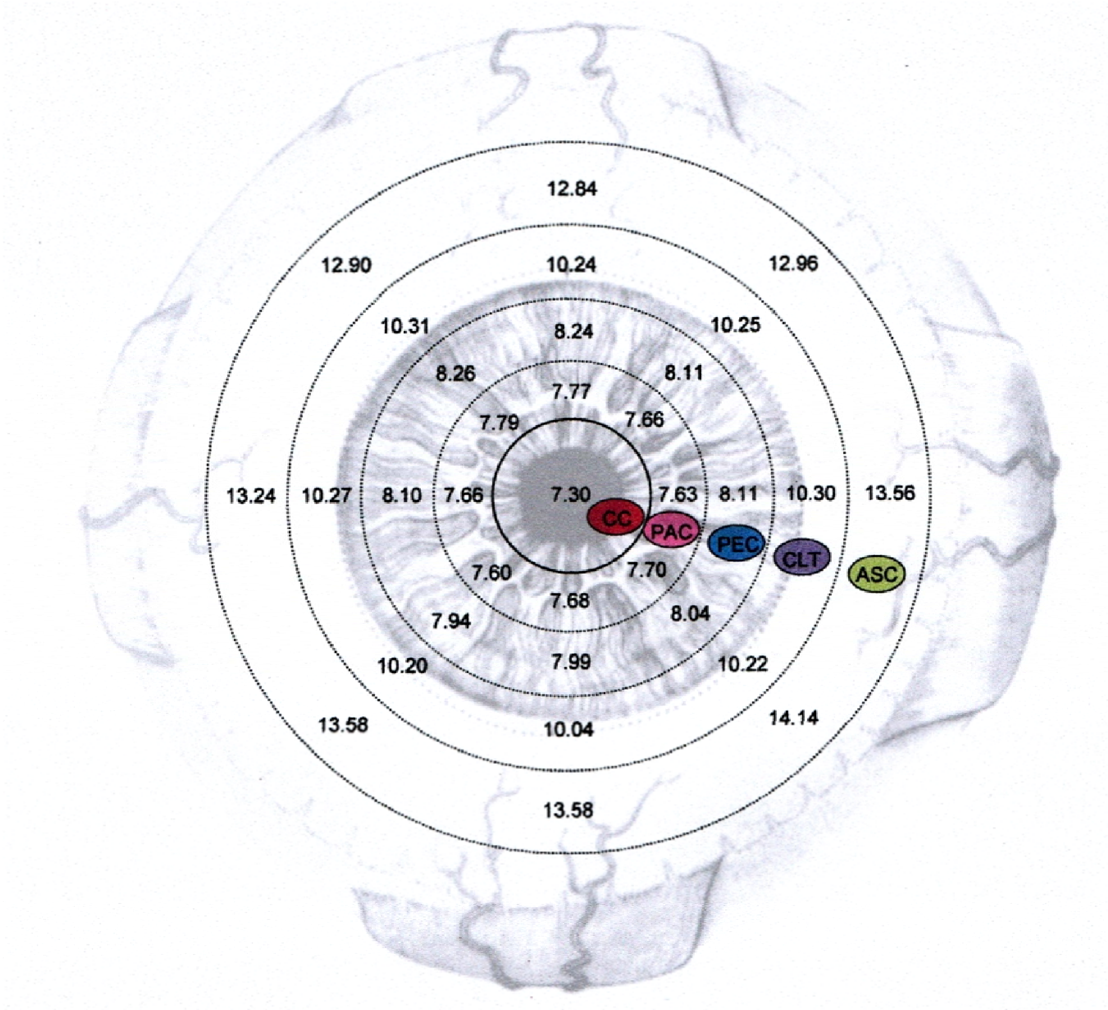

Figure 9.1: Diagram of the anterior ocular surface anatomy, adapted from (Hogan et al., 1971), showing the regions of anatomical interest and mean axial radii of curvature by location.

These have the potential to be used to:

- Refine planning for refractive surgical procedures (Feng et al., 2012), (Chan, Hodge and Sutton, 2010), (Dupps Jr and Wilson, 2006), (Smolek and Klyce, 2005)

- Design custom-made optical and cosmetic scleral shells (Pullum, Parker and Hobley, 1989), (Bowden, 2009),(Ezekiel, 1983)
- Improve the design characteristics of larger diameter (10-16mm) corneal contact lenses (Worp et al., 2002), (Eggink, Beekhuis and Nuijts, 2001)
- Add missing topographic parameters to finite element models of the AOS used to study intraocular pressure (Elsheikh, 2010)
- Improve curvature correction algorithms used by modern topographic data imaging systems (Dunne et al., 2007), (Cairns and McGhee, 2005)
- Provide baseline wide-field topography to understand fundamental changes that occur to the AOS due to abnormality (Saad and Gatinel, 2010), (McMonnies and Boneham, 2007) .

Each of the professions working with AOS morphometrics has varying requirements and tolerances on accuracy needed to fulfil the task criteria. For example, ophthalmic surgeons use femtosecond laser systems to cut corneal flaps to an accuracy of ±0.001mm (Soong and Malta, 2009). This precision is crucial because very small changes to the cornea surface shape affect the refractive outcome which requires surgical planning accuracy in the region of ±0.20mm (Cairns and McGhee, 2005) or less than 0.42D (Smith, 2006). Similarly, contact lens designers work to a manufacturing tolerance of ±0.05mm (BS 18369-2, (BSI, 2006)) and those fitting them are able to discern a clinical difference of 0.05mm (back optic zone radius) (Gill, 2010) for corneal gas permeable contact lenses. Practitioners making and fitting scleral shells are the most forgiving, since this requires artistic skills and experience to work iteratively towards a comfortable, visually acceptable and cosmetically pleasing end-point. Finally, as in this study, researchers often do not know how accurate their requirements will be or need to be until the necessary preliminary studies have been carried out and the intended application identified. Finite mathematical modelling of the AOS used in glaucoma research, requires all aspects of the surface in question to be available to assess the interactive nature of the components as a system and their hierarchy (Elsheikh, 2010).

But not only have clinicians and researchers exacting demands, the outcome expectations for patients is also high; they would like to see clearly without spectacles, wear comfortable contact lenses all day, maintain a healthy optic disc throughout their life, and have prosthetic shells that look identical to the other eye. Until now assumptions about the sphericity and symmetry of the AOS have defined the success and reliability of any intervention using topographic measurements as the predominant data source.

This thesis has quantified the historic observations of glass blowers (Bowden, 2009) and scleral lens makers (Marriott, 1966) and expanded the scope of topographic knowledge of the anterior ocular surface to the hidden extremities. It has demonstrated the influence of accepted methods of examining AOS curvature variation over the design of modern ocular surface imaging devices and subsequent interpretation of the output.

Future Work

- Revisiting magnetic resonance imaging as a non-invasive method of data collection for the entire AOS.
- Compare AOS data obtained by ocular impression/casting with reconstruction from magnetic resonance imaging to obtain a 3-dimensional difference map of the entire surface.
- Optimising the profile sampling of the AOS using Orbscan and Pentacam to provide a 3-dimensional difference map.
- Carrying out biochemical analysis of the interaction between the AOS and Orthoprint.
- Investigating the optimal quantity of Tresident required producing the most accurate ocular impression.
- Reverse engineering the mean AOS to provide an anatomically accurate surface with which to further validate the CEP.
- Increasing the sample size of the cohort for the comparison of human AOS *in-vivo* and it's representative cast
- Developing a method of 3-dimensional mapping of the compression caused by ocular impression taking.
- Improving the design of ocular impression trays.
- Using curvature correction to factor out systematic flattening of the AOS caused by AS-OCT Visante™
- Increasing the sample size of database of white European eyeshape by a factor of 10, to provide an adequate population sample.
- Creating 3-dimensional difference maps to analyse the regional curvature variation between genders and groups with increasing myopic refractive error.
- Considering other methods of analysing complex curvature variation over a 3-dimensional surface.

Appendix

Poster and Oral Presentations

Turner J M, Le Chi H, Murphy P J, Nakajima T, Choppinet P, and Purslow C (2008) What shape is the front of the eye? Ocular impressions and casting. In: Speaking of Science. Cardiff University

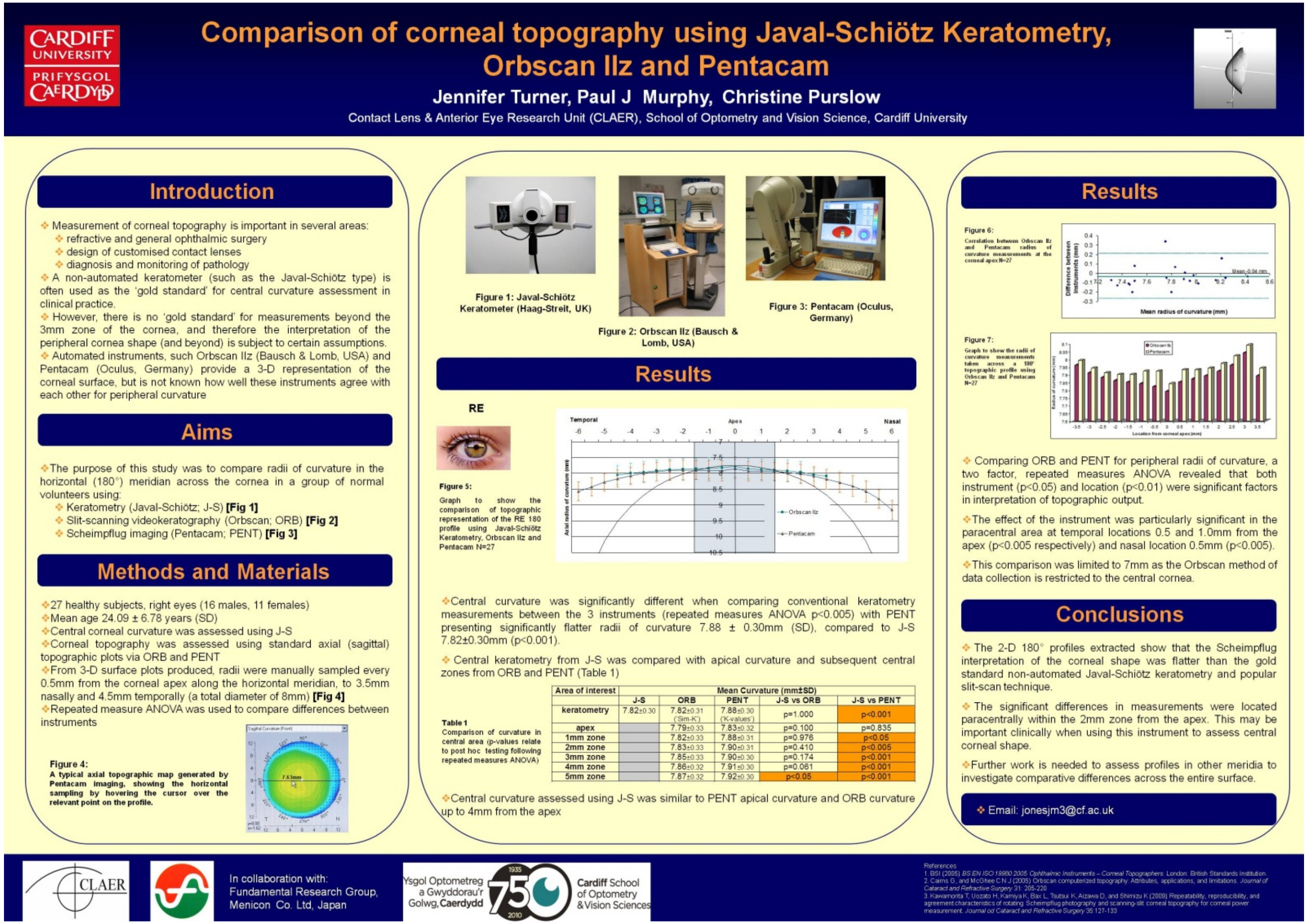

Comparison of corneal topography using Javal-Schiötz Keratometry, Orbscan IIz and Pentacam

Jennifer Turner, Paul J Murphy, Christine Purslow

Contact Lens & Anterior Eye Research Unit (CLAER), School of Optometry and Vision Science, Cardiff University

Introduction

- Measurement of corneal topography is important in several areas:
  - refractive and general ophthalmic surgery
  - design of customised contact lenses
  - diagnosis and monitoring of pathology
- A non-automated keratometer (such as the Javal-Schiötz type) is often used as the 'gold standard' for central curvature assessment in clinical practice.
- However, there is no 'gold standard' for measurements beyond the 3mm zone of the cornea, and therefore the interpretation of the peripheral cornea shape (and beyond) is subject to certain assumptions.
- Automated instruments, such Orbscan IIz (Bausch & Lomb, USA) and Pentacam (Oculus, Germany) provide a 3-D representation of the corneal surface, but is not known how well these instruments agree with each other for peripheral curvature

Aims

- The purpose of this study was to compare radii of curvature in the horizontal (180°) meridian across the cornea in a group of normal volunteers using:
  - Keratometry (Javal-Schiötz; J-S) **[Fig 1]**
  - Slit-scanning videokeratography (Orbscan; ORB) **[Fig 2]**
  - Scheimpflug imaging (Pentacam; PENT) **[Fig 3]**

Methods and Materials

- 27 healthy subjects, right eyes (16 males, 11 females)
- Mean age 24.09 ± 6.78 years (SD)
- Central corneal curvature was assessed using J-S
- Corneal topography was assessed using standard axial (sagittal) topographic plots via ORB and PENT
- From 3-D surface plots produced, radii were manually sampled every 0.5mm from the corneal apex along the horizontal meridian, to 3.5mm nasally and 4.5mm temporally (a total diameter of 8mm) **[Fig 4]**
- Repeated measure ANOVA was used to compare differences between instruments

Figure 4: A typical axial topographic map generated by Pentacam imaging, showing the horizontal sampling by hovering the cursor over the relevant point on the profile.

Figure 1: Javal-Schiötz Keratometer (Haag-Streit, UK)

Figure 2: Orbscan IIz (Bausch & Lomb, USA)

Figure 3: Pentacam (Oculus, Germany)

Results

RE

Figure 5: Graph to show the comparison of topographic representation of the RE 180 profile using Javal-Schiötz Keratometry, Orbscan IIz and Pentacam N=27

- Central curvature was significantly different when comparing conventional keratometry measurements between the 3 instruments (repeated measures ANOVA p<0.005) with PENT presenting significantly flatter radii of curvature 7.88 ± 0.30mm (SD), compared to J-S 7.82±0.30mm (p<0.001).
- Central keratometry from J-S was compared with apical curvature and subsequent central zones from ORB and PENT (Table 1)

Table 1 Comparison of curvature in central area (p-values relate to post hoc testing following repeated measures ANOVA)

Area of interest	Mean Curvature (mm±SD)				
	J-S	ORB	PENT	J-S vs ORB	J-S vs PENT
keratometry	7.82±0.30	7.82±0.31 ('Sim-K')	7.88±0.30 ('K-values')	p=1.000	p<0.001
apex		7.79±0.33	7.83±0.32	p=0.100	p=0.835
1mm zone		7.82±0.33	7.88±0.31	p=0.976	p<0.05
2mm zone		7.83±0.33	7.90±0.31	p=0.410	p<0.005
3mm zone		7.85±0.33	7.90±0.30	p=0.174	p<0.001
4mm zone		7.86±0.32	7.91±0.30	p=0.061	p<0.001
5mm zone		7.87±0.32	7.92±0.30	p<0.05	p<0.001

- Central curvature assessed using J-S was similar to PENT apical curvature and ORB curvature up to 4mm from the apex

Results

Figure 6: Correlation between Orbscan IIz and Pentacam radius of curvature measurements at the corneal apex N=27

Figure 7: Graph to show the radii of curvature measurements taken across a 180° topographic profile using Orbscan IIz and Pentacam N=27

- Comparing ORB and PENT for peripheral radii of curvature, a two factor, repeated measures ANOVA revealed that both instrument (p<0.05) and location (p<0.01) were significant factors in interpretation of topographic output.
- The effect of the instrument was particularly significant in the paracentral area at temporal locations 0.5 and 1.0mm from the apex (p<0.005 respectively) and nasal location 0.5mm (p<0.005).
- This comparison was limited to 7mm as the Orbscan method of data collection is restricted to the central cornea.

Conclusions

- The 2-D 180° profiles extracted show that the Scheimpflug interpretation of the corneal shape was flatter than the gold standard non-automated Javal-Schiötz keratometry and popular slit-scan technique.
- The significant differences in measurements were located paracentrally within the 2mm zone from the apex. This may be important clinically when using this instrument to assess central corneal shape.
- Further work is needed to assess profiles in other meridia to investigate comparative differences across the entire surface.

Email: jonesjm3@cf.ac.uk

In collaboration with: Fundamental Research Group, Menicon Co. Ltd, Japan

References
1. BSI (2005) *BS EN ISO 19980:2005 Ophthalmic Instruments – Corneal Topographers*. London: British Standards Institution.
2. Cairns G., and McGhee C N J (2005) Orbscan computerized topography: Attributes, applications, and limitations. *Journal of Cataract and Refractive Surgery* 31: 205-220
3. Kawamorita T, Uozato H, Kamiya K, Bax L, Tsutsui K, Aizawa D, and Shimizu K (2009) Repeatability, reproducibility, and agreement characteristics of rotating Scheimpflug photography and scanning-slit corneal topography for corneal power measurement. *Journal od Cataract and Refractive Surgery* 35:127-133

Turner J M, Murphy P J, and Purslow C (2009) Comparison of corneal topography using Javal-Schiötz Keratometry, Orbscan IIz and Pentacam. In: 9th Corneal Conference. Dept of Optometry and Vision Sciences, Cardiff University.

Does ocular impression taking cause distortion of the ocular surface?

Jennifer Turner, Matthew Dobson, Paul J Murphy, Christine Purslow
Contact Lens & Anterior Eye Research (CLAER), School of Optometry & Vision Sciences, Cardiff University, UK

Purpose

Ocular impression taking remains a valuable method of obtaining information about ocular surface contour, but the amount of transient deformation during the procedure is unknown. Modern impression techniques with silicone-based compounds are used in clinical practice to design and manufacture contact lenses with optimal fit and comfort, to fit cosmetic shells that provide a realistic representation of the undamaged ocular surface, and to provide clues to the pathogenesis and development of structural anomalies procedures. The purpose of these two studies is to quantify any changes that may occur to the anterior ocular surface as a result of contact with the impression material and tray.

Study 1: To investigate the effect of ocular impression taking on the central cornea

Methods

To assess the effect of impression taking on the central cornea, 104 healthy white European subjects, (68 males, 35 females) with mean age 24.65±6.74 yrs (SD) were imaged. Central corneal topography was assessed using slit-scanning videokeratoscopy (Orbscan; ORB) [Fig 1]. The right eye of each individual was scanned before and 10 minutes after impression taking (3 repeats).

Figure 1: Orbscan IIz (Bausch & Lomb, USA).

Analysis

Mean axial curvature maps were sampled from the output screen using an overlay grid (0.5mm between points) [Fig 2]. Radii of curvature recorded along the extent of the horizontal and vertical meridia. Comparisons of radii of curvature were made at the apex (instrument axis) and with cumulative means of the radii of chords at 1-9mm away from the designated apex (instrument axis) [Fig 3]. Paired sample t-tests were used to compare differences found.

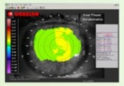

Figure 2: A typical axial topography map generated by slit-scan imaging, the cursor is used to sample the radius by hovering over the required grid point.

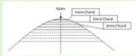

Figure 3: Diagram to show the chords chosen to analyse cumulative mean radii of surface contours.

Results

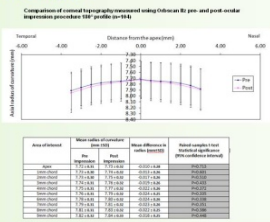

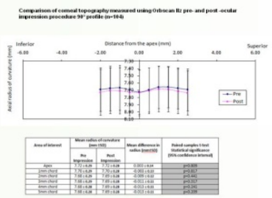

Across the central cornea, small, but insignificant, increases in the radii of curvature occur 10 minutes after impression taking (flattening),+0.018±0.25mm horizontally and +0.013±0.11mm vertically with a range of significance of 0.209<p<0.809. (In comparison, the Orbscan is highly accurate 0.0002±0.00032mm centrally and 0.0007±0.00041mm peripherally on test surfaces *(Cairns et al, 2002)*).

Study 2: Comparison of the impression cast and the ocular surface *in-vivo*

Methods

To compare the eye with a representative cast using AS-OCT techniques,12 healthy white European subjects, (5 males, 7 females) mean age 27.31±4.47 yrs (SD) had ocular impressions taken of the right eye, the ocular surface shape was cast in Type IV gypsum plaster.
Repeated A-scans of 16 x 6 mm were taken of the eye *in-vivo* and a representative cast using anterior segment ocular coherence tomography (AS-OCT Visante™; AS-OCT) [Fig 4 and 5].

Figure 4: AS-OCT Visante (Carl Zeiss Meditec, USA).

Figure 5: The cast was supported in a position aligned with ocular surface *in-vivo*.

Analysis

Horizontal and vertical profiles were extracted from quad scan sequences and the eye and cast profiles digitally aligned using Adobe Photoshop v 7.0. Profiles were sampled using Liberty BASIC 4.0 *(Dunne et al. 2007)* and a screen overlay grid (units of 0.42mm). Comparative profiles were graphed using Excel 2007 and assigned 4th order polynomial functions. These were used to calculate areas under the curves (AUC) using GraphFunc (on-line Java applet *graph.seriesmathstudy.com)*. AUCs were compared at a depth of 2mm for horizontal measures and 1mm vertical measures. Paired sample t-tests were carried out on the differences.

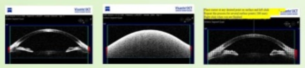

Figure 6: (Left) Horizontal AS-OCT scan output of the eye, (Middle) AS-OCT scan of the cast of the eye, (Right) Horizontal AS-OCT scan showing overlay used for sampling.

Results

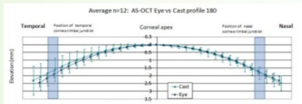

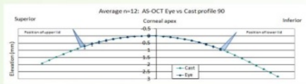

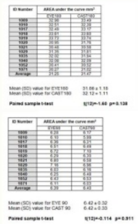

When comparing the eye to the cast, the cast area was slightly larger, but the differences found were insignificant: 0.045±0.16mm² horizontally (AUC depth of 2mm) and +0.018±0.03mm² vertically (AUC depth of 1mm). The area analysed was limited to the corneo-limbal junction horizontally and distance between eyelids vertically.

Conclusions

Modern ocular impression taking has no significant effect on corneal topography, up to 9mm horizontally and 5mm vertically, using slit-scanning methods, 10 minutes after the procedure. When comparing the eye *in-vivo* and its representative cast, the areas under the curve in the principal meridians indicate good reproducibility of eye contour, although this is limited to a more central comparison of contours, up to the corneo-limbal junction, horizontally, and limited by the palpebral aperture, vertically.

References

1. Dunne MC, Davies LN, Wolffsohn JS (2007) The accuracy of cornea and lens biometry using anterior segment optical coherence tomography. *J Biomed Opt* 12(6): 1-5
2. Cairns G, and McGhee C N J (2005) Orbscan computerized topography: Attributes, applications, and limitations. *J Cat Ref Surg* 31: 205-220
3. Kawamorita T, Uozato H, Kamiya K, Bax L, Tsutsui K, Aizawa D, and Shimizu K (2009) Repeatability, reproducibility, and agreement characteristics of rotating Scheimpflug photography and scanning-slit corneal topography for corneal power measurement. *J Cat Ref Surg* 35:127-133
4. Huang D, Li Y, Tang M (2008) Anterior eye imaging with optical coherence tomography. *Optical Coherence Tomography: Technology and applications* eds W Drexler and JG Fujimoto. Springer-Verlag pp 967-971

In collaboration with: Fundamental Research Group, Menicon Co. Ltd, Japan

jonesjm3@cf.ac.uk

Turner J M, Dobson M, Murphy P J, and Purslow C (2010) Does ocular impression taking cause distortion of the ocular surface? In: Tear Film and Ocular Surface Society Conference. Florence, Italy

Invited speaker

35th Annual Hospital Optometrists Conference, Harrogate, Yorkshire.

Which material is best? – A clinical comparison of two materials used for eye impressions.

Jenni Turner[1,2] BSc MCOptom FBDO
Ditipriya Mukhopadhyay[1] BSc MCOptom

[1]Postgraduate Research Optometrist, School of Optometry and Vision Sciences, Cardiff University, CF24 4LU
[2]Optometrist Principal, Cwm Taf Health Board, Royal Glamorgan Hospital, Pontyclun CF72 8XR

Since the early 1930s optical practitioners have been reproducing anterior ocular surface curvature to aid the design of contact lenses required for therapeutic purposes and visual rehabilitation. Ocular impression taking is still the method of choice for patients who have significant structural ocular anomalies for which custom-made contact lenses are required.

This talk will present the results of a recent randomised, masked study that was carried out to compare the materials used in the current practice of impression taking. Clinical conclusions about materials and the efficacy of the procedure will be presented.

References

Adams A J (1987) Axial length elongation, not corneal curvature, as a basis of adult onset myopia. *American Journal of Optometry and Physiological Optics* 64 pp. 150-151

Adams D W, and McBrien N A (1992) Prevalence of myopia and myopic progression in a population of clinical microscopists. *Optometry and Vision Science* 69 pp. 467-473

Akduman E I, Nacke R E, Leiva P M, and Akduman L (2008) Accuracy of ocular axial length measurement with MRI. *Ophthamologica* 222 (6): pp. 397-399

Alex V L (2003) Congenital eye anomalies. *Pediatric Clinics of North America* 50 (1): pp. 55-76

Amano S, Honda N, Amano Y, Yamagami S, Miyai T, Samejima T, Ogata M et al. (2006) Comparison of Central Corneal Thickness Measurements by Rotating Scheimpflug Camera, Ultrasonic Pachymetry, and Scanning-Slit Corneal Topography. *Ophthalmology* 113 (6): pp. 937-941

Anastassiadou V, Dolopoulou V, and Kaloyannides A (1995) The relation between thermal and pH changes in alginate impression materials. *Dental Materials Journal* 11 (3): pp. 182-185

ANSI (2000) American National standard for Safe use of lasers: ANSI Z136.1-2000.*American national standards Institute*. Orlando.

Applegate R A, and Howland H C (1995) Non-invasive measurement of corneal topography. *IEEE Engineering in Medicine and Biology Magazine* 14 pp. 30-42

Apt L (1980) An anatomical reevaluation of rectus muscle insertions. *Transactions of the American Ophthalmological Society* 78 pp. 365-375

Bachmann W, Jean B, Bende T, Seiler T, Csuzda I, and Thiel H J (1993) Silicone impression procedure - principles for determining ablation and healing parameters in-vitro and in-vivo. *Der Ophthalmologe* 90 (2): pp. 178-182

Bachmann W, Jean B, Bende T, Seiler T, Hibst R, and Thiel H J (1992) Silicon cast method for quantification of photoablation. *Journal of Refractive and Corneal Surgery* 8 (5): pp. 363-367

Baïkoff G (2006) Anterior segment OCT and phakic intraocular lenses: A perspective. *Journal of Cataract and Refractive Surgery* 32 (11): pp. 1827-1835

Bailey I L, Bullimore M A, Raasch T W, and Taylor H R (1991) Clinical grading and the effects of scaling. *Investigative Ophthalmology and Vision science* 32 (2): pp. 422-432

Barishak Y R (1992) Embryology of the eye and it's adnexa. In: Straub W [ed.] *Developements in Ophthalmology*. Vol. 24. Basel: Karger.

Bechmann M B, Thiel M J, S N A, Ullrich S, Ludwig K, Kenyon K R, and Ulbig M W (2001) Central corneal thickness measurement with a retinal optical coherence tomography device versus standard ultrasonic pachymetry. *Cornea* 20 (1): pp. 50-54

Belin M W, Cambier J L, Nabors J R, and Ratliff C D (1995) Par Corneal Topography System (Par Cts) - the Clinical-Application of Close-Range Photogrammetry. *Optometry and Vision Science* 72 (11): pp. 828-837

Belin M W, and Khachikian S S (2008) Keratoconus/Ectasia detection with the oculus pentacam: Belin/Ambrosio enhanced ectasia display. *Highlights of Ophthalmology Journal* suppl pp. 3-7

Belin M W, Litoff D, Strods S J, Winn S, and Smith R S (1992) The PAR technology corneal topography system. *Investigative Ophthalmology and Visual Science* 32 (Suppl) pp. 922

Bennett A G, and Rabbetts R B (1991) What does the conventional keratometer measure? *Ophthalmic and Physiological Optics* 11 pp. 239-247

Bergmanson J P G (2006) *Clinical ocular anatomy and physiology*. 13th ed. Houston: Texas eye research and technology centre, University of Houston.

Berkowitz B A, McDonald C, Ito Y, Tofts P S, Latif Z, and Gross J (2001) Measuring the human retinal oxygenation response to a hyperoxic challenge using MRI: Eliminating blinking artifacts and demonstrating proof of concept. *Magnetic Resonance in Medicine* 46 (2): pp. 412-416

Bert R J, Patz S, Ossiani M, D C S, Jara H, Krejza J, and Freddo T F (2006) High-resolution MR imaging of the Human Eye 2005. *Academic Radiology* 13 (3): pp. 368-377

Bibby M M (1976) Computer-assisted photokeratoscopy and contact lens design. *Optician* 171 (4423): pp. 37-43

Bland J M, and Altman D G (1986) Statistical methods for assessing agreement between two methods of clinical measurement. *Lancet* (1): pp. 307-310

Boljika M, Kolar G, and Vidensek J (1994) Toxic side effects of local anaesthetics on the human cornea. *British Journal of Ophthalmology* 78 pp. 386-389

Boote C, Dennis S, Newton R H, Puri H, and Meek K M (2003) Collagen Fibrils Appear More Closely Packed in the Prepupillary Cornea: Optical and Biomechanical Implications. *Investigative Ophthalmology and Visual Science* 44 (7): pp. 2941-2948

Boote C, Hayes S, Abahussin M, and Meek K M (2006) Mapping Collagen Organization in the Human Cornea: Left and Right Eyes Are Structurally Distinct. *Investigative Ophthalmology and Vision science* 47 (3): pp. 901-908

Bourges J-L, Alfonsi N, Laliberté J-F, Chagnon M, Renard G, Legeais J-M, and Brunette I (2009) Average 3-Dimensional Models for the Comparison of Orbscan II and Pentacam Pachymetry Maps in Normal Corneas. *Ophthalmology* 116 (11): pp. 2064-2071

Bowden T J (2009) Developement of Scleral contact lenses.*Contact lenses, the story*. Kent: Bower House Publications, pp. 76-86.

Brammar R, Bullock J, Sunderland S, and Tromans C (1995) Panasil light body impression material study. *Ophthalmic and Physiological Optics* 15 (4): pp. 347

Bron A J, Tripathi R C, and Tripathi B (1997) The eyeball and it's dimensions.*Wolf's anatomy of the eye and orbit*. (8th edn.) London: Chapman and Hall, p. 230.

BSI (1991) *BS EN ISO 4269-2:1991 Dental elastic impression material - Part 2: Specification for alginate impression material*. London: British Standards Institution.

BSI (2000) *BS EN ISO 6873:2000 Dental gypsum products*. London: British Standards Institution.

BSI (2001) *BS EN ISO 4823:2001 Dentistry - Elastomeric impression materials*. London: British Standards Institution.

BSI (2005) *BS EN ISO 19980:2005 Ophthalmic instruments - Corneal topographers*. London: British Standards Institution.

BSI (2006) *BS EN ISO 18369-2:2006 Ophthalmic optics -Contact lenses Part 2: Tolerances*. London: British Standards Institution.

Buckley R J (2010) Decontamination. *Optometry in Practice* 11 pp. 25-29

Buehl W, Stojanac D, Sacu S, Drexler W, and Findl O (2006) Comparison of Three Methods of Measuring Corneal Thickness and Anterior Chamber Depth. *American Journal of Ophthalmology* 141 (1): pp. 7-12

Buehren T, Collins M J, Iskander D R, Davis B, and Lingelbach B (2001) The Stability of Corneal Topography in the Post-Blink Interval. *Cornea* 20 (8): pp. p 826-833

Cairns G, Collins A, and McGhee C N J (2003) A corneal model for slit-scanning elevation topography. *Ophthalmic and Physiological Optics* 23 (3): pp. 193-204

Cairns G, and McGhee C N J (2005) Orbscan computerized topography: Attributes, applications, and limitations. *Journal of Cataract and Refractive Surgery* 31 (1): pp. 205-220

Cairns G, McGhee C N J, Collins M J, Owens H, and Gamble G D (2002) Accuracy of orbscan II slit-scanning elevation topography. *Journal of Cataract and Refractive Surgery* 28 (12): pp. 2181-2187

Carney L G, Mainstone J C, and Henderson B A (1997) Corneal topography and myopia. A cross-sectional study. *Investigative Ophthalmology and Visual Science* 38 (2): pp. 311-320

Chan C C K, Hodge C, and Sutton G (2010) External analysis of the Randleman Ectasia Risk Factor Score System: a review of 36 cases of post LASIK ectasia. *Clinical & Experimental Ophthalmology* 38 (4): pp. 335-340

Chang Y, Wu H-M, and Lin Y-F (2007) The axial misalignment between ocular lens and cornea observed by MRI (I) - at fixed accomodative state. *Vision Research* 47 pp. 71-84

Cheah P S, Norhani M, Bariah M A, Myint M, Lye M S, and Azian A L (2008) Histomorphometric profile of the corneal response to short-term reverse-geometry orthokeratology lens wear in primate corneas: A pilot study. *Cornea* 27 (4): pp. 461-470

Chee W W L, and Donovan T E (1992) Polyvinyl Siloxane Impression Materials - a Review of Properties and Techniques. *Journal of Prosthetic Dentistry* 68 (5): pp. 728-732

Chen D, and Lam A K C (2009) Reliability and repeatability of the Pentacam on corneal curvatures *Clinical and Experimental Optometry* 92 (2): pp. 110-118

Chew C, Chee W W L, and Donovan T E (1993) The influence of temperature on dimensional stability of poly(vinyl siloxane) impression materials. *International Journal of Prosthodontics* 6 pp. 528-532

Cho P, Lam A K C, Mountford J, and Ng L (2002) The performance of four different corneal topographers on normal human corneas and its impact on on orthokeratology lens fitting. *Optometry and Vision Science* 79 (3): pp. 175-183

Clark B (1973) Conventional keratoscopy - a critical view. *Australian journal of Optometry* 56 pp. 140-155

Cohen I, Swartz T, Lin R-A, and Wang M (2006) Axial, elevation and pachymetric mapping. In: Wang M [ed.] *Corneal topography in the wavefront era: A guide for clinical application*. Thorofare, New Jersey: Slack incorporated, pp. 41-46.

Coleman D J, and Trokel S (1969) Direct-recorded IOP variations in a human subject. *Archives of Ophthalmology* 82 pp. 637-640

Cook R C, and Glasscock R E (1951) Refractive and ocular findings in the newborn. *American Journal of Ophthalmology* 34 (10): pp. 1407-1413

Cook W (1986) Alginate dental impression materials:Chemistry, structure and properties. *Journal of Biomedical Materials Research* 20 pp. 1-24

Corbett M C, Rosen E S, and O'Brart D P S (1999a) Assessment of corneal shape.*Corneal Topography: Principles and applications*. (1st edn.) London: BMJ Publishing Group, pp. 3-11.

Corbett M C, Rosen E S, and O'Brart D P S (1999b) Corneal surface disease.*Corneal Topography: Principles and applications*. (1st edn.) London: BMJ Publishing group, pp. 98-107.

Corbett M C, Rosen E S, and O'Brart D P S (1999c) Presentation of topographic information.*Corneal Topography: Principles and applications*. (1st edn.) London: BMJ Publishing group, pp. 31-59.

Corbett M C, Rosen E S, and O'Brart D P S (1999d) Videokeratoscopes.*Corneal topography; Principles and applications*. London: BMJ Books, London, pp. 12-15.

Craig R G (1988) Review of Dental Impression Materials. *Advances in Dental Research* 2 (1): pp. 51-64

Daily L, and Coe R E (1962) Lack of effect of anaesthetic and mydriatic solutions on the curvature of the cornea. *American Journal of Ophthalmology* 53 pp. 49-51

Dallos J (1936) Contact lenses, the 'invisible spectacles'. *Archives of Ophthalmology* 15 pp. 617-623

Daniel F, John X, Sahar S, John D B F, Thomas M B, and Charles L (2002) Imaging caries lesions and lesion progression with polarization sensitive optical coherence tomography. 7 (4): pp. 618-627

Davies L N, Mallen E A H, Wolffson J S, and Gilmartin B (2003) Clinical evaluation of the Shin-Nippon NVision-K5001/Grand Seiko WR-5100K Autorefractor. *Optometry and Vision Science* 80 (4): pp. 320-324

Detorakis E T, Engstrom R E, Straatsma B R, and Demer J L (2003) Functional anatomy of the anophthalmic socket: Insights from magnetic resonance imaging. *Investigative Ophthalmology and Visual Science* 44 (10): pp. 4307-4313

Dingeldein S A, and Klyce S D (1989) The topography of normal corneas. *Archives of Ophthalmology* 107 pp. 512-518

Doughty M J, and Zaman M L (2000) Human Corneal Thickness and Its Impact on Intraocular Pressure Measures, : A Review and Meta-analysis Approach. *Survey of Ophthalmology* 44 (5): pp. 367-408

Douthwaite W A (2006) Measurement of the cornea.*Contact lens optics and lens design*. Philadelphia: Elsevier Ltd, pp. 144-149.

Douthwaite W A, and Burek H (1995) The Bausch and Lomb keratometer does not measure tangential radius of curvature. *Ophthalmic and Physiological Optics* 15 pp. 187-193

Douthwaite W A, and Parkinson A (2009) Precision of Orbscan II assessment of anterior corneal curvature and asphericity. *Journal of Refractive Surgery* 25 pp. 435-443

Douthwaite W A, and Sheridan M (1989) The Measurement of the Corneal Ellipse for the Contact-Lens Practitioner. *Ophthalmic and Physiological Optics* 9 (3): pp. 239-242

Drexler W, and Fujimoto J G (2008) State-of-the-art retinal optical coherence tomography. *Progress in Retinal and Eye Research* 27 (1): pp. 45-88

Dundas M, Walker A, and Woods R L (2001) Clinical grading of corneal staining of non-contact lens wearers. *Ophthalmic and Physiological Optics* 21 (1): pp. 30-35

Dunne M C M, Davies L N, and Wolffsohn J S (2007) Accuracy of cornea and lens biometry using anterior segment optical coherence tomography. *Journal of Biomedical Optics* 12 (6): pp. 1-5

Dupps Jr W J, and Wilson S E (2006) Biomechanics and wound healing in the cornea. *Experimental Eye Research* 83 (4): pp. 709-720

Eames W B, Sieweke C, Wallace G W, and Rogers L B (1979) Elastomeric impression materials: effect of bulk on accuracy. *Journal of Prosthetic Dentistry* 41 pp. 304-307

Eggink F, Beekhuis H, and Nuijts R (2001) Rigid gas-permeable contact lens fitting in LASIK patients for the correction of multifocal corneas. *Graefe's Archive for Clinical and Experimental Ophthalmology* 239 (5): pp. 361-366

Elsheikh A (2010) Numerical modelling of ocular biomechanics.*Understanding corneal biomechanics through experimental assessment and numerical simulation*. New York: Nova Science publishers Inc, pp. 46-48.

Esperjesi F, and Wolffsohn J S (2007) Clinical instrumentation in contact lens practice. In: Phillips A J, and Speedwell L [eds.] *Contact Lenses*. Philadelphia: Butterworth Heinemann Elsevier, pp. 159-162.

Ezekiel D (1983) Gas permeable haptic lenses. *Journal of The British Contact Lens Association* 6 (4): pp. 158-161

Feng Y, Chen S, Stojanovic A, and Wang Q (2012) Comparison of Clinical Outcomes between ‘On-Flap’ and ‘Off-Flap’ Epi-LASIK for Myopia: A Meta-Analysis. *Ophthalmologica* 227 (1): pp. 45-54

Fick A (1888) Eine Contactbrille. *Archive für Augen Heilkinde* 18 pp. 279-289

Fledelius H C, and Christensen A C (1996) Reappraisal of the human ocular growth curve in fetal life, infancy, and early childhood. *British Journal of Ophthalmology* 80 (10): pp. 918-921

Forrester J, Dick A, McMenamin P, and Lee W (1999) Embryology and early developement of the eye and adnexa.*The eye: Basic sciences in practice*. London: W B Saunders, p. 90.

Gemoules G (2008) A novel method of fitting scleral lenses using high resolution optical coherence tomography. *Eye and Contact lens* 34 (2): pp. 80-83

Georgouli T, James T, Tanner S, Shelley D, Nelson M, Chang B, Backhouse O et al. (2008) High-Resolution Microscopy Coil MR-Eye. *Eye* 22 (8): pp. 994-996

Gill F (2010) *Turning the tide for gas permeable contact lenses.* PhD Thesis, Cardiff University.

Glasgow B (2006) *What is the anatomy of the human eyelid* [Online]. Available at: http://medrounds.org.ocular-pathology-study-guide/2006/03/what is the anatomy of the human eyelid [Accessed: 23rd July].

Golding T R, and Brennan N A (1993) Evaluation of cotton thread tear test as a replacement for the schirmer test. *Clinical and Experimental Optometry* 76 pp. 182-186

Gordon R A, and Donzis P B (1985) Refractive development of the human eye. *Archives of Ophthalmology* 103 (6): pp. 785-789

Goto T, Klyce S D, Zheng X, Maeda N, Kuroda T, and Ide C (2001) Gender- and age-related differences in corneal topography. *Cornea* 20 pp. 270-276

Green K, and Tonjum A (1971) Influence of various agents on corneal permeability. *American Journal of Ophthalmology* 72 pp. 897-902

Gullstrand A (1924) Helmholtz's treatise on Physiological Optics. Vol. 1. Rochester, USA: Optical society of America, pp. 9-14.

Hall L A, Young G, Wolffsohn J S, and Riley C (2011) The Influence of Corneoscleral Topography on Soft Contact Lens Fit. *Investigative Ophthalmology and Visual Science* 52 (9): pp. 6801-6806

Hansson O, and Eklund J (1984) A historical review of Hydrocolloids and an investigation of the dimensional accuracy of new alginates for crown and bridge impressions when using stock trays. *Journal of Swedish Dentistry* 8 pp. 81-95

Hay E D, and Revel J-P (1969) Fine structure of the developing avian cornea. In: Wolsky A, and Chen P S [eds.] *Monographs in developemental biology*. Vol. 1. Basel: Karger, S, pp. 1-144.

Hirji N K, Patel S, and Challender M (1989) Human tear film pre-rupture phase time (TP-PRT). A non-invasive technique for evaluating pre-corneal tear film using a novel keratometer mire. *Ophthalmic and Physiological Optics* 9 pp. 139-142

Hogan M J, Alvarado J A, and Weddell J E (1971) Eyeball.*Histology of the human eye*. Philapelphia: Saunders, W B, pp. 47-55.

Holladay J T, Dudeja D R, and Chang J (1999) Functional vision and corneal changes after laser in situ keratomileusis determined by contrast sensitivity, glare testing and corneal topography. *Journal of Cataract and Refractive Surgery* 25 (5): pp. 663-669

Horner D G, Salmon T O, and Soni P (2006) Corneal Topography. In: Benjamin W J [ed.] *Borish's Clinical Refraction*. Philapelphia: Butterworth Heinemann Elsevier, pp. 656-660.

Huang D, and Izatt J A (2008) Physics and fundamentals of Anterior Segment Optical Coherence Tomography. In: Steinert R F, and Huang D [eds.] *Anterior Segment Optical Coherence Tomography*. Thorofare, NJ: Slack Incorporated, pp. 1-9.

Huang D, Li Y, and Tang M (2008) Anterior eye imaging with optical coherence tomography. In: Drexler W, and Fujimoto J G [eds.] *Optical Coherence Tomography - Technology and Applications*. New York: Springer-Verlag, pp. 960-981.

Huang D, Swanson E A, Lin C P, Schuman J S, Stinson W G, Chang W, Hee M R et al. (1991) Optical coherence tomography. *Science* v254 (n5035): pp. p1178(1174)

Imbery T A, Nehring J, Janus C, and Moon P C (2010) Accuracy and dimensional stability of extended-pour and conventional alginate impression materials. *journal of American Dental Association* 141 (1): pp. 32-39

Ip J M, Huynh S C, Kifley A, Rose K A, Morgan I G, Varma R, and Mitchell P (2007) Variation of the Contribution from Axial Length and Other Oculometric Parameters to Refraction by Age and Ethnicity. *Investigative Ophthalmology and Visual Science* 48 (10): pp. 4846-4853

John F S (2000) Safety of Strong, Static Magnetic Fields. *Journal of Magnetic Resonance Imaging* 12 (1): pp. 2-19

Johnson C S, Mian S I, Moroi S, Epstein D, Izatt J, and Afshari N A (2007) Role of Corneal Elasticity in Damping of Intraocular Pressure. *Investigative Ophthalmology and Visual Science* 48 (6): pp. 2540-2544

Johnson M E, and Murphy P J (2005) The effect of instilled fluorescein solution volume on the values and repeatability of TBUT measurements. *Cornea* 24 (7): pp. 811-817

Jonas J B, and Vossmerbäumer U (2004) Femtosecond laser penetrating keratoplasty with conical incisions and positional spikes. *Journal of Refractive Surgery* 20 pp. 397-401

Jongsma F H M, De Brabander J, Hendrikse F, and Stultiens B A T (1998) Development of a Wide Field Height Eye Topographer: Validation on Models of the Anterior Eye Surface. *Optometry and Vision Science* 75 (1): pp. 69-77

Karpecki P M (2006) Bausch and Lomb Orbscan II/IIz Anterior segment analysis system. In: Wand M [ed.] *Corneal topography in the wavefront era: A guide for clinical application*. Thorofare, NJ: Slack Incorporated, pp. 191-197.

Keay L, Edwards K, Naduvilath T, Taylor H R, Snibson G R, Forde K, and Stapleton F (2006) Microbial Keratitis: Predisposing Factors and Morbidity. *Ophthalmology* 113 (1): pp. 109-116

Kiely P M, Carney L G, and Smith G (1983) Menstral cycle variations of corneal topography and thickness. *American journal of optometric and physiological optics* 60 pp. 822-829

Kim S W, Byun Y J, Kim E K, and Kim I T (2007) Central corneal thickness measurements in unoperated eyes and eyes after PRK for myopia using Pentacam, Orbscan II and Ultrasonic pachymetry. *Journal of Refractive Surgery* 2007 (33): pp. 1701-1707

Kim S W, Sun H J, Chang J H, and Kim E K (2009) Anterior segment measurements using Pentacam and Orbscan II 1 to 5 years after refractive surgery. *Journal of Refractive Surgery* 25 pp. 1091-1097

King-Smith P E, Fink B A, Fogt N, Nichols K K, Hill R M, and Wilson G S (2000) The Thickness of the Human Precorneal Tear Film: Evidence from Reflection Spectra. 41 (11): pp. 3348-3359

Koretz J F, Strenk S A, Strenk L M, and Semmlow J L (2004) Scheimpflug and high-resolution magnetic resonance imaging of the anterior segment: a comparative study. *Journal of the Optical Society of America A. Optics and Image Science* 21 (3): pp. 346-354

Lamb J, and Sabell A (2007) The History of Contact Lenses. In: Phillps A J, and Speedwell L [eds.] *Contact Lenses*. (5th edn.) Butterworth Heinemann Elsevier, pp. 1-20.

Le Chi H (2008) Hyscan 45c scanning accuracy of anterior ocular surface casts*. Personal communication.*

Lehmann S P (1967) Corneal areas used in keratometry. *Optician* 154 pp. 261-264

Leibowitz H M (2000) The Red Eye. *New England Journal of Medicine* 343 (5): pp. 345-351

Leite M T, Alencar L M, Gore C, Weinreb R N, Sample P A, Zangwill L M, and Medeiros F A (2010) Comparison of Corneal Biomechanical Properties Between Healthy Blacks and Whites Using the Ocular Response Analyzer. *American Journal of Ophthalmology* 150 (2): pp. 163-168

Lemke A J, Hosten N, Wiegel T, Prinz R D, Richter M, Bechrakis N E, Foerster P I et al. (2001) Intraocular metastases: differential diagnosis from uveal melanomas with high resolution MRI using a surface coil. *European Radiology* 11 (12): pp. 2593-2601

Lewinstein I, and Craig R G (1990) Accuracy of impression materials measured with a vertical height gauge. *Journal of Oral Rehabilitation* 17 (303-310):

Leyland M (2004) Validation of Orbscan II posterior corneal curvature measurment for intraocular lens power calculation. *Eye* 18 pp. 357-360

Lindsay R, Smith G, and Atchison D (1998) Descriptors of corneal shape. *Optometry and Vision Science* 75 pp. 156-158

Liu Z, Huang A J, and Pflugfelder S C (1999) Evaluation of corneal thickness and topography in normal eyes using the Orbscan corneal topography system. *British Journal of Ophthalmology* 83 (7): pp. 774-778

Llorente L, Barbero S, Merayo J, and Marcos S (2004) Changes in corneal and total aberrations induced by LASIK surgery for hyperopia. *Journal of Refractive Surgery* 20 pp. 203-216

Logan N S, Gilmartin B, Wildsoet C F, and Dunne M C M (2004) Posterior Retinal Contour in Adult Human Anisomyopia. 45 (7): pp. 2152-2162

Ludlam W M, Wittenberg S, Rosenthal J, and Harris G (1967) Photographic analysis of the ocular dioptric components. *American Journal of Optometry and Archives of American Academy of Optometry* 44 pp. 276-296

Lyle W M, and Page C (1975) Possible adverse effects from local anaesthetics and the treatment of these reactions. *American Journal of Optometry and Physiological Optics* 52 pp. 736-744

Mandell R B (1961) Profile methods of measuring corneal curvature. *Journal of the American Optometric Association* 32 pp. 627-631

Mandell R B (1963) Methods to measure the peripheral corneal curvature, part 3: Ophthalmometry. *Journal of American Optometric Association* 33 pp. 889-892

Mandell R B (1969) Position and curvature of the corneal apex. *American Journal of Optometry and Archives of American Academy of Optometry* 46 (1): pp. 25-29

Mandell R B (1988) Corneal topography.*Contact lens practice*. Springfield, Illanois: Charles C Thomas, pp. 25-39.

Mandell R B (1992) The Enigma of the Corneal Contour. 18 (4): pp. 267-273

Mandikos M N (1998) Polyvinyl siloxane impression materials: An update on clinical use. *Australian Dental Journal* 43 (5): pp. 428-434

Marriott P J (1966) An analysis of the global contours and haptic contact lens fitting. *British Journal of Physiological Optics* 23 (1): pp. 1-40

Marsh-Tootle W L, and Frazier M G (2006) Infants, toddlers and children. In: Benjamin W J [ed.] *Borish's clinical refraction*. (2nd edn.) Philadelphia: Butterworth Heinemann elsevier, p. 1396.

Matsuda L M, Woldorff C L, Kame R T, and Hayashida J K (1992) Clinical Comparison of Corneal Diameter and Curvature in Asian Eyes with Those of Caucasian Eyes. 69 (1): pp. 51-54

Maurice D M (1969) Cornea and sclera. In: Davson H [ed.] *Physiology of the eye*. Boston: Little, Brown and Co, pp. 6-15.

Maurice D M (1972) The location of the fluid pump in the cornea. *Journal of Physiology (London)* 221 pp. 43-45

Mazzanti G, Daniele C, Tita B, Vitali F, and Signore A (2005) Biological evaluation of a polyvinyl siloxane impression material. *Dental Materials* 21 (4): pp. 371-374

McBrien N A, Cornell L M, and Gentle A (2001) Role of the sclera in the developement and pathological complications of myopia. *Progressive retinal eye research* 22 pp. 307-338

McBrien N A, and Millodot M (1987) A biometric investigation of late onset myopic eyes. *Acta Ophthalmologica* 65 pp. 461-468

McCaffery S, Simon E M, Fischbein N J, Rowley H A, Shimikawa A, Lin S, and O'Brien J M (2002) Three-dimensional high-resolution magnetic resonance imaging of ocular and orbital malignancies. *Archives of Ophthalmology* 120 (6): pp. 747-754

McMonnies C W, and Boneham G C (2007) Corneal curvature stability with increased intraocular pressure. *Eye and Contact lens* 33 pp. 130-137

McMonnies C W, and Schief W S (2006) Biomechanically coupled curvature transfer in normal and keratoconus corneal collagen. *Eye and Contact lens* 32 (1): pp. 51-62

Meek K M (2008) The cornea and sclera. In: Fratzl P [ed.] *Collagen - Structure and Mechanics*. New York: Springer, pp. 359-393.

Meek K M, and Leonard D W (1993) Ultrastructure of the corneal stroma: a comparative study. *Biophysical Journal* 64 (1): pp. 273-280

Meller D, Peters K, and Meller K (1997) Human cornea and sclera studied by atomic force microscopy. *Cell and Tissue Research* 228 pp. 111-118

Menicon (2010) *Zone Quick: An Integral Part of The LASIK Pre-op Regimen* [Online]. Available at: http://www.menicon.com/pro/news/menicon-horizons-newsletter/206-zone-quick-an-integral-part-of-the-lasik-pre-op-regimen [Accessed: 20/06/11].

Meredith M A, and Goldberg S J (1986) Contractile differences between muscle units in the medial rectus and lateral rectus muscles in the cat. *Journal of Neurophysiology* 56 (1): pp. 50-62

Miller M W (1975) Syneresis in alginate impression materials. *British Dental Journal* 139 pp. 425-430

Mishima S (1965) Some physiological aspects of the precorneal tear film. *Archives of Ophthalmology* 73 pp. 223-241

Moergeli J J R, Fraleigh E M, Ostrowski J S, and Pelleu J G B (1985) Irritation of ocular tissue by irreversible hydrocolloids. *The Journal of Prosthetic Dentistry* 54 (2): pp. 286-290

Morgan P B, and Maldonado-Codina C (2009) Corneal staining: Do we really understand what we are seeing? *Contact Lens and Anterior Eye* 32 (2): pp. 48-54

Morrow R M, Brown J C E, Stansbury B E, deLorimier J A, Powell J M, and Rudd K D (1971) Compatibility of alginate impression materials and dental stones. *The Journal of Prosthetic Dentistry* 25 (5): pp. 556-566

Moseley I, Brant-Zawadski M, and Mills C (1983) Nuclear magnetic resonance imaging of the orbit. *British Journal of Ophthalmology* 67 pp. 333-342

Murphy P J, Lau J S C, Sim M M L, and Woods R L (2007) How red is a white eye? Clinical grading of normal conjunctival hyperaemia. *Eye* 21 pp. 633-638

Murube J, and Rivas L (2003) Impression cytology on conjunctiva and cornea in dry eye patients establishes a correlation between squamous metaplasia and dry eye clinical severity. *European Journal of Ophthalmology* 13 (2): pp. 115-127

Nallamuthu N, Branden M, and Patel M P (2006) Dimensional changes of alginate dental materials. *Journal of Material Science: Materials in Medicine* 17 (12): pp. 1205-1210

Nelson J D (1982) Ocular surface impressions using cellulose acetate filter material. Ocular Pemphigoid. *Survey of Ophthalmology* 27 (1): pp. 67-69

Németh J, Erdélyi B, and Csákány B (2001) Corneal topography changes after a 15 second pause in blinking. *Journal of Cataract and Refractive Surgery* 27 (4): pp. 589-592

Norman R E, Flanagan J G, Rausch S M K, Sigal I A, Tertinegg I, Eilaghi A, Portnoy S et al. Dimensions of the human sclera: Thickness measurement and regional changes with axial length. *Experimental Eye Research* 90 (2): pp. 277-284

Norn M S (1970) Micropunctate fluorescein vital staining of the cornea *Acta Ophthalmologica* 48 pp. 108-118

O'Brien W J (2002) Dental Materials and their selection.*Chapter 7: Impression Materials*. (3rd edn.) Michigan, USA: Quintessential Publishing Co Inc, pp. 163-202.

Obata T, Uemura K, Nonaka H, Tamura M, Tanada S, and Ikehira H (2006) Optimizing T2-weighted magnetic resonance sequences for surface coil microimaging of the eye with regard to lid, eyeball and head moving artefacts. *Magnetic Resonance Imaging* 24 pp. 97-101

Obrig T E (1938) Molded contact lenses. *Archives of Ophthalmology* 19 pp. 735-758

Obrig T E (1943) A new ophthalmic impression material. *Archives of Ophthalmology* 30 pp. 626-630

Oh W Y, Yun S H, Tearney G J, and Bouma B E (2005) 115kHz tuning repetition rate ultrahigh-speed wavelength-swept semiconductor laser. *Optics Letters* 30 (23): pp. 3159-3161

Olsen T W, Aaberg S Y, Geroski D H, and Edelhauser H F (1998) Human sclera: Thickness and surface area. *American Journal of Ophthalmology* 125 (2): pp. 237-241

Ousley P J, and Terry M A (1996) Hydration effects on corneal topography. *Archives of Ophthalmology* 114 pp. 181-185

Pakravan M, Parsa A, Sanagou M, and Parsa C F (2007) Central corneal thickness and correlation to optic disc size: a potential link for susceptibility to glaucoma. *British Journal of Ophthalmology* 91 (1): pp. 26-28

Parthasaradhi S T V, Derakhshani R, Hornak L A, and Schuckers S A C (2005) Time-series detection of perspiration as a liveness test in fingerprint devices. *Systems, Man, and Cybernetics, Part C: Applications and Reviews, IEEE Transactions on* 35 (3): pp. 335-343

Patel H, Gilmartin B, Cubbidge R P, and Logan N S (2011) In vivo measurement of regional variation in anterior scleral resistance to Schiotz indentation. *Ophthalmic and Physiological Optics* 31 (5): pp. 437-443

Patz S, Bert R J, Frederick E, and Freddo T F (2007) T1 and T2 measurements of the fine structures of the in vivo and enucleated human eye. *Journal of Magnetic Resonance Imaging* 26 (3): pp. 510-518

Pau H W, Lankenau E, Just T, and Hüttmann G (2008) Imaging of Cochlear Structures by Optical Coherence Tomography (OCT). Temporal bone experiments for an OCT-guided cochleostomy technique. *Laryngo- Rhino- Otologie* 87 (9): pp. 641-646

Pham D T, and Le Chi H (2008) Reverse engineering - Hardware and Software. In: Raja V, and Fernandes K J [eds.] *Reverse Engineering - An industrial perspective*. London: Springer-Verlag, pp. 33-69.

Pinero D P, Belen Plaza A, and Alio J L (2008) Anterior segment biometry with 2 imaging technologies: Very-high-frequency ultrasound scanning versus optical coherence tomography. *Journal of Cataract and Refractive Surgery* 34 (1): pp. 95-102

Porter J, Guirao A, Cox I G, and Williams D R (2001) Monochromatic aberrations of the human eye in a large population. *Journal of the Optical Society of America A. Optics and Image Science* 18 pp. 1793-1803

Powers J M, and Sakaguchi R L (2006) Impression Materials.*Craig's Restorative Dental Materials*. (12th edn.) St Louis: Mosby, pp. 269-312.

Pullum K W (1987) Feasibility study for the production of gas permeablescleral lenses using ocular impression techniques. *Journal of The British Contact Lens Association* 10 (Supplement 1): pp. 35-39

Pullum K W (2002) Use of Tresident as an ocular impression material*. Personal communication.*

Pullum K W (2007) Eye Impressions. In: Phillips A J, Speedwell L, and Morris J [eds.] *Contact Lenses*. (5 edn.) Elsevier Butterworth-Heineman, p. 343.

Pullum K W, Parker J H, and Hobley A J (1989) The josef dallos award lecture 1989development of gas permeable scleral lenses produced from impressions of the eye. *Journal of The British Contact Lens Association* 12 (Supplement 2): pp. 77-81

Pullum K W, Whiting M A, and Buckley R J (2005) Scleral contact lenses: The expanding role. *Cornea* 24 (3): pp. 269-277

Pult H (2008) *The predictive ability of clinical tests for dry eye in contact lens wear.* PhD Thesis, Cardiff University.

Quantock A J, and Young R D (2008) Development of the corneal stroma and collagen-proteoglycan associations that help define its structure and function. *Developmental Dynamics* 237 (10): pp. 2607-2621

Raasch T W, Bailey I L, and Bullimore M A (1998) Repeatability of Visual Acuity Measurement. *Optometry and Vision Science* 75 (5): pp. 342-348

Rabbetts R B (1998a) Measurement of ocular dimensions.*Bennett & Rabbetts' Clinical visual optics*. Oxford: Butterworth-Heinemann, pp. 380-388.

Rabbetts R B (1998b) Measurement of ocular dimensions.*Bennett and Rabbetts' Clinical visual optics*. Oxford: Butterworth-Heinemann Ltd, pp. 395-397.

Rabinowitz Y S, Yang H, Brickman Y, Akkina J, Riley C, Rotter J I, and Elashoff J (1996) Videokeratography database of normal human corneas. *British Journal of Ophthalmology* 80 (7): pp. 610-616

Radhakrishnan S, Rollins A M, Roth J E, Yazdanfar S, Westphal V, Bardenstein D S, and Izatt J A (2001) Real-Time Optical Coherence Tomography of the Anterior Segment at 1310 nm. *Archives of Ophthalmology* 119 (8): pp. 1179-1185

Ragain J C, Grosko M L, Raj M, Ryan T N, and Johnston W M (2000) Detail reproduction, contact angles, and die hardness of elastomeric impression and gypsum die material combinations. *International Journal of Prosthodontics* 13 pp. 214-220

Read S A, Collins M J, Carney L G, and Franklin R J (2006a) The Topography of the Central and Peripheral Cornea. *Investigative Ophthalmology and Visual Science* 47 (4): pp. 1404-1415

Read S A, Collins M J, Carney L G, and Iskander D R (2006b) The morphology of the palpebral fissure in different directions of vertical gaze. *Optometry and Vision Science* 83 (10): pp. 715-722

Reinstein D Z, Archer T J, Silverman R H, and Coleman D J (2006) Accuracy, repeatability, and reproducibility of Artemis very high-frequency digital ultrasound arc-scan lateral dimension measurements. *Journal of Cataract and Refractive Surgery* 32 (11): pp. 1799-1802

Richdale K, Wassenaar P, Teal Bluestein K, Abduljalil A, Christoforidis J A, Lanz T, Knopp M V et al. (2009) 7 Tesla MR imaging of the human eye in vivo. *Journal of Magnetic Resonance Imaging* 30 (5): pp. 924-932

Roberts C (1994) Characterisation of inherent error in the spherically-biased corneal topography systen in mapping a radially aspheric surface. *Refractive and Corneal Surgery* 10 pp. 103-116

Rolfs M (2009) Microsaccades: Small steps on a long way. *Vision Research* 49 (20): pp. 2415-2441

Rowsey J J, Reynolds A E, and Brown R (1981) Corneoscope. *Archives of Ophthalmology* 99 pp. 1093-1100

Ruben M (1975) Introduction to kerato-topography and keratometry.*Contact lens practice; Visual, therapeutic and prosthetics*. London: Bailliere Tyndall.

Ruskell G L, and Bergmanson J P G (2007) Anatomy and physiology of the cornea and related structures. In: Phillips A J, and Speedwell L [eds.] *Contact Lenses*. Philadelphia: Butterworth Heinmann Elsevier, pp. 21-31.

Saad A, and Gatinel D (2010) Topographic and Tomographic Properties of Forme Fruste Keratoconus Corneas. *Investigative Ophthalmology and Visual Science* 51 (11): pp. 5546-5555

Salmon T O, and Thibos L N (2002) Videokeratoscope–line-of-sight misalignment and its effect on measurements of corneal and internal ocular aberrations. *Journal of the Optical Society of America A. Optics and Image Science* 19 (4): pp. 657-668

Santodomingo - Rubido J, Mallen E A H, Gilmartin B, and Wolffsohn J S (2002) A new non-contact optical device for ocular biometry. *British Journal of Ophthalmology* 86 pp. 458-462

Saunders H (1982) The possible correlation of intraocular pressure and the volume of the anterior chamber. *Ophthalmic and Physiological Optics* 2 (2): pp. 119-134

Savini G, Barboni P, Carbonelli M, and Hoffer K J (2011) Accuracy of a dual Scheimpflug analyzer and a corneal topography system for intraocular lens power calculation in unoperated eyes. *Journal of Cataract and Refractive Surgery* 37 (1): pp. 72-76

Scheiner C (1619) *Oculus; hoc est, fundamentum opticum; in quo ... radius sua visioni in oculo sedes decernitur; anguli visiorii ingenium a aperitur etc.* Oeniponti.

Schueler A O, Hosten N, Bechrakis N E, Lemke A J, Foerster P, Felix R, Foerster M H et al. (2003) High resolution magnetic resonance imaging of retinoblastoma. *British Journal of Ophthalmology* 87 (3): pp. 330-335

Segal O, Barkana Y, Hourovitz D, Behrman S, Kamun Y, Avni I, and Zadok D (2003) Scleral contact lenses may help where other modalities fail. *Cornea* 22 (4): pp. 308-310

Shankar H, Taranath D, Santhirathelagan C T, and Pesudovs K (2008) Anterior segment biometry with the Pentacam: Comprehensive assessment of repeatability of automated measurements. *Journal of Cataract and Refractive Surgery* 34 pp. 103-113

Shaw A J, Collins M J, Davis B A, and Carney L G (2008) Eyelid pressure: Inferences from corneal topographic changes. In: *ARVO*. Fort Lauderdale 1026/D882, 27th April. IOVS.

Sheppard A L, and Davies L N (2010) Clinical evaluation of Grand Seiko Auto Ref/Keratometer WAM-5500. *Ophthalmic and Physiological Optics* 30 pp. 143-151

Siegwart J T, and Norton T T (1999) Regulation of the mechanical properties of tree shrew sclera by the visual environment. *Vision Research* 39 (2): pp. 387-407

Singh K D, Logan N S, and Gilmartin B (2006) Three-dimensional modeling of the human eye based on magnetic resonance imaging. *Investigative Ophthalmology and Visual Science* 47 (6): pp. 2272-2279

Smith G (2006) Refraction and visual acuity measurements: what are their measurement uncertainties? *Clinical and Experimental Optometry* 89 (2): pp. 66-72

Smith T W (1977) Corneal topography. *Documenta Ophthalmologica* 43 (2): pp. 249-276

Smolek M K, and Klyce S D (1997) The principles of computerised videokeratoscopy. In: McGhee C N [ed.] *Excimer Lasers in Ophthalmology*. London: Martin Dunitz Ltd, pp. 79-96.

Smolek M K, and Klyce S D (2005) Goodness-of-prediction of Zernike polynomial fitting to corneal surfaces. *Journal of Cataract & Refractive Surgery* 31 (12): pp. 2350-2355

Snepvangers A (2010) *Meye Optics - Eye surface profiler* [Online]. Available at: http://meyeoptics.com/Eye_Surface_Profiler.html [Accessed: 13/11/2011].

Snook R K (1995) Pachymetry and true topography using Orbscan system.*Corneal Topography: State of the Art*. New Jersey: Slack Inc, pp. 90-103.

Soong H K, and Malta J B (2009) Femtosecond Lasers in Ophthalmology. *American Journal of Ophthalmology* 147 (2): pp. 189-197.e182

Srivannaboon S, Ling L K, Cheng A C K, and Bor F H (2007) A clinician's guide to slit-scanning corneal topography. Tan Tock Seng: Dr Fam Han Bor, pp. 63-75.

Stenström S (1948) Investigation of the variation and the correlation of the optical elements. *American Journal of Optometry and Archives of American Academy of Optometry* 58 pp. 1-71

Storey J K (1972) The possible use of polysulphide rubber impression material in contact lens work. *Ophthalmic Optician* 12 (October): pp. 1017-1018

Storey J K (1987) The use of panasil-C silicone rubber impression material in contact lens work. *Optometry Today* 27 pp. 711-714

Storey J K, and Vale M J (1970) A rubber moulding material for ocular impressions in contact lens work. *Ophthamic Optician* 10 pp. 948

Strenk S A, Semmlow J L, Strenk L M, Munoz P, Gronlund-Jacob J, and DeMarco J K (1999) Age-related changes in human ciliary muscle and lens: a magnetic resonance imaging study. *Investigative Ophthalmology and Vision science* 40 pp. 1162-1169

Strenk S A, Strenk L M, and Guo S (2006) Magnetic resonance imaging of aging, accomodating, phakic, and pseudophakic ciliary muscle diameters. *Journal of Cataract and Refractive Surgery* 32 pp. 1792-1798

Sunderraj P (1992) Clinical Comparison of Automated and Manual Keratometry in Preoperative Ocular Biometry. *Eye* 6 pp. 60-62

Swartz T, Liu Z G, Yang X, Zhang M, and Wang M (2006) Topographic technologies. In: Wang M [ed.] *Corneal topography in the wavefront era: A guide for clinical application*. Thorofare, NJ: Slack Incorporated, pp. 33-39.

Tiffany J M, Grande E F, and Todd B S (2004) Measurement of scleral curavture by scheimpflug photography. *Investigative Ophthalmology and Vision science* 45 (Suppl 1): pp. U930

Tomlinson A, and Schwartz C (1979) The position of the corneal apex in the normal eye. *American Journal of Optometry and Physiological Optics* 56 pp. 236-240

Van der Worp E, Graf T, and Caroline P (2010) Exploring beyond the corneal borders. *Contact lens Spectrum* June (June): pp. 1-7

Vawda F, Ranatunga K W, and Geeves M A (1995) Pressure-induced changes in the isometric contractions of single intact frog muscle fibres at low temperatures. *Journal of Muscle Research and Cell Motility* 16 (4): pp. 412-419

Wang M, Hill S, and Swartz T (2006) Three-dimensional stereo corneal topographic system: The AstraMax. In: Wang M [ed.] *Corneal topography in the wavefront era*. Thorofare, New Jersey: Slack Incorporated, pp. 23-24.

Warnicki J W, Rehkof P G, Curtin S A, Burns S A, Arffa R C, and Stuart J C (1988) Corneal topography using computer analysed rasterstereographic images. *Applied Optics* 27 pp. 1135-1140

Watson P G, Hazleman B, Pavésio C, and Green W R (2004) Anatomical, physiological and comparative aspects. In: Fam P [ed.] *The sclera and systemic disorders*. Elsevier Ltd, pp. 23-27.

Watson P G, and Young R D (2004) Scleral structure, organisation and disease. A review. *Experimental Eye Research* 78 (3): pp. 609-623

Wichmann W (2002) Magnetic Resonance Imaging (MRI). In: Müller-Forell W S [ed.] *Imaging of Orbital and Visual Pathway Pathology*. Berlin: Springer-Verlag, pp. 18-24.

Williams J R, and Craig R G (1988) Physical properties of addition silicones as a function of composition. *Journal of Oral Rehabilitation* 15 pp. 639-650

Wirtschafter J D, Berman E L, and McDonald C S (1992) Fundamentals of MRI and CT scanning.*Magnetic Resonance Imaging and Computerised Tomography: Clinical Neuro-orbital anatomy*. Vol. 6. San Francisco: American Academy of Ophthalmology, pp. 21-27.

Wolffsohn J S (2008) Anterior eye imaging. In: Doshi S, and Harvey W [eds.] *Ophthalmic Imaging*. Philadephia: Butterworth Heinemann Elsevier, p. 77.

Worp E v d, Brabander J d, Lubberman B, Marin G, and Hendrikse F (2002) Optimising RGP lens fitting in normal eyes using 3D topographic data. *Contact Lens and Anterior Eye* 25 (2): pp. 95-99

Worp E v d, Graf T, and Caroline P (2010) Exploring beyond the corneal borders. *Contact lens Spectrum* June pp. 1-7

Yamamoto S, Hitomi J, Shigeno M, Sawaguchi S, Abe H, and Ushiki T (1997) Atomic force microscopic studies of isolated collagen fibrils of bovine cornea and sclera. *Archives of Histology and Cytology* 60 pp. 371-378